

# Advances in Coastal HF and Microwave (S- or X-Band) Radars

Guest Editors: Weimin Huang, Xiongbin Wu, Björn Lund, and Khalid El-Darymli



---



# **Advances in Coastal HF and Microwave (S- or X-Band) Radars**

International Journal of Antennas and Propagation

---

**Advances in Coastal HF and  
Microwave (S- or X-Band) Radars**

Guest Editors: Weimin Huang, Xiongbin Wu, Björn Lund,  
and Khalid El-Darymli



---

Copyright © 2017 Hindawi Publishing Corporation. All rights reserved.

This is a special issue published in "International Journal of Antennas and Propagation." All articles are open access articles distributed under the Creative Commons Attribution License, which permits unrestricted use, distribution, and reproduction in any medium, provided the original work is properly cited.

## Editorial Board

Ana Alejos, Spain  
Mohammad Ali, USA  
Jaume Anguera, Spain  
Rodolfo Araneo, Italy  
Alexei Ashikhmin, USA  
Herve Aubert, France  
Paolo Baccarelli, Italy  
Xiulong Bao, Ireland  
T. Björninen, Finland  
Stefania Bonafoni, Italy  
Djuradj S. Budimir, UK  
Paolo Burghignoli, Italy  
Shah Nawaz Burokur, France  
Giuseppe Castaldi, Italy  
Luca Catarinucci, Italy  
Felipe Catedra, Spain  
Marta Cavagnaro, Italy  
Deb Chatterjee, USA  
Shih Yuan Chen, Taiwan  
Yu Jian Cheng, China  
Renato Cicchetti, Italy  
Riccardo Colella, Italy  
Lorenzo Crocco, Italy  
Claudio Curcio, Italy  
Francesco D'Agostino, Italy  
M. Elena de Cos Gómez, Spain  
Tayeb A. Denidni, Canada  
Giuseppe Di Massa, Italy  
Michele D'Urso, Italy  
Hala A. Elsadek, Egypt

Francisco Falcone, Spain  
M. Ferrando Bataller, Spain  
Flaminio Ferrara, Italy  
Vincenzo Galdi, Italy  
Claudio Gennarelli, Italy  
Farid Ghanem, Algeria  
Sotirios K. Goudos, Greece  
Rocco Guerriero, Italy  
Kerim Guney, Turkey  
Song Guo, Japan  
Mohamed Himdi, France  
Tamer S. Ibrahim, USA  
Mohammad T. Islam, Malaysia  
M. Ramlee Kamarudin, Malaysia  
Slawomir Koziel, Iceland  
Luis Landesa, Spain  
Ding-Bing Lin, Taiwan  
Angelo Liseno, Italy  
P. Lombardo, Italy  
Giampiero Lovat, Italy  
Lorenzo Luini, Italy  
Atsushi Mase, Japan  
Diego Masotti, Italy  
C. F. Mecklenbräuker, Austria  
Massimo Migliozi, Italy  
A. T. Mobashsher, Australia  
Ananda S. Mohan, Australia  
J.-M. Molina-Garcia-Pardo, Spain  
G. Montisci, Italy  
Marco Mussetta, Italy

N. Nasimuddin, Singapore  
Miguel Navarro-Cia, UK  
Mourad Nedil, Canada  
Symeon Nikolaou, Cyprus  
Giacomo Oliveri, Italy  
Pablo Otero, Spain  
A. D. Panagopoulos, Greece  
I. Park, Republic of Korea  
Josep Parrón, Spain  
Matteo Pastorino, Italy  
M. Pieraccini, Italy  
Xianming Qing, Singapore  
Ahmad Safaai-Jazi, USA  
S. Safavi-Naeini, Canada  
M. Salazar-Palma, Spain  
Stefano Selleri, Italy  
Prabhakar Singh, India  
R. Solimene, Italy  
Gino Sorbello, Italy  
Seong-Youp Suh, USA  
Sheng Sun, Hong Kong  
Larbi Talbi, Canada  
L. Tarricone, Italy  
Parveen Wahid, USA  
Wen-Qin Wang, China  
Shiwen Yang, China  
Yuan Yao, China  
Jingjing Zhang, Denmark

# Contents

---

**Advances in Coastal HF and Microwave (S- or X-Band) Radars**

Weimin Huang, Xiongbin Wu, Björn Lund, and Khalid El-Darymli  
Volume 2017, Article ID 3089046, 2 pages

**Cross Spectral Analysis of CODAR-SeaSonde Echoes from Sea Surface and Ionosphere at Taiwan**

Chien-Ya Wang, Ching-Lun Su, Kang-Hung Wu, and Yen-Hsyang Chu  
Volume 2017, Article ID 1756761, 14 pages

**The Vertical Ionosphere Parameters Inversion for High Frequency Surface Wave Radar**

Xuguang Yang, Changjun Yu, Aijun Liu, Linwei Wang, and Taifan Quan  
Volume 2016, Article ID 8609372, 8 pages

**Application of HF Radar in Hazard Management**

Mal Heron, Roberto Gomez, Bernd Weber, Anna Dzvonkovskaya, Thomas Helzel, Nicolas Thomas, and Lucy Wyatt  
Volume 2016, Article ID 4725407, 14 pages

**A General Range-Velocity Processing Scheme for Discontinuous Spectrum FMCW Signal in HFSWR Applications**

Mengguan Pan, Baixiao Chen, and Minglei Yang  
Volume 2016, Article ID 2609873, 13 pages

**Observation of Zenneck-Like Waves over a Metasurface Designed for Launching HF Radar Surface Wave**

Florent Jangal, Nicolas Bourey, Muriel Darces, François Issac, and Marc Hélier  
Volume 2016, Article ID 6184959, 5 pages

**Wind Speed Inversion in High Frequency Radar Based on Neural Network**

Yuming Zeng, Hao Zhou, Hugh Roarty, and Biyang Wen  
Volume 2016, Article ID 2706521, 8 pages

**A New Method of Wave Mapping with HF Radar**

Lijie Jin, Biyang Wen, and Hao Zhou  
Volume 2016, Article ID 4135404, 7 pages

**Study of Ocean Waves Measured by Collocated HH and VV Polarized X-Band Marine Radars**

Zhongbiao Chen, Yijun He, and Wankang Yang  
Volume 2016, Article ID 8257930, 12 pages

**Bistatic High Frequency Radar Ocean Surface Cross Section for an FMCW Source with an Antenna on a Floating Platform**

Yue Ma, Weimin Huang, and Eric W. Gill  
Volume 2016, Article ID 8675964, 9 pages

## Editorial

# Advances in Coastal HF and Microwave (S- or X-Band) Radars

**Weimin Huang,<sup>1</sup> Xiongbin Wu,<sup>2</sup> Björn Lund,<sup>3</sup> and Khalid El-Darymli<sup>4</sup>**

<sup>1</sup>*Faculty of Engineering and Applied Science, Memorial University, St. John's, NL, Canada A1B 3X5*

<sup>2</sup>*School of Electronic Information, Wuhan University, Wuhan, Hubei 430072, China*

<sup>3</sup>*Rosenstiel School of Marine and Atmospheric Science, University of Miami, Miami, FL 33149, USA*

<sup>4</sup>*Northern Radar Inc., St. John's, NL, Canada A1B 3E4*

Correspondence should be addressed to Weimin Huang; [weimin@mun.ca](mailto:weimin@mun.ca)

Received 24 October 2016; Accepted 24 October 2016; Published 28 February 2017

Copyright © 2017 Weimin Huang et al. This is an open access article distributed under the Creative Commons Attribution License, which permits unrestricted use, distribution, and reproduction in any medium, provided the original work is properly cited.

Ground-based high frequency (3–30 MHz) surface wave radar (HFSWR) and microwave (S-band: ~3 GHz or X-band: ~10 GHz) marine radar have been widely used in ocean remote sensing for over four decades. HFSWR systems are able to monitor sea surface currents, winds, waves, and targets “over the horizon” (up to 300 km) due to the strong interaction between HF radio signals and ocean gravity waves. Compact microwave marine radar covers the “line-of-sight” area with a relatively high spatial resolution finer than 10 m and can be deployed on ships or land. This enables S-band or X-band radar to be an ideal sensor for marine navigation or provide finer sea surface currents, waves, and winds measurement for the area of interest.

Due to increasing development of HF radar networks worldwide and new applications of regular microwave marine radars for expanding coastal ocean observing capabilities and improving safety of human marine activity, the purpose of this special issue is to present the state-of-the-art developments and associated challenges in ocean remote sensing applications by leading researchers and practitioners of both HF and microwave radars.

Eight papers related to HF radar research are included in this issue. Both the first- and second-order bistatic radar ocean cross sections for an antenna on a floating platform have been derived for the case of a frequency-modulated continuous-wave (FMCW) source in the paper titled “Bistatic High Frequency Radar Ocean Surface Cross Section for an FMCW Source with an Antenna on a Floating Platform.” The effect of platform motion on the radar cross sections for an FMCW waveform is investigated and compared with that for a pulsed source based on simulated data. The results

have important implications in the application of increasing bistatic HFSWR for ocean remote sensing and will possibly improve corresponding performance. In the paper titled “Observation of Zenneck-Like Waves over a Metasurface Designed for Launching HF Radar Surface Wave,” an infrared method is used to visualize a Zenneck-like wave above a metasurface located on a dielectric slab based on simulation and experimentation. The work may provide a way to enhance surface wave excitation for HFSWR. A general range-velocity processing scheme for the discontinuous spectrum-FMCW (DS-FMCW) HF radar applications is presented in the paper titled “A General Range-Velocity Processing Scheme for Discontinuous Spectrum FMCW Signal in HFSWR Applications.” The effectiveness of the proposed scheme is validated based on satisfactory target detection results from simulated data. Ionospheric clutter contamination has been a problem that affects the performance of HFSWR for a long time. Based on field data, the characteristics of the first-order sea echoes and ionospheric interferences are analyzed in the paper titled “Cross Spectral Analysis of CODAR-SeaSonde Echoes from Sea Surface and Ionosphere at Taiwan.” The results show that the sea and ionospheric echoes in the CODAR-SeaSonde observed cross power spectrum may be distinguished according to the discrepancies in the characteristics of the coherence and phases between the sea and ionospheric echoes. In the paper titled “The Vertical Ionosphere Parameters Inversion for High Frequency Surface Wave Radar,” an inversion method utilizing range-Doppler spectrum of HFSWR radar is proposed to extract ionosphere information, such as the electron density, the plasma frequency of irregularities, and the plasma drift velocity

of irregularities, from the ionospheric clutter. An artificial neural network (ANN) based method to estimate the wind speed from HF radar data is presented in the paper titled "Wind Speed Inversion in High Frequency Radar Based on Neural Network." The method utilizes the ANN to map the relationship between the wind speed and the sea state parameters. The results from a one-month-long 13 MHz SeaSonde HFSWR's data collected in 2012 showed that the ANN is an efficient tool for wind speed estimation from HFSWR data in operational scenarios. The paper titled "A New Method of Wave Mapping with HF Radar" retrieves the significant wave height from the ratio of the second-harmonic peak to the Bragg peak. This method can be applied to both narrow and broad-beam HF radars, and results are in good agreement with reference buoy data. The review paper titled "Application of HF Radar in Hazard Management" illustrates many important applications of HFSWR in improving the management of the coastal environment such as pollution control and tsunami monitoring.

Although only one paper associated with microwave radar research is collected in this special issue, the interest in such radar has been increasing significantly. In the paper titled "Study of Ocean Waves Measured by Collocated HH and VV Polarized X-Band Marine Radars," significant wave height estimates from marine radars with different polarization have been compared against buoy measurements. The results obtained with VV polarization are found to be more accurate, especially under low wind conditions.

## **Acknowledgments**

The editors would like to thank all the authors for contributing their interesting work associated with the topic of this special issue and the anonymous reviewers for their time and effort expended on providing valuable comments.

*Weimin Huang  
Xiongbin Wu  
Björn Lund  
Khalid El-Darymli*

## Research Article

# Cross Spectral Analysis of CODAR-SeaSonde Echoes from Sea Surface and Ionosphere at Taiwan

Chien-Ya Wang,<sup>1</sup> Ching-Lun Su,<sup>2</sup> Kang-Hung Wu,<sup>2</sup> and Yen-Hsyang Chu<sup>2,3</sup>

<sup>1</sup>Department of Optoelectric Physics, Chinese Culture University, Taipei, Taiwan

<sup>2</sup>Institute of Space Science, National Central University, Chung-Li, Taiwan

<sup>3</sup>Taiwan Ocean Research Institute, National Applied Research Laboratories, Kaohsiung, Taiwan

Correspondence should be addressed to Yen-Hsyang Chu; [yhchu@jupiter.ss.ncu.edu.tw](mailto:yhchu@jupiter.ss.ncu.edu.tw)

Received 7 July 2016; Revised 19 September 2016; Accepted 10 October 2016; Published 23 February 2017

Academic Editor: Weimin Huang

Copyright © 2017 Chien-Ya Wang et al. This is an open access article distributed under the Creative Commons Attribution License, which permits unrestricted use, distribution, and reproduction in any medium, provided the original work is properly cited.

It is well known that the primary targets responsible for first-order sea echoes observed by a High-Frequency (HF) radar are the advancing and receding ocean waves with the wavelengths at Bragg scales. However, in light of the fact that the ionospheric sporadic E (Es) and F layers may be present in the viewing range of the HF radar for ocean wave detection, the radar returns reflected from the F and Es layers may significantly contaminate the ocean wave power spectrum. The characteristics of the first-order sea echoes and ionospheric interferences measured by the CODAR-SeaSonde in Taiwan area are analyzed and presented in this article. The coherences and phases of the normalized cross spectra of the sea and ionospheric echoes between different pairs of the receiving channels are calculated, respectively. One of the striking features presented in this report is that the ionospheric echo heights scaled from the ionogram observed by the Chung-Li ionosonde are about 30 km lower than those observed by the DATAN CODAR-SeaSonde. It is also found that the coherences of the sea echoes are generally smaller than those of the ionospheric echoes by about 15% on average, and the phase fluctuations (standard deviations) of the sea echoes are substantially larger than those of the ionospheric layer reflection echoes. In addition, statistics show that the sum of the mean phases of the ionospheric echoes between the three receiving channel pairs is approximately zero, while it is not for the sea echoes. These results seem to suggest that the use of the discrepancies in the characteristics of the coherences and phases between the sea and ionospheric echoes may provide a potential means to be helpful to distinguish the sea and ionospheric echoes in the CODAR-SeaSonde observed cross power spectrum.

## 1. Introduction

Taiwan is a large island covering an area of about 35,883 km<sup>2</sup> with a total coastline length of approximately 1,200 km. This island is in a subtropical monsoon region with frequent occurrences of mesoscale systems in spring, tropical cyclone (typhoon) and convective storms during the summer, and frontal system with strong wind velocity and heavy rainfall in the winter. These various wind systems may drive local sea surface water to form varied and different currents in the ocean surrounding Taiwan Island. In addition to the wind-driven surface currents caused by the abovementioned weather systems, the interaction between the western boundary current and the persistent warm current Kuroshio combined with the rough and rugged seafloor topography makes the current system around Taiwan more complex

[1]. Besides the main island, there are more than 100 small islands distributed in the near coast region 100 km from the main island, which may play a role in altering the current velocity and direction. Consequently, the ocean condition is complicated, and the safety of the ships voyaging nearby Taiwan will be potentially threatened. In order to routinely monitor the current and the sea state surrounding Taiwan, the Taiwan Ocean Radar Observing System (TOROS) that consists of more than 17 sets of CODAR-SeaSonde radars was established in 2009 and operated and maintained by Taiwan Ocean Research Institute (TORI), National Applied Research Laboratories (NARL). The map of the TOROS-observed hourly surface current velocity vectors around Taiwan can be found on the website <http://med.tori.org.tw/TOROS/>.

Since the first observation of the Doppler spectrum of sea surface wave echoes recorded by a HF radar operating

at 13.56 MHz made by Crombie [2], the field of radar oceanography that aims to remotely measure and monitor the sea current and the sea state by using radars operated at various frequencies has emerged and nowadays becomes an indispensable field to the community of marine science and technology. The observed Doppler spectrum of the sea echoes is primarily composed of two types of spectral components originating from different sources. One is the first-order spectral components that result from Bragg scatter (or, more precisely, diffraction) of the traveling ocean gravity waves with the wavelength of one-half of the incident radar wavelength and characterized by two very sharp spectral peaks with almost identical Doppler frequency shifts but opposite signs. The angular Doppler frequency shift  $\omega_B (=2\pi f_B, f_B$  is Doppler frequency shift) of the first-order spectral peaks is given below [2]:

$$\omega_B = \pm \sqrt{2gk_0}, \quad (1)$$

where the plus (minus) sign of  $\omega_B$  represents the ocean wave propagating toward (away) the radar,  $g$  is the gravitational acceleration ( $9.8 \text{ m s}^{-2}$ ), and  $k_0$  is the incident radar wave number ( $k_0 = 2\pi/\lambda$ ,  $\lambda$  is radar wavelength). For a HF radar with a central frequency of 4.58 MHz, the corresponding Bragg diffraction frequency  $f_B$  of the sea echo is 0.218 Hz. Another spectral type is the second-order components that are present in a form of a spectral continuum surrounding the first-order spectral peaks, which are thought to be generated through an indirect two or more steps' scattering (or reflecting) process of the radar waves that are generated by the ocean waves with relevant wave vectors and eventually the scattered waves are received by the radar [3].

In addition to the spectral components of the sea echoes, the radar returns reflected from ionospheric F and sporadic E (Es) layers can also frequently appear in the Doppler spectrum observed by a HF radar with echo range larger than 200 km. The Es layers at low and middle latitudes, which mainly occur in a height range from about 90 to 125 km, are primarily formed through the convergence effect of neutral wind shear on ionization particles [4]. The neutral winds in ionospheric E region at low latitude over Taiwan are dominated by semidiurnal tides that are characterized by a descending rate of 0.9–1.6 km/hr [4]. The maximum frequency of the HF wave that can be reflected by the sporadic E layer can be as large as 30 MHz or more, depending on solar activity, incident angle of the EM wave, and local ionospheric condition [5]. It is noteworthy that the Es layer occurs most frequently in summer during the local time (LT) between 6 LT and around local midnight. There is a tendency for the Es layer to occur less frequently in winter during the morning period 3–6 LT. In addition to the Es layer, the ionospheric echoes reflected from normal F layers, that is, F1 and F2 layers that occasionally appear in the height below 250 km, may occasionally be detected by CODAR-SeaSonde and consequently contaminate the Doppler spectrum of the sea echoes backscattered from ocean waves. The ionospheric echoes may seriously contaminate and interfere the sea echo Doppler spectrum, leading to severe degradation of the

quality of the retrieved current and sea state beyond the range of about 90 km where the ionospheric layers exist.

Because the echoing mechanisms responsible for the sea echoes and ionospheric echoes are very different, it is expected that the characteristics of the radar returns backscattered from sea surface waves will be different from those reflected by the ionospheric layers. Note that almost all of the ionospheric echoes received by the FMCW CODAR-SeaSonde operating at High-Frequency (HF) band are reflected from overhead ionospheric layers usually containing electron density irregularities at various scales that are moving in the ionosphere. As a result, the ionospheric echoes in a range-Doppler frequency-intensity plot is characterized by relatively intense backscatter, limited range extent, small mean Doppler shift, and broad spectral width. In addition, the second-order sea echoes and radio interferences from unknown sources may occasionally appear in the spectral window that the ionospheric echoes occupy in Doppler spectral domain. Therefore, developing a reliable and robust approach to discern and separate ionospheric echoes from these nonionospheric signals is very crucial to improve the data quality of the CODAR-SeaSonde. In this article, an attempt is made to investigate the discrepancies in the amplitudes (coherences) and phase angles of the cross spectra between sea echoes and interference and ionospheric layer echoes. It appears that the coherence and the phase angle may serve as effective indicators for the discrimination of the echoes from various sources in Doppler spectrum. This article is organized as follows. The data employed for this research and the background of cross spectral analysis are described in Section 2. Statistical properties of amplitudes and phases of the cross spectra for the sea echoes and ionospheric echoes are presented in Section 3. Discussion is made in Section 4, and conclusions are drawn in Section 5.

## 2. Signal Processing and Cross Spectral Analysis of Radar Returns

The radar returns employed in this study are observed by the CODAR-SeaSonde located at DATAN ( $25.02^\circ\text{N}, 121.06^\circ\text{E}$ ), Taiwan, for the period 15 June–31 July, 2015. The radar parameters set for the radar observation are listed below. The central frequency of the radar wave is 4.58 MHz (corresponding to a wavelength of 65.5 m), the bandwidth  $B$  of the transmitted linear frequency modulation (FM) pulse is 40.439 KHz, the FM pulse repetition frequency PRF (or pulse swept rate) is 1 Hz, the number  $M$  of samples (or range bins) in a FM pulse for range determination is 4096 at a sampling interval  $\Delta t$  of 243  $\mu\text{s}$ , the blank period is 1.9456 ms, and the blank delay is 8.55  $\mu\text{s}$ . Corresponding to the radar parameters given above, the characteristics of the radar returns can be specified below: the nominally maximum range ( $R_m = cT/4\Delta tB$ ,  $T$  is the FM pulse length) set for the radar observation is about 7500 km; the practical range extent that the radar echoes can be collected is from 12.9 km to 291.84 km; the range resolution ( $\Delta R = c/2B$ ,  $c$  is light speed,  $B$  is bandwidth) of the radar returns at each range bin is 3.7 km; the time resolution of the observed radar returns is 1 s; the Nyquist frequency

( $f_{Ny} = 1/T$ ) of the observed Doppler radar spectrum is 0.5 Hz and the corresponding maximum Doppler velocity of the radar echoes that the radar can resolve is about 16.4 m/s.

In order to obtain information on range and Doppler frequency of the radar returns, the processes of analyzing radar signal of a FMCW radar are very different from those of a conventional pulse radar operating at a specific carrier frequency. For the latter, the target range is determined from the propagation time of the pulsed radar returns from the target. The echoes are detected by the radar receiver to generate complex quadrature signal (i.e., in-phase and quadrature, I/Q in short, components) after passing through mixer and matched filter. The I/Q components are, respectively, sampled by analog-to-digital converters (ADC) at a time step controlled by a precise master clock to obtain the information of range gates with a range resolution  $\Delta R$  given by  $\Delta R = c\tau/2$  and  $\tau$  is the transmitted radar pulse length. The Doppler frequency shifts of the complex radar returns at a specific range bin are then calculated in terms of Fourier transform algorithm. As for the CODAR-SeaSonde FMCW radar implemented at DATAN, the sampled output signals of a FM pulse from the mixer and analog-to-digital convertor (ADC) of the receiver are first processed by a 4096-point FFT algorithm to obtain spatial distribution of the echo amplitude over range within the FM pulse. The Fourier transform of the time series of the complex radar returns of the successive FM pulses at a specific range bin for each receiving channel is then performed by using a 1024-point FFT algorithm to obtain a 17-min averaged Doppler spectrum that contains the Doppler velocity information of the targets at this range bin. We then calculate the cross spectra of the radar returns for every pairs of the three receiving channels. The normalized complex cross spectrum  $N_{ij}$  of the complex autospectra  $S_i$  and  $S_j$  for the  $i$ th and  $j$ th receiving channels has been widely used by the community of radar oceanography to extract the sea surface information from the radar returns detected by difference receiving channels, which is defined as follows:

$$N_{ij} = \frac{\langle S_i S_j^* \rangle}{\langle |S_i|^2 \rangle^{1/2} \langle |S_j|^2 \rangle^{1/2}} = A \exp(i\Delta\phi_{ij}), \quad (2)$$

where  $S_i$  and  $S_j$  are, respectively, the autospectra of the  $i$ th and  $j$ th receiving channels,  $\langle S_i S_j^* \rangle$  is the ensemble averaged cross spectrum of  $S_i$  and  $S_j$ , \* represents complex conjugate,  $A$  is coherence defined as the modulus of the normalized  $\langle S_i S_j^* \rangle$  that signifies correlation of the echoes between  $S_i$  and  $S_j$ , and  $\Delta\phi_{ij}$  is the phase difference of the echoes between  $i$ th and  $j$ th receiving channels that is defined below:

$$\Delta\phi_{ij} = \phi_i - \phi_j. \quad (3)$$

Note that the value of  $A$  tends to be small and fluctuates randomly in the spectral frequency domain for uncorrelated random noises or radar returns from diffusive targets distributed uniformly and randomly in echoing region, and its value is expected to approximate 1 for the echoes from highly localized and structured targets with high signal-to-noise ratio (SNR). Theoretical analysis shows that the magnitude

of the coherence is a function of signal-to-noise ratio (SNR) and the number of raw spectra for the ensemble average [6, 7]. From  $\Delta\phi_{ij}$ , the spatial location of the target in echoing region can be obtained, provided the lengths of the baselines between spaced antenna pairs are known. It is evident that, for a radar with 3 receiving channels, the summation of the phase differences of the radar echoes from distinct and localized target should comply with the following relation:

$$\Sigma\Delta\phi = \Delta\phi_{21} + \Delta\phi_{32} + \Delta\phi_{13} \sim 0. \quad (4)$$

However, for the echoes from diffusive targets or random noises, their phase differences between the receiving channels will not satisfy the above relations.

In general, the HF radar Doppler spectrum of the sea surface echoes is dominated by two prominent first-order spectral peaks generated from the backscattered radar returns from the ocean waves with a Bragg wavelength at one-half of the incident radar wavelength. The ocean current can be estimated from the Doppler shift of the first-order peaks with respect to their theoretical Bragg frequencies in the spectral domain [8]. In addition to the first-order spectral components, the second-order spectral peaks that are present in a form of a spectral continuum surrounding the first-order spectral peaks can usually be seen in the sea echo Doppler spectrum. The second-order echoes are thought to be generated through a two-step scattering process [3]. Namely, the incident radar wave vector  $\mathbf{k}_0$  first interacts with the ocean wave  $\mathbf{k}$  to produce an intermediate scattering radar wave vector  $\mathbf{K}$  that subsequently interacts with another pertinent ocean wave vector  $\mathbf{k}'$  to generate second scattered radar wave that can be detected by the radar. The ocean wave vectors that interact with the radar waves and are eventually responsible for the generation of the second-order echoes should fulfill the following constraint [3]:

$$\vec{k}' + \vec{k} = -2\vec{k}_0. \quad (5)$$

Therefore, it is anticipated from (5) that there are a number of combinations of the ocean wave vectors  $\mathbf{k}$  and  $\mathbf{k}'$  that can produce the second-order echoes. In light of the fact that the second-order echoes are resulting from the ocean waves with different propagating directions and wavelengths, their coherences are expected to be low in values and phase differences of the cross spectra are disorganized in the spectral domain.

### 3. Statistical Results of Cross Spectral Analysis

In order to perform cross spectral analysis for obtaining coherence and phase difference of the radar echoes, a 1024-sec time series (corresponding to a duration of 17 minutes) of the radar echoes at 1-sec time resolution at every range bin is first divided into 4 segments and each segment of the time series is analyzed by a 256-point FFT to obtain raw Doppler spectra. As a result, the spectral resolution of the raw Doppler spectrum will be approximately 0.004 Hz. The coherence and phase difference of the radar echoes for each pair of the receiving channel are then computed by taking coherent

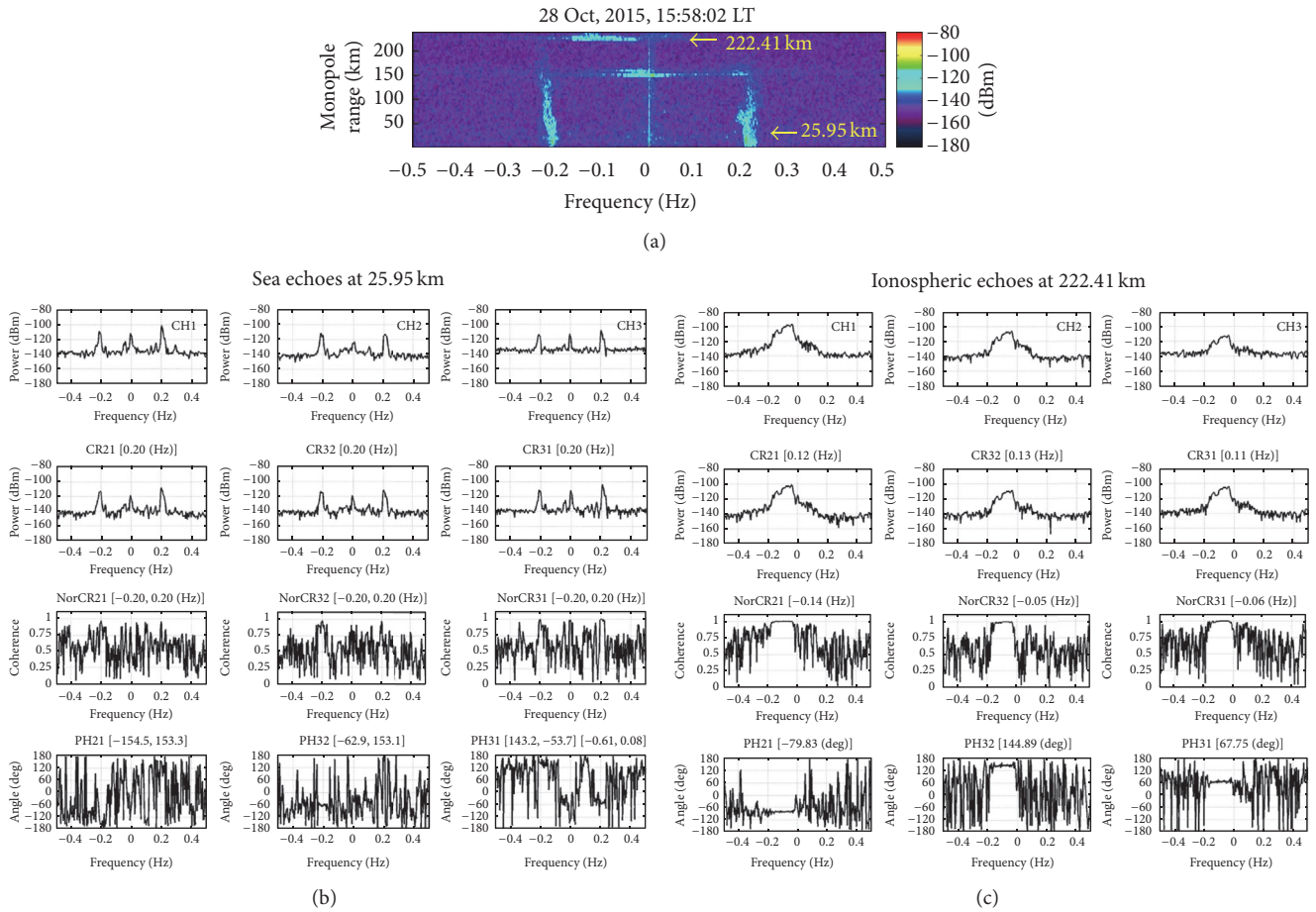


FIGURE 1: (a) shows examples of the range-Doppler frequency-intensity distribution of the sea and the ionospheric echoes recorded by the receiving channel 3 of the DATAN CODAR-SeaSonde on 15 October, 2015, at 15:58:02 LT, and (b, c) present Doppler power autospectra (first row), cross spectra (second row), coherence spectra (third row), and phase spectra (bottom row) of the normalized cross spectra for the sea echoes at 25.95 km (b) and ionospheric echoes at 222.41 km (c), respectively.

averages of the 4 successive cross spectra in accordance with (2). Note that the coherence value will be equal to 1 if no ensemble average of the cross spectrum is performed. Figure 1(a) shows an example of the range-Doppler intensity distribution of the Doppler power spectra of the sea and the ionospheric echoes recorded by the receiving channel 3 of the DATAN CODAR-SeaSonde on 28 October, 2015, at 15:58:02 LT, and Figures 1(b) and 1(c) present the Doppler power autospectra (first row) of the sea echoes of the three receiving channels at range of 25.95 km, the cross spectra (second row), the coherence spectra (third row), and phase spectra (bottom row) of the normalized cross spectra of the sea echoes at the same range, respectively. Note that the autospectra labeled by CH1 and CH2 (i.e., channel 1 and 2) are the observations of the two receiving loop antennas and the autospectrum marked by CH3 (i.e., channel 3) is the one observed by the monopole antenna of the CODAR-SeaSonde. The cross spectra marked by CR21, CR32, and CR31 are, respectively, the spectra computed from the autospectral pairs of CH1-CH2, CH2-CH3, and CH3-CH1 in accordance with (2). As shown in Figure 1(a) and the first and second rows in Figure 1(b), two distinct spectral peaks located at around  $\pm 0.218$  Hz are

clearly seen, which correspond to advancing and receding ocean gravity waves with wavelength of 32.75 m that are responsible for the first-order radar echoes through Bragg backscatter. From the coherence spectra (the third row of Figure 1(b)), it is clear to see that the distribution patterns of the coherences are very organized and structured in the frequency band characterized by high coherence value and intense echo power, signifying strong correlation between the sea echoes detected by different pairs of the receiving channels inside these Doppler frequency bands. Outside the frequency bands, the coherences decrease considerably in values and vary irregularly with the Doppler frequency. Nevertheless, as shown in bottom row of Figure 1(b), the phases of the cross spectra fluctuate randomly with the Doppler frequency.

Analogous to the sea echoes, Figure 1(a) presents examples of the Doppler spectra of the ionospheric echoes at ranges 150 km and 220 km, respectively, that occurred on October 28, 2015, at 15:58 LT. The former is believed to originate from the reflection of sporadic E layer and the latter is thought to reflect from F layer. In order to validate the sources of these ionospheric echoes, concurrent ionogram

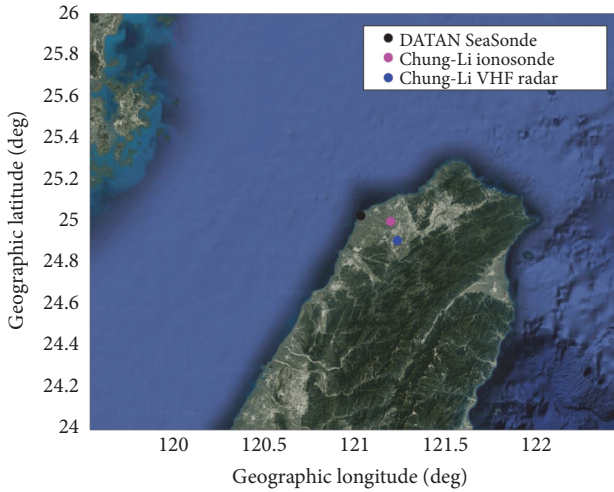


FIGURE 2: Geographic locations of DATAN CODAR-SeaSonde, Chung-Li ionosonde, and Chung-Li VHF radar site.

observed by the Chung-Li ionosonde that is an instrument vertically transmitting a FM pulse with a frequency range of 0.5–30 MHz to exclusively detect the echoes from ionospheric layers and electron density irregularities is adopted for comparison. This ionosonde is routinely operated and maintained by National Communication Council (NCC). For the characteristics of the Chung-Li ionosonde, please refer to Chu et al. [9]. The geographic locations of the DATAN SeaSonde and the Chung-Li ionosonde are shown in Figure 2. Note that the echo traces recorded by ionogram can reveal the vertical structures of different ionospheric layers, including layer height, peak electron density, and plasma irregularities. Figure 3 presents the Chung-Li ionosonde-observed ionogram that is almost concurrent with the CODAR-SeaSonde echoes presented in Figure 1. The echo traces marked by O-wave and X-wave represent the right-hand polarized ordinary wave and left-hand polarized extraordinary wave, respectively, that are separated from a linear polarized wave when the wave propagates into ionosphere [10]. From Figure 3, the critical frequency of the F layer is about 15.2 MHz that is scaled from the normal O-wave trace at the point of maximum frequency, which corresponds to a peak electron density of  $2.87 \times 10^{12}$  electron/m<sup>3</sup>. For the waves with frequencies larger than the critical frequency, they will penetrate through the ionosphere and are not detected by the ionosonde. In addition to the normal F layer traces, the 2nd and 3rd reflections of the F layer traces can also be seen occasionally in the ionogram, which are formed by multiple bounces of the waves between ionospheric F layer and earth surface. In addition, the virtual heights of the ionospheric echoes reflected from F and Es layers are, respectively, at around 150 and 220 km, which are consistent with the ranges of the ionospheric echoes observed by CODAR-SeaSonde shown in Figure 1. A comparison between Figures 1 and 3 supports the assertion that the CODAR-SeaSonde-observed ionospheric echoes at ranges around 150 and 220 km shown in Figure 1 are indeed resulting from the reflections of the

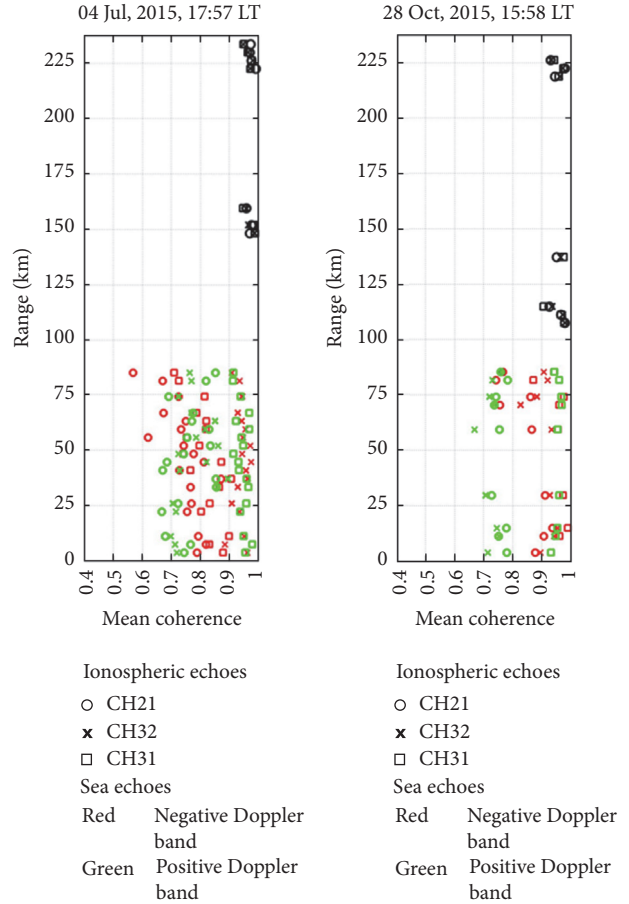


FIGURE 3: Two examples comparing coherences between sea echoes (symbols in red and green) and ionospheric echoes (symbols in black), in which red (green) symbols represent the coherences of the sea echoes computed from the negative (positive) Doppler spectral components and black symbols signify the coherences of the ionospheric echoes calculated from a Doppler spectral band from  $-0.2$  Hz to  $0.2$  Hz.

ionospheric F and Es layers, respectively. A more detailed comparison in occurrence of ionospheric Es layer echoes between ionosonde and CODAR-SeaSonde will be made later in Discussion.

As shown in Figure 1, the spectral bandwidths of the ionospheric echoes are so broad that they extend to a frequency range covering the Doppler spectral bands of the sea echoes. Obviously, these ionospheric echoes with broad spectral width that may interfere with the sea echoes will lead to inaccurate estimates of ocean current and wave parameters. Moreover, an example presented in Figure 1 shows that the mean Doppler velocity of the ionospheric echoes at 222.41 km is noticeably different from zero, irrespective of the ionospheric echoes that primarily come from vertical reflection from the overhead ionospheric layers. The ionospheric echoes with relatively large mean Doppler velocities observed by CODAR-SeaSonde in Taiwan area are not uncommon. In order to realize the discrepancies in the coherences between sea echoes and ionospheric echoes, we compare the range variations of the coherences for these two

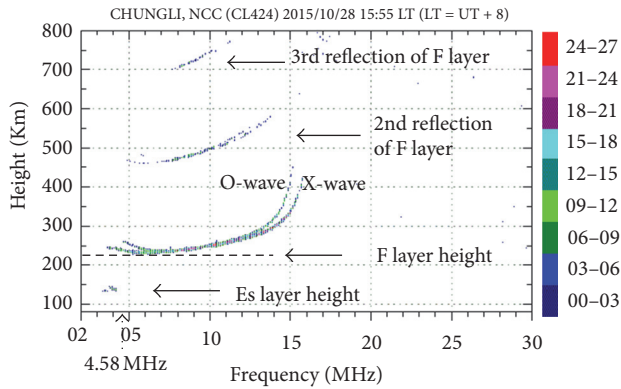


FIGURE 4: Chung-Li ionosonde-observed ionogram that is concurrent with the CODAR-SeaSonde-measured echoes shown in Figures 1 and 2. The echo traces marked by O-wave and X-wave represent the right-hand polarized ordinary wave and left-hand polarized extraordinary wave, respectively. The F layer height is indicated by a dashed line, and the central operation frequency 4.58 MHz of the DATAN SeaSonde is marked by an arrow.

types of the echoes. Figure 4 shows two examples of the variations of the coherences over range for the sea echoes (symbols in red and green) and ionospheric echoes (symbols in black) for different pairs of the receiving channels, in which the symbols open circle, cross, and open square represent the coherences of the receiving channel pairs of CH21, CH32, and CH31, respectively. The DATAN SeaSonde echo data we used for analysis are taken on July 4, 2015, 17:57 LT, and October 28, 2015, 15:58 LT, for 17 minutes. The red (green) symbols represent the coherences computed from the first-order sea echoes with negative (positive) Doppler spectral components within the frequency bands  $\pm(0.15-0.25)$  Hz and black symbols signify the coherences of the ionospheric echoes calculated from a Doppler spectral band from  $-0.2$  Hz to  $0.2$  Hz. The ionospheric and sea echoes that are selected for calculating coherences are required to have their peak spectral powers in respective spectral bands greater than the noise level by 15 dBm. In this study, the noise level is estimated by taking average of the lowest 30% of the spectral power components in the whole Doppler spectral domain. From Figure 4, it is clearly seen that the coherences of the ionospheric echoes are concentrated in a small range with high coherence values, whereas those of the sea echoes are spread in a wide range and substantial disagreements in the coherences between three receiving channel pairs are evident. This feature strongly implies that the coherence can be used as an plausible parameter to separate the ionospheric and sea echoes.

Figure 5 compares the histograms of the mean Doppler frequencies (a, c) and the spectral widths (b, d) of the ionospheric echoes (a, b) and those of the sea echoes (c, d). The arrow shown in (c) indicates the location of the theoretical Bragg resonant frequency of the first-order sea echoes at 0.218 Hz for comparison. As shown, relative to this nominal Bragg frequency, the range of the change in the observed Doppler frequencies of the first-order sea echoes is about

0.025 Hz. However, it is about 0.2 Hz for the ionospheric echoes, compared to their mean Doppler frequency that is very close to 0 Hz. On average, the spectral width of the ionospheric echoes is about one order of magnitude larger than that of the first-order sea echoes. Note that the spectral resolution of the Doppler spectrum employed in this study is about 0.004 Hz that is about one order of magnitude narrower than the spectral width of the first-order sea echoes. Obviously, in addition to the windowing effect, some factors play major roles in broadening the Doppler spectrum of the first-order sea echoes, which are needed to explore in near future.

Figure 6 compares the histograms of the coherences of the ionospheric echoes (a, b) with those of sea echoes (c, d), in which only the results from the receiving channel pair 1 and 2 are displayed. The vertical dashed lines in each panel mark the coherence values of 0.6 (a, c) and 0.7 (b, d) on respective histograms for comparison. Figures 6(a) and 6(c) show the histograms of the coherences that are obtained by taking average of the 256 coherence values of the whole cross spectrum for each range bin, and Figures 6(b) and 6(d) are the averaged results of the coherence values estimated from the spectral components in the respective spectral bands that are utilized to obtain Figures 1, 4, and 5. It is evident from Figure 6 that, no matter what means are employed, the coherences of the sea echoes are systematically smaller than those of the ionospheric echoes by a factor of about 15% in average. An examination shows that about 95% of the whole cross spectrum-averaged coherences for the ionospheric echoes are greater than 0.6, and the percentage of those for the sea echoes with the coherence values greater than 0.6 is about 16%. However, this distinct discrepancy between ionospheric and sea echoes cannot be seen in the statistic results of the coherence values averaged within respective spectral bands, as shown in Figures 6(b) and 6(d). This result seems to suggest that the whole cross spectrum-averaged coherence may be a potential indicator used for discriminating the ionospheric and sea echoes in the CODAR-SeaSonde observed power spectrum.

Figure 7 presents histograms of the phases of the cross spectra for different receiving channel pairs, in which (b) is the results of ionospheric (sea) echoes and the phases are averaged for the spectral components within the respective frequency bands that are similar to those used in Figures 1, 4, and 5. The three vertical dashed lines shown in (a) mark the mean phases of the respective major groups of the data. The summation of the mean phases of the three receiving channels pairs is about  $5^\circ$ , very close to zero. This result supports the nature of the ionospheric echoes reflected from distinct layers that the phase relation of the echoes between different pairs of the receiving channels fulfills the expression of (4). Note that there are three minor groups of the phase histograms with relative small number of the data points that seems to follow the phase relation given by (4) as well. It is believed that these groups of the data are also the ionospheric echoes that come from the ionospheric targets different from those of the major groups. Examining the distributions of the phases of the sea echoes presented in Figure 7(b) demonstrates that their phases do not follow

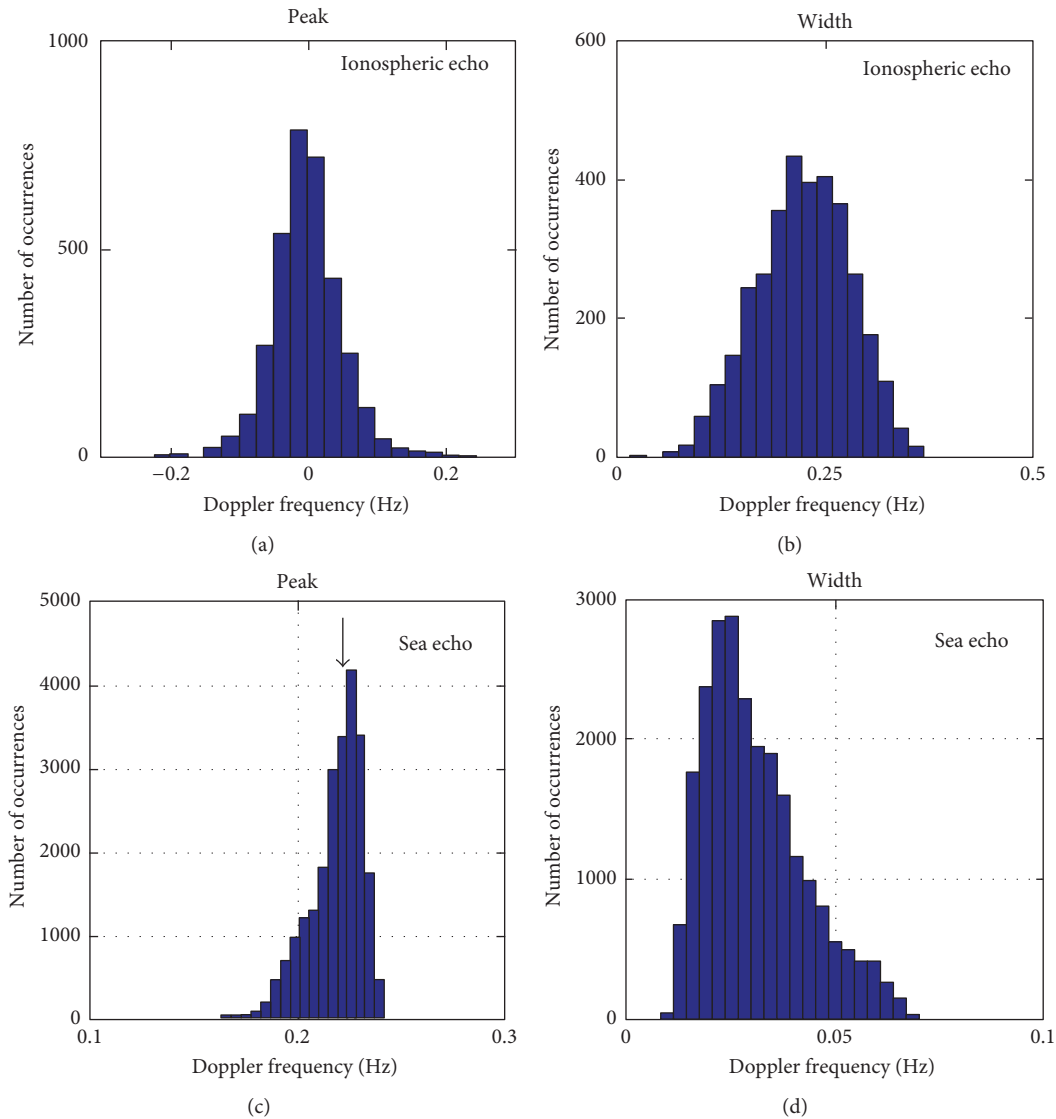


FIGURE 5: Comparison of the histograms of the spectral peak locations (a, c) and the spectral widths (b, d) of the ionospheric echoes (a, b) with those of the sea echoes (c, d). The arrow shown in bottom left panel indicates the location of the first-order Doppler spectral peak of the sea echoes at 0.218 Hz for comparison.

the relation of (4). Obviously, this is because the ocean waves distribute randomly in the echoing region over sea; the echoing process through the diffusive Bragg backscatter will lead to a random nature of the phases of the sea echoes. As a result, their phase relation cannot be described in terms of (4).

As shown in Figures 1 and 7, the phase distributions of the ionospheric echoes in the spectral ranges with high coherences are much more structured and organized than those of the sea echoes. It is then anticipated that the degree of the phase fluctuations for the ionospheric echoes will be very different from that for the sea echoes. Figure 8 compares the histograms of the standard deviations of the phases of the ionospheric echoes (a) with those of the sea echoes (b), in which the spectral bands employed for the calculations of the standard deviations of the phases are the same as

Figures 1, 4, and 7. As expected, the overwhelming majority (80% or more) of the standard deviations of the phases of the ionospheric echoes for the three receiving channel pairs mainly distribute in a small range of  $0^\circ$ – $20^\circ$ . However, for the sea echoes their standard deviations distribute in a relatively broad range, primarily between  $0^\circ$  and  $90^\circ$ .

#### 4. Discussion

The cross spectral analysis has been widely used by the community of radar oceanography to extract the sea surface information from the radar returns detected by difference receiving channels. As shown in Section 3, the cross spectral analysis of the radar returns may offer an opportunity to realize the correlation of the echoes between different receiving channels in spectral domain. Our analyses indicate

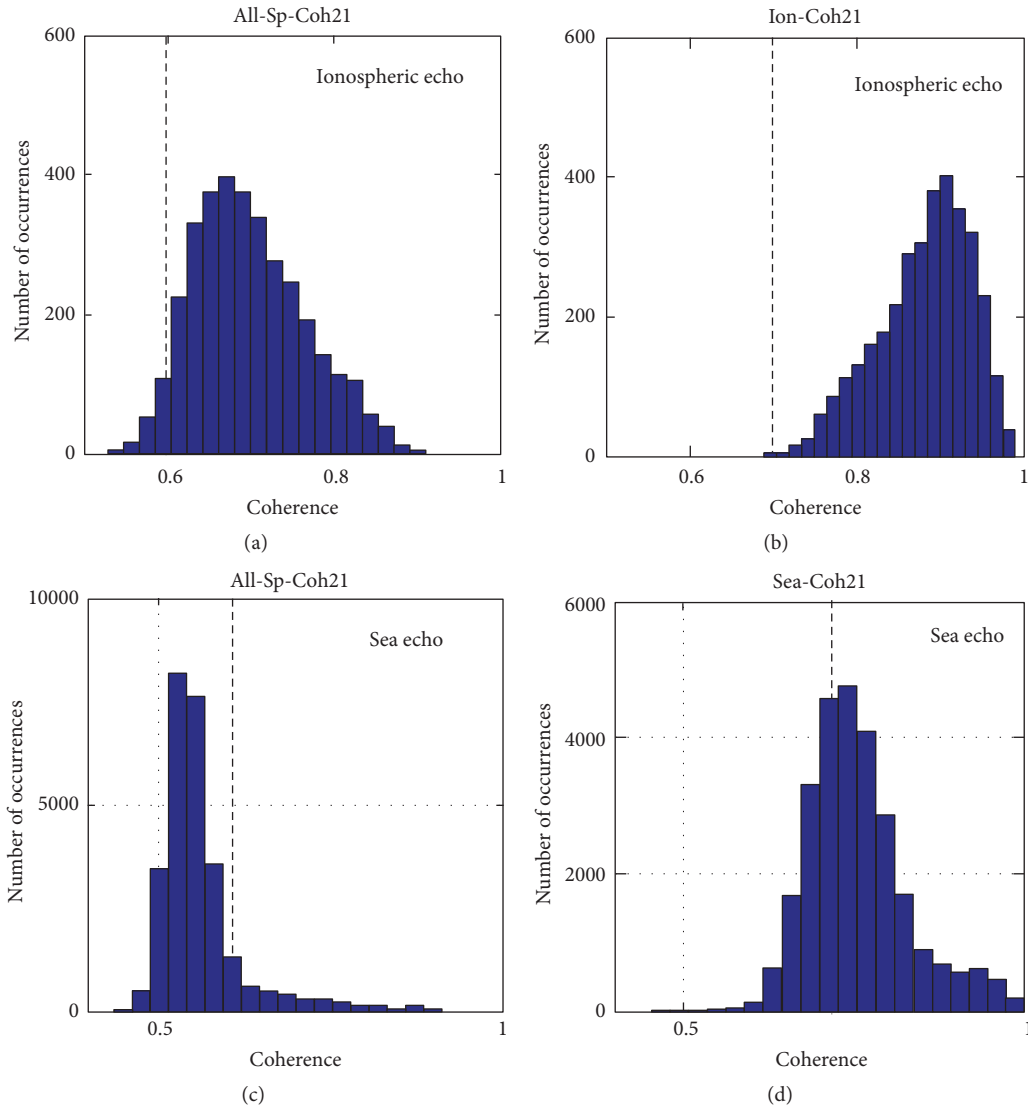


FIGURE 6: Comparison of the histograms of the coherences of the ionospheric echoes (a, b) with those of sea echoes (c, d), in which only the results from the receiving channels 1 and 2 are displayed. The dashed lines in every panels mark the coherence values of 0.6 (a, c) and 0.7 (b, d) on respective histograms for comparison.

that the coherences of the normalized cross spectra are high for the echoes from organized and structured targets, that is, ionospheric layers, whereas the coherences will be low for the radar returns from randomly distributed diffusive targets, that is, ocean waves, in echoing region. Additionally, for the distinct and isolated targets, such as ionospheric layers, the phase differences of the cross spectra of the echoes between receiving channel pairs also exhibit organized and structured patterns in the spectral domain and their phase relations should comply with the relation given by (4). However, for the first-order sea echoes generated from Bragg backscatter of the random ocean waves, our results show that their phase relation may not necessarily comply with the relation given by (4) due to the random nature of their phases. With these properties, the coherence and the phase of the echoes observed by a sea radar operated at HF band may be employed as indicators for the discrimination

of the ionospheric echoes from the sea echoes in the spectral domain to improve the data quality of the measured current and ocean waves.

For a HF sea-wave radar with echo range larger than 200 km, the observed Doppler spectrum is susceptible to the ionospheric echoes reflected from sporadic E (Es) layer that occurs in a height range from about 90 to 150 km. Note that the mechanisms responsible for the formation of the Es layers vary with the geomagnetic latitudes. At geomagnetic equator, the Es layers (or Es plasma irregularities) are thought to be generated through the processes of the plasma instabilities, including two-stream or gradient drift instabilities [11]. However, at high latitude, the formations of the Es plasma irregularities are associated with the plasma instabilities or bombardment effect of charged particles from upper ionosphere [12]. At low and middle latitudes, the Es layers are primarily formed due to convergence effects

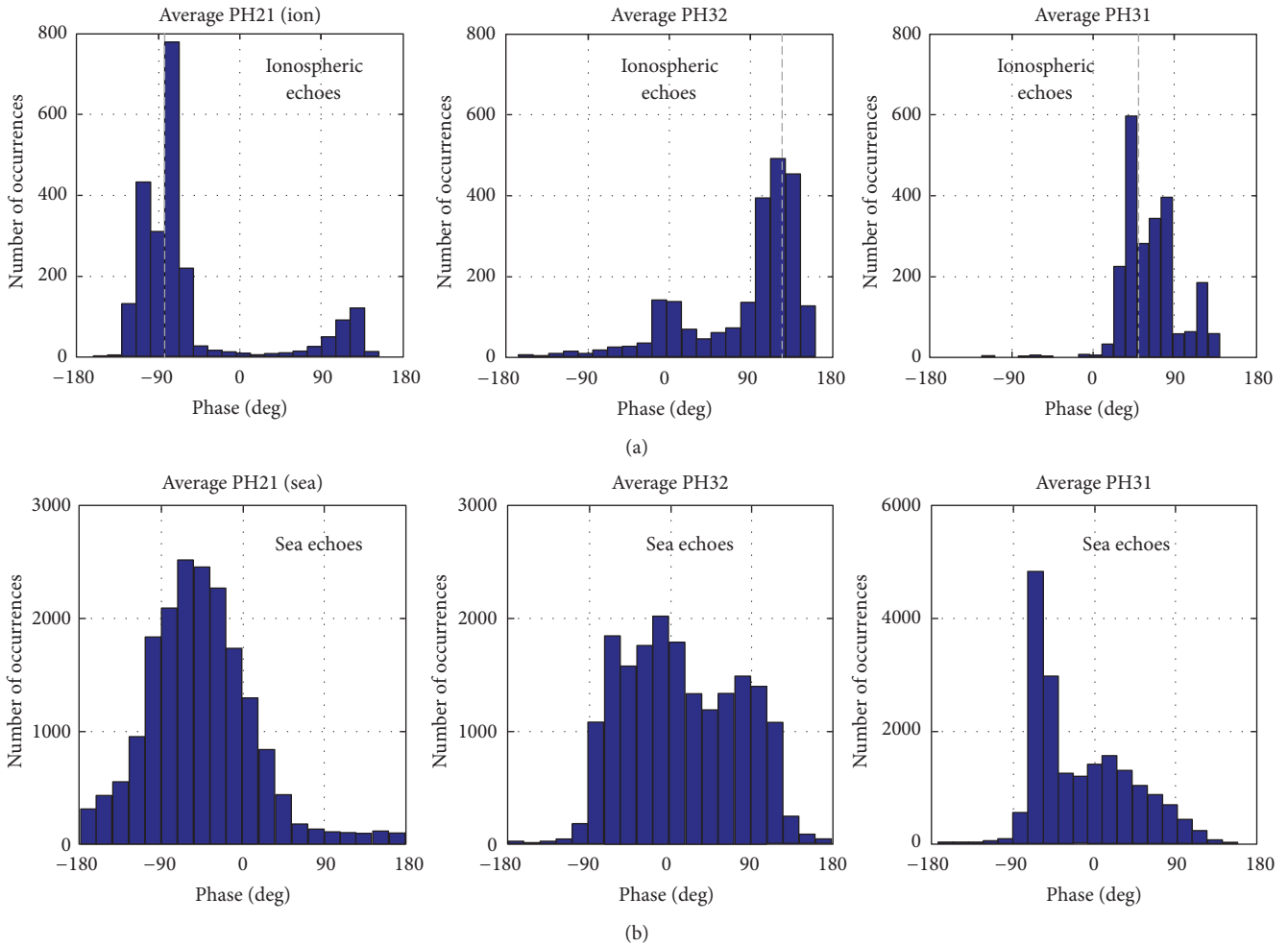


FIGURE 7: Histograms of the phases of the cross spectra for different receiving channel pairs, in which (a, b) are the results of ionospheric (sea) echoes and the phases are averaged for the spectral components within the specific frequency bands that are similar to those used in Figure 5.

of neutral wind shear and/or electric field on ionization particles [4, 13, 14]. Figure 9 compares the range-time distribution of the number of occurrences of the ionospheric echoes detected by the CODAR-SeaSonde at DATAN (b) and observed by the Chung-Li ionosonde (a) for the period from 30 June to 31 July, 2015. A prominent feature shown in Figure 9 is the distinct descent of the Es layer echoes during daytime from 6 to 18 LT in the range extent 90–150 km, at a descending rate of about 1.2 km/hr. Obviously, this feature is in good agreement with the descending rate of the wind shear zone of a vertically propagating semidiurnal tide [15, 16]. Therefore, the ionospheric echoes detected by CODAR-SeaSonde can, in principle, be used for the investigation of the characteristic and dynamic behavior of the F and/or Es layers in ionosphere. Although their patterns of the echo range-local time variations in the occurrence of the ionospheric Es layers are in general agreement with each other, there is a tendency for the echo heights of the ionosonde-observed Es layers to be about 30 km lower than those measured by the CODAR-SeaSonde. In addition, the number of occurrences of the ionosonde-observed Es layer echoes is also larger

than that of the CODAR-SeaSonde measurements, especially during nighttime. The causes of these inconsistencies in the number of occurrence and the echo range of the Es layer between Chung-Li ionosonde and CODAR-SeaSonde may be attributed to the differences in the system characteristics, echo processing procedure, data sifting criterion, and so on. This issue will be explored in the near future to clarify the causes of these inconsistencies between these two radar systems.

Figure 10 displays the range variations of the Doppler spectra of the first-order and second-order sea echoes taken on July 10, 2015, at 04:50:05 LT, in which the Doppler spectra observed by 3 receiving antennas (two of them are identical loop antennas and the other one is monopole antenna) are presented, respectively. As shown in Figure 10(a), the second-order Doppler spectral components that appeared in a spectral region surrounding the first-order spectral peaks are clearly seen. In addition to the weak spectral continuum around direct current (DC) component with zero Doppler frequency, two noticeable second-order spectral peaks at 0.308 and 0.37 Hz are, respectively, clearly identified

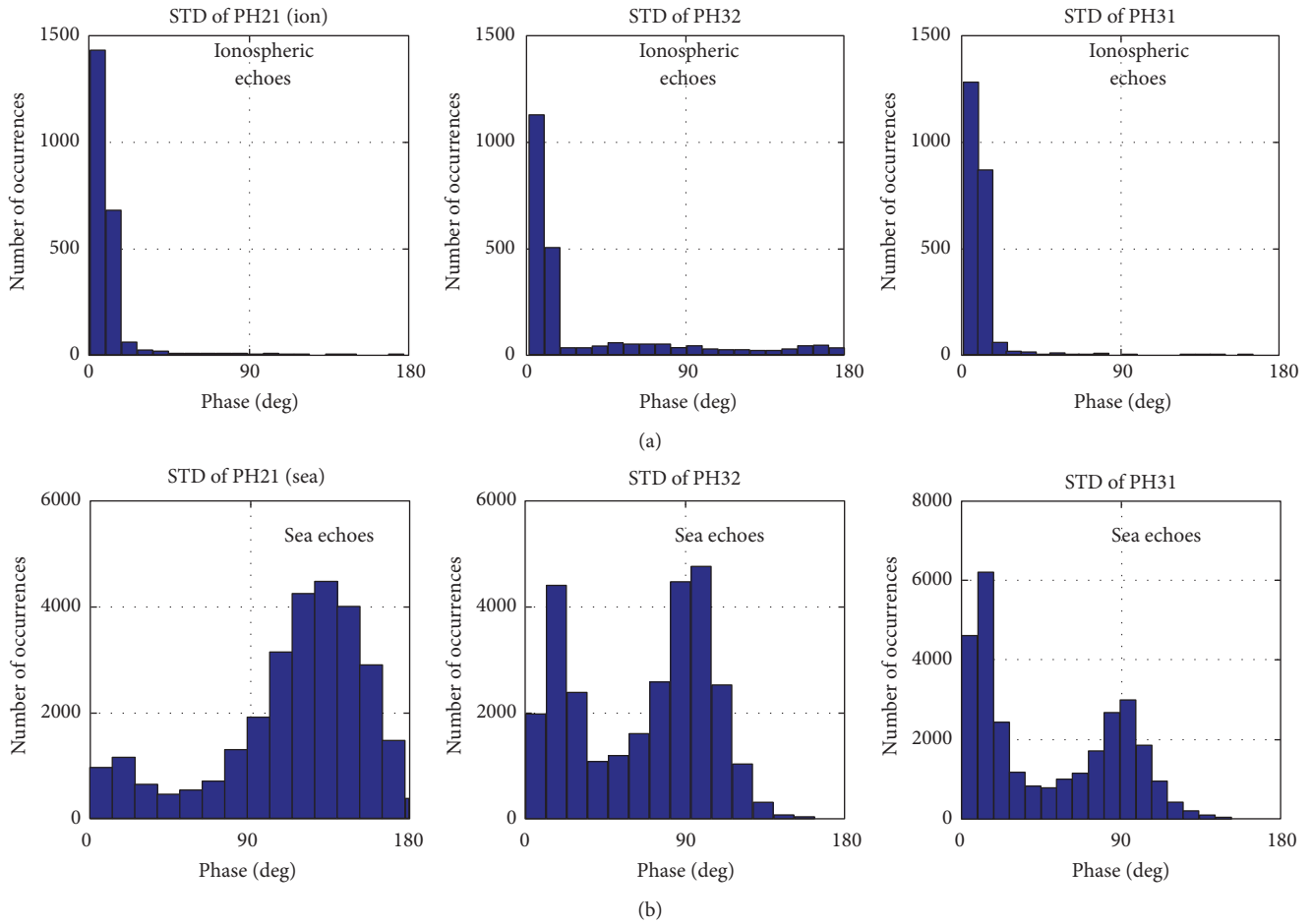


FIGURE 8: Comparison of the histograms of the standard deviations of the phases of the ionospheric echoes (a) with those of the sea echoes (b), in which the spectral bands employed for the calculations of the standard deviations of the phases are the same as Figures 5 and 7.

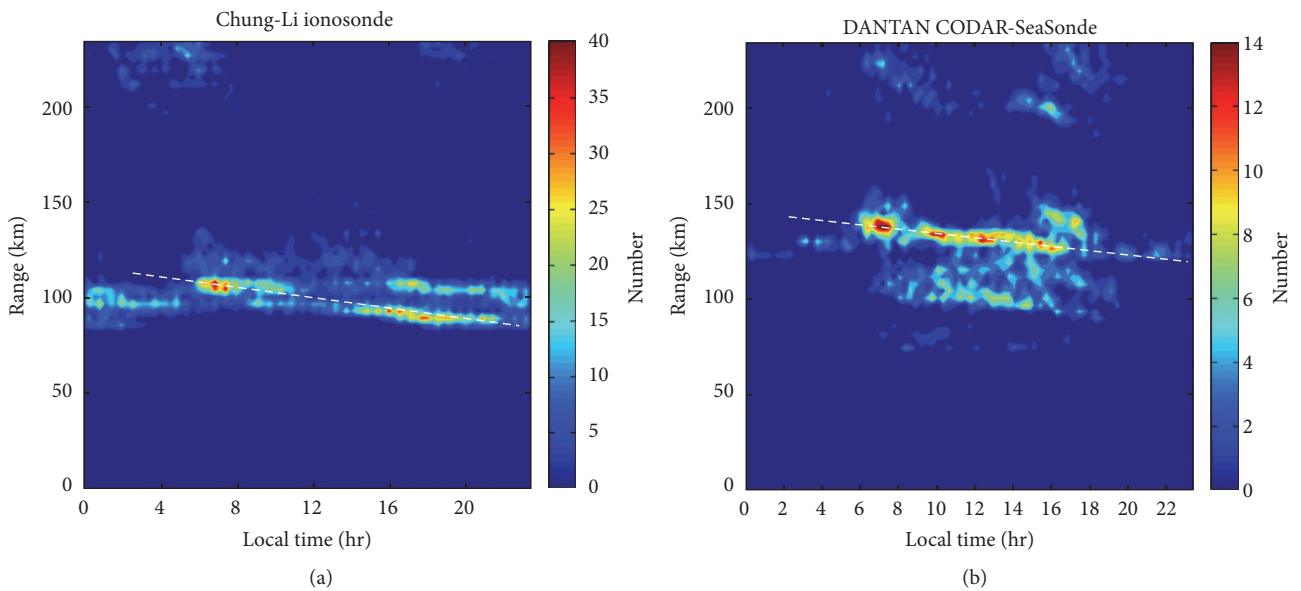


FIGURE 9: Range-local time distributions of the numbers of occurrences of the ionospheric Es layer (90–150 km) and F layer echoes (above 200 km) detected by the Chung-Li ionosonde (a) and DANTAN COAR-SeaSonde (b) for the period from 30 June to 31 July, 2015.

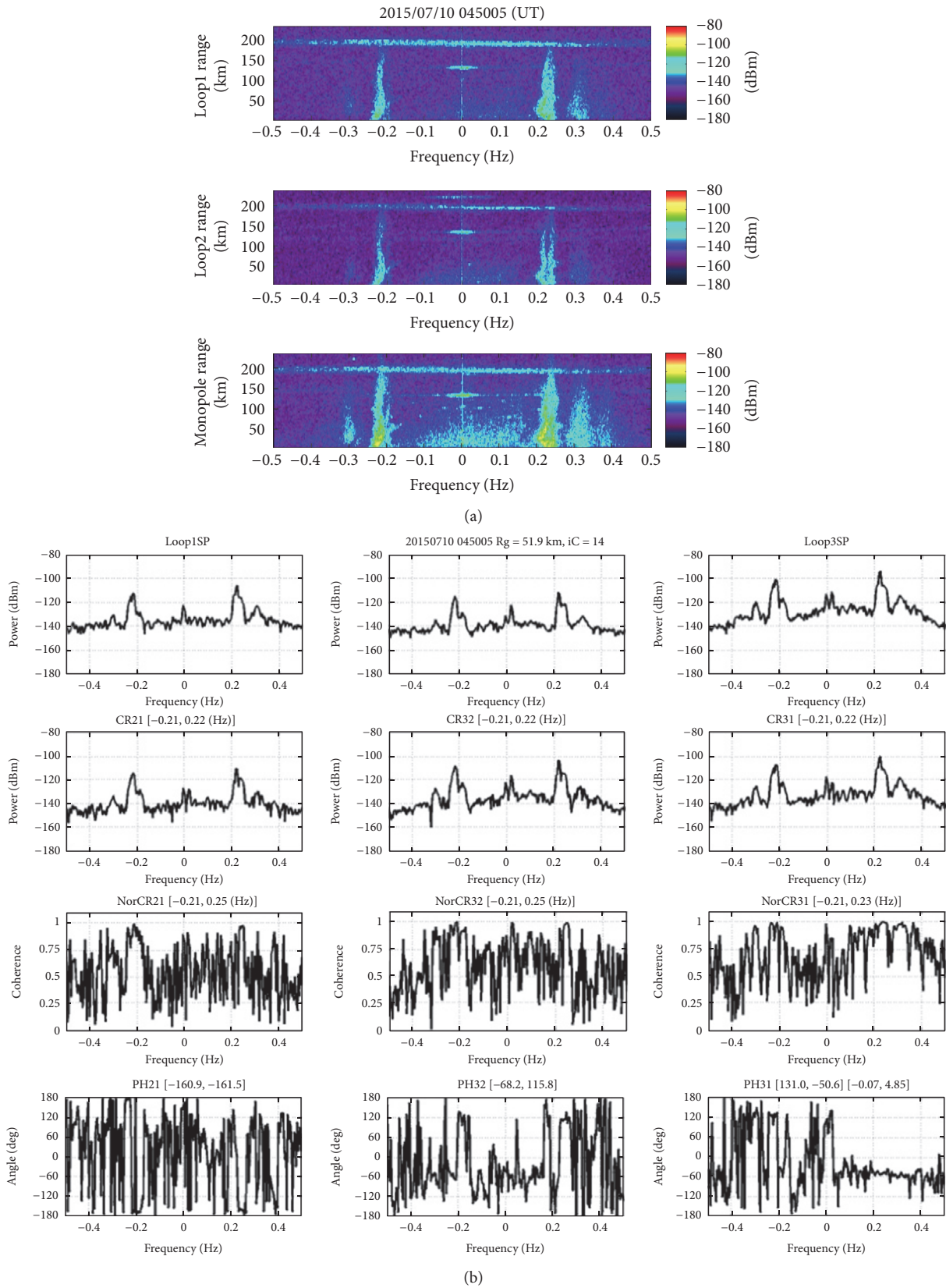


FIGURE 10: (a) Examples of range variations of the Doppler spectra of the first-order and second-order sea echoes. Note that the first-order spectral peaks locate at  $\pm 0.218$  Hz. The top and middle panels are the Doppler spectra observed by the identical two loop antennas, and the bottom panel shows the Doppler spectra from monopole antenna. (b) Autospetra (top), cross spectra between different receiving channels (2nd panels), coherence spectra (3rd panels), and phase spectra (bottom panels) of the sea echoes for the data at range of 51.9 km presented in (a).

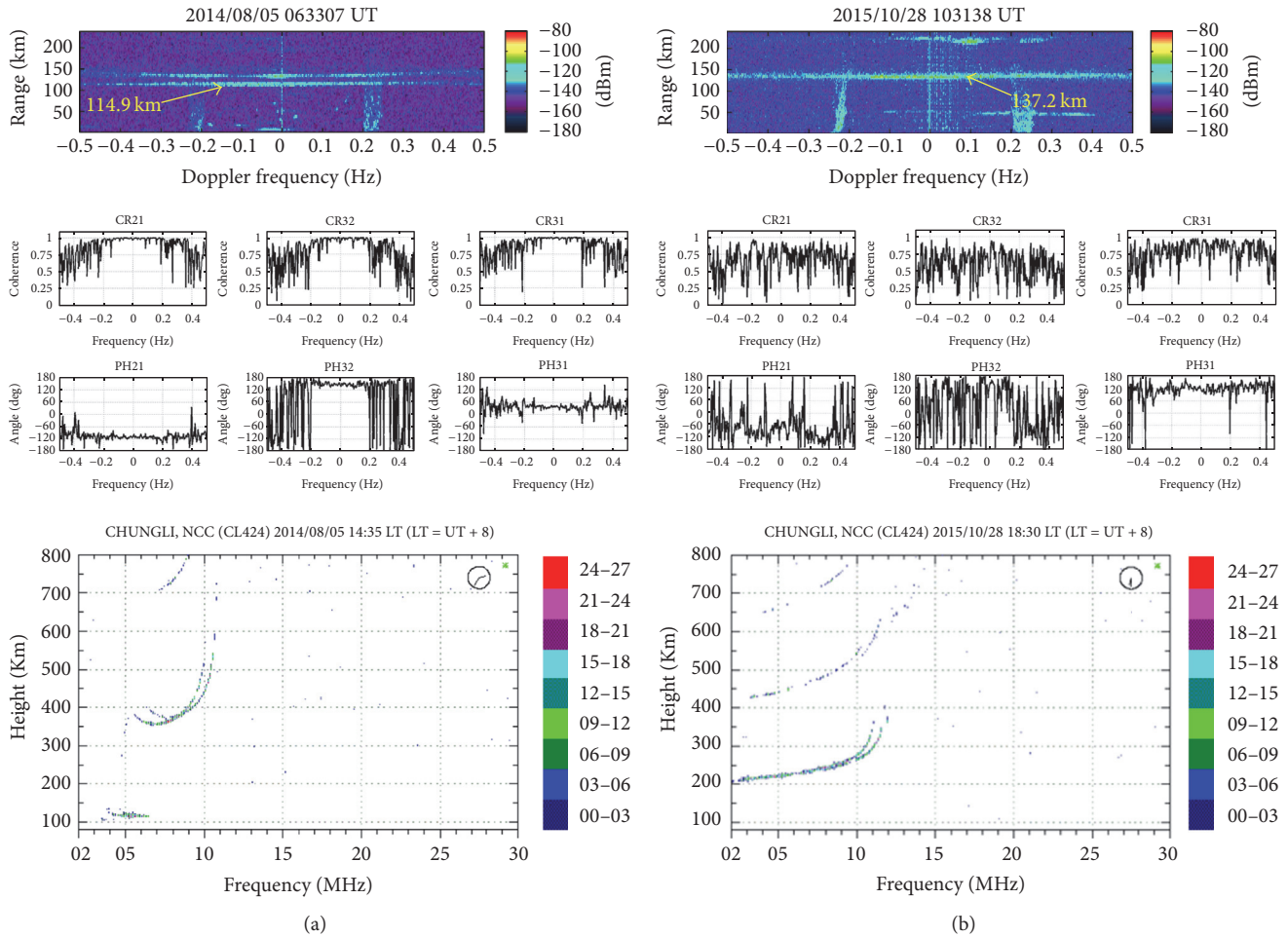


FIGURE 11: A comparison in coherence and phase angle between ionospheric Es layer echoes (a) and external radio interference (b).

in the Doppler spectra observed by the monopole antenna. These features are consistent with the theoretical prediction that the spectral peaks of the second-order sea echoes are predicted to situate at  $2^{1/2}f_B$  and  $2^{3/4}f_B$ , where  $f_B$  is the Doppler frequency shift of the first-order spectral peaks [17]. Figure 10(b) displays autospectra (1st row), cross spectra between different receiving channels (2nd row), coherence spectra (3rd row), and phase spectra (bottom row) of the sea echoes for the data at a range of 51.9 km presented in Figure 10(a). As shown, two intense first-order spectral components with significantly large coherence values that are very close to 1 are clearly seen and discerned in the power and coherence spectra of the three receiving channels, although the phases within the corresponding frequency bands of the first-order spectral peaks fluctuate considerably. However, for the second-order spectral components, their spectral appearances in the three different receiving channels are very different. They are easily discernible in the receiving channel 3, but the spectral components at  $2^{3/4}f_B$  are vague and hard to distinguish in the channels 1 and 2. As a result, the coherences of the second-order spectral components are not as vivid and organized as those of the first-order echoes

in magnitude. In addition, the phase fluctuations of the second-order echoes are also random and irregular. From this case report, one should be cautious to analyze and interpret the coherence and the phase of the cross spectra of the second-order echoes detected by the CODAR-SeaSonde.

As mentioned before, the ionospheric echoes characterized by broad spectral width and limited range extent in range-Doppler frequency-intensity (RDI) plot may interfere with the Doppler spectral bands of the sea echoes, as shown in the examples presented in Figures 2 and 10. Note that the appearance of such ionospheric echoes may bear a strong resemblance to that of the radio interference from unknown source, leading to a difficulty of discerning them in RDI plot. Figure 11 compares the appearances of the ionospheric echoes and interference in RDI plots. As shown, the upper panels of (a) and (b) are, respectively, the ionospheric echoes and the interference that occupy a very broad frequency range covering the spectral bands of the sea echoes. From the ionogram shown in the bottom panels of Figure 11(a), the presence of a distinct Es layer centered at a virtual height of about 114 km is clearly found and is coincident with the ionospheric echoes presented in upper panel of Figure 11(a), whereas no

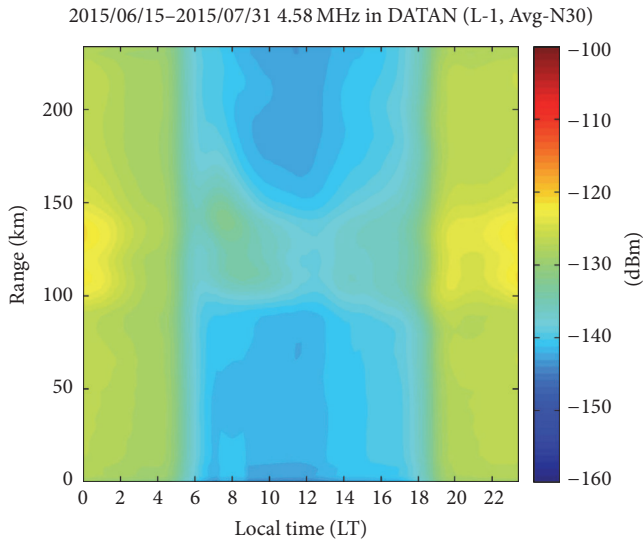


FIGURE 12: Variation of background noise over range and local time.

Es layer is found in the virtual height range 100–150 km in the bottom panel of Figure 11(b). Because of this, we consider the echoes that appeared at a range of 137 km in the upper panel of Figure 11(b) to be very likely a radio interference with unknown source. Although they are difficult to discern in RDI plot, the ionospheric echoes and the interference can be easily distinguished in terms of coherence and phase angle of normalized cross spectra. As shown in the middle panels of Figure 11, the patterns of the frequency distributions of the coherences and the phase angles for the different pairs of the receiving channels for the ionospheric echoes are very organized and structured, which are very different from those of the interference characterized by random fluctuations in the coherences and phase angles. In addition, the summation of the mean phase angles of the ionospheric echoes fully complies with the relation given by (4), but it is not for the interference. Compared to the coherent ionospheric echoes, the random properties of the interference strongly imply the incoherent nature of the signals from the unknown source. An examination of the coherences and phase angles of the sea echoes presented in Figure 11 indicates that the ionospheric echoes and external interference can significantly disrupt the spectral properties of the sea echoes, causing the degradation of the data quality of the estimated ocean current and wind wave parameters. Therefore, understanding the spectral properties of the ionospheric echoes characterized by broad spectral width and interference is very crucial to improve the data quality of a HF sea radar by coming up with an efficient ways for the data processing and analysis.

Figure 12 presents variations of background noise intensity over range and local time, in which the noise intensity is estimated by averaging the lowest 30% of the spectral power components in the observed Doppler spectrum to avoid the potential contaminations of nonocean echoes and external radio interference on the noise estimate. As shown, a striking diurnal variation of the background noise intensity is present, low during daytime and high during nighttime

with a maximum difference of up to 15 dBm in the noise intensities between daytime and nighttime. A comparison indicates that the noise level estimated from the lowest 30% of the spectral components is in general 3 dB smaller than that calculated from 20% of the spectral components toward the higher frequency ends in the Doppler spectrum, that is, in the frequency bands of  $\pm(0.4-0.5)$  Hz that are close to the Nyquist frequency, irrespective of daytime and nighttime. Note that the electromagnetic waves at lower HF bands are capable of being effectively reflected by the ionosphere. During their propagation in the ionosphere, the HF waves are susceptible to the absorption of free electrons through neutral-electron collision process in lower ionosphere to reduce their intensity through the nondeviation absorption effect that is inversely proportional to the electron density in lower ionosphere [5]. Therefore, the larger the electron density during daytime is, the lower the HF wave intensity will be, and vice versa. Figure 12 also demonstrates that, relative to the background noises in other ranges, there is a tendency for the noise level to slightly increase in a range extent between 100 and 150 km by about 5 dB. A comparison between Figures 9 and 12 indicates that the slight increase in the background noise in this range extent is coincident with the occurrence of ionospheric echoes. This feature suggests that the ionospheric echoes may affect the estimate of the background noise in terms of averaging the spectral power components, no matter what methods are employed. Therefore, we should be more cautious in interpreting the range variation of the background noise intensity in the presence of the ionospheric echoes.

## 5. Conclusions

In this study, the radar returns taken by CODAR-SeaSonde at DATAN in Taiwan are analyzed. The concurrent ionospheric traces in the ionogram observed by the Chung-Li ionosonde are also employed in this study to help to identify the ionospheric echoes detected by the SeaSonde radar. We confirm that the echo traces shown in ionogram provide vital background information on vertical structures of the ionospheric layers that can be used to validate the sources of the concurrent ionospheric echoes observed by CODAR-SeaSonde. A comparison indicates that the ionospheric Es layer heights scaled from the ionograms observed by the Chung-Li ionosonde are in general about 30 km lower than those measured by the CODAR-SeaSonde. The work needs to be done in near future to examine the causes of the discrepancy in the echo heights between these two radars.

The coherences and phases of the normalized cross spectra of the sea and ionospheric echoes between different pairs of the receiving channels are, respectively, calculated. Because of their diffusive scattering nature, the degree of the phase fluctuations of the sea echoes is expected to be much larger than that of the ionospheric echoes reflected from the distinct ionospheric layers. We show in this study that the coherences of the sea echoes are generally smaller than those of the ionospheric echoes by about 15% on average, and the phase fluctuations (standard deviations) of the sea echoes are substantially larger than those of the ionospheric layer

reflection echoes. In addition, statistics show that the sum of the mean phases of the ionospheric echoes between the three receiving channel pairs is approximate to zero, while it is not for the sea echoes. In addition, analysis shows that the coherences of the ionospheric echoes that is obtained by taking average of the spectral components of the whole cross spectra can be easily distinguishable from those of the sea echoes. Therefore, it suggest that the use of coherence and phase of the normalized cross spectra of the three different receiving channel pairs would be helpful in separating the ionospheric reflection echoes from the CODAR-SeaSonde sea echoes in the spectral domain.

## Competing Interests

The authors declare that they have no competing interests.

## Acknowledgments

This work is supported by the Taiwan Ocean Research Institute (TORI), National Applied Research Laboratory (NARL), Taiwan. The CODAR-SeaSonde is operated and maintained by TORI, NARL.

## References

- [1] J. Yang, "An oceanic current against the wind: how does Taiwan Island steer warm water into the East China Sea?" *Journal of Physical Oceanography*, vol. 37, no. 10, pp. 2563–2569, 2007.
- [2] D. D. Crombie, "Doppler spectrum of sea echo at 13.56 Mc./s.," *Nature*, vol. 175, no. 4459, pp. 681–682, 1955.
- [3] B. J. Lipa and D. E. Barrick, "Extraction of sea state from HF radar sea echo: mathematical theory and modeling," *Radio Science*, vol. 21, no. 1, pp. 81–100, 1986.
- [4] Y. H. Chu, C. Y. Wang, K. H. Wu et al., "Morphology of sporadic e layer retrieved from COSMIC GPS radio occultation measurements: wind shear theory examination," *Journal of Geophysical Research: Space Physics*, vol. 119, no. 3, pp. 2117–2136, 2014.
- [5] H. Rishbeth and O. K. Garriott, *Introduction to Ionospheric Physics*, Academic Press, San Diego, Calif, USA, 1969.
- [6] Y. Chu and S. J. Franke, "A study of the frequency coherence of stratospheric and tropospheric radar echoes made with Chung-Li VHF radar," *Geophysical Research Letters*, vol. 18, no. 10, pp. 1849–1852, 1991.
- [7] P. R. Julian, "Comments on the determination of significance levels of the coherence statistic," *Journal of the Atmospheric Sciences*, vol. 32, no. 4, pp. 836–837, 1975.
- [8] K.-W. Gurgel, H.-H. Essen, and S. P. Kingsley, "High-frequency radars: physical limitations and recent developments," *Coastal Engineering*, vol. 37, no. 3-4, pp. 201–218, 1999.
- [9] Y.-H. Chu, P. S. Brahmanandam, C.-Y. Wang, C.-L. Su, and R.-M. Kuong, "Coordinated sporadic E layer observations made with Chung-Li 30MHz radar, ionosonde and FORMOSAT-3/COSMIC satellites," *Journal of Atmospheric and Solar-Terrestrial Physics*, vol. 73, no. 9, pp. 883–894, 2011.
- [10] D. E. Kerr, *Propagation of Short Radio Waves*, vol. 13 of *The MIT Radiation Laboratory Series*, McGraw-Hill, New York, NY, USA, 1951.
- [11] B. G. Fejer and M. C. Kelley, "Ionospheric irregularities," *Reviews of Geophysics*, vol. 18, no. 2, pp. 401–454, 1980.
- [12] B. R. Clemesha, "Sporadic neutral metal layers in the mesosphere and lower thermosphere," *Journal of Atmospheric and Terrestrial Physics*, vol. 57, no. 7, pp. 725–736, 1995.
- [13] J. D. Whitehead, "The formation of the sporadic-E layer in the temperate zones," *Journal of Atmospheric and Terrestrial Physics*, vol. 20, no. 1, pp. 49–58, 1961.
- [14] T. Nygrén, L. Jalonon, J. Oksman, and T. Turunen, "The role of electric field and neutral wind direction in the formation of sporadic E-layers," *Journal of Atmospheric and Terrestrial Physics*, vol. 46, no. 4, pp. 373–381, 1984.
- [15] Q. Wu, T. L. Killeen, D. A. Ortland et al., "TIMED Doppler interferometer (TIDI) observations of migrating diurnal and semidiurnal tides," *Journal of Atmospheric and Solar-Terrestrial Physics*, vol. 68, no. 3-5, pp. 408–417, 2006.
- [16] C. L. Su, H. C. Chen, Y. H. Chu et al., "Meteor radar wind over Chung-Li (24.9°N, 121°E), Taiwan, for the period 10–25 November 2012 which includes Leonid meteor shower: comparison with empirical model and satellite measurements," *Radio Science*, vol. 49, no. 8, pp. 597–615, 2014.
- [17] D. E. Barrick, "Extraction of wave parameters from measured HF radar sea-echo Doppler spectra," *Radio Science*, vol. 12, no. 3, pp. 415–424, 1977.

## Research Article

# The Vertical Ionosphere Parameters Inversion for High Frequency Surface Wave Radar

Xuguang Yang,<sup>1,2</sup> Changjun Yu,<sup>3</sup> Aijun Liu,<sup>3</sup> Linwei Wang,<sup>3</sup> and Taifan Quan<sup>1</sup>

<sup>1</sup>Department of Electronic and Information Engineering, Harbin Institute of Technology, Harbin, China

<sup>2</sup>Department of Science, Harbin Engineering University, Harbin, China

<sup>3</sup>Department of Information and Communication Engineering, Harbin Institute of Technology, Weihai, China

Correspondence should be addressed to Changjun Yu; [yuchangjun@hit.edu.cn](mailto:yuchangjun@hit.edu.cn)

Received 7 May 2016; Revised 1 September 2016; Accepted 13 October 2016

Academic Editor: Khalid El-Darymli

Copyright © 2016 Xuguang Yang et al. This is an open access article distributed under the Creative Commons Attribution License, which permits unrestricted use, distribution, and reproduction in any medium, provided the original work is properly cited.

High Frequency Surface Wave Radar (HFSWR), which is currently applied in over-the-horizon detection of targets and sea states remote sensing, can receive a huge mass of ionospheric echoes, making it possible for the ionospheric clutter suppression to become a hot spot in research area. In this paper, from another perspective, we take the ionospheric echoes as the signal source rather than clutters, which provides the possibility of extracting information regarding the ionosphere region and explores a new application field for HFSWR. Primarily, pretreatment of threshold segmentation as well as connected region generation is used in the Range-Doppler (R-D) Spectrum to extract the ionospheric echoes. Then, electron density and plasma frequency of field aligned irregularities (FAIs) caused by plasma instabilities in the F region are obtained by the coherent backscattered radar equation. The plasma drift velocity of FAIs can also be estimated from Doppler shift. Ultimately, the effectiveness of inversion is verified by comparing with IRI2012.

## 1. Introduction

HFSWR, taking advantage of the sea-surface diffraction character of vertical polarized wave, has won great success in over-the-horizon sea target detection [1] and sea states remote sensing [2]. Ideally, a perfect conductive plane consisting of sea surface is infinite in coverage area, thus making electromagnetic wave of HFSWR completely travel along the sea. But considering the actual antenna pattern characteristics, poor ground, and array error, partial energy is radiated into sky and reflected by ionosphere. Finally the echoes arrived at radar receiver in various paths, interfering target detection severely as ionospheric clutter [3, 4].

Many investigations have been made on the suppression of ionospheric clutter [4–7], which have also obtained many characteristics of ionospheric clutter. Ionospheric clutter coming from different ionosphere layers has different Doppler shift, for example, Doppler shift from E layer is less than that of F layer. Partial ionosphere clutter has obvious directivity [8]. According to statistical results, the amplitude of most ionospheric clutter is approximate to Rayleigh

distribution, while others satisfy Weibull distribution [9]. In addition, the specular clutter coming from near-vertical direction exhibits no apparent resultant directivity while the spread clutter coming from lower elevation angle has high directivity [10]. Furthermore, ionospheric clutter occupying a few range bins, such as specular scattering from Es layer or F layer, has coincident directivity, while ionospheric clutter occupying more range bins, such as from the spread F layer, does not have directivity. And the directivity of ionospheric clutter does not change with frequency [11].

In this paper, we take the ionosphere clutter as signal source to obtain relative parameters. The clutter signal definitely contains characteristic information of the ionosphere for its reflection from ionosphere. Currently there are two common methods for ionosphere sounding: statistical model and sounding in real-time. The widely used statistical model is the International Reference Ionosphere (IRI). For a given geography and time, the IRI can provide monthly averages of electron density, electron temperature, the molecular composition of the ions, and several additional parameters in the range of altitudes from 50 km to 2000 km. The latest

standard is IRI-2012. The advantage of IRI is that it develops as a data-based model to avoid uncertainty of theory-based models. The amplitude of these longitudinal variations is generally smaller in IRI than what is observed because IRI is based on monthly averages and the averaging process smoothes out some of structures. The disadvantage of IRI is strongly dependent on the underlying database. Regions and time periods that are not well covered by the database will result in diminished reliability of the model in these areas [12]. There are only 20–30 ionosphere stations in China; thus the IRI parameters of most regions coming from interpolation should have certain deviations from the actual measurement. Ionosonde is the widely used instrument for ionosphere sounding. Electron density profile, virtual heights, polarization, and Doppler shift can be obtained according to the ionogram of 1–30 MHz scanning-frequency results. But the limitations of the Doppler resolution from ionosonde are too low to measure the ionosphere disturbance [13]. In [13, 14], Zhou et al. tried to use HFSWR to sounding the information regarding ionosphere. More precisely, in [13], the authors obtained the time-varying ranges, virtual heights, and horizontal drifting speeds of ionosphere irregularities by using the method of time-frequency distribution and continuous hours of long time observations. In [14], the authors observed that the distance, Doppler shift, and multipath propagation of ionospheric backscatter signals changed with time. But there are few interpretations on the physical mechanism of ionospheric clutter. This paper thus tries to explain the physical mechanism between the HFSWR wave and ionosphere while estimating the electron density, plasma frequency, and drift velocity of irregularities created by plasma instabilities in the corresponding ionosphere region by the coherent backscattered radar equation.

The organization of this paper is as follows. In Section 2, the HFSWR system is introduced. In Section 3, the method to obtain the vertical ionospheric echoes from the R-D spectrum is given. In Section 4, the electron density, plasma frequency, and drift velocity of irregularities are obtained. In Section 5, experiments had proceeded at different time and were compared with IRI2012 to verify the effectiveness of the method. Conclusions are summarized in Section 6.

## 2. High Frequency Surface Wave Radar System

In this paper, measured data come from the HFSWR which is designed by Harbin Institute of Technology. The radar system transmits a frequency modulated interrupted continuous waveform with operating frequency between 3 and 15 MHz. The radar comprises an 18-element log periodic dipole transmitting antenna and an 8-element quadlet (one array element, which is formed by four vertical elements with 1/4 wavelength spacing) vertically polarized antenna receiving arrays, as shown in Figures 1 and 2, respectively, at Weihai, Shandong.

Figures 3 and 4 show sketch maps of the log periodic dipole transmitting antenna and the vertically polarized antenna receiving arrays, respectively. Figure 5 shows the pattern of log periodic dipole transmitting antenna by High Frequency Structure Simulator (HFSS). It obviously shows



FIGURE 1: Transmitting antenna.



FIGURE 2: Receiving antenna arrays.

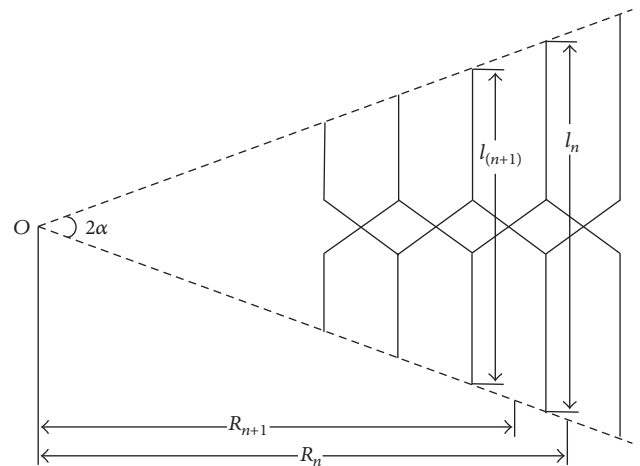


FIGURE 3: Log periodic dipole antenna.

that the antennae radiate partial electromagnetic wave to elevation especially to the zenith regardless of frequency. Figure 6 shows the pattern of receiving antenna at 9 MHz also from HFSS. We can see that the receiving gain of zenith remains about  $-8$  dB on an ideal conductive plane. If considered on a nonideal conductive plane (the electrical parameters for the poor ground are  $\sigma_1 = 0.003 \Omega^{-1} \text{m}^{-1}$ ,  $\epsilon_{rl} = 4$ , where  $\sigma_1$  is the conductivity and  $\epsilon_{rl}$  is relative dielectric constant of the land), the zero of vertical pattern shifts from zenith to left, whether in transmit or receive pattern [4]. So HFSWR certainly can receive the ionosphere echoes from zenith in practical engineering system.

## 3. Pretreatment of Ionospheric Echoes

Generally, HFSWR transmits frequency modulated interrupted continuous (FMICW) and receives signals by the

uniform liner array (ULA). By using pulse compression, digital beam forming (DBF), and fast Fourier transformation (FFT) for the receiving signals from every antenna element, we can obtain the Range-Doppler (R-D) spectrums of arbitrarily azimuth angles. Since each R-D spectrum includes ionosphere echoes from all elevation angles, it is required to extract the vertical ionospheric echoes firstly.

The R-D spectrum of each beam contains the ionospheric echoes with all elevation angles, so the overlaps of all the beams only cover the elevation direction of 90 degrees. Therefore, the vertical ionospheric echoes can be obtained by extracting overlaps of all beams at the same time.

But R-D spectrum also contains sea clutter, meteoric trail, and atmospheric noise, so it should be pretreated. The pretreatment procedure includes the threshold segmentation and generation of connected region.

**3.1. Threshold Segmentation.** The threshold segmentation mainly eliminates the background noise. Since the ionosphere echoes from high frequency wave should not exist for less than 60 km in R-D spectrum, the average power in this area is nearly equal to noise power. Generally, clutter noise ratio is about 20~35 dB, so let  $\delta = P_N + 20$  to preserve ionosphere clutter, where  $\delta$  is the threshold and  $P_N$  is the noise power.

**3.2. Generation of Connected Region.** The disadvantage of threshold segmentation is that it ignores the shape characteristics of the ionosphere echoes, which are always displayed as plane or band. Consequently, the next processing is the image segmentation by connected region generation.

The R-D spectrum after the second step still contains sporadic noise and a little sea clutter. The widest connected region is chosen as the ionospheric echoes based on the prior information of height. Then the vertical ionosphere echoes can be obtained.

## 4. Modeling HFSWR Ionospheric Backscatter Characteristics

**4.1. Electron Density Estimations by Radar Equation.** The classical radar equation for a monostatic HFSWR is defined as

$$P_r = \frac{P_t G_t G_r \lambda^2}{(4\pi)^3 R^4 L_s} \sigma, \quad (1)$$

where  $P_r$  is the received power;  $P_t$  is the transmitted power;  $G_t$  is the transmitter antenna gain;  $G_r$  is the receiver antenna gain;  $\sigma$  is the radar cross section (RCS);  $\lambda$  is the radar wavelength;  $R$  is the target range;  $L_s$  is the system loss.

The ionospheric scatters cannot be modeled as a single point scatter but distributed scattering from a three-dimensional volume. Thus, a more appropriate form of the generalized radar equation can be given by

$$P_r = \frac{P_t \lambda^2}{(4\pi)^3 L_s} \int_{\Delta V(R, \theta, \phi)} \frac{G_t(\theta, \phi) G_r(\theta, \phi)}{R^4} d\sigma(R, \theta, \phi), \quad (2)$$

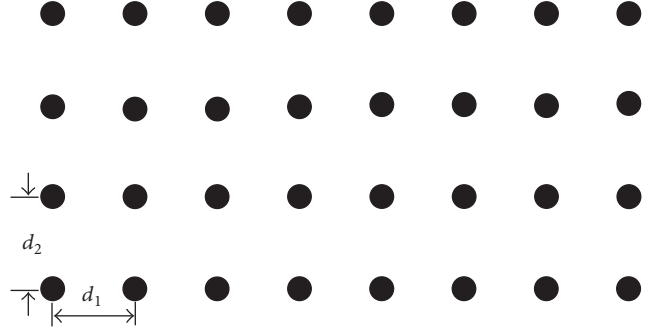


FIGURE 4: Receiving antenna arrays.

where  $\Delta V(R, \theta, \phi)$  is the volume of the resolution cell at nominal coordinates  $(R, \theta, \phi)$ , and

$$\Delta V(R, \theta, \phi) = \frac{\pi}{4} R^2 \Delta R \theta_3 \phi_3 \approx R^2 \Delta R \theta_3 \phi_3, \quad (3)$$

where  $\Delta R$  is the range resolution and  $\theta_3, \phi_3$  are the 3 dB beam widths in azimuth and elevation. Considering the attenuation of electromagnetic wave propagation in ionosphere and using approximation, we can reduce (2) to the range equation for ionosphere scatters:

$$P_r = \frac{P_t \lambda^2 G_t G_r \eta V}{(4\pi)^3 R^4 L_s L_p}, \quad (4)$$

where  $\eta$  is the reflectivity of effective scatter volume (ESV) which is formed by the intersection of radar beam with ionosphere.  $V$  is the volume of ionospheric scatter.  $L_p$  is the attenuation of electromagnetic wave propagation in ionosphere.  $\eta$  and  $L_p$  are discussed in detail as follows.

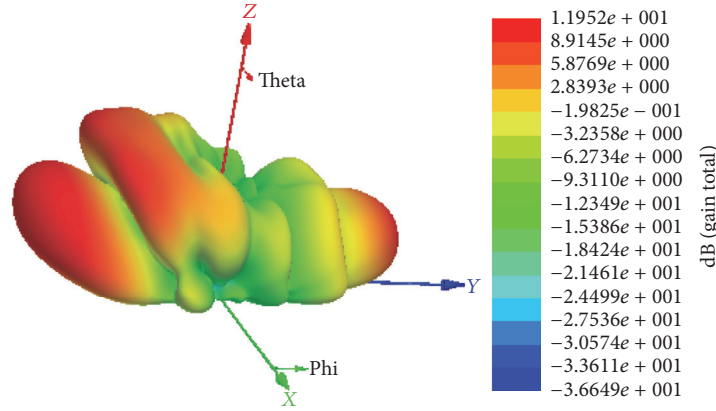
**4.1.1. ESV Reflectivity.** It is convincing that the ionospheric echoes of HFSWR mainly occur from coherent scattering between electromagnetic wave and irregularities caused by plasma instabilities. According to the Bragg scatter conditions for monostatic backscatter [15],

$$\lambda_{\text{irr}} = \frac{\lambda_{\text{radar}}}{2}, \quad (5)$$

where  $\lambda_{\text{irr}}$  is the scale size of ionosphere irregularities, which means that the scale size of irregularities between 5 and 50 m can be observed by HFSWR. For the magnetic plasma in the ionosphere region, irregularities at these scale sizes are highly anisotropic and aligned with the geomagnetic field lines. The reflectivity of effective scatter volume irregularities can be expressed as follows [16]:

$$\eta \propto \overline{\Delta N^2} \exp \left\{ -2k^2 \left( l_{\parallel}^2 \psi^2 + l_{\perp}^2 \right) \right\}, \quad (6)$$

where  $\overline{\Delta N^2}$  is the average level of the electron density fluctuations,  $k$  is the radar wave-vector in the medium, and  $l_{\parallel, \perp}$  is the scale size of irregularities along and across the external magnetic field  $\vec{B}$ , respectively.  $\psi$  is the aspect angle between  $k$  and  $\vec{B}$ . Equation (6) is based on the assumption



(a) 3D pattern of transmitting antenna at 9 MHz

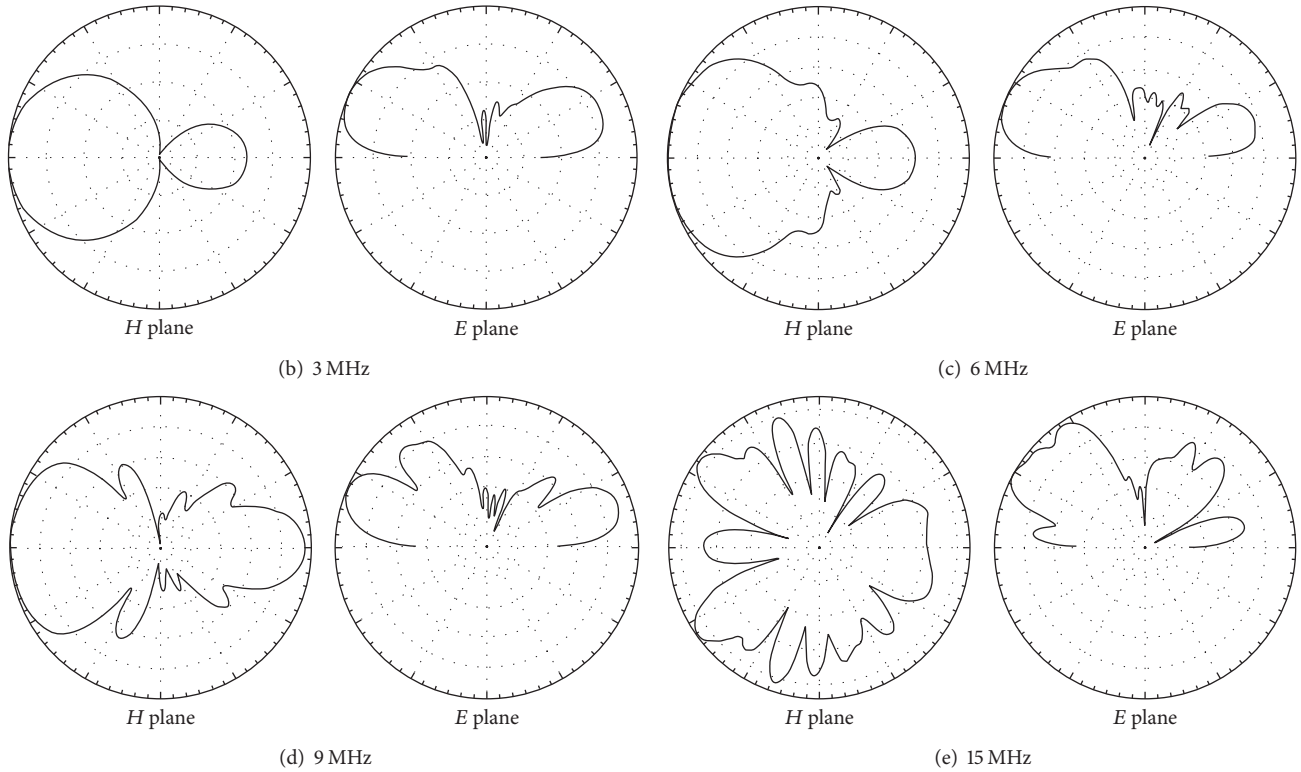


FIGURE 5: Pattern of log periodic dipole transmitting antenna. The maximum length is 12.5 m. The minimum length is 2.5 m. The copper ground screen is 100 m<sup>2</sup>. The diameter of grid is 10 cm.

that  $l_{\parallel} \gg l_{\perp}$  and  $kl_{\parallel} \gg 1$  so that  $\eta$  exhibits peak when  $\psi = 0^\circ$ , namely,  $\vec{k} \perp \vec{B}$ . To simplify (6), we make another assumption:  $\overline{\Delta N^2} \propto N^2$ . That implies that magnitude of electron density fluctuations with fixed Bragg scale size  $\lambda_{\text{irr}}$  has linear relationship with the electron density, which is also consistent with experimental results [17]. Assuming that other parameters are constant, (6) reduces to

$$\eta \propto CN^2. \quad (7)$$

**4.1.2. The Attenuation of Electromagnetic Wave Propagation in Ionosphere.** In the mid-latitude region, attenuation of high

frequency wave propagation mainly contains the absorption and additional attenuation [18]:

$$L_p = 2A_{ie} + A_z, \quad (8)$$

where  $A_{ie}$  is the absorption of D layer and  $A_z$  is the additional attenuation. Generally,

$$A_{ie} = \frac{677.2I}{(f + f_H)^{1.98} + 10.2}, \quad (9)$$

where  $I$  is the absorption index:

$$I = (1 + 0.0037R_{12}) [\cos(0.881\chi)]^{1.3}, \quad (10)$$

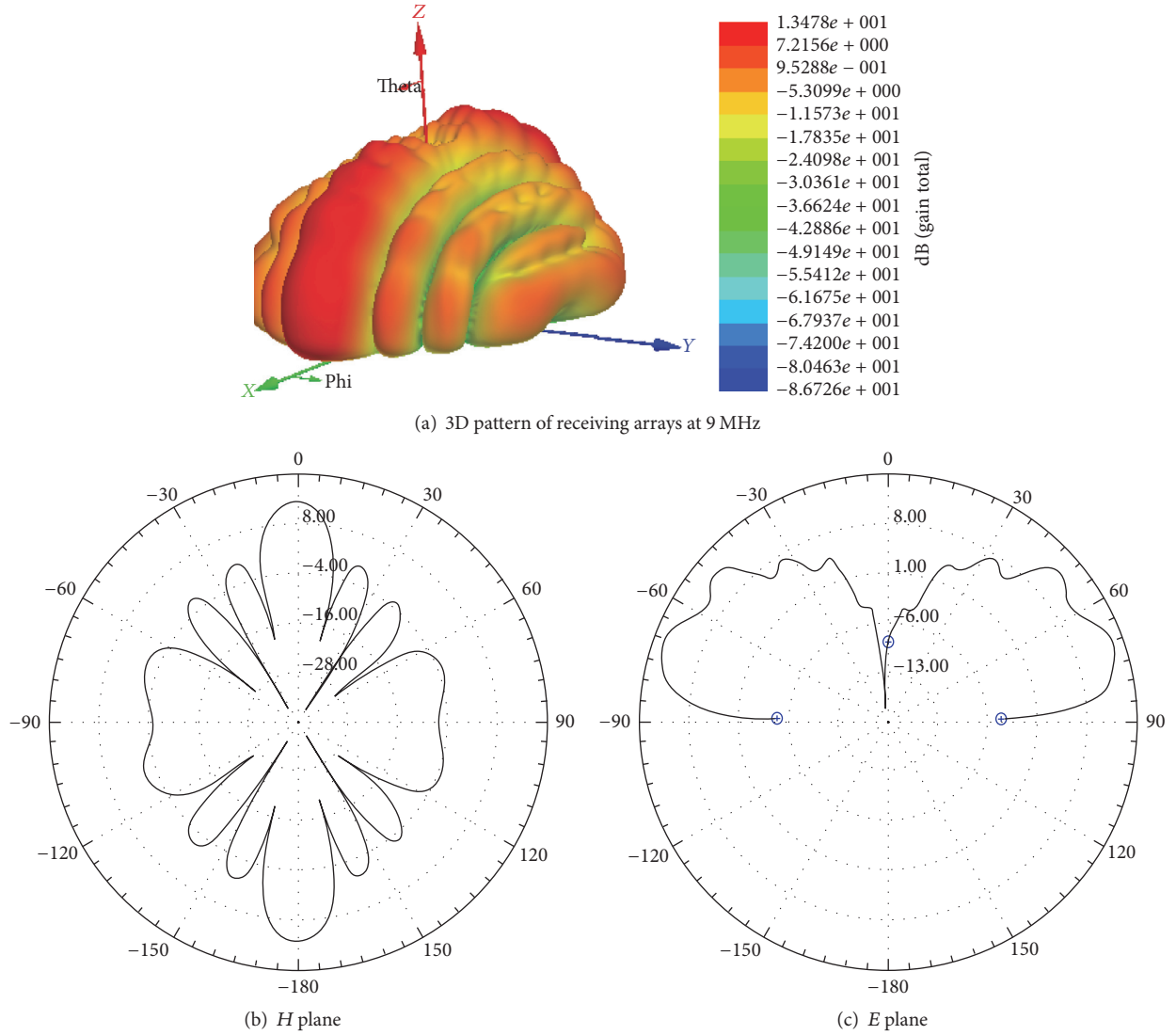


FIGURE 6: Pattern of vertically polarized antenna receiving arrays at 9 MHz. The element length is 6.5 m.  $d_1 = 14.5$  m and  $d_2 = 8$  m. The copper ground screen is about  $100 \text{ m}^2$ . The diameter of grid is 10 cm.

where  $R_{12}$  is the mean value of sunspot in the year.  $\chi$  is the local solar zenith angle.

Considering actual impact such as polarization coupling attenuation, ionospheric irregularities, focus, and defocus, usually  $A_z = 9.9$  dB. So the electron density can be obtained by

$$N_e = \sqrt{\frac{P_r R^4 L_s L_p}{C P_t \lambda^2 G_t G_r V}}. \quad (11)$$

**4.2. Plasma Frequency Estimations from HFSWR.** According to the Appleton-Hartree formula, the plasma frequency can be expressed as

$$f_p \approx \sqrt{80.6 N_e} \quad (12)$$

when

$$\begin{aligned} \frac{\nu}{f_0} &\ll 1, \\ \frac{f_B^2}{f_0^2} &\ll 1 \end{aligned} \quad (13)$$

holds, where  $\nu$  is the ionospheric electron collision frequency and  $f_B$  is the ionospheric electron cyclotron frequency. For the operating frequency of HFSWR  $f_0 \approx 3\text{--}15$  MHz, those conditions are easy to be satisfied in the whole E and F layer.

**4.3. Irregularities Drift Velocity Estimations from HFSWR.** The velocity of irregularities caused by plasma instabilities can be obtained from the Doppler shift of the HFSWR coherent backscatter signal:

$$v_{\text{irr}} = -\frac{\lambda_0}{2} f_d, \quad (14)$$

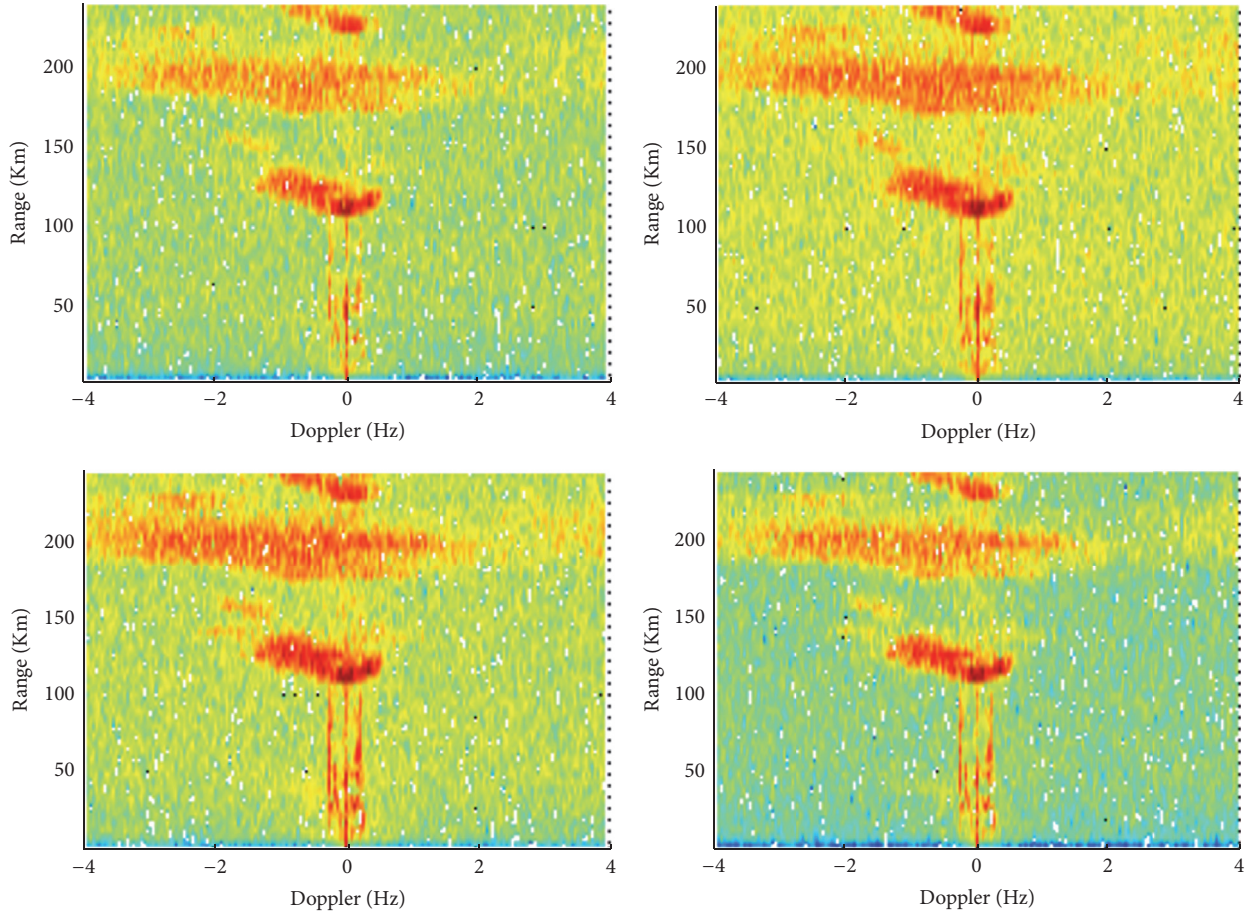


FIGURE 7: R-D spectrums.

where  $v_{\text{irr}}$  is the HFSWR line-of-sight velocity of irregularities, which drift at the  $\vec{E} \times \vec{B}$  direction in the ionospheric region.  $\lambda_0$  is the HFSWR wavelength and  $f_d$  is the Doppler shift. For a given range bin of ionosphere echoes, the mean drift velocity of plasma is the first moment of Doppler spectrum:

$$\overline{v_{\text{irr}}} = \frac{\int f_d s(f_d) df_d}{\int s(f_d) df_d}, \quad (15)$$

where  $s(f_d)$  is the power spectral density function of  $f_d$ .

## 5. Experiments and Analysis

The HFSWR location is as follows:

longitude: 122.1° and latitude: 37.5°.

The main system parameters are as follows:

Pulse repetition frequency:  $T_p = 4$  ms.

Sweep period:  $T_{\text{sw}} = 32 \times T_p = 128$  ms.

Coherent processing interval:  $T_A = T_{\text{sw}} \times 256 = 32.8$  s.

Bandwidth:  $B_w = 30$  kHz.

Range resolution:  $\Delta R = 5$  km.

Peak transmitting power:  $P_t = 2$  kW.

Beam direction (1-7):  $-48^\circ, -32^\circ, -16^\circ, 0^\circ, 16^\circ, 32^\circ,$  and  $48^\circ$ .

The experiments were conducted at night, morning, and afternoon, respectively. Figure 7 is the R-D spectrum of the beams with operating frequency 5.5 MHz at Beijing time 2014.5.23.20:31, local time 2014.5.23.20:41.

Generally the height of E layer is about 90–150 km above the surface of earth while 150–500 km corresponds to F layer. There are three parts of ionosphere echoes appearing at about 120 km, 200 km, and 240 km, with Doppler shift between  $[-1, 0]$  Hz,  $[-4, 1]$  Hz, and  $[-1, 0]$  Hz, respectively. The former echoes occupying a few range bins may come from the specular reflection of Es layer, since E layer usually disappears at night. The middle echoes may come from spread of F layer since it occupied about 8 range bins (40 km) and a large number of Doppler bins. The last echoes probably are the Es layer second-bounce since they have the same Doppler distribution and the radar operating frequency is much lower than  $f_0F2$ .

After threshold segmentation and connected region generation, the vertical ionosphere echoes are shown in Figure 8. Although the peak power of Es layer echoes is higher than

TABLE 1: Experimental results compared with IRI2012.

Time	Radar frequency $f/\text{MHz}$	Ionosphere height $h/\text{km}$	Electron density $N_e/\text{m}^{-3}$	IRI2012 estimation $N_e/\text{m}^{-3}$	Plasma frequency $f_p/\text{MHz}$	IRI2012 estimation $f_p/\text{MHz}$	Mean velocity $v/\text{m/s}$
20:20	4.5	215	$7.76e + 11$	$2.54E + 10$	7.93	1.44	1.71
20:31	5.5	215	$5.15e + 11$	$2.23E + 10$	6.46	1.34	-45.68
20:41	6.5	225	$1.35e + 12$	$4.15E + 10$	10.44	1.83	-1.29
21:04	7.5	215	$8.81e + 11$	$1.84E + 10$	8.45	1.22	-5.00
15:32	4.7	185	$9.27e + 11$	$3.07E + 11$	8.67	4.98	1.65
15:41	5.6	200	$7.34e + 11$	$4.19E + 11$	7.71	5.83	5.43
15:52	6.4	220	$6.87e + 11$	$5.97E + 11$	7.46	6.96	9.10
9:44	4.7	160	$1.89e + 11$	$2.95E + 11$	3.92	4.89	-15.45
10:03	6.5	185	$7.07e + 11$	$4.02E + 11$	7.57	5.71	4.34
10:14	8.1	215	$3.22e + 11$	$5.86E + 11$	5.11	6.89	-11.83

F layer echoes; the total power is just the opposite. The mean Doppler shifts of ionosphere echoes from Es layer and F layer are  $-0.48$  Hz and  $-1.68$  Hz, respectively. So the mean drift velocities of irregularities are  $-13$  m/s and  $-45$  m/s, respectively. The electron density and plasma frequency corresponding to ionospheric scattering volume also can be estimated by (11) and (12), respectively. Table 1 shows the experimental results compared with that of IRI2012 in the order of time: May 23 evening, 24 afternoon, and 25 morning 2014.

Table 1 shows that the electron density from (11) roughly has the same order of magnitude as IRI. The difference between estimation values and IRI may be caused by the assumption of constant in (6). The estimated values of the day accord with the IRI better than that of the night. The observational data at night has always been different from IRI. For example, there are so many intense ionospheric echoes from E layer for HFSWR while E layer disappeared in IRI. And those echoes always tend to last a few hours and occupy several range bins which is different from Es layer. Therefore Jiang et al. refer to the new ionospheric structure as spread E layer [11].

## 6. Conclusions

The main purpose of this paper is to reveal the physical mechanism of the ionospheric clutter for HFSWR. Unlike most papers concentrating on ionospheric clutter suppression, this paper tries to preform sounding ionosphere by the received ionospheric clutter. Therefore the HFSWR can not only detect target in over-the-horizon detection and ocean remote sensing but also perform sounding the ionosphere in the range of radar coverage. Firstly, the pattern of transmitting antenna and receiving antenna is simulated by HFSS so that we can know the spatial distribution of the ionosphere. After the pretreatment of ionospheric echoes we get the vertical HFSWR ionosphere echoes. Then we discussed the coherent scattering mechanism and established the mathematical modeling of the receiving power and electron density of irregularities. So the electron density of FAIs created by plasma instabilities in the corresponding ionosphere region can be obtained by the coherent backscattered radar equation

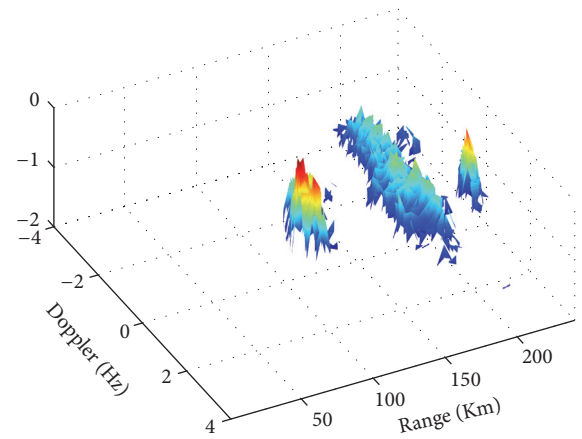


FIGURE 8: The vertical ionospheric echoes.

while plasma frequency and drift velocity can be obtained at the same time. Most of the experimental results are roughly consistent with IRI2012 except data in the evening.

The function of HFSWR looks like ionosonde in this paper. In fact, this is just the first step of our future works. Next we will retrieve the ionospheric parameters of the whole HFSWR coverage region which may have over ten thousand cubic kilometers and be hardly detected by other ionosphere soundings. The ionospheric information will be very beneficial to shortwave communication, frequency selection for high frequency sky wave radar and HFSWR, and the relationship between ionosphere and sea state.

## Competing Interests

The authors declare that they have no competing interests.

## Acknowledgments

The authors would like to express their sincere thanks to the National Natural Science Foundation of China (Grants nos. 61171188 and 61571159) and members of the school of Electronics and Information Engineering, Research Center, Harbin Institute of Technology, for technical support.

## References

- [1] E. D. R. Shearman, "Propagation and scattering in MF/HF ground wave radar," *IEE Proceedings, Part F: Communications, Radar and Signal Processing*, vol. 130, no. 7, pp. 579–590, 1983.
- [2] D. Barrick, "History, present status, and future directions of HF surface-wave radars in the U.S.," in *Proceedings of the International Conference on Radar (RADAR '03)*, Adelaide, Australia, September 2003.
- [3] H. C. Chan and E. K. L. Hung, "An investigation in interference suppression for HF surface wave radar," Tech. Rep. 2000-028, Defense R&D Canada, Ottawa, Canada, 1999.
- [4] L. Sevgi, A. Ponsford, and H. C. Chan, "An integrated maritime surveillance system based on high-frequency surface-wave radars, Part I: theoretical background and numerical simulations," *IEEE Antennas and Propagation Magazine*, vol. 43, no. 4, pp. 28–43, 2001.
- [5] A. M. Ponsford, L. Sevgi, and H. C. Chan, "An integrated maritime surveillance system based on high-frequency surface-wave radar, part II: operational status and system performance," *IEEE Antennas and Propagation Magazine*, vol. 43, no. 5, pp. 52–63, 2001.
- [6] X. Zhang, Q. Yang, and W. Deng, "Weak target detection within the nonhomogeneous ionospheric clutter background of HF/SWR based on STAP," *International Journal of Antennas and Propagation*, vol. 2013, Article ID 382516, 11 pages, 2013.
- [7] Y. Li, Y. Wei, R. Xu, Z. Wang, and T. Chu, "An ionospheric Es layer clutter model and suppression in HF surfacewave Radar," *International Journal of Antennas and Propagation*, vol. 2013, Article ID 320645, 18 pages, 2013.
- [8] H. C. Chan, "Characterization of ionospheric clutter in HF surface-wave radar," Tech. Rep. 2003-114, Defence R&D, Ottawa, Canada, 2003.
- [9] S. Shang, N. Zhang, and Y. Li, "Ionospheric clutter statistical properties in HF/SWR," *Chinese Journal of Radio Science*, vol. 26, no. 3, pp. 521–527, 2011.
- [10] X. Wan, X. Xiong, F. Cheng, and H. Ke, "Experimental investigation of directional characteristics for ionospheric clutter in HF surface wave radar," *IET Radar, Sonar & Navigation*, vol. 1, no. 2, pp. 124–130, 2007.
- [11] W. Jiang, W. Deng, and J. Shi, "Characteristic study of ionospheric clutter in high frequency over the horizon surface wave radar," in *Proceedings of the IEEE China Youth Conference on Information and Communications Technology*, pp. 154–157, Beijing, China, 2009.
- [12] D. Bilitza, D. Altadill, Y. Zhang et al., "The international reference ionosphere 2012—a model of international collaboration," *Journal of Space Weather & Space Climate*, vol. 4, article A07, 2014.
- [13] H. Zhou, B. Wen, and S. Wu, "Ionosphere probing with a high frequency surface wave radar," *Progress In Electromagnetics Research C*, vol. 20, pp. 203–214, 2011.
- [14] H. Gao, G. Li, Y. Li, Z. Yang, and X. Wu, "Ionospheric effect of HF surface wave over-the-horizon radar," *Radio Science*, vol. 41, no. 6, Article ID RS6S36, 2006.
- [15] K. Schlegel, "Coherent backscatter from ionospheric E-region plasma irregularities," *Journal of Atmospheric and Terrestrial Physics*, vol. 58, no. 8-9, pp. 933–941, 1996.
- [16] P. V. Ponomarenko, J.-P. St-Maurice, C. L. Waters, R. G. Gillies, and A. V. Koustov, "Refractive index effects on the scatter volume location and Doppler velocity estimates of ionospheric HF backscatter echoes," *Annales Geophysicae*, vol. 27, no. 11, pp. 4207–4219, 2009.
- [17] C. Haldoupis, E. Nielsen, and K. Schlegel, "Dependence of radar auroral scattering cross section on the ambient electron density and the destabilizing electric field," *Annals of Geophysics*, vol. 8, no. 3, pp. 195–211, 1900.
- [18] CCIR Recommendation 252-2, Second CCIR computer-based interim method for estimation sky-wave field strength and transmission loss at frequencies between 2 and 30 MHz, 1992.

## Review Article

# Application of HF Radar in Hazard Management

**Mal Heron,<sup>1</sup> Roberto Gomez,<sup>2</sup> Bernd Weber,<sup>3</sup> Anna Dzvonkovskaya,<sup>2</sup> Thomas Helzel,<sup>2</sup> Nicolas Thomas,<sup>4</sup> and Lucy Wyatt<sup>1,5</sup>**

<sup>1</sup>James Cook University, Townsville, QLD, Australia

<sup>2</sup>Helzel Messtechnik GmbH, Kaltenkirchen, Germany

<sup>3</sup>gempa GmbH, Potsdam, Germany

<sup>4</sup>ACTIMAR, Brest, France

<sup>5</sup>University of Sheffield, Sheffield, UK

Correspondence should be addressed to Mal Heron; [mal.heron@ieee.org](mailto:mal.heron@ieee.org)

Received 10 June 2016; Accepted 28 August 2016

Academic Editor: Weimin Huang

Copyright © 2016 Mal Heron et al. This is an open access article distributed under the Creative Commons Attribution License, which permits unrestricted use, distribution, and reproduction in any medium, provided the original work is properly cited.

A review is given of the impact that HF radars are having on the management of coastal hazards. Maps of surface currents can be produced every 10–20 minutes which, in real time, improve navigation safety in restricted areas commonly found near ports and harbours. The time sequence of surface current maps enables Lagrangian tracking of small parcels of surface water, which enables hazard mitigation in managing suspended sediments in dredging, in emergency situations where flotsam and other drifting items need to be found, and in pollution control. The surface current measurement capability is used to assist tsunami warnings as shown by the phased-array data from Chile following the Great Tohoku Earthquake in 2011. The newly launched Tsunami Warning Center in Oman includes a network of phased-array HF radars to provide real-time tsunami monitoring. Wind direction maps can be used to locate the position of cold fronts in the open ocean and to monitor the timing and strength of sea-breeze fronts in key locations.

## 1. Introduction

Most HF radars that have been installed over the past 20 years have been predominantly for research and development. During this period the technology has become widely accepted as a significant tool in the research and management of the coastal environment. As a result we are now in a new era in which HF radars are being installed primarily for operational management and also for hazard warning and mitigation. HF radars are capable of mapping currents over large coastal areas (up to 200 km) on a fine grid (down to 1 km) as shown by Shay et al. [1] and Mao and Luick [2]. The primary parameter that HF radars measure is the surface current, with the effective depth of measurement being  $\delta = c/(8\pi f)$ , where  $c$  is the electromagnetic phase speed and  $f$  is the radar frequency (Stewart and Joy [3]). For a 16 MHz radar  $\delta$  is 0.75 m. At this depth the currents are driven by winds and tides as well as the underlying large-scale circulation. It is this capacity to map the surface layer over a wide area in real time that makes the technology particularly well suited

to hazard mitigation. In addition to surface currents, the phased-array genre of HF radar has the capacity to map significant wave heights on a grid over an area (Essen et al. [4]), and wind directions can be monitored on a spatial grid. In this paper the discussion focusses on WERA phased-array radar systems. Other systems have different levels of errors, resolution and accuracy, and perform rather differently in hazard management.

Real-time quality control is essential for operational data, and Section 2 discusses some of the procedures used for HF radar surface current data.

With surface currents on a fine spatial grid, repeating on a short time lapse, it is useful to calculate the Lagrangian tracks that floating objects would follow, provided that special care is taken to assure the quality of the data described by Mantovanelli et al. [5]. Phased-array HF radar technology has the comparative advantage of high resolution and accuracy that are needed for Lagrangian tracking. This has applications in pollution control, salvage, and search-and-rescue operations and is demonstrated in Section 3 of this paper.

Tsunamis are shallow water gravity waves, even in the deepest oceans. In deep ocean water they are undetectable with HF radar because their amplitudes are small and their wavelengths are long (>100 km). However, in shallow water on the continental shelf, the signatures of the tsunami are amplified and it has been shown that HF radar can detect the surge currents of the orbiting surface particles as the tsunami wave train passes a point (Heron et al. [6]). HF radars are now being installed specifically to monitor the coastal ocean for approaching tsunamis, and Section 4 shows how this is being done in Oman.

The capacity to plot maps of surface wind directions is being evaluated to feed in to the forecasting of the movement of cold fronts in the southern ocean in the Great Australian Bight. This is an area of sparse weather stations in a place where the movement of cold fronts is a key parameter, particularly in the management of bush fires in South Australia and Victoria. This is discussed in Section 5 of the paper.

An example of the use of HF radar in routine management of a busy port is given in Section 6, using data from the WERA radar installed at the Port of Rotterdam in Netherlands (Van Heteren et al. [7]). These initiatives in Europe as well as developments like The US Ports Infrastructure Projects recognise the need for operational use of current monitoring around ports. The dual-purpose use of HF radar for emergency as well as routine management was illustrated by its notable absence in the demise of the MV Rena off Tauranga in New Zealand in 2011.

## 2. Real-Time Quality Control for Hazard Management

Ocean surface data provided by HF radar show sporadically nonrealistic values in some areas, particularly at the outer edges of the radar coverage, which do not correspond to the measured phenomena. Some reasons for the appearance of such measurements are radio frequency interference, lightning, ionosphere clutter, and ship echoes. Several techniques have been developed for phased-array type HF radars to mitigate (Gurgel et al. [8]) or to overcome (Heron and Prytz [9]) such disturbances in the data, drastically reducing their appearance. Despite such efforts, it is impossible to avoid some poor quality data in the output from the radar system. Additionally, limitations which are inherent to the system itself such as the geometric arrangement when combining data sets of radial components, azimuthal resolution at far ranges, and signal-to-noise variation between day and night may degrade the accuracy of measured data.

For hazard applications, the reliability of the data is essential and quality control criteria need to be set at appropriate levels. Furthermore, in cases of time-sensitive applications (like tsunami detection or forecast for search-and-rescue and oil spill scenarios) QC needs to be performed immediately on each data set as it becomes available (near real-time).

To cover this need for QC, the WERA HF radar system includes QC routines which are integrated into the data processing chain and applied in near real-time. The QC processing parameters can be tuned to the specific dynamic

characteristics of the ocean being measured for optimal performance.

Although most applications require the horizontal and vertical components of the current velocity, the WERA QC procedure focusses on the step immediately preceding that and is applied to each radial component value on the common and predefined Cartesian grid. This has the advantage of dealing with data at the earliest point before any averaging or combining of data from two stations to form the surface current vectors on the Cartesian grid. The procedure consists of performing a series of tests on measurements in each grid cell in the latest radial current dataset obtained. The tests evaluate the measurements and analyze their consistency with past measured values. At the end, each grid cell will be given a quality level number from 1 to 5, where quality level 1 is the best quality and quality levels 4 and 5 are considered to be corrupted data. The processing chain may automatically exploit this option to obtain cleaner current velocity vector maps in eastward and northward components by combining radial velocities from two or more radars in which undesired quality levels are omitted.

It is important to note that no data are deleted during the QC procedure. The data points are just individually marked with a quality level.

Similar methodologies are applied to wave data and wind direction data provided by the WERA system.

*2.1. Case Study: QC at South Florida.* As reported by Gomez et al. [10], the QC procedure was implemented on the current velocities measured by a pair of WERA HF radar systems of the University of South Florida (labelled in Figure 1 as Ft DeSoto and Venice) and tested for a period of 9 months. The QC parameters used in this experiment were empirically tuned using data for one month from both stations. The performance of the QC procedure was evaluated by comparing the data from Venice station with the radial projection of the current velocity measured every hour by an Acoustic Doppler Current Profiler (the red dot in Figure 1 labelled as C10) and calculating a correlation coefficient. The correlation coefficients of radar data compared to ADCP data were obtained excluding different levels of quality. The results are shown in Table 1.

It can be observed that data which are identified by the WERA QC process to be corrupted represent a very small percentage of the total data and indeed as a separate group show a very poor agreement with the ADCP. Excluding these low-quality data from the data set produces an overall improvement of the correlation coefficient. Furthermore, different levels of quality effectively classify different levels of reliability in the measured data.

*2.2. Improve Reliability of Metocean Warnings.* The data provided by an HF radar may be used by port authorities or civil-protection as an additional complementary source of information when deciding upon metocean warnings. Such an application is a clear example that requires both real-time access and reliability on the data.

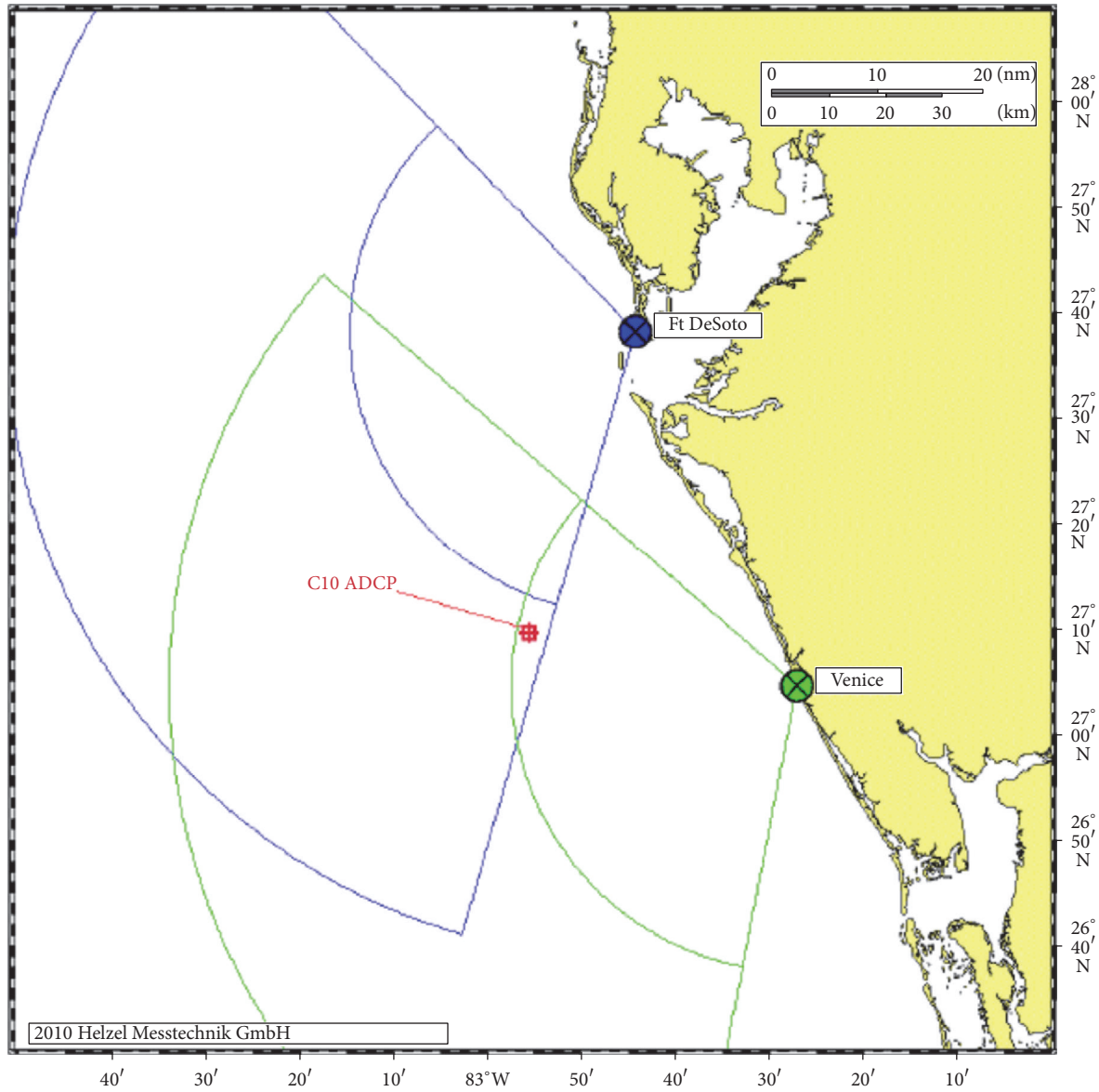


FIGURE 1: Position and range of WERA systems and ADCP location used for the case study in South Florida.

TABLE 1: Correlation coefficients for different quality levels of data provided by Venice site at the location of ADCP.

Condition to satisfy to be included in correlation calculation	Number of data points	Correlation coeff. ( <i>R</i> )
All data available	2316 (100%)	0.87
Quality level > 3 (corrupted data only)	28 (1.2%)	0.44
Quality level ≤ 3 (all valid meas.)	2288 (98.8%)	0.90
Quality level = 3 (deficient but still ok)	171 (7.4%)	0.68
Quality level = 2 (medium quality)	495 (21.4%)	0.83
Quality level = 1 (best quality)	1622 (70%)	0.93

A straight forward application of HF radar data for metocean warnings is to search for high values of current or wave height measured at the last data set available from the radar. The search could be either at predefined critical points in the ocean (port entrance) or at the whole monitored area. If the measured parameters exceed a certain threshold,

an automatic warning notification can be sent. However, if the data sporadically show spikes of corrupted data, there is a high risk of registering false warnings.

One way to reduce the occurrence of false warnings is to apply spatial averaging which can potentially mitigate the effects of a local spike. This is the least satisfactory approach

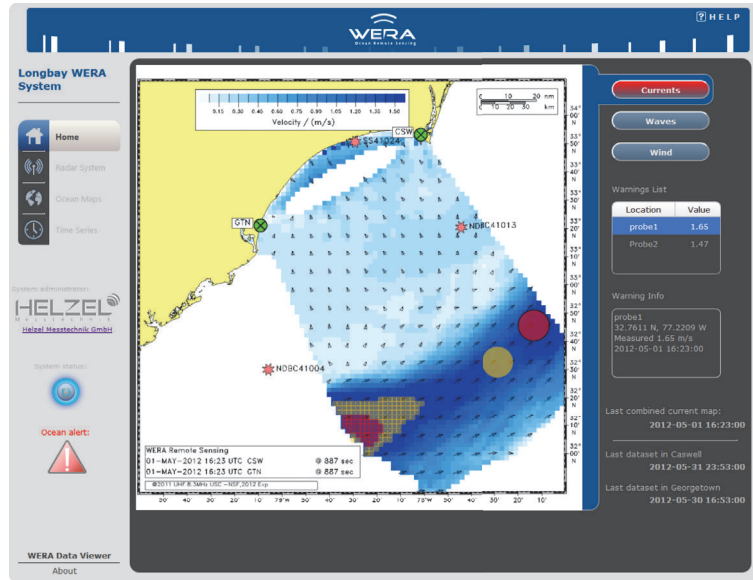


FIGURE 2: Ocean warning displayed on the WERA Data Viewer web interface. Coloured circles correspond to warnings on specific locations being monitored; small squares correspond to areas where global thresholds set on the whole coverage area have been exceeded. Yellow zone represents a low risk warning and red zone represents a high risk warning. To avoid congestion, current direction arrow is shown at every 5th grid cell.

because contaminated data become woven into the final result in the process of averaging. In the case of artefacts which are spatially spread (e.g., radio frequency interference) or in the case of highly dynamic seas a simple average is particularly unreliable. Applying QC to the data in near real time before searching for spikes and artefacts may eliminate or highly reduce the risk of false warnings. To further increase the level of confidence, the use of HF radar data for critical decisions may be limited to data with a certain level of reliability (i.e., quality levels 2 and 1 when using the flags adopted by the WERA QC procedure).

Figure 2 shows a screenshot of the WERA Ocean Warning add-on feature in the Data Viewer web interface of WERA. The software can be configured to ignore data values that do not fulfil a certain level of quality, size-configurable spatial averaging, and two different threshold levels (for high and low risk) for specific coordinates or for the whole covered area. Warnings are automatically send to competent authorities or decision makers via email.

### 3. Lagrangian Tracking of Surface Drifters and Short-Term Forecasting

The availability of gridded current data at short return periods of less than one hour invites the calculation of Lagrangian tracks and short-term forecasting. With the availability of surface currents on a fine spatial grid, repeating at short time intervals, the empirical Lagrangian tracking method uses water velocity at one point in time and space to step forward one time increment to a new position. These products are derived after a special QC process by analyzing the different physical drivers of surface currents and processing each of

the driving effects to improve quality and make interpolations and extrapolations as required.

*3.1. Lagrangian Tracking.* At any time and location the current can be derived and applied to a notional parcel of surface water which is projected on to a new location after one time step. At the new location the current velocity is interpolated and another step is taken and so on. Mathematically, this is risky because it is an integration process where errors are cumulative and can become quite large. This is why some authors use surface drifters to validate HF radar surface currents, measure the drifter displacement over a short time interval to calculate current velocity, and compare that with the radar currents (Ohlmann et al. [11]). This removes the integration problem but is no good for tracking drifting particles. While many HF radar installations can forecast a general direction for Lagrangian drifters (Ullman et al. [12]), a phased-array radar with careful quality control on the real-time data is shown to produce tracks that are within a few kilometres of the true position over many tidal cycles.

In practice special QC processing is required, even with good quality WERA data because Lagrangian tracking requires a filled spatial grid and filled time series. This means that data values that have a low QC flag have to be replaced as accurately as possible to maintain the accuracy of the Lagrangian tracking. It is clear in Figure 3(a) that the biggest rates of change are derived from the tidal component of the current. There are two points to note about this: one is that it is difficult to identify “spikes” in the data and the second is that the tidal component of the current is predictable. We carry out a tidal analysis to get the tidal constituents over the last 30-day period and remove the tidal signal from the

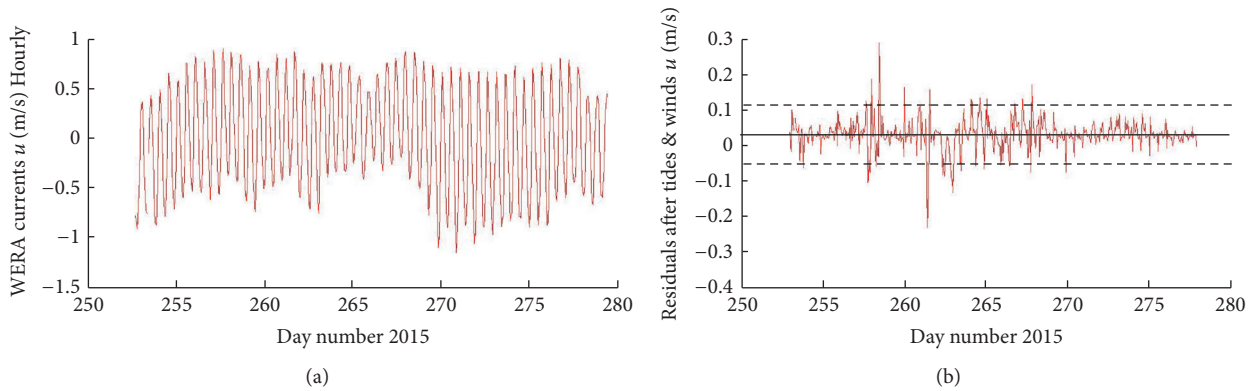


FIGURE 3: A time series of WERA  $u$ -component (a) with residuals after tidal and wind-driven  $u$ -components are removed (b). The horizontal black dash lines indicate  $\pm 2$  standard deviations. Data points in the residual outside these lines are replaced by interpolation in the residual time series. The WERA  $u$ -component of current is then reconstructed by adding wind-driven and tidal  $u$ -components. The data shown are from a site near Rotterdam in the North Sea.

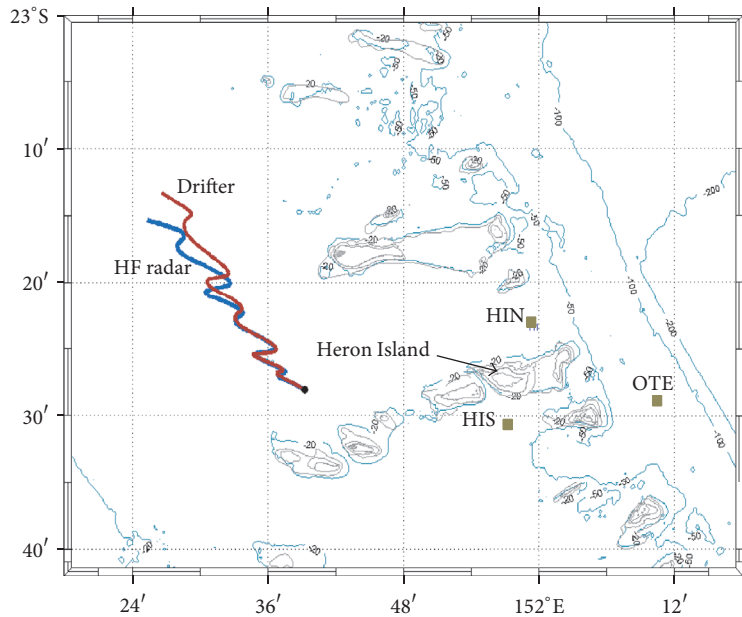


FIGURE 4: A surface drifter tracked by satellite follows the red line, while a track derived from HF radar data using the same starting location and time follows the blue line. The zigzags are due to the dominant 12-hour tide, and the trend towards the northwest is due to the synoptic surface wind. The site is on the Great Barrier Reef, Australia.

radar time series. If there are reliable wind data then a fitted wind-driven current may also be removed. The residual thus produced (Figure 3(b)) is smaller in amplitude and spikes can be identified. The rms of the residual is calculated, and any point that exceeds  $2x$  rms is removed and replaced by a value that is interpolated in the time/space domain at the residual level. This process is repeated until it stabilises and then the tidal component is added back into the time series. The strength of this method is that we are interpolating only that part of the signal that has unknown driving forces (e.g., wind, diffusion, and mesoscale currents) (Mantovanelli et al. [5]), and we are accurately calculating the value of the tidal current. When the spikes are removed the interpolation is only in the residual signal where errors in interpolation are

reduced. The final step is to reconstruct the surface current vector by adding the tidal and wind-driven components to the amended residual time series.

An example of this procedure is shown in Figure 4 which depicts a section of area covered for surface current mapping by WERA HF radar stations located at Tannum Sands and Lady Elliot Island in the southern Great Barrier Reef region. The radar operated at 8.38 HMz with a 50 KHz bandwidth. A surface drifter with a GPS receiver and satellite communications link was released at the black dot. A feature of interest in the data in Figure 4 is the abrupt separation of the tracks after about 36 hours (zigzags are tidally driven and occur at 12 hour intervals). Prior to that event, the tracks are very close (inseparable on the diagram), and afterwards

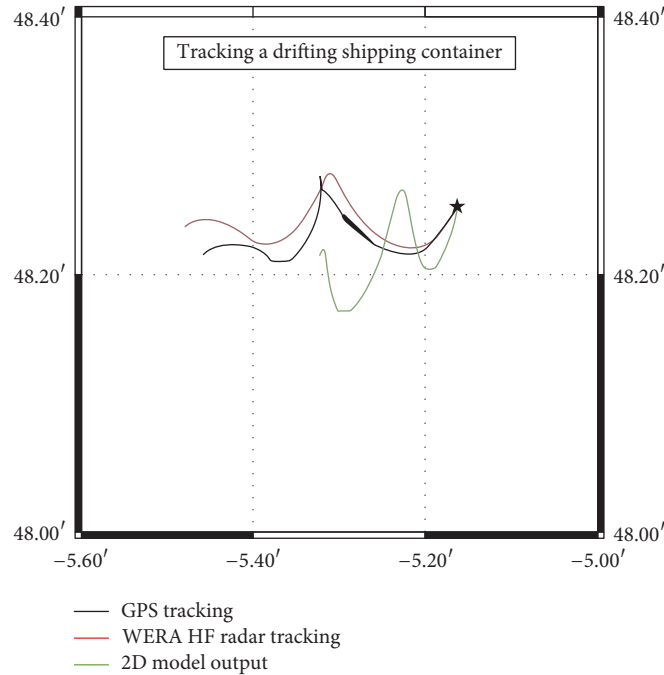


FIGURE 5: Tracking a drifting shipping container in the Iroise Sea. The HF radar Lagrangian tracking position is about 5 km off the actual position after 18 hours. The fluctuations in the tracks are due to the semidiurnal tides.

there is a steadily increasing separation. This phenomenon is repeated when we consider two closely spaced drifters (Mantovanelli et al. [13]) or alternatively two radar tracked points which start closely spaced. This is the focus of ongoing research because there is a feature in time or space that causes a dramatic change in the horizontal diffusivity at the surface that has similar characteristics to Lagrangian Coherent Structures (LCS) described by Shadden et al., [14].

An independent example of successful Lagrangian tracking is shown in Figure 5 in the Iroise Sea using a WERA radar system operating at 12.38 MHz and bandwidth of 100 KHz by ACTIMAR on the west coast of Bretagne (Helzel et al. [15]). A drifting shipping container followed the track drawn in black for approximately 18 hours, while the radar-based track is shown in red. The effective depth of tracking for the radar at 12.38 MHz is 0.97 m.

These examples show that WERA HF radar produces Lagrangian tracks that are based on real data and have none of the assumptions of diffusion coefficients, wind effects, or other parameterisations that exist in hydrodynamic models. With the precautions discussed, particles have been tracked on the shelf for up to 4 days (with errors typically 2–4 km per day). The research applications of these techniques include spatial and temporal changes in diffusivity and larval connectivity between reefs. There are obvious applications in search-and-rescue, pollution management, and port management.

**3.2. Short-Term Forecasting.** Statistical forecasting of the surface current fields is one of the possibilities offered by ocean surface radars. Statistical forecasting means predicting

the future based on past data and using only statistical algorithms, without any physical model. It must be distinguished from physical forecasting which uses dynamic equations to propagate data from the past, for instance, with an ocean model and its initial conditions.

Since HF radar currents can cover a significant coastal area with a good spatial resolution and a high temporal resolution, the signature of most of the local ocean physical processes that contribute to the evolution of surface currents can be captured. If processes are well captured and the system is predictable, statistical algorithms are able to extrapolate currents into the near future (24–48 h) after a learning phase.

A statistical forecast solution for the surface currents based on a space-time EOF analysis was developed and integrated into the commercial tool CurExtrap©. An example of CurExtrap© output is presented in Figure 6. Obviously, the quality of the forecast produced relies on the quality of the input measurements and on the possibility to assess the effective quality of the input data during the statistical analysis.

## 4. HF Ocean Radar Support for Tsunami Early Warning Systems

**4.1. Observations of Tsunamis by Phased-Array HF Radar.** A tsunami is a series of waves that can be generated when earth plate boundaries abruptly move and vertically displace the overlying water. Although a tsunami cannot be prevented, the impact of a tsunami can be mitigated through community preparedness, timely warnings, and effective response.

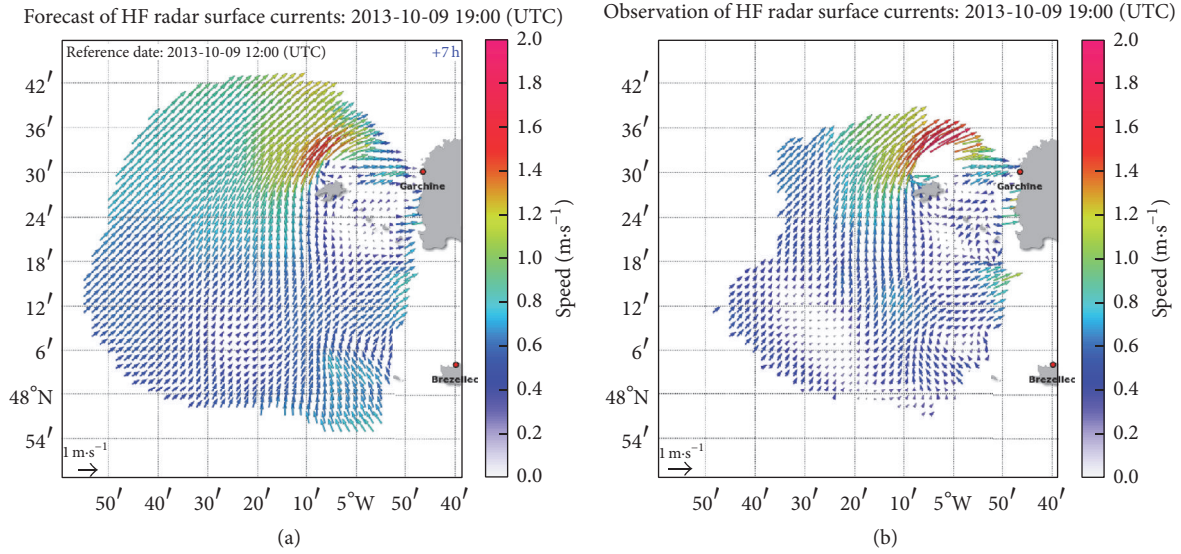


FIGURE 6: Example of a forecast of surface currents with CurExtrap in a tidal environment observed by 2 WERA radars, in Iroise Sea, France. (a) Statistical forecast made at 1200 h UTC. (b) Validation of the forecast by the radar measurements 7 hours later at 1900 h UTC. Radar data source: SHOM (Service Hydrographique et Océanographique de la Marine); figures provided by ACTIMAR.

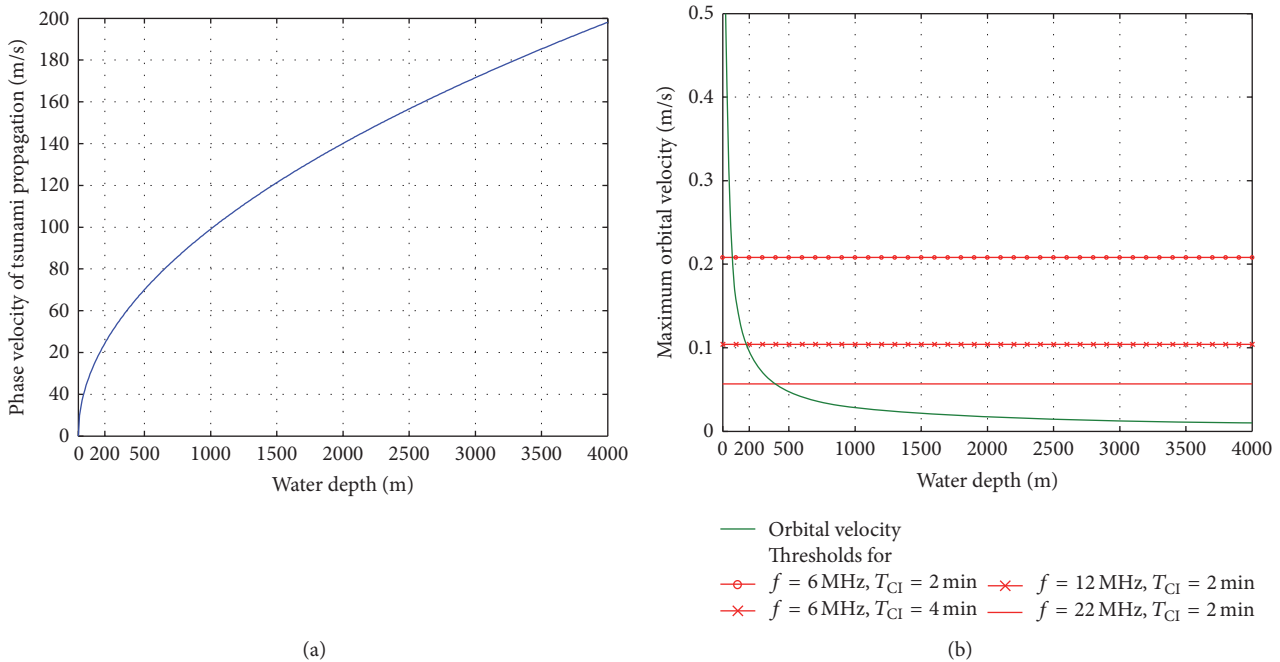


FIGURE 7: Linear theory results. (a) Tsunami phase velocity of propagation as a function of water depth; (b) the maximum horizontal velocity (surface current velocity) of orbiting surface particles in a tsunami wave (green line) and lower boundaries for tsunami detection by phased-array HF radar (red lines).

Tsunami Early Warning Systems (TEWS) meet the challenge of near field warning with extremely short warning time. When tsunamigenic earthquakes have epicentres close to the shore, the time between a seismic event and the issue of a warning may be limited to just a few minutes.

When tsunami disturbances propagate in the deep ocean as shallow water gravity waves with zero dispersion the

phase velocity can be approximated by linear wave theory as  $c = \sqrt{gd}$ , where  $g$  is the gravity acceleration and  $d$  is the water depth. The phase velocity dependency is shown in Figure 7(a). As the tsunami approaches the coast and the waters become shallow, the wave is compressed due to wave shoaling and its speed slows down to 20 m/s. Its wavelength typically diminishes to less than 20 km and its amplitude

grows enormously, producing a distinctly visible wave as described by Green's Law (Green [16]).

The orbital motions of surface particles, as the shallow water gravity wave propagates past a point, are horizontally elongated ellipses with the semiminor axis (water elevation) given by Kinsman [17]. The application of linear theory for the maximum orbital velocity (surface current velocity) as a function of depth is given by  $v_m = a(d)\sqrt{g/d}$ , where  $a(d)$  is the tsunami wave amplitude in water of depth  $d$  and  $g$  is gravitational acceleration. This is illustrated by the green lines in Figure 7(b) for a tsunami wave with an initial elevation of 0.2 m in a deep ocean. It can be easily seen that surface current velocities induced by a tsunami are many orders of magnitude smaller than the phase velocity of tsunami propagation. Nevertheless, these current velocities can be accurately measured with high spatial and temporal resolution using the phased-array HF ocean radar technology. The sensitivity of the radar in resolving the surface current velocities strictly depends on the operating radar frequency  $f$  and integration time  $T_{CI}$  as shown in Figure 7(b) by red dashed lines. These lines are velocity resolution thresholds derived from radar characteristics. All tsunami current velocities with values above these thresholds have a chance to be detected offshore. While the tsunami wave is approaching the continental shelf, the surface current pattern changes from small magnitudes in deep water to more significant values in the shelf area as shown by Gurgel et al. [18]. This strong change of the surface current can be detected by a WERA system in real-time monitoring. The fact gives an opportunity to issue an automated tsunami watch message by the WERA radars to TEWS. The detection with a WERA radar system will be in the vicinity of 300 m depth depending on the magnitude of the tsunami. For a shelf of average depth 50 m and width 100 km the warning time before the tsunami impacts the coast will be about 75 minutes. Hence by measuring the surface current velocities, HF ocean radars are able to contribute to the development and improvement of TEWS. If these radar systems have been already installed at the coast then their upgrade for tsunami observation is easy and inexpensive.

Observations of tsunamis by HF radar are sparse, but a case presented itself on March 11, 2011. One WERA HF radar station was in operation when the Great Tohoku Earthquake in Japan produced tsunami waves that hit the Chilean coast after 22 hours of propagation across the Pacific Ocean. The radar was located near Rumena, Chile, and supplied ocean surface monitoring in that region. The radar measurements at 22-MHz frequency were recorded and archived for several hours while the tsunami wave train was impacting the Chilean coast.

The radial velocities of ocean surface currents were estimated from the radar spectra. To obtain the pure tsunami-induced currents, a filtering technique was applied to eliminate the natural surface current field, which included tidal components. The velocity measurements were achieving accuracy of a few cm/s, which means that the sensitivity of radar measurements was good enough to catch the small changes caused by the tsunami in deep water. Moreover, it can be clearly seen that the tsunami current velocity became higher as the wave entered the shelf area. This fact is in line

with the model assumptions in (Gurgel et al. [18]). Although the shelf width is only 10–20 km, a slight inclination in range of the measured currents shows that tsunami waves crossed the shelf within a few minutes.

The estimated tsunami wave periods were in the range 14–32 minutes. This suggests that any potential tsunami monitoring by ocean radar requires a continuous operation mode with a fast update of about 2 minutes for the ocean surface current measurements.

The HF ocean radar does not measure the approaching wave front (wave height) of a tsunami; however, it can detect the surface current velocity signature, which is generated when tsunami reaches the shelf edge. The HF ocean radar could provide valuable information to increase the reliability of TEWS under fulfilment of certain conditions:

- (i) The ocean bathymetry within the radar coverage is to be known in sufficient detail to plan an ocean radar installation with maximum effectiveness for tsunami monitoring.
- (ii) The spatial radar resolution must be sufficient to resolve the current signature. It is necessary for the radar system to achieve high signal-to-noise performance and narrow beam directivity. These features can be obtained using an array type WERA system with multiple channels and a beamforming technique.
- (iii) The temporal resolution of the radar must be high enough to pick up the fast changing surface velocity vectors. The potential tsunami areas should be monitored in a fast acquisition mode, which provides a quick update of the ocean surface current fields, for example, at a 2-minute rate. Based on this mode, an algorithm to detect a tsunami signature in the HF radar data is developed.

The output data of WERA processing software can be easily integrated into existing TEWS due to flexible data format, fast update rate, and quality control of measurements as well as be a part of systems, which provide simulation and assimilation for different tsunami scenarios. The data can be also archived for further hazard analysis and research purposes.

*4.2. Case Study: Operational Tsunami Warning System in Oman.* The newly launched Tsunami Warning Center in Oman is one of the most sophisticated tsunami warning system worldwide applying a mix of well proven state-of-the-art subsystems while otherwise applying newest technologies. It serves as a benchmark for the integration of HF radar data into the tsunami warning procedure.

The core of the tsunami warning system is the seismic real-time analysis system SeisComp3 described by Hanka et al. [19] and used in most tsunami warning centers globally. The tsunami simulation and decision support system is based on the Tsunami Observation and Simulation Terminal (TOAST) system developed by gempa GmbH, which integrates a precalculated tsunami scenario database and a GPU-based based "on the fly" simulation allowing the system to react to atypical earthquakes that are not considered by the

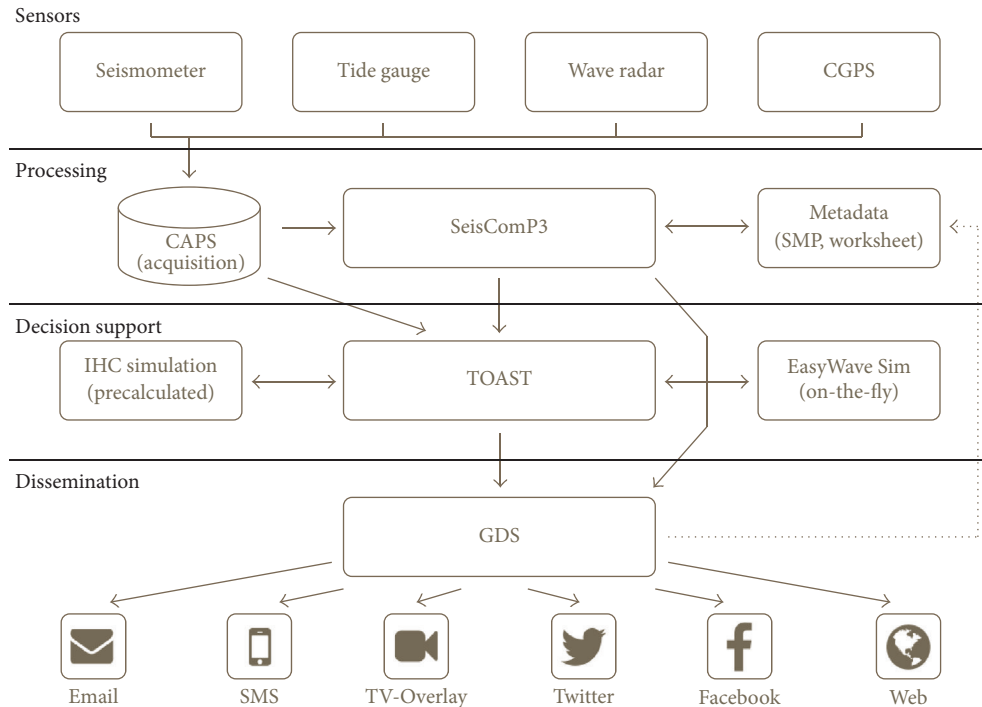


FIGURE 8: Architecture and data flow of the tsunami warning system in Oman processing seismic, tide gauge, wave radar, and cGPS data.

precalculated database. Simulations can be verified by the comparison of simulated and measured oceanographic data.

Most tsunami early warning centers employ tide gauges. Due to high costs, buoys are rare. The Omani TEWS also integrates measurements of a modern network of phased-array HF radars to verify simulations in TOAST giving additional scenario quality information and confirmation to the decision support. The CAPS (Common Acquisition Protocol Server) developed by gempa GmbH greatly simplifies the integration of multisensor data in TOAST. CAPS allows the acquisition of data from many different sensor systems including seismic stations, GNSS, tide gauge, and HF radar in one acquisition system providing access to all sensor data through a common interface (Figure 8).

While tide gauge data are integrated as traditional time series (sometimes called mariograms), the radar tsunami data are integrated in TOAST as a chain of “virtual” oceanographic sensors located at the shelf edge. The data are displayed in form of velocity streams generated at the virtual sensors and are treated in a similar way to tide gauge or buoy data. HF radars measure surface orbital within the waves of passing tsunami wave-trains and can be used for picking the tsunami onset time (Figure 8, bottom) and can be used to confirm wave amplitudes using the linear transform given in Section 4.1 to calculate amplitude from the maximum velocity and water depth. These onsets can be used to verify arrival times of the simulated scenarios and give additional information about the exact location of the rupture area.

The wave radar allows offshore monitoring, providing valuable input to the tsunami verification. If the tsunami genesis is far distant, the SeisComP3 and TOAST systems

will already be alerted and the HF radar data serve as confirmation of timing and severity of the hazard. When the tsunami genesis is close the HF radar data take a dominant role in the warning system. In some cases HF radar is used as an alternative to the expensive and maintenance-intense buoys.

## 5. Maps of Surface Wind Fields

The first-order Bragg lines in the spectra of beamforming phased-array HF ocean radar systems are echoes from two specific wind waves in the target cell of the radar. One of the Bragg lines is from the resonant wave approaching the radar station (line (a) in Figure 9) and the other is from the receding resonant wave (line (b) in Figure 9). Wind waves, at a given wavelength, have a directional spreading form that has a maximum in the direction of the wind and a near null in the up-wind direction.

By assuming a shape for this spreading, the wind direction can be derived by observing the ratio of Bragg peaks (a) and (b) illustrated in Figure 9 following Heron and Rose [20]. This is a closed form when data from two radar stations are used, and the wind directions can be calculated for each grid cell. Wyatt et al. [21] used a  $3 \times 3$  set of pixels in a maximum likelihood method to extract the two parameters of wind direction and the directional spreading of the wind. These two parameters are shown in the case study of Figure 10 with the region of high directional spreading clearly marking the position of the front. Here the interpretation depends on the assumption that the wind direction is that of the dominant

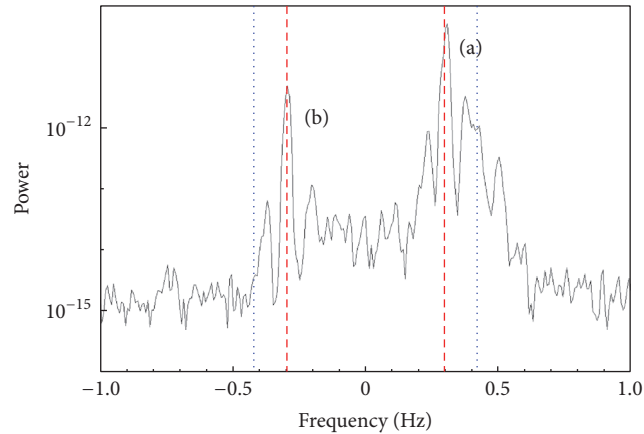


FIGURE 9: Spectra from phased-array radars are produced for each grid point, and the ratio of amplitudes of the sharp Bragg peaks (a and b) are used to estimate the direction of the wind.

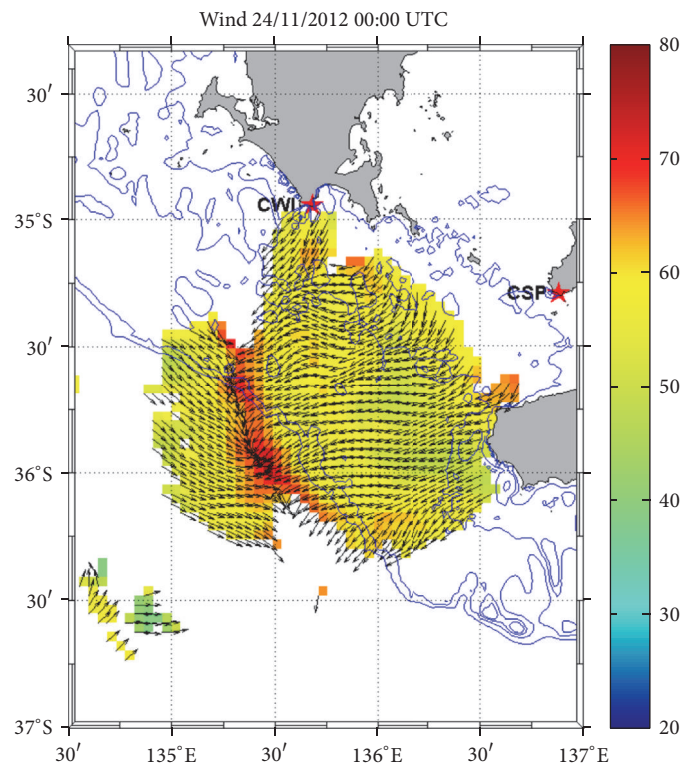


FIGURE 10: Data from the two radar stations (red stars at CWI and CSP) are combined at each grid point to calculate the wind direction shown by a field of arrows of equal length. The colour bar represents spread in the wind direction in degrees.

wind-wave direction. Wyatt [22] examined the accuracy of this assumption.

Maps of wind directions are particularly useful in the southern ocean where meteorological stations are sparse. The mapping of cold fronts moving across the area shown in Figure 10 off South Australia can be used to improve the forecasting of wind events in the eastern part of South Australia and in Victoria. In the summertime it is these frontal systems with high wind speeds and rapidly changing directions that exacerbate the hazard of bushfires. The timing

of the arrival of the fronts is a key parameter for managing bush fires and is accurately determined from the HF radar monitoring.

## 6. HF Radar in Port Management

One of the hazards in the operation of coastal ports is the strength of the alongshore current at the seaward end of the breakwater or training walls so that the pilot can compensate and avoid grounding. Real-time surface current data in the

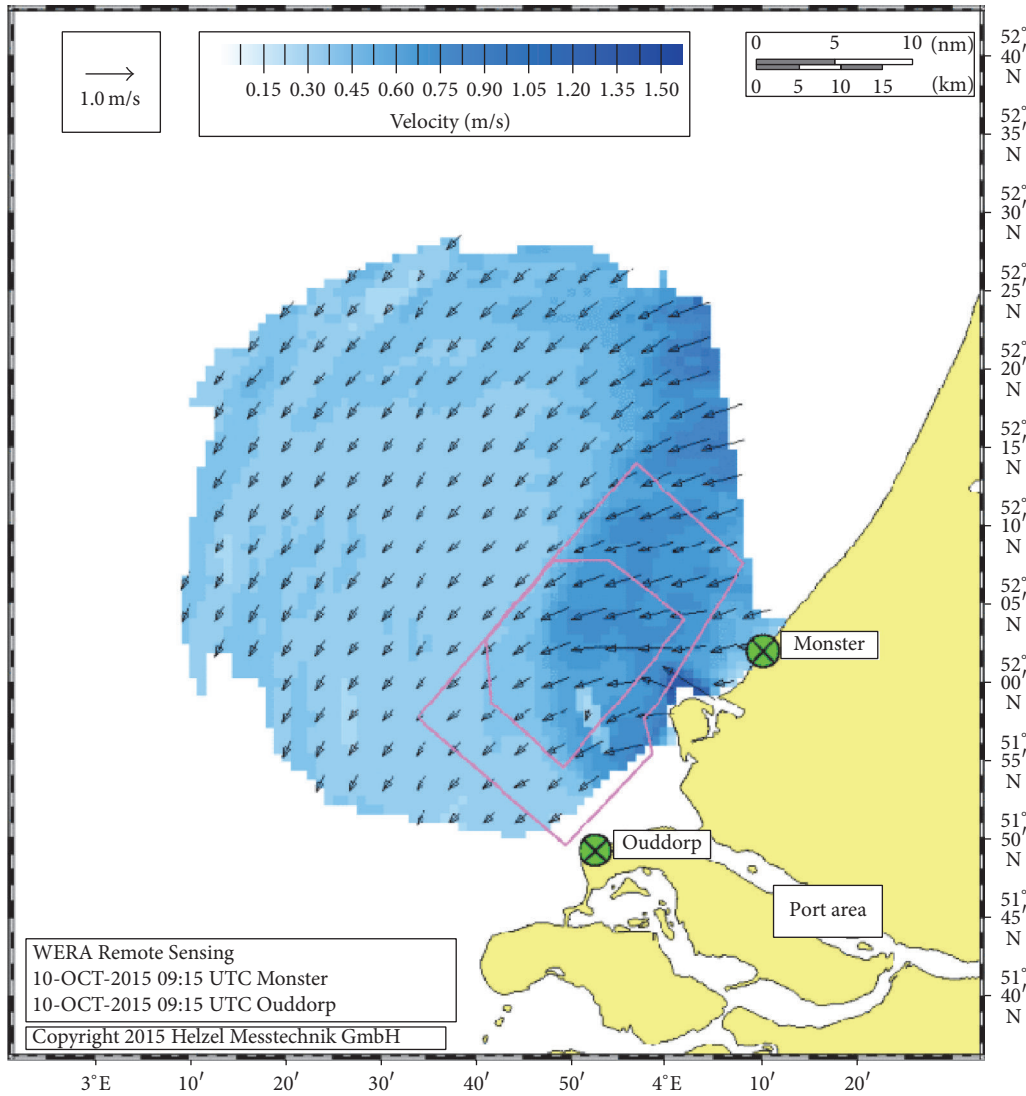


FIGURE 11: Typical output from the WERA radars at the Port of Rotterdam showing the radar station sites (green cross) and the main port area. The pink boxes indicate areas with different requirements on radar data availability in the real-time system.

outer port area can also be used to reduce hazards in the case of emergencies and for routine dredging operations.

**6.1. Case Study: Real-Time HF Radar Current Maps at the Port of Rotterdam.** The Port of Rotterdam experiences alongshore currents of up to 2 knots, which are mainly tidal but also driven by winds, terrestrial outflow, and some larger-scale circulation in the North Sea (Van Heteren [7]). WERA phased-array radars have been installed at each side of the port to map surface currents in the critical area for shipping. A typical map is shown in Figure 11.

A new data management system as described in the next section provides easy and fast access to all archived current, wave, and wind data. The data are stored in an archive and can be accessed as time series plots for individual grid cells or as animated maps for the entire measured area. For each grid cell all data are marked with quality flags which can be used to exclude suspicious data from the analysis. Various

output formats are available to compare the ocean radar data with data acquired from other sensors or numerical models (Schroevens et al. [23]).

**6.2. Data Management System Structure.** The new WERA data management system uses a MySQL database to store measured data. MySQL is a very powerful open-source relational database management system (RDMS) and allows subsequent tools in the WERA system to have a structured base from which data can be retrieved and stored. Using a database, in comparison with having data stored in text files, brings several benefits; some of them are as follows:

- (i) Data can be stored in binary form, not in ASCII characters, reducing space requirements.
- (ii) RDMS allows setting indexes, foreign keys, queries from simultaneous users, and other benefits which

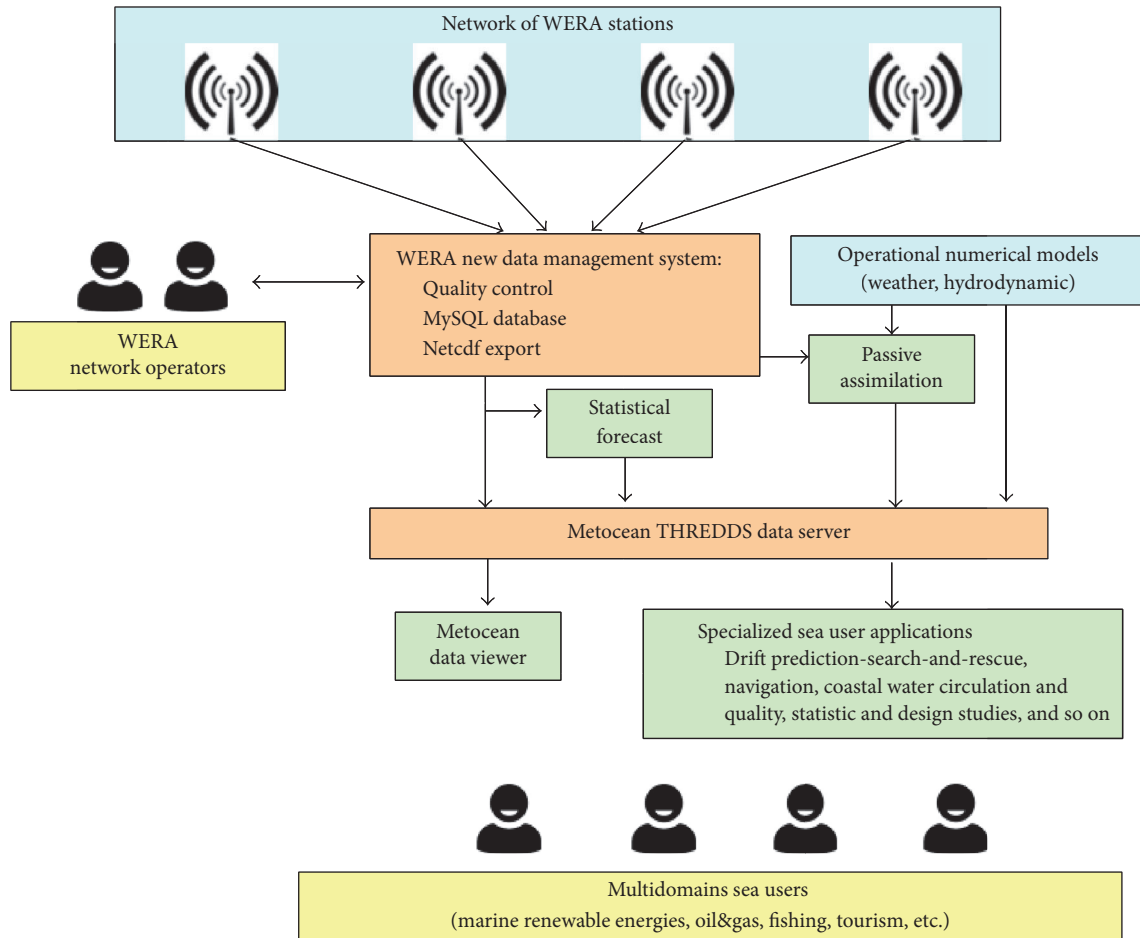


FIGURE 12: Example of data flow from the WERA stations to the end users using as center elements the WERA Data Management System and a Metocean TDS system.

allow a faster, ordered, and secure way of storing and retrieving data.

- (iii) RDMS use the standard and widely known SQL code. This allows users of WERA systems to develop their own routines or modify the existing structure of the database to satisfy particular needs.
- (iv) WERA users can access other types of open-source software (e.g., phpMyAdmin for MySQL databases).

The WERA data management system includes several software tools which process and store the oceanographic data measured by reading the data files provided by WERA and storing the information to the database in an organized manner using SQL commands as summarised in Figure 12. In standard configuration, these tools are executed automatically without any human intervention.

Additionally, the data management system includes a user-friendly web application that allows access to all the data stored in the database (please refer to Figure 2), as well as creating time series and exporting the data to different formats.

The relatively easy access to the data provided by the database can be readily exploited to implement the raft of hazard reduction applications in coastal zones.

## 7. Conclusion

Phased-array HF ocean radars have the capability to monitor the ocean surface far beyond the horizon because of the accuracy, resolution, and capacity to apply quality control flags to individual data points. The real-time tracking and forecast tracking of surface drifters are a leading feature of this radar technology and examples show that they can be tracked for up to 4 days with a spatial error of typically 2–4 km per day. The economic advantage of this in emergency search-and-rescue is significant and the application of Lagrangian tracking to coastal operations like dredging and construction reduces risks and hazards to the environment and other marine users.

The capability of phased-array HF radars to observe tsunami signatures in deeper waters adjacent to the continental shelf provides a useful element in assessing the impact of an approaching tsunami. The integration of radar data into an operational tsunami warning system is demonstrated by

the case study of the operational Tsunami Warning Center in Oman. The radar measurements can be used to confirm the timing and magnitude of the tsunami following prewarning from the seismic and buoy elements of the system. Based on actual (not simulated) tsunami measurements a set of requirements for the WERA ocean radar have been developed to enable its integration into the TEWS system. The requirements include a high range resolution, a narrow beam directivity of antennas, and a fast data update mode to provide a possibility of tsunami detection in real time.

Routine real-time maps of wind directions from phased-array HF radars in Australia can be used to identify the position and movement of meteorological fronts over the southern ocean. In the spring and summer the abrupt wind changes exacerbate the hazard of bush fires in the southeastern states, and accurate forecasting assists in the hazard reduction efforts.

An example of phased-array HF radar integrated into a port management system is given for the Port of Rotterdam in the Netherlands. Real-time, quality controlled data provide for the outer port area to reduce hazards of alongshore currents at the exit point of the sheltered channel as ships move in and out of the busy port. In general for coastal ports phased-array HF radars have potential for multipurpose hazard reduction. In this paper we have shown in separate case studies the various capabilities. The need for hazard reduction is brought to a focus in port areas where an HF radar can be used as a routine navigation aid (e.g., ship movements), for development work (e.g., dredging), search-and-rescue and pollution management (Lagrangian drifter tracking), and meteorological support (wind directions and wave heights) and serve as an element in a tsunami warning system. An explicit case where all of these features, except the last, would have combined to reduce the economic, environmental, and social burden is that of the MV *Rena* which went aground in the outer area of the Port of Tauranga in New Zealand on 5 October 2011, broke up, and eventually sank on 4 April 2012. She was a 52,000 tonnes vessel bunkered with 1,800 tonnes of oil and carrying 1,368 containers. About 850 tonnes of debris were removed from the sea during the 6-month period. Freely drifting containers, leaked oil, and salvage difficulties created the greatest hazards. The case study of the MV *Rena* supports the concept that every coastal port would be well-served by a phased-array HF radar system.

## Competing Interests

The authors declare that they have no competing interests.

## Acknowledgments

Archived data were sourced from Rijkswaterstaat, Netherlands, and the Integrated Marine Observing System (IMOS), Australia. IMOS is a national collaborative research infrastructure, supported by Australian Government. It is led by University of Tasmania in partnership with the Australian marine and climate science community. Helzel Messtechnik GmbH is the manufacturer of the WERA radar systems.

gempa GmbH developed the Tsunami Observation and Simulation Terminal (TOAST) system.

## References

- [1] L. K. Shay, H. C. Graber, D. B. Ross, and R. D. Chapman, "Mesoscale ocean surface current structure detected by high-frequency radar," *Journal of Atmospheric and Oceanic Technology*, vol. 12, no. 4, pp. 881–900, 1995.
- [2] Y. Mao and J. L. Luick, "Circulation in the southern Great Barrier Reef studied through an integration of multiple remote sensing and in situ measurements," *Journal of Geophysical Research: Oceans*, vol. 119, no. 3, pp. 1621–1643, 2014.
- [3] R. H. Stewart and J. W. Joy, "HF radio measurements of surface currents," *Deep-Sea Research and Oceanographic Abstracts*, vol. 21, no. 12, pp. 1039–1049, 1974.
- [4] H.-H. Essen, K.-W. Gurgel, and T. Schlick, "Measurement of ocean wave height and direction by means of HF radar: an empirical approach," *Deutsche Hydrografische Zeitschrift*, vol. 51, no. 4, pp. 369–383, 1999.
- [5] A. Mantovanelli, M. L. Heron, A. Prytz, C. R. Steinberg, and D. Wisdom, "Validation of radar-based Lagrangian trajectories against surface-drogued drifters in the Coral Sea, Australia," in *Proceedings of the IEEE OCEANS '11 MTS/IEEE Kona*, Waikoloa, Hawaii, USA, September 2011.
- [6] M. Heron, A. Dzvonkovskaya, and T. Helzel, "HF radar optimised for tsunami monitoring," in *Proceedings of the MTS/IEEE OCEANS*, IEEE, Genova, Italy, May 2015.
- [7] D. M. Van Heteren, A. Schaap, and H. C. Peters, "Rijkswaterstaat's interest in HF radar," *IEEE Journal of Oceanic Engineering*, pp. 235–240, 1986.
- [8] K.-W. Gurgel, Y. Barbin, and T. Schlick, "Radio frequency interference suppression techniques in FMCW modulated HF radars," in *Proceedings of the IEEE OCEANS Conference*, pp. 538–541, Aberdeen, UK, June 2007.
- [9] M. L. Heron and A. Prytz, "The data archive for the phased array HF radars in the Australian coastal ocean radar network," in *Proceedings of the IEEE OCEANS 2011*, Santander, Spain, June 2011.
- [10] R. Gomez, T. Helzel, C. R. Merz et al., "Real-time quality control of current velocity data on individual grid cells in WERA HF radar," in *Proceedings of the OCEANS MTS/IEEE Conference*, Taipei, Taiwan, April 2014.
- [11] C. Ohlmann, P. White, L. Washburn, E. Terrill, B. Emery, and M. Otero, "Interpretation of coastal HF radar-derived surface currents with high-resolution drifter data," *Journal of Atmospheric and Oceanic Technology*, vol. 24, no. 4, pp. 666–680, 2007.
- [12] D. S. Ullman, J. O'Donnell, J. Kohut, T. Fake, and A. Allen, "Trajectory prediction using HF radar surface currents: Monte Carlo simulations of prediction uncertainties," *Journal of Geophysical Research*, vol. 111, no. 12, 2006.
- [13] A. Mantovanelli, M. L. Heron, S. F. Heron, and C. R. Steinberg, "Relative dispersion of surface drifters in a barrier reef region," *Journal of Geophysical Research: Oceans*, vol. 117, no. 11, Article ID C11016, 2012.
- [14] S. C. Shadden, F. Lekien, and J. E. Marsden, "Definition and properties of Lagrangian coherent structures from finite-time Lyapunov exponents in two-dimensional aperiodic flows," *Physica D: Nonlinear Phenomena*, vol. 212, no. 3–4, pp. 271–304, 2005.

- [15] T. Helzel, V. Marriette, and M. Pavec, "Coastal radar WERA: a tool for harbour management," *European Journal of Navigation*, vol. 8, no. 1, 2010.
- [16] G. Green, "On the motion of waves in a variable canal of small depth and width," *Transactions of the Cambridge Philosophical Society*, vol. 6, pp. 457–462, 1838.
- [17] B. Kinsman, *Wind Waves*, Prentice-Hall, Englewood Cliffs, NJ, USA, 1965.
- [18] K.-W. Gurgel, A. Dzvonkovskaya, T. Pohlmann, T. Schlick, and E. Gill, "Simulation and detection of tsunami signatures in ocean surface currents measured by HF radar," *Ocean Dynamics*, vol. 61, no. 10, pp. 1495–1507, 2011.
- [19] W. Hanka, J. Saul, B. Weber, J. Becker, and P. Harjadi, "Real-time earthquake monitoring for tsunami warning in the Indian Ocean and beyond," *Natural Hazards and Earth System Science*, vol. 10, no. 12, pp. 2611–2622, 2010.
- [20] M. L. Heron and R. J. Rose, "On the application of HF ocean radar to the observation of temporal and spatial changes in wind direction," *IEEE Journal of Oceanic Engineering*, vol. OE-11, no. 2, pp. 210–218, 1986.
- [21] L. R. Wyatt, L. J. Ledgard, and C. W. Anderson, "Maximum likelihood estimation of the directional distribution of 0.53 Hz ocean waves," *Journal of Atmospheric and Oceanic Technology*, vol. 14, no. 3, pp. 591–603, 1997.
- [22] L. R. Wyatt, "Shortwave direction and spreading measured with HF radar," *Journal of Atmospheric & Oceanic Technology*, vol. 29, no. 2, pp. 286–299, 2012.
- [23] M. Schroevers, M. Verlaan, F. Zijl, P. Verburgh, and F. Buschman, "Navigation information for the Rotterdam Harbour by assimilating HF radar in a 3D model," in *Proceedings of the 11th IEEE/OES Current, Waves and Turbulence Measurement (CWTM '15)*, pp. 1–3, IEEE, St. Petersburg, Fla, USA, March 2015.

## Research Article

# A General Range-Velocity Processing Scheme for Discontinuous Spectrum FMCW Signal in HFSWR Applications

Mengguan Pan,<sup>1,2</sup> Baixiao Chen,<sup>1,2</sup> and Minglei Yang<sup>1,2</sup>

<sup>1</sup>National Laboratory of Radar Signal Processing, Xidian University, Xi'an 710071, China

<sup>2</sup>Collaborative Innovation Center of Information Sensing and Understanding at Xidian University, Xi'an, China

Correspondence should be addressed to Baixiao Chen; [bxchen@xidian.edu.cn](mailto:bxchen@xidian.edu.cn)

Received 5 May 2016; Accepted 15 August 2016

Academic Editor: Xiongbing Wu

Copyright © 2016 Mengguan Pan et al. This is an open access article distributed under the Creative Commons Attribution License, which permits unrestricted use, distribution, and reproduction in any medium, provided the original work is properly cited.

Discontinuous spectrum signal which has separate subbands distributed over a wide spectrum band is a solution to synthesize a wideband waveform in a highly congested spectrum environment. In this paper, we present a general range-velocity processing scheme for the discontinuous spectrum-frequency modulated continuous wave (DS-FMCW) signal specifically. In range domain, we propose a simple time rearrangement operation which converts the range transform problem of the DS-FMCW signal to a general spectral estimation problem of nonuniformly sampled data. Conventional periodogram results in a dirty range spectrum with high sidelobes which cannot be suppressed by traditional spectral weighting. In this paper, we introduce the iterative adaptive approach (IAA) in the estimation of the range spectrum. IAA is shown to have the ability to provide a clean range spectrum. On the other hand, the discontinuity of the signal spectrum has little impact on the velocity processing. However, with the range resolution improved, the influence of the target motion becomes nonnegligible. We present a velocity compensation strategy which includes the intersweep compensation and in-sweep compensation. Our processing scheme with the velocity compensation is shown to provide an accurate and clean range-velocity image which benefits the following detection process.

## 1. Introduction

High frequency surface wave radar (HFSWR) refers to a classification of radar that operates in the HF band (3–30 MHz) and utilizes the surface wave mode of propagation. These systems can be used both in surveillance to detect and track vessels and in oceanography to measure surface current and ocean wave parameters [1–6].

However, the HF band is a heavily congested part of the radio spectrum which makes it difficult to find a continuous silent frequency band to transmit radar signals. This limits the signal bandwidth of the HF radar system and results in a poor range resolution [7, 8]. In [7], a continuous measurement of noise and interference data in the frequency band of 3–6 MHz at Cape Race, Newfoundland, Canada, in the period between August 1, 1998, and May 10, 2000, shows that channels with a bandwidth of 20 kHz are readily available and a bandwidth of 100 kHz is not available.

To overcome the trouble of limited band, Green and Kutuzov proposed a waveform design idea which utilizes several discontinuous but clean subbands to synthesize a signal with the desired bandwidth [9–11]. The discontinuity of the signal spectrum leads to high sidelobe levels of the matched filter output which cannot be suppressed by conventional spectral weighting. Therefore, most of the efforts at present focused on applying the sidelobe suppression technique in the matched filtering output. The first category of the methods is the mismatched filter (or instrumental variable filter) approach. It is a data-independent method which gets the filter coefficients by optimizing the autocorrelation function (ACF) and applies the filter to the matched filter output. The second category uses the CLEAN algorithm to reconstruct the target signal [12]. The third category is based on spectrum reconstruction; this includes using AR model [9, 13] or regularization interpolation [12] to fill the “gap” parts of the spectrum. And, on the other hand, [14–16] considered

suppressing the sidelobes from a perspective of waveform designing rather than signal processing.

While some papers use the model of frequency hopped pulse signal [16–18], some other papers consider a more abstract discontinuous spectrum signal model and concentrate on the analysis of the autocorrelation function and the power spectrum density (PSD) [14, 15]; only a few papers use a signal model of FMCW [12, 13]. As the FMCW signal [19] and its variation FMICW signal [20] are widely used in HF radar applications such as the SeaSonde [3] and WERA [5] systems and they are quite different from the pulsed signal both in receiver structure and following signal processing method, we focus on the processing of discontinuous spectrum FMCW (DS-FMCW) signal specifically. Similar to the conventional FMCW signal, DS-FMCW uses stretch processing instead of correlation processing used in pulsed radar in the range domain. And we call this process range transform compared to the commonly used term “pulse compression” in pulsed radar.

Different from the conventional FMCW radar which outputs a constant-frequency complex sinusoid (beat signal) after mixing with the transmitted reference signal, the DS-FMCW radar outputs a constant-frequency signal but with phase hopped at specific locations. In this paper, we propose a kind of transformation applied on the time variable, by which the hopped phase is converted to a kind of “hopped” sampling instants. This process may be implicit in former works [12, 13] and we choose to call it time rearrangement operation here. After the time rearrangement operation, the sampled postmixing signal becomes a nonuniformly sampled sequence of a complex sinusoid. Therefore, we set up a general spectral analysis model for the range processing of the DS-FMCW signal and the crux of the matter now becomes the spectral estimation of a nonuniformly sampled data sequence.

The spectral analysis of nonuniformly sampled data has drawn much attention since the nonuniformity in the data is common in various applications [21]. And a large number of methods have emerged recently. The classical Fourier transform based periodogram suffers from the heavy leakage problem which leads to a low resolution and high sidelobe levels. Therefore, it is not applicable in the processing of DS-FMCW signal. In this paper, we apply the iterative adaptive approach (IAA) algorithm in the range spectrum estimation of the DS-FMCW signal. IAA was first proposed in [22] for target direction of arrival (DOA) estimation. It can be interpreted as an iteratively weighted least-square periodogram which eliminates almost completely the leakage problems of the conventional periodogram method in a fully data-adaptive manner [22, 23]. It is quite suitable to be applied in the range spectrum estimation of DS-FMCW signal. However, other spectral analysis methods suitable for the line spectrum estimation can also be taken into consideration. We use IAA as an example in this paper.

We consider the range-velocity processing of the DS-FMCW signal afterwards. With the range resolution improved, some subtle issues may occur due to target motion. Accordingly, we propose a velocity compensation strategy in

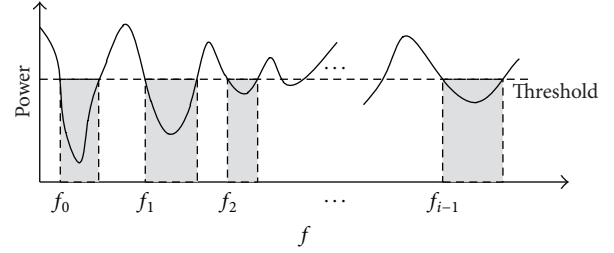


FIGURE 1: HF spectrum distribution illustration.

this paper. Finally, we present a general range-velocity processing scheme for the DS-FMCW signal.

This paper is organized as follows. Section 2 formulates the signal model and the range processing model of the DS-FMCW signal. The time rearrangement operation is introduced in this section. Section 3 extends the model to range-velocity processing and gives a velocity compensation strategy. A general range-velocity processing scheme for the DS-FMCW signal is presented at the end of this section. Section 4 gives a design example of a DS-FMCW signal and shows the effectiveness of our proposed processing scheme by several experiments. The final section concludes this paper.

## 2. DS-FMCW Signal Model and Range Transform

**2.1. Signal Model and Time Rearrangement Operation.** The HF radar system using discontinuous spectrum signal should cooperate with a spectrum monitor which monitors the spectrum environment before the radar starts to transmit a signal. A typical HF spectrum distribution is illustrated in Figure 1. The shading areas below the threshold correspond to the silent frequency bands which can be used by the radar. There are  $I$  relative silent segments in the frequency span  $f_0$  to  $f_0 + \Delta F$ . Let the start frequency and start time of each segment be  $f_i$  and  $t_i$ ,  $i = 0, 1, \dots, I - 1$ ,  $t_0 = 0$ . Then, the duration of each segment is  $T_i = t_{i+1} - t_i$ ,  $i = 0, 1, \dots, I - 1$ , and the sweep period is  $T_m = \sum_{i=0}^{I-1} T_i$ . We use a linear frequency sweep in each segment and fix the sweep slope to  $\mu = B/T_m$ , in which  $B$  is the total frequency bandwidth occupied by the radar signal. The ratio of the occupied frequency bandwidth of the radar signal to the whole frequency span is defined as the occupied frequency ratio (OFR) of the signal. Thus,  $\text{OFR} = B/\Delta F$ . The resulting operation waveform is the so-called discontinuous spectrum-frequency modulated continuous wave (DS-FMCW) signal. The transmitted and received signal frequency time characteristics are shown in Figure 2.

The transmitted signal in a single sweep period is

$$s(t) = \sum_{i=0}^{I-1} \text{rect}\left(\frac{t - T_i/2 - t_i}{T_i}\right) \exp(j\pi\mu(t - t_i)^2) \cdot \exp(j2\pi f_i(t - t_i)), \quad (1)$$

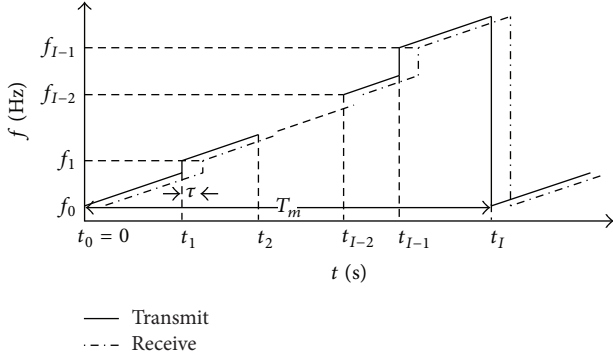


FIGURE 2: DS-FMCW transmitted/received signal frequency time characteristic.

where

$$\text{rect}\left(\frac{t}{T}\right) = \begin{cases} 1, & t \leq \left\lfloor \frac{T}{2} \right\rfloor \\ 0, & \text{others} \end{cases} \quad (2)$$

is a rectangular window function. The received signal from a single target is an attenuated, delayed, and Doppler-shifted version of the transmitted signal. In this section, we only consider a stationary point target and leave the discussion of the Doppler/velocity processing to the next section. Then, the received signal is given by

$$y(t) = A \sum_{i=0}^{I-1} \text{rect}\left(\frac{t - T_i/2 - t_i}{T_i}\right) \exp(j\pi\mu(t - t_i - \tau)^2) \cdot \exp(j2\pi f_i(t - t_i - \tau)) \quad (3)$$

in which  $A$  represents the attenuation factor which is mainly related to the target radar cross section (RCS) and  $\tau$  is the round-trip time for the signal to propagate from the radar system and back. A multitarget case can be seen as a superposition of the different echoes at the receiver. Note that the effect of the target delay on the rectangular envelope is omitted since in HF radar applications the maximum potential target delay usually satisfies  $\tau_{\max} \ll T_m$  [19].

Similar to the stretch processing of the conventional FMCW signal, the received signal is mixed with the transmitted signal at the receiver. This process is also called deramp processing or dechirp processing. Stretch processing is a technique to reduce the sampling-rate requirements of the following analog-to-digital converter (ADC) [24]. The output of the mixer is

$$x(t) = y(t) s^*(t) = A \sum_{i=0}^{I-1} \text{rect}\left(\frac{t - T_i/2 - t_i}{T_i}\right) \exp(j\phi_i(t)) \quad (4)$$

in which the phase term of the  $i$ th segment  $\phi_i(t)$  is

$$\phi_i(t) = 2\pi \left[ -(f_i - \mu t_i) \tau - \mu \tau t + 0.5\mu \tau^2 \right], \quad 0 \leq i \leq I-1. \quad (5)$$

Unlike the mixer output of the conventional FMCW signal, which is a constant-frequency complex sinusoid (beat signal), the corresponding output of the DS-FMCW signal is more analogous to a kind of phase-coded signal with  $I$  subpulses of each having a different initial phase related to the target delay. Thus, the range spectrum cannot be obtained by a direct FFT/IFFT operation. However, with a simple transform of (5),

$$\phi_i(t) = -2\pi\mu\tau \left( t + \frac{f_i}{\mu} - t_i \right) + \pi\mu\tau^2, \quad 0 \leq i \leq I-1, \quad (6)$$

the unknown phase hopping quantity converts to a time domain shift related to the waveform parameters which are predefined. Therefore, a rearrangement of the time variable in each segment eliminates the phase hopping. The time vector after the rearrangement operation is

$$t' = t + \frac{f_i}{\mu} - t_i, \quad t_i \leq t < t_{i+1}. \quad (7)$$

For each segment, we have

$$\begin{aligned} t \in [t_0, t_1) &\longrightarrow t' \in [t_0, t_1), \\ t \in [t_1, t_2) &\longrightarrow t' \in \left[ \frac{f_1}{\mu}, t_2 - t_1 + \frac{f_1}{\mu} \right), \\ &\vdots \\ t \in [t_{I-1}, t_I) &\longrightarrow t' \in \left[ \frac{f_{I-1}}{\mu}, t_I - t_{I-1} + \frac{f_{I-1}}{\mu} \right). \end{aligned} \quad (8)$$

When the receiver samples the deramped signal at a uniform interval  $T_s$  and by letting  $t_n$ ,  $0 \leq n < N$ ,  $N = \lfloor T_m/T_s \rfloor$  be the sampling instants ( $\lfloor \cdot \rfloor$  represents the notion of being rounded down), the corresponding sampling instants after the time rearrangement  $t'_n$  turn out to be nonuniform (or, more accurately, piecewise uniform). This process of time rearrangement is illustrated in Figure 3. Figure 3(b) shows that the phase hopping is eliminated after the rearrangement.

Accordingly, the sampled deramped signal can be represented as

$$\begin{aligned} x[n] &= A \exp(j\psi) \exp(-j2\pi\mu\tau(t'_n)) \\ &= \tilde{s} \cdot \exp(-j2\pi\mu\tau(t'_n)), \end{aligned} \quad (9)$$

$$0 \leq n < N,$$

in which  $\psi = \pi\mu\tau^2$  is a constant phase term and  $\tilde{s} = A \exp(j\psi)$  represents a complex amplitude.

From (9), the sampled time series  $x[n]$  is a constant-frequency complex sinusoid signal sampled at time  $t'_n$ . Thus, the range transform problem of the DS-FMCW signal converts to the problem of spectral estimation of nonuniformly sampled data.

We can denote the sampled signal in vector form as

$$\mathbf{x} = [x[0], x[1], \dots, x[N-1]]^T = \tilde{s} \cdot \mathbf{a}(\tilde{f}), \quad (10)$$

where  $(\cdot)^T$  represents the transpose operation,  $\mathbf{x} \in \mathbb{C}^{N \times 1}$ ,  $\tilde{f} = \mu\tau \in F \subset \mathbb{R}$  is the beat frequency which is proportional

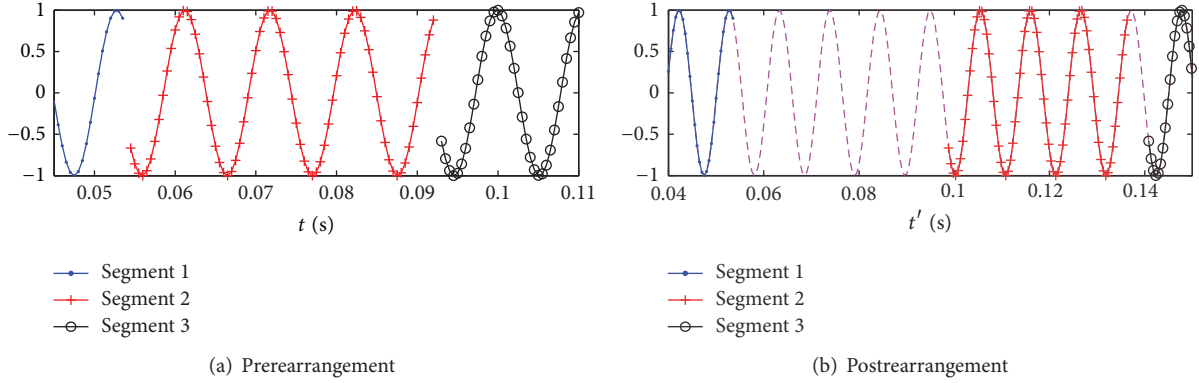


FIGURE 3: Time rearrangement illustration.

to target delay  $\tau$ , in which  $F$  is the considered frequency range, and  $\mathbf{a}(\cdot) : F \rightarrow \mathbb{C}^{N \times 1}$  is a known function which solely depends on the spectrum distribution of the DS-FMCW signal; the function output is the matched filter vector (similar to the steering vector in the spatial processing) in the range domain

$$\mathbf{a}(f) = \begin{bmatrix} \exp(-j2\pi f t'_0) \\ \exp(-j2\pi f t'_1) \\ \vdots \\ \exp(-j2\pi f t'_{N-1}) \end{bmatrix}. \quad (11)$$

Consider the multitarget situation; the sampled data sequence of the deramped signal is

$$\mathbf{x} = \sum_{l=1}^L \mathbf{a}(\tilde{f}_l) \tilde{s}_l + \boldsymbol{\epsilon}, \quad (12)$$

where  $\boldsymbol{\epsilon} \in \mathbb{C}^{N \times 1}$  is a noise term and  $L$  is the unknown number of targets. Equation (12) is a common model of spectral analysis of nonuniformly (irregularly) sampled data.

To assist in explaining the spectral analysis algorithms, we extend the model of (12). Let the considered frequency range be  $F = \{f : f_{\min} \leq f \leq f_{\max}\}$ , in which the maximum and the minimum beat frequencies are decided by the considered range window:

$$f_{\max} = \mu \frac{2R_{\max}}{c}, \quad (13)$$

$$f_{\min} = \mu \frac{2R_{\min}}{c}.$$

We then use a uniform grid  $\{f_k\}_{k=1}^K$  to cover  $F$ , with a specific fine step, and assume that  $\{\tilde{f}_l\}$  lie on (practically, close to)

the grid. This means that there exist  $k_1, \dots, k_L$  such that  $\tilde{f}_l = f_{k_l}$ ,  $l = 1, \dots, L$ . Also, let

$$\mathbf{a}_k = \mathbf{a}(f_k), \quad k = 1, \dots, K, \quad (14)$$

$$s_k = \begin{cases} \tilde{s}_l, & k = k_l \quad (l = 1, \dots, L) \\ 0, & \text{elsewhere.} \end{cases} \quad (14)$$

Using this notation, we can rewrite (12) as

$$\mathbf{x} = \sum_{k=1}^K \mathbf{a}_k s_k + \boldsymbol{\epsilon}. \quad (15)$$

**2.2. Periodogram Range Spectrum.** The most intuitive method is the classical Fourier transform based periodogram (FP), which is also known as single-frequency least-square (SFLS) method, matched filtering method, or beam-forming method (in array signal processing applications). It uses filter coefficients matched to the received signal structure, which yields the optimum output signal-to-noise ratio (SNR). The periodogram method can also be derived from a solution to the following least-squares (LS) data fitting problem:

$$\hat{s}(f) = \arg \min_{s(f)} \|\mathbf{x} - s(f) \mathbf{a}(f)\|^2. \quad (16)$$

The solution to the above problem is

$$\hat{s}(f) = \frac{\mathbf{a}^H(f) \mathbf{x}}{\|\mathbf{a}(f)\|^2}. \quad (17)$$

Then, the spectrum estimation at the frequency grid  $\{f_k\}_{k=1}^K$  is given by

$$\hat{s}_k = \frac{\mathbf{a}_k^H \mathbf{x}}{\|\mathbf{a}_k\|^2}, \quad k = 1, \dots, K. \quad (18)$$

The resolution of the periodogram method is proportional to the reciprocal of the observation time interval.

According to (7), in the DS-FMCW situation, the observation interval after a rearrangement of the sampling instants is

$$\begin{aligned} \Delta t &= t'_{N-1} - t'_0 = T_m + \frac{f_{I-1}}{\mu} - t_{I-1} \\ &= \frac{(f_{I-1} + \mu(T_m - t_{I-1}))}{\mu} = \frac{\Delta F}{\mu}, \end{aligned} \quad (19)$$

where  $\Delta F$  is the total frequency span. Thus, the observation interval is stretched from  $T_m = B/\mu$  to  $\Delta F/\mu$  after the rearrangement of the sampling instants. Then, the range resolution is given by

$$\Delta R = \frac{1}{\Delta t \cdot \mu} \cdot \frac{c}{2} = \frac{c}{2\Delta F}. \quad (20)$$

Therefore, the range resolution solely depends on the total frequency span ( $\Delta F$ ) of the DS-FMCW signal. By adopting the waveform in an appropriate frequency span, we can obtain the desired range resolution. However, the development of the spectral analysis has led to many methods which can resolve targets whose range separation is within  $\Delta R$ . Therefore, we call the resolution of periodogram the inherent resolution.

However, the spectrum discontinuity in the frequency span leads to high sidelobes when applying the conventional periodogram method which cannot be suppressed by conventional spectral weighting. The sidelobe levels are related to the waveform occupied frequency ratio (OFR) and the specific spectrum distribution in the frequency span. The larger the OFR and the more uniform the distribution, the lower the sidelobe levels. In this paper, we do not consider extreme cases such as the occupied frequency being at the two sides of the frequency span or being all concentrated into a large continuous block, in which the situation degrades to a continuous spectrum. We assume the occupied frequency is distributed uniformly in the frequency span which is more likely encountered in the practical situation.

**2.3. IAA Range Spectrum.** The inherent limitations of the periodogram approach motivate a more effective spectral analysis method to be applied here. IAA is a nonparametric and user parameter free weighted least-squares based spectral analysis method first proposed for spatial spectral estimation [22]. It is a periodogram related spectral analysis method which eliminates almost completely the leakage problems of the periodogram method in a fully data-adaptive manner. The range spectrum estimation problem is equivalent to a direction of arrival (DOA) estimation problem with single snapshot in the array processing applications. And IAA can properly handle this situation. Consequently, IAA is quite suitable to be applied in the situation of range spectrum estimation of the DS-FMCW signal.

Periodogram uses solution to the LS fitting problem (16) as the estimate in each frequency scan point. It is a data-independent approach. While estimating a spectrum value of a specific frequency point  $f_k$ , the other components located at frequencies different from  $f_k$  perform as interferences.

Prewhitening of the other frequency components except the current processing one can cancel strong interferences in the data. Therefore, IAA uses a weighted least-squares (WLS) fitting criterion with the weight matrix equal to the inversion of the interferences and noise covariance matrix:

$$\hat{s}_k = \arg \min_{s_k} \|\mathbf{x} - s_k \mathbf{a}_k\|_{\mathbf{R}_{i+n,k}^{-1}}^2, \quad k = 1, \dots, K, \quad (21)$$

in which  $\mathbf{R}_{i+n,k}$  is the interferences (signals at range cells other than the range cell  $k$  of current interest) and noise covariance matrix and square of the weighted  $\ell_2$ -norm is defined as  $\|\mathbf{x}\|_{\mathbf{W}}^2 \triangleq \mathbf{x}^H \mathbf{W} \mathbf{x}$ .

The iterative solution to the WLS problem (21) leads to the IAA algorithm. As the range transform problem of the DS-FMCW signal is equivalent to a general spectral analysis problem of nonuniformly sampled data, the standard IAA algorithm can be directly applied here [22, 23].

### 3. Extension to Range-Velocity Processing

Conventional FMCW radar uses Fast Fourier Transform (FFT) on the range domain (fast time) and pulse domain (slow time), respectively, to form a range-Doppler spectrum (RD image), thus attaining the target range and Doppler information. In the last section, we have proposed that the range transform of the DS-FMCW signal is equivalent to a spectral estimation problem of a nonuniformly sampled data set. Then, we can replace the FFT adopted by FMCW in the range domain processing with a more effective spectral analysis method. However, the spectrum discontinuity of the waveform has little impact on the Doppler processing. We can still employ FFT in the Doppler processing which is essentially a matched filter bank. But since the carrier frequency of the signal changes at different time segments, a single target's velocity corresponds to different Doppler frequencies. Therefore, we use a matched filter bank in the velocity domain directly which is more intuitive than processing in the Doppler domain and then adjusting different Doppler cells into a single velocity cell according to their carrier frequencies. This is the reason why we use the term range-velocity processing instead of the commonly used term range-Doppler processing.

In this section, we present a scheme for the range-velocity processing of the DS-FMCW signal. We change the sequence of processing steps with applying velocity domain matched filtering first followed by range domain spectral analysis at each velocity channel. This modification has the following benefits:

- (1) The matched filter coefficients in the velocity domain for each range bin can be easily decided since their carrier frequency is predefined.
- (2) After velocity processing, we can compensate the range bias caused by the Doppler shift in a single sweep period by multiplying a correction factor in each velocity channel. This bias is usually omitted in the RD processing of conventional FMCW HF radar.

(3) If we choose a spectral analysis method which does not reserve the phase information at the output, we have to do the velocity processing first.

Suppose there are  $M$  sweep periods in a coherent processing interval (CPI); the transmitted signal can be expressed as

$$s(t) = \sum_{m=0}^{M-1} \sum_{i=0}^{I-1} \text{rect}\left(\frac{t - T_i/2 - t_i - mT_m}{T_i}\right) \cdot \exp\left(j\pi\mu(t - t_i - mT_m)^2\right) \cdot \exp\left(j2\pi f_i(t - t_i - mT_m)\right). \quad (22)$$

The received signal from a moving target can be expressed as

$$y(t) = A \sum_{m=0}^{M-1} \sum_{i=0}^{I-1} \text{rect}\left(\frac{t - T_i/2 - t_i - mT_m}{T_i}\right) \cdot \exp\left(j\pi\mu(t - t_i - mT_m - \tau(t))^2\right) \cdot \exp\left(j2\pi f_i(t - t_i - mT_m - \tau(t))\right). \quad (23)$$

The impact of the target delay on the signal envelope is omitted as before;  $A$  represents the attenuation factor. And the delay function is

$$\tau(t) = \frac{2(R_0 - vt)}{c} = \tau_0 - \frac{2vt}{c}, \quad (24)$$

where  $R_0$  is the initial range of the target,  $\tau_0$  is the corresponding delay, and  $v$  is the radial velocity of the target towards the radar. After mixing the received signal with the transmitted signal, we get the deramped output

$$\begin{aligned} x(t) &= y(t) s^*(t) \\ &= A \sum_{m=0}^{M-1} \sum_{i=0}^{I-1} \text{rect}\left(\frac{t - T_i/2 - t_i - mT_m}{T_i}\right) \cdot \exp(-j2\pi f_i \tau(t)) \cdot \exp(-j2\pi\mu\tau(t)(t - t_i - mT_m) + j\pi\mu\tau^2(t)) \\ &= A \sum_{m=0}^{M-1} \sum_{i=0}^{I-1} \text{rect}\left(\frac{t - T_i/2 - t_i - mT_m}{T_i}\right) \cdot \exp(j\phi_{m,i}(t)), \end{aligned} \quad (25)$$

in which the phase term is

$$\phi_{m,i}(t) = -2\pi\mu\tau(t)\left(t - t_i + \frac{f_i}{\mu} - mT_m\right) + \pi\mu\tau^2(t). \quad (26)$$

Let  $\Delta t_i = f_i/\mu - t_i$  and substitute (24) into (26); we get

$$\begin{aligned} \phi_{m,i}(t) &= -2\pi\mu\tau_0(t + \Delta t_i - mT_m) \\ &\quad + 2\pi\mu\frac{2vt}{c}(t + \Delta t_i - mT_m) \\ &\quad + \pi\mu\left(\tau_0 - \frac{2vt}{c}\right)^2 \\ &\triangleq \phi_{1(m,i)}(t) + \phi_{2(m,i)}(t) + \phi_{3(m,i)}(t). \end{aligned} \quad (27)$$

Let  $t_1$  be the time vector in a single sweep period; then the time vector in the  $m$ th sweep period is  $t = t_1 + mT_m$ . Thus, the first phase term is

$$\phi_{1(m,i)}(t) = -2\pi\mu\tau_0(t_1 + \Delta t_i) \quad (28)$$

which is the same as the stationary model (6) in Section 2. After a time rearrangement, we can get the range spectrum from this term using a spectral analysis method.

We next consider the third term of  $\phi_{m,i}(t)$

$$\begin{aligned} \phi_{3(m,i)}(t) &= \pi\mu\tau_0^2 - 2\pi\mu\tau_0\frac{2vt}{c} + \pi\mu\frac{4v^2t^2}{c^2} \\ &\triangleq \phi_{3(m,i)}^{(1)}(t) + \phi_{3(m,i)}^{(2)}(t) + \phi_{3(m,i)}^{(3)}(t). \end{aligned} \quad (29)$$

We have three contributions to the phase: a constant, a linear term in time  $t$ , and a quadratic term in time,  $t^2$ . Firstly, consider the phase variation of the quadratic term in a CPI. Assume that the target's distance of movement in a CPI is less than 3 km; then,  $vt/c < 10^{-5}$ . And the sweep slope of a HF FMCW signal is usually at the order of  $(10^6)$ ; thus, the variation of the quadratic term  $\phi_{3(m,i)}^{(3)}(t)$  in a CPI is at the order of  $2\pi \times 10^{-4}$ , which can be omitted. Then, consider the linear term  $\phi_{3(m,i)}^{(2)}(t) = -2\pi\mu\tau_0(2vt/c)$ , which is proportional to the target velocity. As we will see in the following analysis,  $\phi_{2(m,i)}$  (see (33)) is the so-called Doppler term and has the same form as  $\phi_{3(m,i)}^{(2)}$ . Since  $\mu\tau_0 \ll f_0$ , the phase term  $\phi_{3(m,i)}^{(3)}$  can also be omitted. In conclusion,

$$\phi_{3(m,i)} = \Psi_3, \quad (30)$$

where  $\Psi_3$  is a constant.

For the second term of  $\phi_{(m,i)}(t)$ ,

$$\begin{aligned} \phi_{2(m,i)}(t) &= 2\pi\mu\frac{2vt}{c}(t - mT_m) + 2\pi\mu\frac{2vt}{c}\Delta t_i \\ &\triangleq \phi_{2(m,i)}^{(1)}(t) + \phi_{2(m,i)}^{(2)}(t) \end{aligned} \quad (31)$$

in which the first phase term is

$$\begin{aligned} \phi_{2(m,i)}^{(1)}(t) &= 2\pi\mu\frac{2v(t - mT_m)^2}{c} \\ &\quad + 2\pi\mu\frac{2vmT_m}{c}(t - mT_m) \\ &\triangleq \phi_{2(m,i)}^{(1,1)} + \phi_{2(m,i)}^{(1,2)}. \end{aligned} \quad (32)$$

$\phi_{2(m,i)}^{(1,1)}$  represents the quadratic disturbance term caused by the target velocity during a sweep period. Its phase variation during a sweep period is at the order of  $(2\pi \times 10^{-4})$ .  $(\phi_{2(m,i)}^{(1,2)})$  has the same form as the intersweep Doppler term (the term  $(\phi_{2(m,i)}^{(2,2)}(t))$  in (33)), and  $(\mu(t - mT_m))$  is comparable to signal carrier frequency; thus, we should consider it in matched filtering in the velocity domain.

Lastly, the second term of  $(\phi_{2(m,i)}(t))$

$$\begin{aligned} \phi_{2(m,i)}^{(2)}(t) &= 2\pi \frac{2(f_i - \mu t_i)vt}{c} \\ &= 2\pi \frac{2(f_i - \mu t_i)v}{c} (t - mT_m) \\ &\quad + 2\pi \frac{2(f_i - \mu t_i)v}{c} mT_m \\ &\triangleq \phi_{2(m,i)}^{(2,1)}(t) + \phi_{2(m,i)}^{(2,2)}(t) \end{aligned} \quad (33)$$

is the so-called Doppler term. The term  $(\phi_{2(m,i)}^{(2,1)}(t))$  in (33) is the in-sweep Doppler term. It will cause a range bias in range processing. And the term  $(\phi_{2(m,i)}^{(2,2)}(t))$  in (33) is the intersweep Doppler term.

In conclusion, the terms influenced by target velocity are

$$\begin{aligned} \phi_{v(m,i)} &= 2\pi \frac{2(f_i - \mu t_i)v}{c} (t - mT_m) \\ &\quad + 2\pi \frac{2(f_i - \mu t_i)v}{c} mT_m \\ &\quad + 2\pi \frac{2\mu(t - mT_m)v}{c} mT_m. \end{aligned} \quad (34)$$

Note that the first term and the last term in (34) also exist in conventional FMCW radar, but, in HF applications, they are usually omitted as their impact is minor. However, the neglect of the third term will lead to both a velocity bias and a range bias and the neglect of the first term will lead to a range bias. Thus, we choose to compensate both terms in our system. As the compensation of the third term is handled along the slow time domain and the compensation of the first term is handled along the fast time domain, we call them intersweep compensation and in-sweep compensation, respectively.

Intersweep compensation can be achieved by merging the compensation coefficients into the velocity domain matched filter coefficients. Let the  $n$ th sampling point in the fast time domain be  $t_1[n] = t[n + mT_m] - mT_m$ ; then, we can get the velocity domain matched filter coefficients at the point  $t_1[n]$ :

$$\mathbf{a}_n(v) = \begin{bmatrix} 0 \\ \exp\left(j2\pi \frac{2(f_i - \mu t_i)T_m v}{c}\right) \cdot \exp\left(j2\pi \frac{2\mu t_1[n]T_m v}{c}\right) \\ \vdots \\ \exp\left(j2\pi \frac{2(f_i - \mu t_i)(M-1)T_m v}{c}\right) \cdot \exp\left(j2\pi \frac{2\mu t_1[n](M-1)T_m v}{c}\right) \end{bmatrix}. \quad (35)$$

$f_i$  and  $t_i$  in  $\mathbf{a}_n(v)$  have to be chosen according to current fast time point.

Let the considered velocity range be  $V = \{v : v_{\min} \leq v \leq v_{\max}\}$ , and, similar to the range domain, we use a uniform grid  $\{v_p\}_{p=1}^P$  to cover  $V$ . Since the  $p$ th velocity channel after the velocity domain matched filtering represents the fast time echoes from all the targets with the specific velocity  $v_p$ , we can compensate the range bias caused by the target velocity according to the first term of  $\phi_{v(m,i)}$  at each velocity channel. The in-sweep compensation coefficient  $\mathbf{B}$  in the  $n$ th fast time sampling point of the  $p$ th velocity channel is

$$\begin{aligned} B_{p,n} &= \exp\left(2\pi \frac{2(f_i - \mu t_i)v_p}{c} t_1[n]\right), \\ 1 &\leq p \leq P, 1 \leq n \leq N, \end{aligned} \quad (36)$$

in which  $f_i$  and  $t_i$  are decided from the current fast time sampling point  $t_1[n]$ .

The block diagram of the DS-FMCW radar system is shown in Figure 4. We employ a stretch processing based

receiver and signal processor. The signal processor part follows our proposed range-velocity processing scheme with the details shown in Algorithm 1. Consider a series of  $M$  sweeps; after the postmixing sampling, we have the sampled sequence  $y[n]$ ,  $n = 0, 1, \dots, MN-1$ . With each sweep placed as a row, we get  $M \times N$  data matrix  $\mathbf{Y}$ . The samples in each row of  $\mathbf{Y}$  are successive samples of the returns in a single sweep, that is, successive range bins. Each column represents a series of measurements from the same range bin over successive sweep periods. We denote the  $m$ th row of a matrix  $\mathbf{Y}$  by  $\mathbf{Y}_{m,:}$  and the  $n$ th column of a matrix  $\mathbf{Y}$  by  $\mathbf{Y}_{:,n}$ . We also denote the velocity matched filtering matrix at the range bin  $n$  by  $\mathbf{A}_n$ , which includes all the vectors at different velocity grids

$$\mathbf{A}_n \triangleq [\mathbf{a}_n(v_1), \dots, \mathbf{a}_n(v_p)]. \quad (37)$$

In Figure 4 and Algorithm 1,  $\mathbf{Z} \in \mathbb{C}^{P \times N}$  is the velocity domain matched filtering output. After the velocity compensation in each velocity channel, we get the compensated output  $\mathbf{Z}^{(c)} = \mathbf{Z} \circ \mathbf{B}^* \in \mathbb{C}^{P \times N}$ , where  $\circ$  stands for the

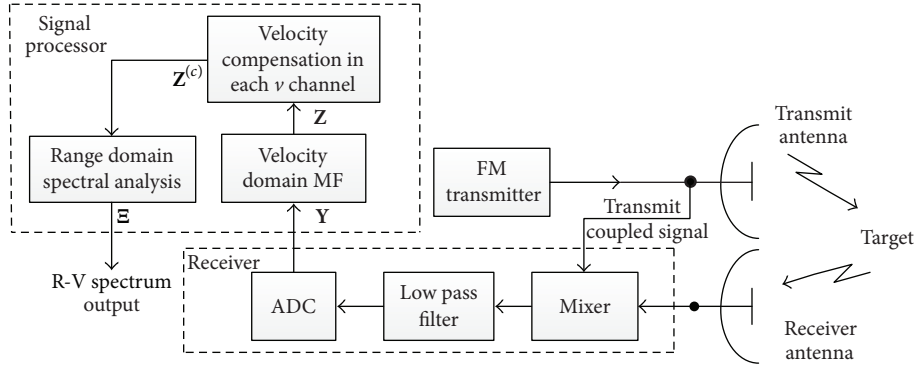


FIGURE 4: Block diagram of DS-FMCW radar system.

**input:** data matrix of  $M$  sweeping periods  $\mathbf{Y}$   
**step 1** velocity domain matched filtering  
 for each range bin  $n$   
 $\mathbf{Z}_{:,n} = \mathbf{A}_n^H \mathbf{Y}_{:,n}$   
 endfor  
**step 2** velocity compensation in each velocity channel  
 $\mathbf{Z}^{(c)} = \mathbf{Z} \odot \mathbf{B}^*$   
**step 3** range spectrum estimation in each velocity channel  
 for each velocity channel  $p$   
 $\Xi_{p,:}$  = applying spectral analysis to  $\mathbf{Z}_{p,:}^{(c)}$   
 endfor  
**output:** range-velocity spectrum  $\Xi$

ALGORITHM 1: DS-FMCW range-velocity processing scheme.

Hadamard (element-wise) product and  $(\cdot)^*$  denotes the conjugate operator. Finally, the spectral analysis in each velocity channel gives the final range-velocity spectrum  $\Xi \in \mathbb{C}^{P \times K}$ , in which  $K$  is the range bin number that coincides with the range domain model in Section 2.

#### 4. Numerical Experiments

In the first experiment, we demonstrate the determination of the postmixing sampling rate by using the spectral window method [25]. In the second experiment, we illustrate the range spectrum formed by the periodogram and the IAA algorithm. In the third experiment, we evaluate the performance of IAA when applying it in range domain spectral analysis as the OFR of the DS-FMCW signal varies by several Monte Carlo simulations. The second and third experiments only consider the range domain processing while the fourth experiment gives a complete range-velocity processing result in accordance with the processing scheme shown in Figure 4 and Algorithm 1.

In Experiments 1, 2, and 4, we use the same DS-FMCW signal designed according to Canada 1999 (summer) HF band spectrum monitoring result [7]; the available frequency band distribution is shown in Table 1.

The designed DS-FMCW signal utilizes all the clear bands between the start frequency  $f_0 = 5.11$  MHz and the end

TABLE 1: Canada 1999 summer available spectrum.

Channel	Frequency range (MHz)	Bandwidth (kHz)
1	5.11~5.14	30
2	5.26~5.27	10
3	5.29~5.31	20
4	5.37~5.39	20
5	5.46~5.48	20
6	5.51~5.52	10
7	5.54~5.59	50
8	5.64~5.66	20
9	5.72~5.73	10
10	5.77~5.80	30

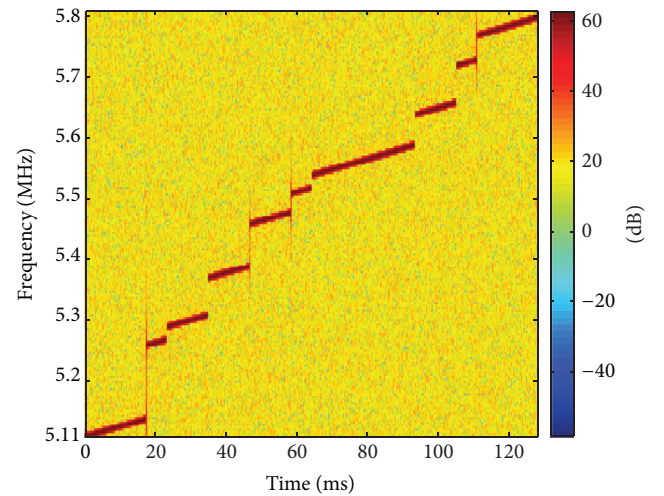


FIGURE 5: Time-frequency characteristic of the transmit signal.

frequency  $f_0 + \Delta F = 5.80$  MHz as shown in Table 1. Hence, it has the frequency span  $\Delta F = 690$  kHz and total clear bandwidth  $B = 220$  kHz. Then, the inherent range resolution of the DS-FMCW signal is  $\Delta R = c/2\Delta F = 217$  m. And the sweep period  $T_m$  is set to 128 ms. The time-frequency characteristic of the transmitted signal is shown in Figure 5. The time is continuous and the frequency is hopped at specific locations.

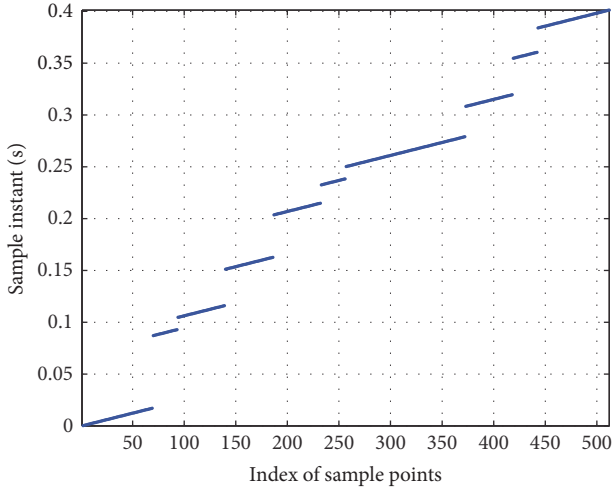


FIGURE 6: Sampling instants in a single sweep period after the time rearrangement operation.

**4.1. Experiment 1: Determination of Postmixing Sampling Rate.** In a stretch processing receiver, the sampling process comes after the mixer, by which the sampling rate can be much less than the signal bandwidth. In a conventional FMCW radar, the minimum postmixing sampling rate without any aliasing problem is proportional to the considered range window extent:

$$F_s > \Delta F \cdot \frac{2R_{\text{win}}/c}{T_m}, \quad (38)$$

where  $R_{\text{win}} = R_{\text{max}} - R_{\text{min}}$ . This is defined through the Nyquist-Shannon sampling theorem essentially. However, for the DS-FMCW signal, the sampling instants after the time rearrangement operation become nonuniform (Figure 6), and there is no well accepted definition of the nonaliasing sampling rate for the nonuniformly sampled data sequence. In this paper, we adopt the Nyquist or rollover frequency definition for nonuniform samples described in [25], which is called the spectral window method. Given  $N$  nonuniform samples with sampling instants  $\{t_n\}_{n=1}^N$ , the spectral window at any frequency  $f$  is defined as

$$W(f) = \left| \frac{1}{N} \sum_{n=1}^N \exp(j2\pi f t_n) \right|^2. \quad (39)$$

We can easily verify that  $W(0) = 1$ , and the frequency range without any aliasing problem can be determined by examining the largest range for  $f$  in which the only peak with height equal (or close) to 1 is at  $f = 0$ .

For our designed DS-FMCW signal, at a postmixing sampling rate of  $F_s = 4$  kHz, the sampling instants after the time rearrangement operation ( $t'_n$ ) are shown in Figure 6. Figure 6 shows that the postrearrangement sampling instants  $t'_n$  are nonuniformly (more precisely, piecewise uniformly) distributed and total observation interval is stretched from the sweep period  $T_m = 128$  ms to an equivalent virtual interval of  $\Delta F/\mu = 402$  ms. And, on the other hand,

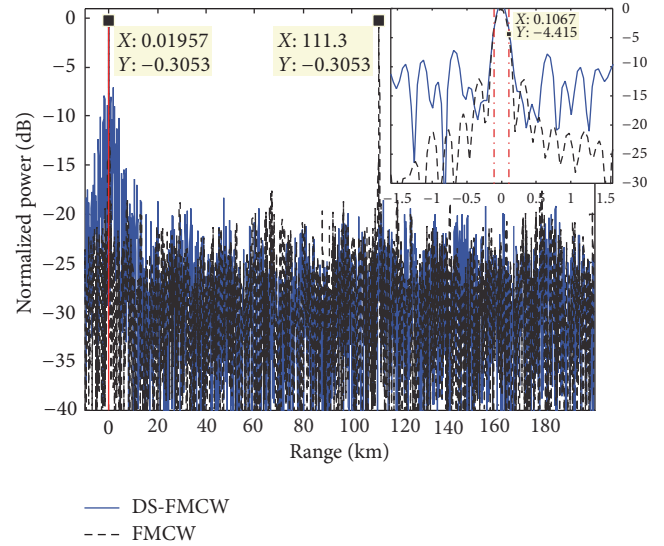


FIGURE 7: Spectral window of the designed DS-FMCW signal and a continuous FMCW signal within the same frequency span.

comparing with Figure 5, we can see that two figures have an identical distribution. This illustrates the role of the time rearrangement which is converting the discontinuity of the signal spectrum to the discontinuity of the sampling instants.

In fact, we can derive that the periodogram spectrum is just a superposition of spectral windows with different shift amount related to the target range. Thus, the spectral window and the periodogram spectrum have the same spectral shape. We use a range scan step  $\delta R$  that is five times smaller than the traditional range resolution according to (20):

$$\delta R = \frac{1}{5} \cdot \frac{c}{2\Delta F}. \quad (40)$$

The spectral window of the designed DS-FMCW signal is shown in Figure 7, and the spectral window of a full occupied FMCW signal in the same frequency span ( $f_0 \sim f_0 + \Delta F$ ) is plotted in the same figure for comparison.

In Figure 7, the spectral window of the FMCW signal is aliased in the range window 0~200 km while the DS-FMCW signal is not. And the maximum range window for the FMCW signal is 111.3 km which is consistent with (38). Therefore, the spectral window can be used to ensure that the range spectrum of the DS-FMCW signal is unambiguous under the selected sampling rate.

Figure 7 also indicates that, compared with the conventional FMCW signal within the same frequency span, the range spectrum of the DS-FMCW signal has the same main lobe width ( $c/(2\Delta F)$ ) but has much higher sidelobe levels. Thus, other methods rather than periodogram should be considered to be applied in the range spectrum estimation of the DS-FMCW signal.

**4.2. Experiment 2: Periodogram Range Spectrum and IAA Range Spectrum.** In this experiment, we illustrate the improvement of the sidelobe levels and range resolution provided by IAA when applied in the range spectrum analysis.

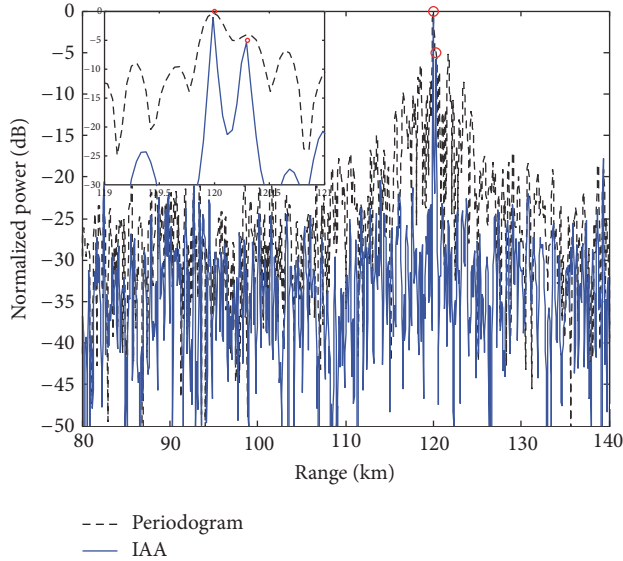


FIGURE 8: Range spectrum generated by periodogram and IAA.

We consider two targets located at the range of 120 km and 120.3 km whose separation is slightly larger than the inherent range resolution and with the input SNR of 0 dB and  $-5$  dB, respectively. The range profiles generated by periodogram and IAA are shown in Figure 8. It can be inferred from Figure 8 that the periodogram method suffers from heavy leakage problems which make the peak of weaker target almost masked by the high sidelobes of a strong target nearby. And the high sidelobe level also causes false alarms and contaminates the detection output. IAA, on the other hand, resolves two closely separated targets clearly and has a much lower sidelobe level. The sidelobe level of the IAA spectrum can hardly be determined from Figure 8 as it is even lower than the noise power. In fact, the spectrum output of IAA is quite close to a line spectrum. There are sharp peaks at the locations of the targets and near-zero values at the other locations.

**4.3. Experiment 3: Performance of the IAA Range Spectrum.** This subsection designs two Monte Carlo experiments to investigate the performance of IAA when applied in the range processing of the DS-FMCW signal. In these two experiments, we use a similar waveform parameter of the DS-FMCW signal. We fix the total frequency span  $\Delta F$  to 600 kHz. As stated at the end of Section 2, we do not consider the extreme situations and when we consider a specific OFR, we generate randomly a uniformly distributed discontinuous spectrum with total free bandwidth  $B = \Delta F \cdot \text{OFR}$  at each Monte Carlo trial.

Firstly, we examine the peak sidelobe level (PSL) of the IAA range spectrum of the DS-FMCW signal as the OFR varies. PSL is defined as the ratio of the maximum sidelobe level to the main lobe level. In this experiment, we fix the SNR to 10 dB. Figure 9 shows the PSL of periodogram and IAA range spectrum via 500 Monte Carlo trials when the OFR varies from 20% to 100%. We can infer from the figure that

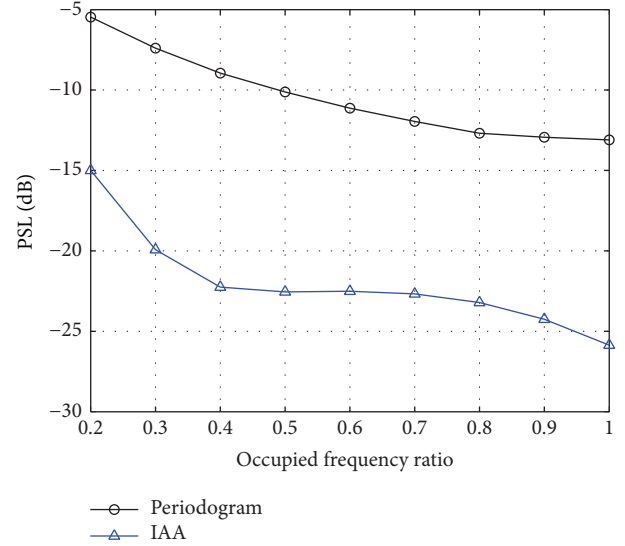


FIGURE 9: PSL of IAA range spectrum versus OFR.

TABLE 2: Simulated target information.

Index	Range (km)	Velocity (km/h)	SNR (dB)
1	120	40	0
2	120	50	$-5$
3	120.3	40	0
4	120.3	50	0
5	120	0	0

as the PSL of IAA spectrum can be lower than  $-20$  dB with an OFR larger than 40%, the PSL of periodogram is larger than  $-13$  dB at any OFR and cannot be suppressed via spectral weighting when the OFR is less than 1.

The second Monte Carlo simulation examines the capability of resolving closely spaced targets by IAA. Two targets are placed at ranges 120 km and 120.2 km, whose separation is slightly less than the inherent range resolution. By definition, two targets are resolved in a given run if both  $|\hat{R}_1 - R_1|$  and  $|\hat{R}_2 - R_2|$  are smaller than  $|R_1 - R_2|/2$ , where  $\hat{R}_k$  and  $R_k$  denote the estimated and true range for the  $k$ th target, respectively. Figure 10 shows that, at a SNR higher than 0 dB and an OFR higher than 40%, IAA can properly resolve the targets.

**4.4. Experiment 4: A Complete Range-Velocity Processing Example of DS-FMCW Signal.** In this subsection, we demonstrate the whole range-velocity process shown in Figure 4 and Algorithm 1. The velocity domain matched filtering is done first followed by correcting in each velocity channel the phase offset caused by the target velocity in a single sweep period (in-sweep compensation), and the range spectrum analysis is then done in each velocity channel to output the final range-velocity spectrum.

We consider five targets whose information is shown in Table 2. The first to the fourth targets are closely spaced both in range and in velocity domain, and the fifth target

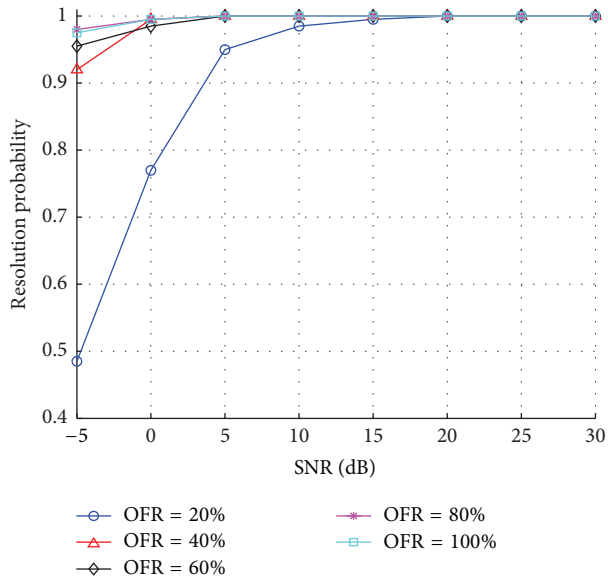


FIGURE 10: IAA resolution probability versus SNR for closely located targets at different OFR.

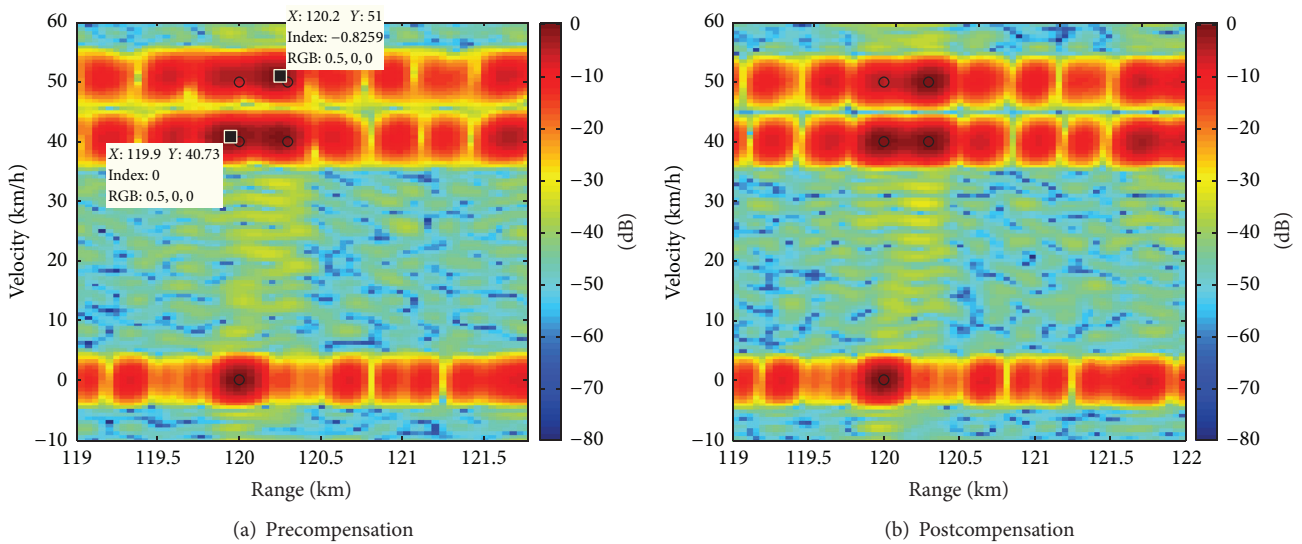


FIGURE 11: Range-velocity image generated by periodogram.

is a stationary one for comparison. We process 256 pulses in a single CPI, which results in an integration time of 32.8 seconds and a velocity resolution of about 3 km/h. A Taylor window with sidelobe level set to  $-35$  dB is used in the matched filtering of velocity domain.

Figure 11 is the range-velocity spectrum generated by periodogram, where the circles represent the true positions of the targets in the range-velocity space. The heavy leakage problem in the range domain is clearly illustrated in the figure.

We also show the indispensability of the intersweep and in-sweep compensation as mentioned in Section 3. Figure 11(a) is the result with neither compensation applied. The

data cursors mark two of the spectrum peaks of the moving targets. The peaks of the four moving targets have several bins shifted from the truth in both range and velocity domain while peak position of the stationary one is accurate. After applying both the intersweep and in-sweep compensation, as shown in Figure 11(b), the peak positions of all the five targets turn out to be accurate.

Figure 12 is the range-velocity spectrum formed by IAA. It shows that IAA significantly outperforms periodogram both in main lobe width and in sidelobe levels which result in a higher resolution and a much better detection performance.

Similar to Figure 11, we also lay out the processing result with and without the velocity compensation. It shows that

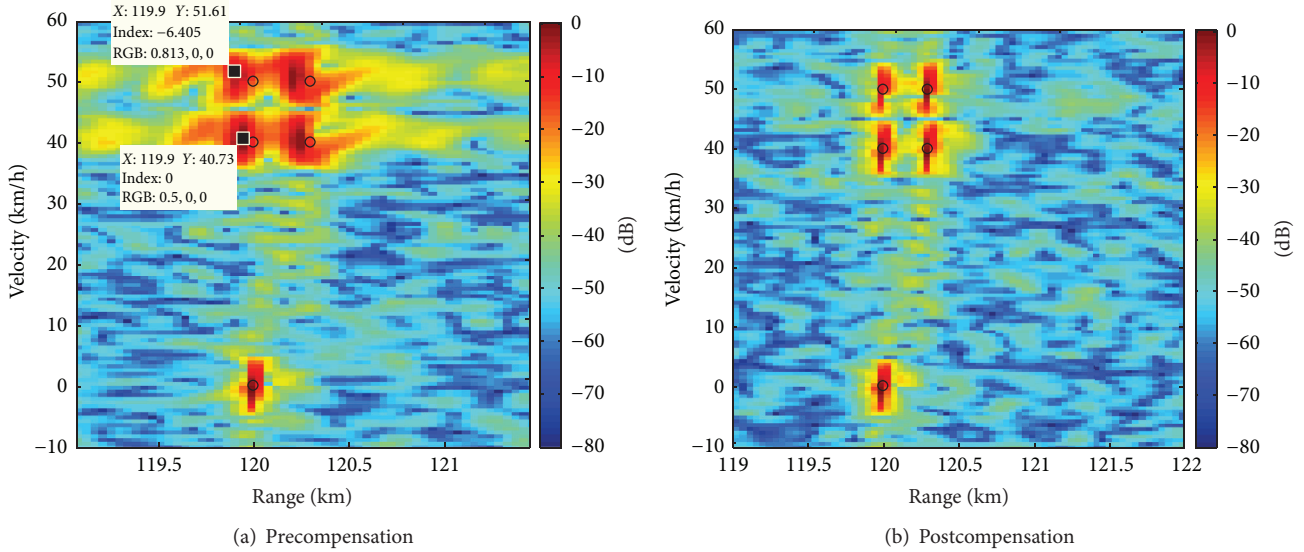


FIGURE 12: Range-velocity image generated by IAA.

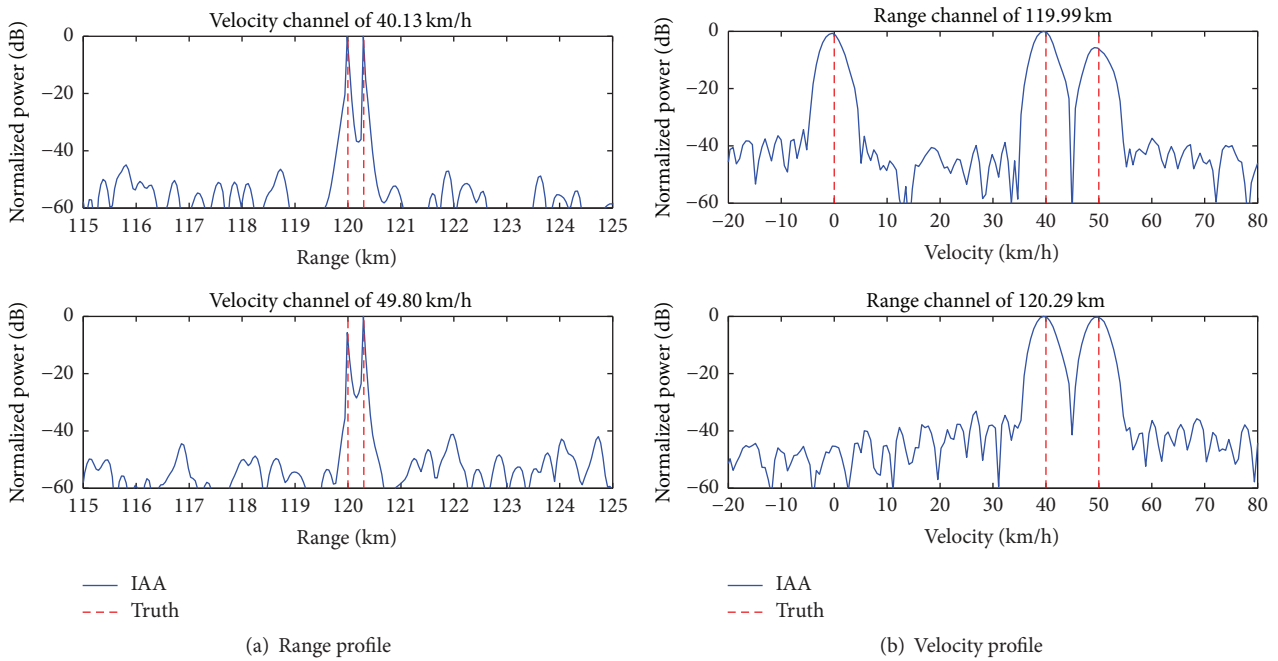


FIGURE 13: Range and velocity profile of postcompensation IAA spectrum at the target positions.

the IAA spectrum of moving targets suffers from a range and velocity bias and range migration without the velocity compensation. However, with the velocity compensation, the range migration phenomenon is eliminated, and the IAA spectrum has a sharp peak located precisely at the target positions. And, finally, Figure 13 shows the range and velocity profile of the postcompensation range-velocity image formed by IAA at the target positions. The closely spaced targets are properly resolved.

### 5. Conclusion

DS-FMCW signal is a variation of the conventional FMCW signal. It uses several discontinuous narrow bands to synthesize a waveform with desired bandwidth and is able to achieve the same range resolution as a full-band conventional FMCW signal in the same frequency span. This paper has presented a general range-velocity processing scheme for the DS-FMCW signal. The sequence of processing steps is adjusted

with velocity domain processing coming first, followed by range domain processing in each velocity channel. For the range domain processing, we propose a time rearrangement operation which converts the range transform problem to a general spectral estimation problem of a nonuniformly sampled data sequence. We have presented the periodogram range spectrum and the IAA range spectrum. IAA is shown to outperform the periodogram method both in resolution and in sidelobe levels. And IAA has a quite ideal spectrum output with sharp peaks at the target positions and near-zero values at other positions. The Monte Carlo simulation shows that, with a waveform OFR above 40% and a signal SNR above 0 dB, the range spectrum of the DS-FMCW signal generated by IAA can achieve quite a low sidelobe level and an acceptable resolving ability. For the velocity processing, we propose a strategy of velocity compensation which includes the intersweep and in-sweep compensation. Finally, a complete design example showed the indispensability of the velocity compensation and validated the effectiveness of the proposed range-velocity processing scheme.

## Competing Interests

The authors declare that there are no competing interests regarding the publication of this paper.

## References

- [1] D. E. Barrick, "History, present status, and future directions of HF surface-wave radars in the U.S.," in *Proceedings of the International Radar Conference*, pp. 652–655, Adelaide, Australia, September 2003.
- [2] A. M. Ponsford and J. Wang, "A review of high frequency surface wave radar for detection and tracking of ships," *Turkish Journal of Electrical Engineering and Computer Sciences*, vol. 18, no. 3, pp. 409–428, 2010.
- [3] H. J. Roarty, D. E. Barrick, J. T. Kohut, and S. M. Glenn, "Dual-use of compact HF radars for the detection of mid and large-size vessels," *Turkish Journal of Electrical Engineering & Computer Sciences*, vol. 18, no. 3, pp. 373–388, 2010.
- [4] D. E. Barrick, J. M. Headrick, R. W. Bogle, and D. D. Crombie, "Sea backscatter at HF: interpretation and utilization of the echo," *Proceedings of the IEEE*, vol. 62, no. 6, pp. 673–680, 1974.
- [5] K.-W. Gurgel, H.-H. Essen, and T. Schlick, "HF surface wave radar for oceanography—a review of activities in Germany," in *Proceedings of the International Radar Conference (RADAR '03)*, pp. 700–705, Adelaide, Australia, September 2003.
- [6] K.-W. Gurgel and G. Antonischki, "Measurement of surface current fields with high spatial resolution by the HF radar WERA," in *Proceedings of the IEEE International Geoscience and Remote Sensing Symposium (IGARSS '97)*, vol. 4, pp. 1820–1822, August 1997.
- [7] H. W. Leong and B. Dawe, "Channel availability for east coast high frequency surface wave radar systems," Tech. Rep., Defence R&D, Toronto, Canada, 2001.
- [8] A. Dzvonkovskaya and H. Rohling, "Software-improved range resolution for oceanographic HF FMCW radar," in *Proceedings of the 14th International Radar Symposium (IRS '13)*, pp. 411–416, June 2013.
- [9] V. M. Kutuzov, "Synthesis of non-regular multitone signals and algorithms of their processing," in *Proceedings of the 3rd International Conference on Signal Processing (ICSP '96)*, vol. 1, pp. 813–816, October 1996.
- [10] S. D. Green and S. P. Kingsley, "Improving the range/time sidelobes of large bandwidth discontinuous spectra HF radar waveforms," in *Proceedings of the 7th International Conference on HF Radio Systems and Techniques*, pp. 246–250, July 1997.
- [11] S. D. Green and S. P. Kingsley, "Investigation of wide bandwidth HF radar waveforms," in *Proceedings of the IEE Electronics Division Colloquium on Advanced Transmission Waveforms*, pp. 2/1–2/8, June 1995.
- [12] Q. Wang, Z. Yang, X. Wan, and J. Xiong, "Range sidelobe suppression for HF surface wave radar with discontinuous spectra," in *Proceedings of the 8th International Symposium on Antennas, Propagation and EM Theory (ISAPE '08)*, pp. 645–648, Beijing, China, November 2008.
- [13] J. Yu and J. Krolik, "Multiband chirp synthesis for frequency-hopped FMCW radar," in *Proceedings of the 43rd Asilomar Conference on Signals, Systems and Computers*, pp. 1315–1319, November 2009.
- [14] M. J. Lindenfeld, "Sparse frequency transmit and receive waveform design," *IEEE Transactions on Aerospace and Electronic Systems*, vol. 40, no. 3, pp. 851–861, 2004.
- [15] G. Wang and Y. Lu, "Designing single/multiple sparse frequency waveforms with sidelobe constraint," *IET Radar, Sonar and Navigation*, vol. 5, no. 1, pp. 32–38, 2011.
- [16] W. X. Liu, Y. L. Lu, and M. Lesturgie, "Optimal sparse waveform design for HFSWR system," in *Proceedings of the International Conference on Waveform Diversity and Design (WDD '07)*, pp. 127–130, IEEE, Pisa, Italy, June 2007.
- [17] Y. Wei and Y. Liu, "New anti-jamming waveform designing and processing for HF radar," in *Proceedings of the CIE International Conference on Radar Proceedings*, pp. 281–284, October 2001.
- [18] D. Zhang and X. Liu, "Range sidelobe suppression for wide-band randomly discontinuous spectra OTH-HF radar signal," in *Proceedings of the IEEE Radar Conference*, pp. 577–581, April 2004.
- [19] D. E. Barrick, "FM/CW radar signals and digital processing," Tech. Rep., National Oceanic and Atmospheric Administration, Boulder, Colo, USA, 1973.
- [20] H. C. Chan, "Evaluation of the FMICW waveform in HF surface radar applications," Tech. Rep., Defence Research Establishment, Ottawa, Canada, 1994.
- [21] P. Babu and P. Stoica, "Spectral analysis of nonuniformly sampled data—a review," *Digital Signal Processing*, vol. 20, no. 2, pp. 359–378, 2010.
- [22] T. Yardibi, J. Li, P. Stoica, M. Xue, and A. B. Baggeroer, "Source localization and sensing: a nonparametric iterative adaptive approach based on weighted least squares," *IEEE Transactions on Aerospace and Electronic Systems*, vol. 46, no. 1, pp. 425–443, 2010.
- [23] P. Stoica, J. Li, and H. He, "Spectral analysis of nonuniformly sampled data: a new approach versus the periodogram," *IEEE Transactions on Signal Processing*, vol. 57, no. 3, pp. 843–858, 2009.
- [24] M. A. Richards, *Fundamentals of Radar Signal Processing*, McGraw-Hill, New York, NY, USA, 2nd edition, 2014.
- [25] L. Eyer and P. Bartholdi, "Variable stars: which Nyquist frequency?" *Astronomy and Astrophysics Supplement Series*, vol. 135, no. 1, pp. 1–3, 1999.

## Research Article

# Observation of Zenneck-Like Waves over a Metasurface Designed for Launching HF Radar Surface Wave

Florent Jangal,<sup>1</sup> Nicolas Bourey,<sup>2</sup> Muriel Darces,<sup>2</sup> François Issac,<sup>1</sup> and Marc Hélier<sup>2</sup>

<sup>1</sup>ONERA-The French Aerospace Lab, 91123 Palaiseau Cedex, France

<sup>2</sup>Sorbonne Universités, UPMC University of Paris 06, UR2, L2E, 75005 Paris, France

Correspondence should be addressed to Florent Jangal; [florent.jangal@onera.fr](mailto:florent.jangal@onera.fr)

Received 4 May 2016; Revised 2 September 2016; Accepted 18 September 2016

Academic Editor: Weimin Huang

Copyright © 2016 Florent Jangal et al. This is an open access article distributed under the Creative Commons Attribution License, which permits unrestricted use, distribution, and reproduction in any medium, provided the original work is properly cited.

Since the beginning of the 20th century a controversy has been continuously revived about the existence of the Zenneck Wave. This wave is a theoretical solution of Maxwell's equations and might be propagated along the interface between the air and a dielectric medium. The expected weak attenuation at large distance explains the constant interest for this wave. Notably in the High Frequency band such a wave had been thought as a key point to reduce the high attenuation observed in High Frequency Surface Wave Radar. Despite many works on that topic and various experiments attempted during one century, there is still an alternation of statements between its existence and its nonexistence. We report here an experiment done during the optimisation of the transmitting antennas for Surface Wave Radars. Using an infrared method, we visualize a wave having the structure described by Zenneck above a metasurface located on a dielectric slab.

## 1. Introduction

In 1907, Zenneck was aiming to explain Marconi's experiments on transatlantic propagation [1]. Since ionization of the atmosphere was mainly thought as the result of Earth radioactivity and was limited to ten kilometers or so [2], Zenneck logically stated that the ionization of the atmosphere could not explain Marconi's results [1]. He assumed that transatlantic propagation was due to the creation of a new kind of electromagnetic wave which was propagated along the interface between the air and the ground. Zenneck claimed that this wave was a valid solution of Maxwell's equations and had the main features of a confined wave. Moreover it might have low attenuation along the interface. Two years later, Arnold Sommerfeld confirmed, with a more rigorous approach, that the Zenneck Wave (ZW) was a solution of the Maxwell equations [3]. The controversy then started since the mathematical solution proposed by Sommerfeld was questionable [4, 5]. Among several arguments, a sign mistake was pointed out. This mistake led to the conclusion that the ZW was a calculus artefact and could not exist. Moreover, it froze the discussion in the mathematical domain and kept it

aside the physical aspects [6, 7]. As time goes by, according to mathematical approaches, an abundant terminology has been built to name the confined waves which can be propagated at the interface between two materials [8–12] and the ZW has remained a theoretical object. In this context, the main criticism is dealing with the excitation of the ZW. Indeed, the generation of a sole ZW requires a source of infinite dimension or a finite, but unphysical, phase lens. Those points could reinforce the idea that the ZW is a nonphysical solution [13, 14].

Thereby, many interpretations and beliefs have arisen about the ZW. Today, it is difficult to discern the way to provide a proof regarding its existence [15, 16] or nonexistence [17, 18]. Nevertheless, the wave excited over an air/ground interface is a main issue for High Frequency (HF) Surface Wave Radars (SWR). The HF SWR can take advantage of low loss propagation along the interface. Hence, understanding the Zenneck Wave issue may allow improving the radar coverage by increasing the energy propagated along the ground.

It is well known that to deal with the complexity of wave excitation at air/ground interface we need to use negative

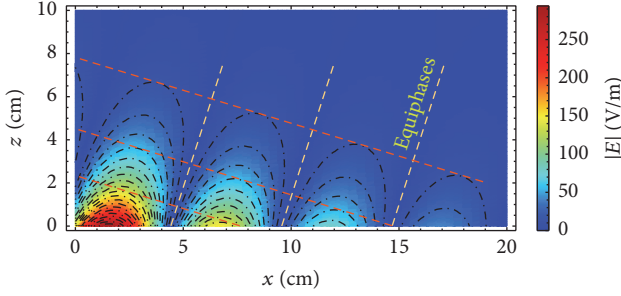


FIGURE 1: Simulation of a Zenneck Wave using Wait's formulation in [5]; the air/metasurface interface is located at  $z = 0$  and the relative permittivity is  $-1.2$ .

permittivity and permeability materials [19]. This is the reason why we are using such materials.

In the next section we recall some theoretical aspects of the Zenneck approach. In Section 3 the measurement results are described. At last, Section 4 contains concluding remarks.

## 2. Theoretical Approach

**2.1. The Zenneck Wave.** More than one century ago, Zenneck himself has suggested some clues to better understand his assumption about the existence of a low loss Surface Wave. Nevertheless, he noticed that the phase speed of this wave exceeded the speed of the light. But, as recalled by Ling et al., the group velocity of the ZW along the interface never exceeds the speed of the light, whatever the phase velocity is [1, 20]. Zenneck also remarked that the propagation vector was tilted toward the dielectric medium. As a result, the equiphase planes and the orthogonal equimagnitude planes are also slanted by comparison with the case of propagation above a perfect electric conductor [21, 22]. The ZW can be represented using notably the formulation of James Wait [5] if a negative permittivity material is chosen for the ground as suggested in [19]. The excited wave is tilted towards the interface. Hence it seems to sink inside the lower dielectric medium (Figure 1). It also differs from the leaky waves by the tilt angle, since leaky waves are growing as they propagate and seem to rise away from the dielectric [19].

Apparently insignificant, that tilt can be one way to identify the ZW. We have to notice here, as shown in Figure 1, that the hypothetical weak attenuation suggested by Zenneck in order to explain Marconi's experiment is not valid since the attenuation is significant along the interface ( $x$  direction) and normally to the interface ( $z$  direction). This is in accordance with Hill and Wait conclusion: the ZW cannot be propagated over long distances [17]. Hence, ZW is not a good candidate to enhance HFSWR performances. But as shown hereafter, the understanding of the link between Surface Wave and Zenneck Wave allows designing Surface Wave launchers.

**2.2. Zenneck Wave and Surface Plasmon Polariton.** Considering the available theoretical studies [20, 23, 24], the physical reality of ZW and their ability to carry energy are still questionable. Those uncertainties are even more important

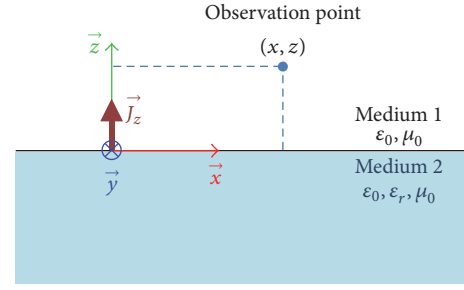


FIGURE 2: Geometry of the problem.

if we consider the doubts of Zenneck about his solution: the above-mentioned tilted equiphase planes violated the initial assumption of plane wave propagation. But, this discrepancy seems not to be a concern, at least for him.

To find a possible enhanced antenna for HFSWR, we proceed from the geometry depicted in Figure 2.

The upper medium is air; the lower medium is a lossy dielectric. The source is an infinite line of  $\vec{z}$  oriented electric dipoles  $\vec{J}_z$  lying along the  $\vec{y}$ -axis (magnitude of  $\vec{J}_z$  is  $1 \text{ A/m}^2$ ). The field at the observation point is the solution of Maxwell's equations obtained with modal decomposition [22]. For convenience, since we are focusing on the vertical electric field at  $z = 0$  and since the line source is located on the interface, the calculation is performed using the surface impedance approach [25–28] rather than with the development of the reflection coefficient at grazing angle [6]. Indeed, the impedance condition replaces the dielectric medium at  $z = 0$  and the vertical electric field is as follows [6]:

$$E_z(x, z)|_{z=0} = -\tilde{Z}_s \cdot H_y(x, z)|_{z=0}, \quad (1)$$

$$\tilde{Z}_s = \sqrt{\frac{\mu_0}{\epsilon_0}} \cdot \sqrt{\frac{1}{\tilde{\epsilon}_r}}, \quad (2)$$

where  $E_z(x, z)|_{z=0}$  is the electric field normal to the interface;  $H_y(x, z)|_{z=0}$  is the magnetic field tangential to the interface;  $\tilde{Z}_s$  is the complex surface impedance of the dielectric; and  $\tilde{\epsilon}_r$ ,  $\epsilon_0$ , and  $\mu_0$  are, respectively, the relative complex permittivity of the dielectric, the free space permittivity, and the free space permeability.

The magnetic field generated by the source can be formally expressed in an orthonormal basis consisting in a ZW (i.e., first term of (3)) and a continuous wave spectrum which can be viewed as spectral decomposition of other propagation modes (i.e., second term of (3)) [27, 28].

$$H_y(x, z)|_{z=0} = -i \cdot k_z \cdot e^{i\sqrt{k_0^2 - k_z^2} \cdot x} + \frac{1}{\pi} \int_0^\infty \frac{p^2 \cdot e^{i\sqrt{k_0^2 - p^2} \cdot x}}{p^2 - k_z^2} \cdot dp, \quad (3)$$

$$k_z = -\tilde{Z}_s \cdot \omega \cdot \epsilon_0, \quad (4)$$

where  $k_z$  is the complex wave number in the  $z$  direction;  $\omega$  is angular frequency; at last, the integrand  $p \in \mathbb{R}$ .

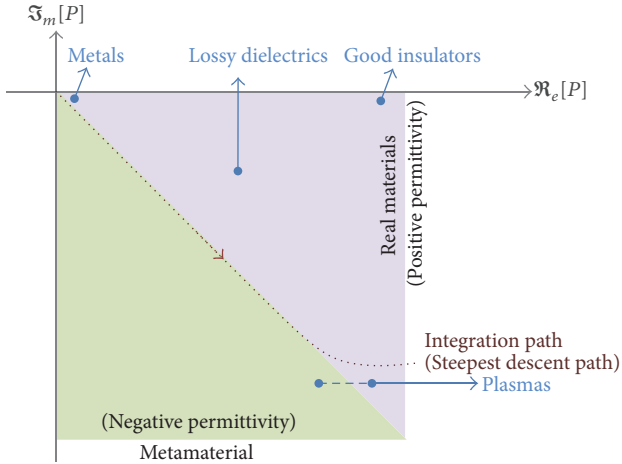


FIGURE 3: Position of pole  $P$  in the complex plane according to the ground properties.

When computing the second part of (1), the pole  $P = -\tilde{Z}_s \cdot \omega \cdot \varepsilon_0$  provides a contribution equal to the ZW term but with a positive sign. Thus, the ZW is not visible in the total field. We have here the mathematical core of the controversy: the ZW term disappears, even if it contributes to the final result. This is not surprising since this point has been largely discussed between Weyl and Sommerfeld early in the 20th century [8, 29] and many other authors. This point confirms the previous assumption of nonefficiency of ZW for long range propagation.

Nevertheless, as in other formulations [7, 9], the location of the pole  $P = -\tilde{Z}_s \cdot \omega \cdot \varepsilon_0$  with respect to the integration path determines the kind of the excited Surface Wave. The possible positions of  $P$  in the complex plane are split near the origin by the steepest descent path. The upper right part corresponds to the usual materials including positive permittivity plasmas and the lower left part to the metamaterials (Figure 3).

The medium which can enhance radiation near the interface should have a pole not surrounded by the SDP. If we choose  $\tilde{Z}_s$  such that the pole does not contribute to the integral in (3), whatever the integrand  $p$  is, the neutralization of the ZW will not occur.

An obvious way to do that is to insert an inductive surface over the dielectric. It has been shown by many authors in the course of the controversy that such a surface can propagate a confined wave traveling at the air-dielectric interface [24, 29, 30]. A metamaterial can provide the needed impedance and move the pole outside the integration path. In this case we will generate the well-known Surface Plasmon Polariton (SPP) which is propagated along an inductive surface [31, 32].

SPP has been extensively studied in optic domain [26, 33]. In optic wavelengths, the waves strongly interact with the free charges in metals [26]. As a result the medium is highly dispersive and the permittivity can reach negative values. In the same way, at radio frequencies, the dispersivity of metamaterials allows reaching such negative values. Hence, it is possible at radio frequencies to generate a wave having the same behaviour as the SPP's one [32, 34, 35].

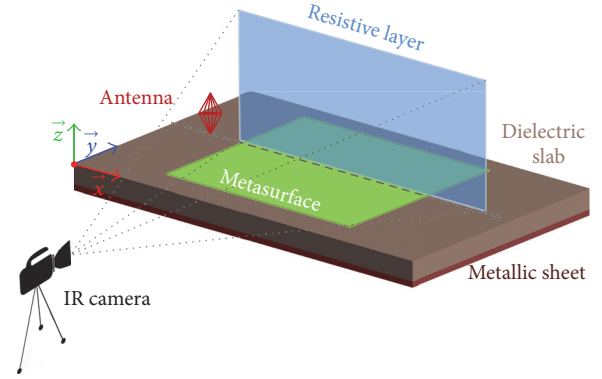


FIGURE 4: Measurement method based on visualization of electromagnetic field heating of a thin resistive layer.

SPP is a slow wave having nontilted equiphase planes [22, 26]. As shown in the next section, SPP is a good candidate for focalization of energy above the interface, at least near the transmitting antennas, since the significant attenuation only occurs normally to the interface ( $z$  direction); the electric field is then oriented in the  $z$  direction while the propagation occurs in the  $x$  direction [32, 34]. The metasurface used here is the basic brick of our Surface Wave launcher.

Nevertheless, a clear formal link appears in (1) between the field at the interface and Zenneck's tilted wave and those tilted waves might be observed when modifying some measurement parameters.

### 3. Measurements

**3.1. Measurement Method.** For obvious reasons, it is not easy to build the set-up in the HF band. Hence we perform the simulation in the HF band and conduct the experimentation in the UHF band, thanks to the scale principle.

The measurement method should characterize the field in the vicinity of the source without disturbing its distribution. That is the reason why we had carried out our measurement with the Electromagnetic and Infrared (EMIR) method. EMIR method consists in setting a thin resistive layer located where the field needs to be known and an infrared camera to image the film temperature (Figure 4). Since the resistive layer has a surface impedance close to the free space one, the local field is almost not disturbed and the temperature's increase is related to the tangential electric field strength [36]. In order to collect exclusively the temperature elevation due to the antenna radiated field, the transmitted UHF carrier is modulated with a very low frequency modulating signal. After demodulation an image which contains only the radiated electromagnetic field is obtained (Figure 4).

**3.2. Results.** Using a metamaterial, we succeed in visualizing SPP, as shown in Figure 5, and confined the energy above the interface [37].

Nevertheless, as mentioned before, a plasmon cannot be assimilated to a ZW. Indeed, the equiphase planes are not tilted and the phase speed is slower than the speed of light

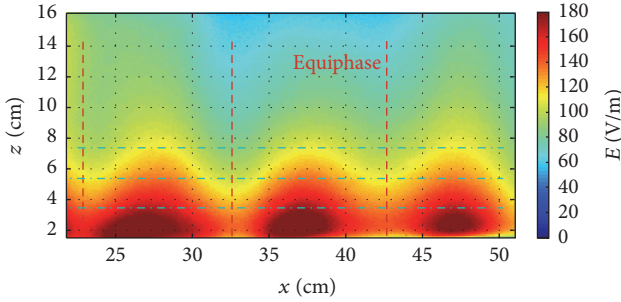


FIGURE 5: The SPP is observed with the EMIR method: equiphase planes are not tilted.

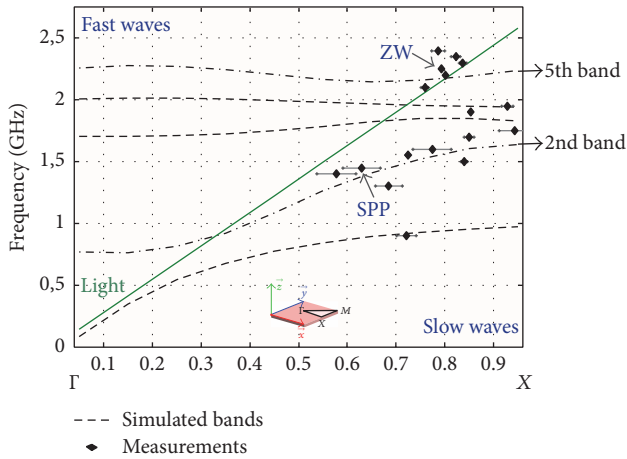


FIGURE 6: Dispersion diagram of the metasurface used for the experiment is drawn between  $\Gamma$  and  $X$ .

although the ZW speed exceeds the speed of light. Therefore, a ZW might be observed if  $\Re\{ \sqrt{k_0^2 - k_z^2} \}$  is less than  $k_0$  when shifting the pole.

As shown in the dispersion diagram (Figure 6) over a dispersive medium such as a metamaterial, this condition may be reached at higher frequencies than in the case of SPP, notably just after a band gap. In Figure 6, we compare simulation results and measurement results. The metasurface is lying over a lossless grounded slab in the  $\{\bar{x}; \bar{y}\}$  plane, and the measurement has been done in the propagation plane from 0.8 GHz up to 3 GHz as shown in Figure 4. The light (black line) separates the diagram into two parts, the fast wave as the ZW (upper left) and the slow waves as the SPP (lower right). The simulations are performed with the eigenvalue mode solver of CST MWS® (dashed lines).

Before the band gap, in the 2nd band at 1.45 GHz, the Surface Plasmon focusses the energy just above the metamaterial (Figure 5). The SPP is well confined below 8 cm (0.6 wavelengths). In contrast, at 2.2 GHz, in the 5th band, a wave propagates obliquely (Figure 7) with a phase speed above the speed of the light. As seen in the literature and observed with simulation, the wave seems to sink towards the interface. To ensure that the observed propagation mode is not due to the grounded slab, a measurement is carried

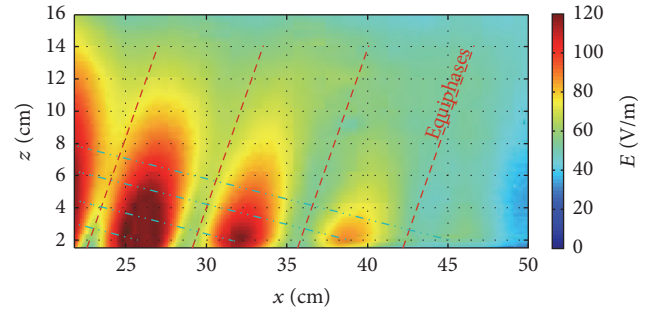


FIGURE 7: Measurement done at 2.2 GHz with EMIR method; the wave seems to sink into the lower dielectric: equiphase planes are tilted.

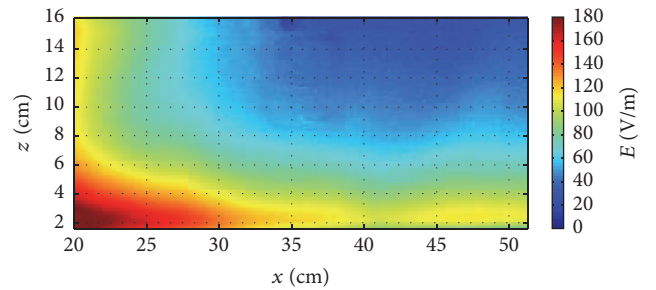


FIGURE 8: Field observed at 2.2 GHz with the EMIR method when the metasurface is removed.

out without the metasurface. Without the dispersion of the metasurface we obtained a classical shape of field over an air/dielectric interface (Figure 8).

## 4. Conclusion

Our first objective was to enhance Surface Wave excitation for HF Surface Wave Radar. Studying the physical problem, it is clear that strong confinement of the energy near the interface can be obtained using negative permittivity materials. A Surface Plasmon Polariton is then generated and imaged by the EMIR method in the UHF instead of HF band for experimentation convenience. Such a metasurface can then be used to improve radiation at low elevation. Nevertheless, at upper frequency than the Surface Plasmon Polariton one, we observed a Zenneck-like structure of wave sinking toward the dielectric. This unusual observation is made thanks to the EMIR method which allows visualizing the electromagnetic field near the source and near the interface with a low impact on the field.

## Competing Interests

The authors declare that there is no conflict of interests regarding the publication of this article.

## References

- [1] J. Zenneck, "On propagation of electromagnetic waves along a flat planar conductor surface and its relation to wireless telegraphy," *Annals of Physics*, vol. 328, no. 10, pp. 846–866, 1907.
- [2] C. A. Ziegler, "Technology and the process of scientific discovery: the case of cosmic rays," *Technology and Culture*, vol. 30, no. 4, pp. 939–963, 1989.
- [3] A. Sommerfeld, "About the propagation of waves in wireless telegraphy," *Annals of Physics*, vol. 333, pp. 665–736, 1909.
- [4] A. Sommerfeld, "About the propagation of waves in wireless telegraphy," *Annalen der Physik*, vol. 367, p. 96, 1920.
- [5] J. R. Wait, "The ancient and modern history of EM ground-wave propagation," *IEEE Antennas and Propagation Magazine*, vol. 40, no. 5, pp. 7–24, 1998.
- [6] P. C. Clemmow, "Radio propagation over a flat earth across a boundary separating two different media," *Philosophical Transactions of the Royal Society of London, Series A: Mathematical and Physical Sciences*, vol. 246, pp. 1–55, 1953.
- [7] T. K. Sarkar, W. Dyab, M. N. Abdallah et al., "Electromagnetic macro modeling of propagation in mobile wireless communication: theory and experiment," *IEEE Antennas and Propagation Magazine*, vol. 54, no. 6, pp. 17–43, 2012.
- [8] D. A. Hill and J. R. Wait, "Ground wave attenuation function for a spherical earth with arbitrary surface impedance," *Radio Science*, vol. 15, no. 3, pp. 637–643, 1980.
- [9] R. W. P. King and S. S. Sandler, "Electromagnetic field of a vertical electric dipole in the presence of a three-layered region," *Radio Science*, vol. 29, no. 1, pp. 97–113, 1994.
- [10] G. Goubau, "On the Excitation of Surface Waves," *Proceedings of the IRE*, vol. 40, no. 7, pp. 865–868, 1952.
- [11] A. F. Wickersham, "Generation, detection and propagation on the earth's surface of HF and VHF radio surface waves," *Nature Physical Science*, vol. 230, pp. 125–130, 1971.
- [12] R. Paknys and D. R. Jackson, "The relation between creeping waves, leaky waves, and surface waves," *IEEE Transactions on Antennas and Propagation*, vol. 53, no. 3, pp. 898–907, 2005.
- [13] D. A. Hill and J. R. Wait, "Excitation of the Zenneck surface wave by a vertical aperture," *Radio Science*, vol. 13, no. 6, pp. 969–977, 1978.
- [14] J. Brown, "Some theoretical results for surface wave launchers," *IRE Transactions on Antennas and Propagation*, vol. 7, no. 5, pp. 169–174, 1959.
- [15] T. Kahan and G. Eckart, "On the electromagnetic surface wave of sommerfeld," *Physical Review*, vol. 76, no. 3, pp. 406–410, 1949.
- [16] A. V. Kukushkin, "A technique for solving the wave equation and prospects for physical applications arising therefrom," *Physics-Uspekhi*, vol. 36, no. 2, pp. 81–93, 1993.
- [17] Y. B. Bashkuev, V. B. Khaptanov, and M. G. Dembelov, "Experimental proof of the existence of a surface electromagnetic wave," *Technical Physics Letters*, vol. 36, no. 2, pp. 136–139, 2010.
- [18] A. V. Kukushkin, A. A. Rukhadze, and K. Z. Rukhadze, "On the existence conditions for a fast surface wave," *Physics-Uspekhi*, vol. 55, no. 11, pp. 1124–1133, 2012.
- [19] R. T. Ling, J. D. Scholler, and P. Y. Ufimtsev, "The propagation and excitation of surface waves in an absorbing layer," *Progress In Electromagnetics Research*, vol. 19, pp. 49–91, 1998.
- [20] A. Ishimaru, J. R. Thomas, and S. Jaruwatanadilok, "Electromagnetic waves over half-space metamaterials of arbitrary permittivity and permeability," *IEEE Transactions on Antennas and Propagation*, vol. 53, no. 3, pp. 915–921, 2005.
- [21] H. M. Barlow and A. L. Cullen, "Surface waves," *Proceedings of the IEE—Part III: Radio and Communication Engineering*, vol. 100, no. 68, pp. 329–341, 1953.
- [22] A. Ishimaru, *Electromagnetic Wave Propagation, Radiation, and Scattering*, Prentice-Hall, Englewood Cliffs, NJ, USA, 1990.
- [23] K. A. Norton, "Propagation of radio waves over a plane earth," *Nature*, vol. 135, no. 3423, pp. 954–955, 1935.
- [24] P. S. Epstein, "Radio-wave propagation and electromagnetic surface waves," *Proceedings of the National Academy of Sciences of the United States of America*, vol. 33, pp. 195–199, 1947.
- [25] S. N. Karp and F. C. Karal, "Phenomenological theory of multi-mode surface wave excitation, propagation and diffraction," Tech. Rep. EM 198, New York University—Institute of Mathematical Sciences—Division of Electromagnetic Research, 1964.
- [26] C. L. C. Smith, N. Stenger, A. Kristensen, N. A. Mortensen, and S. I. Bozhevolnyi, "Gap and channeled plasmons in tapered grooves: a review," *Nanoscale*, vol. 7, no. 21, pp. 9355–9386, 2015.
- [27] L. Petrillo, F. Jangal, M. Darces, J.-L. Montmagnon, and M. Hélier, "Negative permittivity media able to propagate a surface wave," *Progress in Electromagnetics Research*, vol. 115, pp. 1–10, 2011.
- [28] Y. V. Kistovich, "Possibility of observing Zenneck surface waves in radiation from a source with a small vertical aperture," *Soviet Physics: Technical Physics*, vol. 34, pp. 391–394, 1989.
- [29] K. A. Norton, "The propagation of radio waves over the surface of the earth and in the upper atmosphere," *Proceedings of the Institute of Radio Engineers*, vol. 24, no. 10, pp. 1367–1387, 1936.
- [30] V. N. Datsko and A. A. Kopylov, "On surface electromagnetic waves," *Physics-Uspekhi*, vol. 51, no. 1, pp. 101–102, 2008.
- [31] A. Yu Nikitin, S. G. Rodrigo, F. J. García-Vidal, and L. Martín-Moreno, "In the diffraction shadow: norton waves versus surface plasmon polaritons in the optical region," *New Journal of Physics*, vol. 11, Article ID 123020, 2009.
- [32] J. B. Pendry, L. Martín-Moreno, and F. J. Garcia-Vidal, "Mimicking surface plasmons with structured surfaces," *Science*, vol. 305, no. 5685, pp. 847–848, 2004.
- [33] S. A. Maier, *Plasmonics: Fundamentals and Applications*, Springer Science & Business Media, 2007.
- [34] M. J. Lockyear, A. P. Hibbins, and J. R. Sambles, "Microwave surface-plasmon-like modes on thin metamaterials," *Physical Review Letters*, vol. 102, no. 7, Article ID 073901, 2009.
- [35] A. Ishimaru, *Electromagnetic Wave Propagation, Radiation, and Scattering*, Prentice Hall, Chapter 3 Section 11: Slow-Wave Solution for the TM Mode, Chapter 3 Section 12: Zenneck Waves and Plasmons, 1991.
- [36] D. Balageas and P. Levesque, "EMIR: a photothermal tool for electromagnetic phenomena characterization," *Revue Générale de Thermique*, vol. 37, no. 8, pp. 725–739, 1998.
- [37] F. Jangal, L. Petrillo, M. Darces, M. Hélier, and J. Montmagnon, "Inductive surface element," WO2014029947, 2014.

## Research Article

# Wind Speed Inversion in High Frequency Radar Based on Neural Network

Yuming Zeng,<sup>1</sup> Hao Zhou,<sup>1</sup> Hugh Roarty,<sup>2</sup> and Biyang Wen<sup>1</sup>

<sup>1</sup>School of Electronic Information, Wuhan University, Wuhan 430072, China

<sup>2</sup>Institute of Marine and Coastal Sciences, Rutgers University, New Brunswick, NJ 08901, USA

Correspondence should be addressed to Hao Zhou; [zhou.h@whu.edu.cn](mailto:zhou.h@whu.edu.cn)

Received 6 April 2016; Accepted 14 August 2016

Academic Editor: Khalid El-Darymli

Copyright © 2016 Yuming Zeng et al. This is an open access article distributed under the Creative Commons Attribution License, which permits unrestricted use, distribution, and reproduction in any medium, provided the original work is properly cited.

Wind speed is an important sea surface dynamic parameter which influences a wide variety of oceanic applications. Wave height and wind direction can be extracted from high frequency radar echo spectra with a relatively high accuracy, while the estimation of wind speed is still a challenge. This paper describes an artificial neural network based method to estimate the wind speed in HF radar which can be trained to store the specific but unknown wind-wave relationship by the historical buoy data sets. The method is validated by one-month-long data of SeaSonde radar, the correlation coefficient between the radar estimates and the buoy records is 0.68, and the root mean square error is 1.7 m/s. This method also performs well in a rather wide range of time and space (2 years around and 360 km away). This result shows that the ANN is an efficient tool to help make the wind speed an operational product of the HF radar.

## 1. Introduction

After Crombie explained the distinct characteristic of the sea echo Doppler spectra obtained by high frequency (HF) radar with Bragg scattering effect, the potential of the HF radar in remote sensing of the sea state parameters was recognized [1]. Barrick further derived the well-known first- and second-order radar cross section (RCS) equations and directly pushed forward the applications of the HF radars [2, 3]. Due to the unique capabilities of large-area, real-time, and all-weather monitoring over the sea surface, HF radar now has gained much attention and has been widely installed and operated all over the world.

As one data product of HF radar, wind speed estimate over the sea is of great help to the development and utilization of the sea resources. It is important for a wide variety of coastal and marine activities, such as sailing, fishing, and wind power generation. Wind over the oceans is typically strong and steady, representing a rich source of renewable energy [4]. It also plays a key role in many oceanographic processes including the air-sea interaction and the climate systems in both regional and global scales. After thirty years of development, the extraction of current velocity and wind

direction has achieved great success and they have become mature products of the HF radar. The wave height estimation has also reached relatively high accuracy. However, the wind speed estimation is still a challenge. The conventional wind speed estimation is via an indirect process; that is, it is not directly extracted from the radar echo spectrum but from the wave height and period estimates. It is the sea wave that generates the radar echo. The solutions to the wind-wave relationship are mainly based on empirical or semiempirical models, which may have different performances in different sea area. The errors in both of the wind-wave model and the wave estimation make it much more difficult to extract the wind speed.

The relationship between the wave parameters and wind speed has been studied for several decades. The common wave parameters used to estimate the wind speed are significant wave height  $H_s$  and dominant wave frequency  $f_m$ . The SMB relationship is such a semiempirical model [5–9]. It has been widely applied in the marine forecasting. However, the wind speed cannot be given in an analytical solution but should be sought by iteration, which depends on a proper initial value and may converge to a wrong estimate. Power regression is another method reported to estimate the wind speed, but it may lead to big errors for both low and high

TABLE 1: Performance comparison of different algorithms.

	Algorithm					
	Linear regression	Nonlinear regression	RBF	GRNN	ANFIS	BP
RMSE (m/s)	2.50	2.65	2.72	2.69	1.61	1.66
MAE (m/s)	2.00	2.05	2.11	2.09	1.22	1.3
CC	0.67	0.62	0.70	0.83	0.87	0.89
SI	0.38	0.41	0.42	0.41	0.25	0.25

wind speeds due to the high simplification of the wind-wave relationship [10]. Other indices have also been reported to contain wind speed information, for example, the widening of the first-order Bragg peaks and the frequency position of the second-order peak; however, these methods show a limited applicability, and the estimation error does not show an obvious decrease [11, 12]. To achieve better knowledge of the wind-wave relationship, Mathew and Deo introduced the artificial neural network (ANN) into the wind speed extraction [13]. The ANN is a totally data-driven, empirical way that can inverse the nonlinear relationship between the wind speed and other radar-extracted sea state parameters. Four parameters, that is, the significant wave height, average wave period, wave direction, and wind direction, are input to the ANN, and the output gives the corresponding wind speed estimate. The training process relies on the buoy measurements. The results show that the wind speed estimation error has reached an acceptable level and the ANN is a powerful tool for wind speed inversion. Not alone, the ANN method is also used to inverse the wind speed directly from the first-order Bragg peaks in HF radars [14]. Although this first-order method has a narrower range of wind speed estimation because the Bragg wave involved is easier to be blown into saturation under a wind speed not very high, the result is also encouraging and once more shows the capability of the ANN.

In this paper, we continue to use the ANN method proposed by Mathew and Deo for the wind speed extraction in HF radar. Differently, with the consideration that the wave direction estimate is often not very accurate, especially in the small-aperture radars such as the SeaSonde to be discussed here, we remove it from the input. That is, the ANN involved in this paper is a three-in-one-out network. The historical data recorded by the National Data Buoy Center (NDBC) buoy number 44025 near the east coast of the USA are used to train this ANN, and then the wave height, period, and wind direction estimates achieved by the HF radar are input to it to give the wind speed estimate. To cover different sea states, data of a whole year are used in the training process. As a result, the ANN is found to be applicable in rather wide ranges of both time and space. On one hand, the estimation performance of the trained ANN is nearly independent of the data time; for example, the ANN trained by the buoy data in 2008 still works well on the data in 2013. On the other hand, the trained ANN also works well on the data from other buoys as far as several hundreds of kilometers away. The radar involved is a 13 MHz SeaSonde system located at the BRMR site in New Jersey, USA, which serves as part of the Mid Atlantic HF radar network. The radar wind speeds in May, 2012, are estimated by the ANN, which shows a relatively

high correlation coefficient of 0.68 and a small root mean square error (RMSE) of 1.7 m/s compared with the buoy measurements. These results are much better than those obtained by the SMB method and the power regression method. The ANN method opens the possibility of making the wind speed estimate an operational data product of the HF radar.

## 2. Methodology

The ANN is a statistical learning algorithm inspired by animal brains which can perform fast parallel, nonlinear computing and complicated information processing. It can be used to estimate unknown functions that depend on a number of inputs. The ANN consists of a group of interconnected nodes (neurons) and their mutual connections [15]. Each node means a specific transfer function, and different weights are assigned to the interconnections between the nodes, which store the memories of learning. The ANN learning is just accomplished by adjusting the weights of the interconnections based on a given training data set. The backpropagation (BP) neural network is an algorithm developed to train a multilayer ANN so that it can learn the appropriate internal representations to allow it to learn arbitrary input-to-output mappings [16]. The BP calculates the gradient of the network error with respect to the weights and then updates the weights opposite to the gradient direction. The BP ANN has been the most widely applied network in classification, data compression, functional approximation, and nonlinear regression due to its strong abilities of nonlinear mapping and generalization.

To confirm that the BP ANN is the best choice for wind speed inversion, we evaluated six different algorithms, as displayed in Table 1. In this evaluation, the buoy data in 2011 were used to get the best parameters of different algorithms, while the buoy data during 2012 were used to test the different algorithms. For all six algorithms, we found that the BP had the best fitting ability. The linear and nonlinear statistical regressions lack sufficient capacity to fit. It can only fit the wind-derived waves for significant wave height as single input parameter. The fitting abilities of RBF (Radial Basis Function) and GRNN (Generalized Regression Neural Network) in wind speed inversion are not as well as BP ANN and ANFIS. As a combination of fuzzy logic and neural network, ANFIS (Adaptive Neural Network Based Fuzzy Inference System) has good performance but its correlation coefficient is slightly worse than that of BP.

In this study, we construct a three-layer BP network to map the relationship between the wind speed and three other sea state parameters, say the significant wave height, average

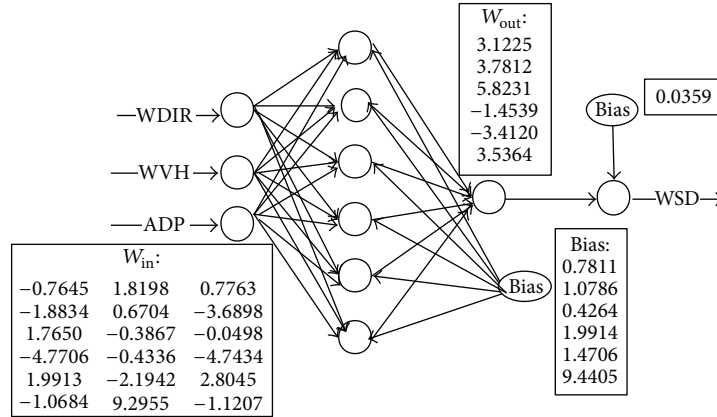


FIGURE 1: The structure of the ANN.

wave period, and wind direction. The hidden layer has six neurons, which is found to offer satisfactory estimation performance. More neurons will make the training slower, while fewer neurons may lead to an insufficient mapping ability. The transfer function of the hidden layer is the log-sigmoid function, and that of the output layer is the tan-sigmoid function. The log-sigmoid function can compress the output value into the range of 0 to 1, and the tan-sigmoid function can compress the output value into the range of  $-1$  to  $1$ . The sigmoid function is advantageous because it can accommodate large signals while allowing pass of small signals without excessive attenuation. The structure of the ANN is shown in Figure 1. To improve the generalization ability of the ANN and avoid overtraining, we use the Bayesian regularization training method, which can improve the performance of the small-scale network by adding the mean sum of the squares of network weights to the objective function [17, 18]. After the ANN converges, it is able to output the wind speed estimate from the input of HF radar measurements.

Each training data set covers a whole year of data from the NDBC buoy number 44025, located at  $40^{\circ}15'3''N$ ,  $73^{\circ}9'52''W$ , with the wind speed, significant wave height, average wave period, and wind direction being recorded every hour. The ANN trained by the buoy data in 2011 is then applied on the data achieved by the 13 MHz SeaSonde radar which is located at the BRMR site ( $39^{\circ}24'30''N$ ,  $74^{\circ}21'41''W$ ) near New Jersey, USA, in 2012. The geographic map is shown in Figure 2 for clarity. The total number of pieces of the buoy data in 2011 is 6292.

To further evaluate the performance of the ANN method, the SMB method and the power regression method are also used on the radar measurements to estimate the wind speed. The SMB relationship is given by

$$\frac{gH_s}{V_{10}^2} = 0.26 \tanh \left[ \frac{(f_m V_{10})^{-3/2} (3.5g)^{3/2}}{100} \right], \quad (1)$$

where  $g$  is the gravity acceleration,  $H_s$  is the significant wave height,  $f_m$  is the peak frequency of the wave height spectrum, and  $V_{10}$  is the wind speed at a height of 10 m above the sea

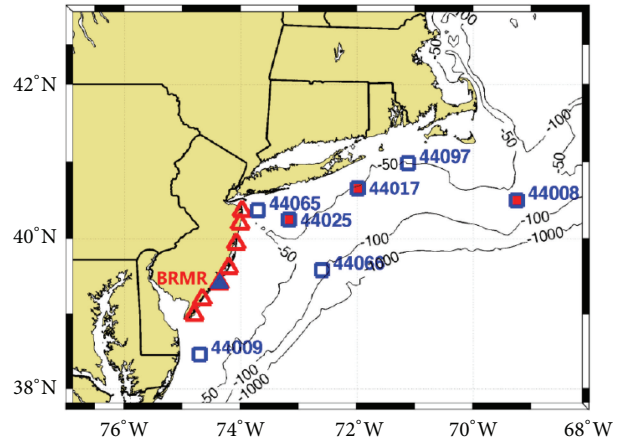


FIGURE 2: Geographic map of the buoys and the SeaSonde site involved (reproduced from [19]).

surface. There is not an analytical solution for  $V_{10}$ , so it should be approached by iteration [6–8]. This equation stands for fetch restricted conditions [9]. The power regression method further ignores the impact of the wave period and directly estimates the wind speed from the wave height by use of the power model:

$$V_{10} = \alpha H_s^\beta, \quad (2)$$

where  $\alpha$  and  $\beta$  are two constant coefficients which can be determined by fitting to the buoy data.

### 3. Data Processing Results

The buoy data set of a whole year is used to train the ANN. We aim to extract wind speed from the HF radar data in 2012, so we choose the buoy data in 2011 to train the ANN. The average wave heights and wind speeds recorded by the NDBC buoy number 44025 in each month of 2011 and 2012 are listed in Tables 2 and 3, respectively. We can see that the average sea states are lower during the summer months, say May till August, than the winter months, say November till February.

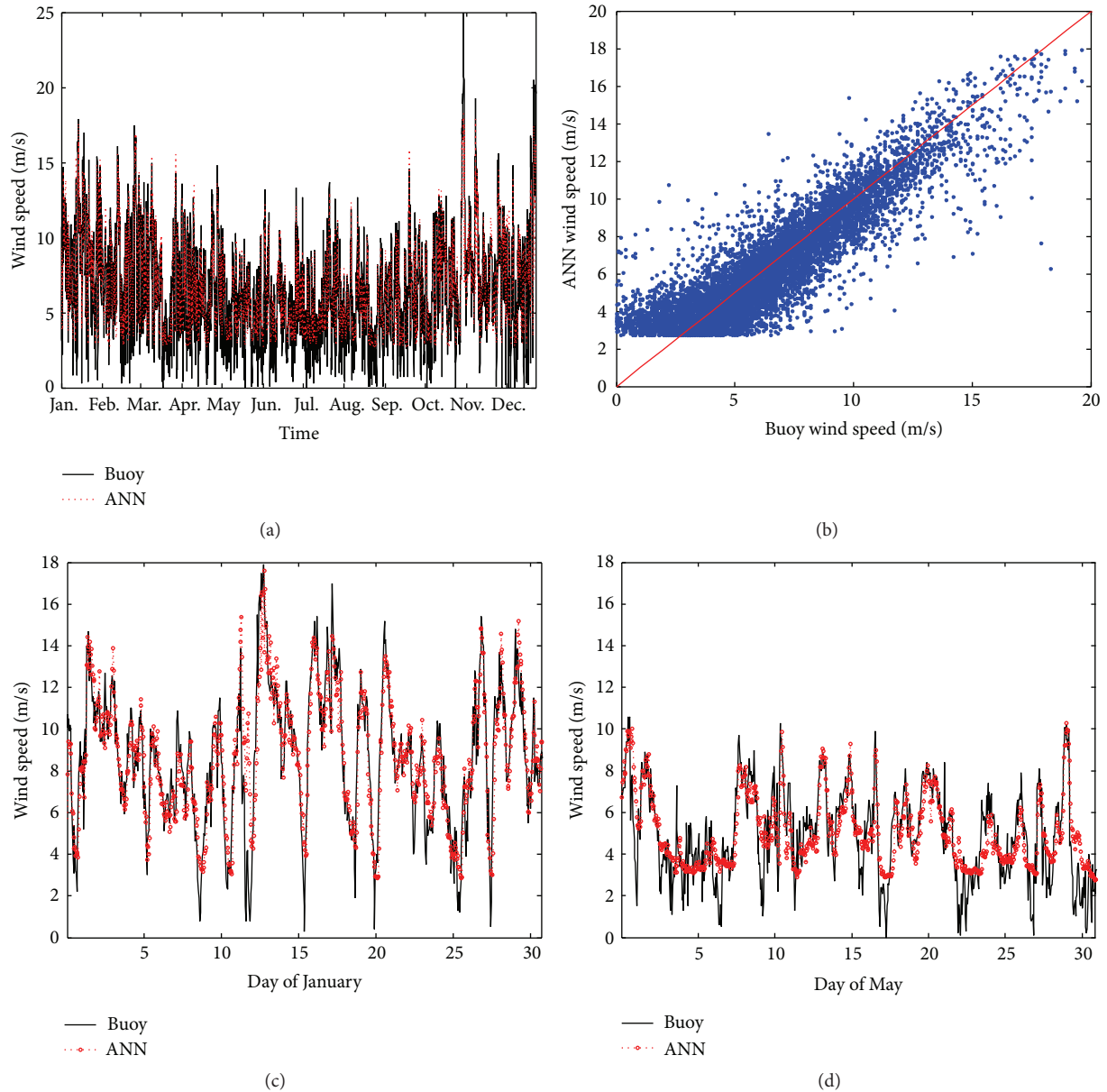


FIGURE 3: Buoy wind speed estimation in 2012 by the ANN trained with the buoy data of 2011. (a) Time sequence of the whole year. (b) Scatter plot. (c) Time sequence in January. (d) Time sequence in May.

TABLE 2: Average wave height and wind speed per month in 2011.

	Month											
	Jan.	Feb.	Mar.	Apr.	May	Jun.	Jul.	Aug.	Sep.	Oct.	Nov.	Dec.
Number of pieces of data	738	665	734	717	742	719	721	0	0	0	513	743
Wind speed (m/s)	7.7	8.0	7.2	6.7	4.8	4.5	4.7	—	—	—	6.7	7.3
Wave height (m)	1.25	1.36	1.38	1.67	1.18	0.89	0.91	—	—	—	1.26	1.32

In the training process, the learning ratio is set to be 0.05. After 141 epochs, the ANN converges. When this trained ANN is applied on the buoy data of 2012, satisfactory wind speed estimates are obtained when the wind speeds are greater than 5 m/s, as shown in Figure 3.

For comparison, the SMB method and the power regression method are also tested with the buoy data. The results are shown in Figure 4. As can be seen, the RMSE by the ANN method varies between 1.45 and 1.80 m/s except that it exceeds 2.2 m/s in October and December, and the

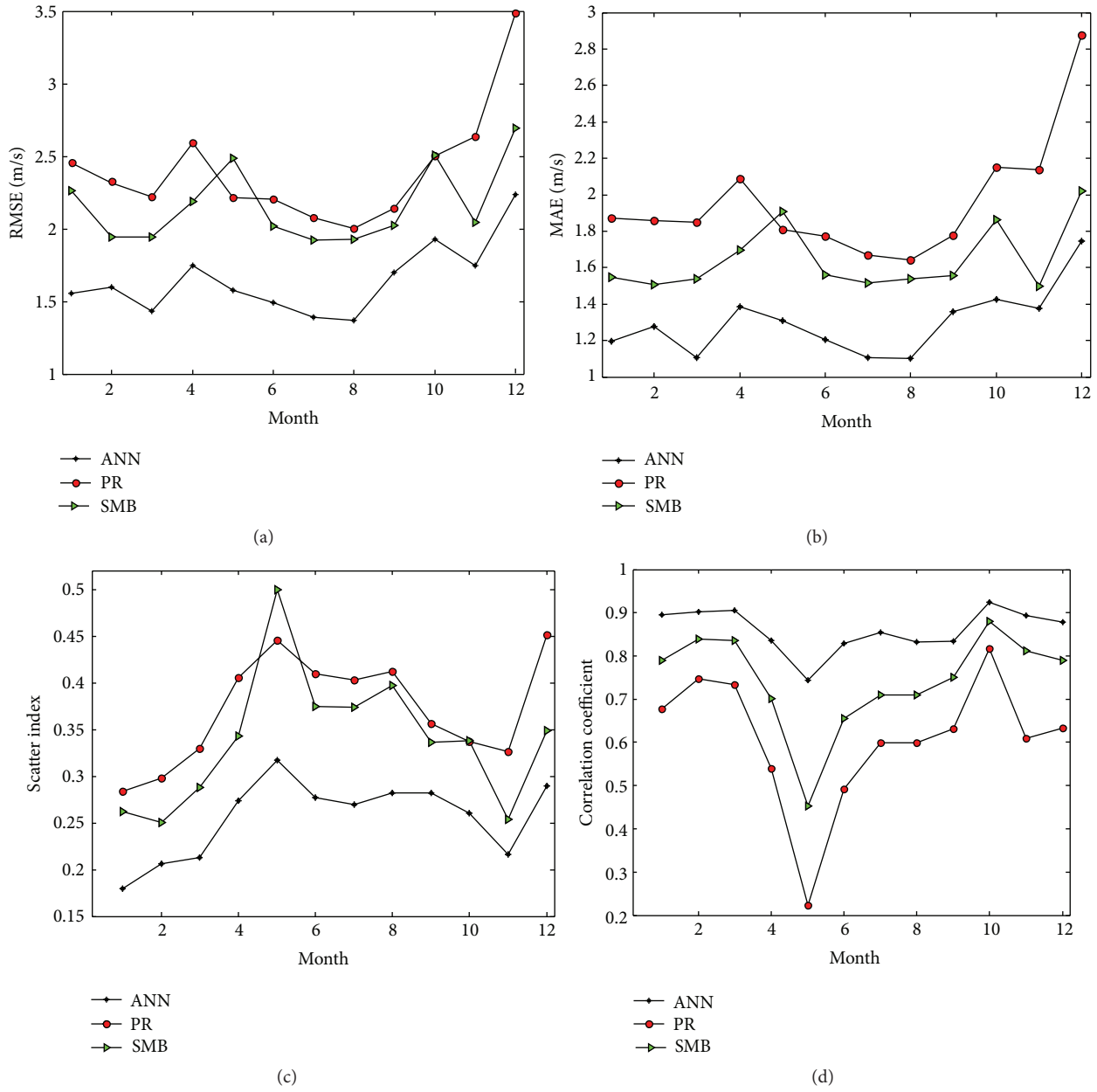


FIGURE 4: Wind speed estimated by the buoy data per month in 2012. (a) RMSE. (b) MAE. (c) CC. (d) SI.

TABLE 3: Average wave height and wind speed per month in 2012.

	Month											
	Jan.	Feb.	Mar.	Apr.	May	Jun.	Jul.	Aug.	Sep.	Oct.	Nov.	Dec.
Number of pieces of data	738	694	742	719	741	718	740	743	715	741	719	528
Wind speed (m/s)	8.6	7.7	6.7	6.3	4.9	5.3	5.1	4.8	6	7.4	8.0	7.7
Wave height (m)	1.54	1.23	1.25	1.14	1.14	0.98	0.91	0.89	1.22	1.53	1.53	1.50

correlation coefficient (CC) is greater than 0.82 (up to 0.91) except that it is 0.78 in May. The sea state in fact has an impact on the wind speed estimation. The big errors in October and December are mainly caused by the relatively fewer training samples corresponding to the large wave heights above 5 m,

and the decrease of the correlation coefficient in May is mainly due to the low wind speed in that month. Generally, the ANN method outperforms the SMB and power regression methods in all the indices, say the RMSE, mean absolute error (MAE), correlation coefficient (CC), and scatter index (SI,

TABLE 4: Performances of wind speed estimation from different buoys in different years by the ANN trained with the buoy data of 2008.

	Buoy number									
	44025				Year	44017			44008	
	2009	2010	2011	2012	2013	2013	2014	2010	2012	
RMSE (m/s)	1.61	1.54	1.45	1.71	1.59	1.47	1.56	2.04	1.77	
MAE (m/s)	1.25	1.14	1.11	1.31	1.28	1.11	1.20	1.48	1.35	
CC	0.90	0.90	0.90	0.88	0.90	0.90	0.90	0.82	0.84	
SI	0.24	0.22	0.22	0.26	0.24	0.21	0.21	0.33	0.29	

defined as the ratio of the standard error to the mean absolute value), and its estimation performance is much less sensitive to the sea states. So the ANN method is expected to offer a promising way to estimate the wind speed in HF radars.

According to Table 3, the wind speed in May is significantly lower than that in April, but the wave height is higher than that of April because of the full developed waves and swells. In terms of scatter index and RMSE, we can see that the performance of PR is slightly better than that of SMB. In addition to swell, it also may be the reason that the SMB method is more suitable for the wave without full development in fetch restricted conditions. In May, the results have an unsatisfactory correlation factor of about 0.45, while they show an excellent correlation factor of 0.9 in October, as shown in Figure 4(d). These show that the performance of SMB method is not stable enough and is only suitable for the wind-derived waves in fetch restricted conditions.

Even though traditional SMB wind-wave empirical equations perform badly in swell and fully developed sea conditions, the ANN performs well in May, as Figure 4 shows. In Table 2, we can see that the wave height in April is higher than that in May, while the wind speed is smaller than that in May for swells coming to this sea area frequently in April. These training data contain the relationship between wind speed and other wave parameters in swell and fully developed sea conditions.

Then the significant wave height, wave period, and wind direction from the SeaSonde in May of 2012 are input to the trained ANN to estimate the wind speed. It should be pointed out that these input parameters are extracted not by the commercial software of the SeaSonde but by that of the OSMAR-S developed by Wuhan University, whose performance has been validated by a series of experiments [20–22]. Figure 5 shows the time sequence of the significant wave height estimates. The RMSE and CC between the significant wave heights from the radar and the buoy are 0.24 m and 0.79, respectively. The wind speed estimation results are shown in Figure 6. It can be seen that the ANN method also gives better wind speed estimation than the SMB and power regression methods. The RMSE, MAE, CC, and SI of the wind speed estimation by the ANN method are 1.70 m/s, 1.37 m/s, 0.68, and 0.34, respectively.

Before it is developed into an operational method, the generalization ability of the ANN should also be considered. To evaluate the generalization ability of the ANN in both of the time and space, we further test it on the buoy data of other

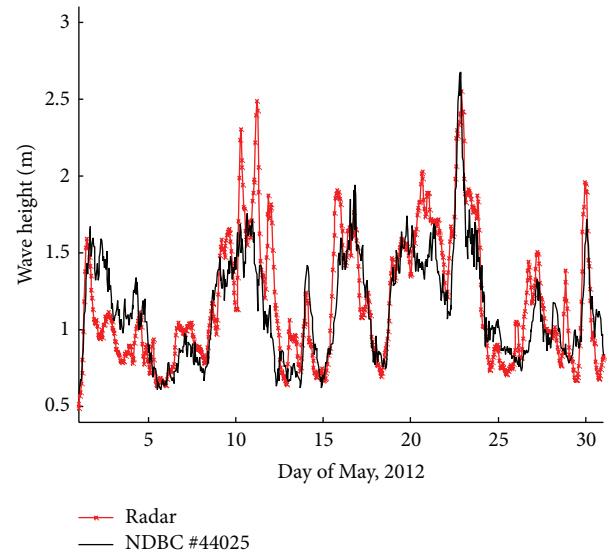


FIGURE 5: Significant wave height extracted from the SeaSonde at the BRMR site in May, 2012.

several years, say 2009 till 2013. The estimation performances in the years are listed in Table 4, from which we can see that the performance of the ANN is almost independent of the time. Even when this ANN is applied on the data of 2012, the result is still satisfactory, quite similar to that achieved by the ANN trained with the data of 2011. This shows strong generalization ability in the time. Then the ANN is applied on the data from other two NDBC buoys, say number 44017 ( $40^{\circ}41'39''N$ ,  $72^{\circ}2'52''W$ ) and number 44008 ( $40^{\circ}30'10''N$ ,  $69^{\circ}14'53''W$ ), which are about 120 and 360 km away from the buoy number 44025, respectively, as shown in Figure 1. The ANN method once more shows a strong generalization ability in the space, which can be seen in Table 4. Even when the distance exceeds 300 km, the correlation coefficient is still above 0.8. The result of number 44008 is slightly worse than that of number 44017, which should be because the former one is much farther from the coast and thus the bathymetry deepens faster and has a larger influence on the wind-wave relationship. Two deductions can be achieved from these results. The inherent relationship between the wind speed and wave parameter is quite stable in both time and space, and the ANN can recognize this relationship well. Since the buoys can provide in situ measurements with high accuracy while they are usually not deployed very closely to each other,

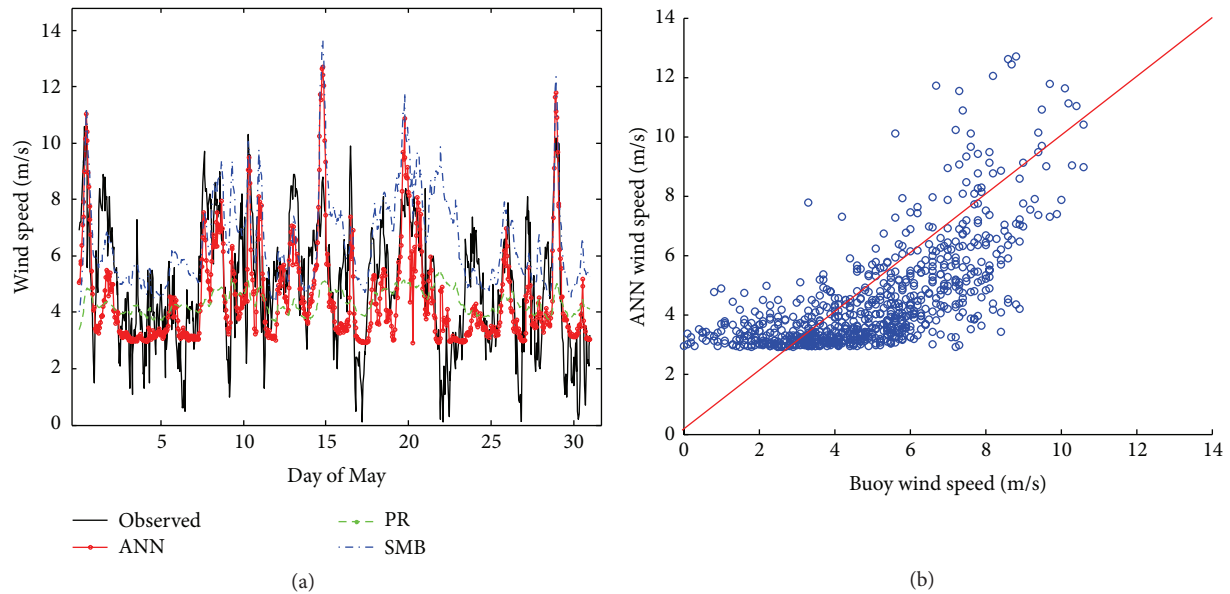


FIGURE 6: Radar wind speed estimation in May, 2012, by the ANN trained with the buoy data of 2011. (a) Wind speed estimates. (b) Scatter plot by the ANN method.

the HF radar just can accomplish the large-area monitoring task with the help of a limited number of buoys. So we can conclude that the ANN is an efficient tool to realize wind speed extraction in HF radar for operational use.

#### 4. Conclusions

The artificial neural network is a powerful tool that can automatically learn and memorize the unknown, complicated relationship between some correlated parameters. The HF radar can achieve wave height, period, and wind direction estimates directly from the echo Doppler spectra, while the wind speed should be estimated in an indirect way. That is, the wind speed is estimated from the wave parameters via an empirical or semiempirical method, so the inconsistency between these models and the actual relation forms a main source of error in wind speed estimation. The wave extraction in HF radar has achieved relatively high accuracy, but the imperfect models make the wind speed estimation be still a challenge. The ANN is such an efficient tool that offers improved performance on wind speed estimation in HF radar. Moreover, it is available in a wide range of time and space (2 years around and 360 km away), which opens the possibility of operational use of wind speed from HF radar.

#### Competing Interests

The authors declare that there are no competing interests regarding the publication of this paper.

#### Acknowledgments

This work was supported by the National Natural Science Foundation of China under Grant no. 61371198 and the

National Special Program for Key Scientific Instrument and Equipment Development of China under Grant no. 2013YQ160793.

#### References

- [1] D. D. Crombie, "Doppler spectrum of sea echo at 13.56 Mc/s.," *Nature*, vol. 175, pp. 681–682, 1955.
- [2] D. E. Barrick, "First-order theory and analysis of MF/HF/VHF scatter from the sea," *IEEE Transactions on Antennas and Propagation*, vol. 20, no. 1, pp. 2–10, 1972.
- [3] D. Barrick, "Remote sensing of sea state by radar," in *Proceedings of the IEEE International Conference on Engineering in the Ocean Environment (Ocean '72)*, pp. 186–192, Newport, RI, USA, September 1972.
- [4] G. J. Koch, Y. J. Beyon, M. Petros et al., "Side-scan Doppler lidar for offshore wind energy applications," *Journal of Applied Remote Sensing*, vol. 6, no. 10, pp. 359–368, 2012.
- [5] H. U. Sverdrup and W. H. Munk, "Empirical and theoretical relations between wind, sea, and swell," *Eos, Transactions American Geophysical Union*, vol. 27, no. 6, pp. 823–827, 1946.
- [6] P. E. Dexter and S. Theodoridis, "Surface wind speed extraction from HF sky wave radar Doppler spectra," *Radio Science*, vol. 17, no. 3, pp. 643–652, 1982.
- [7] W. Huang, S. Wu, E. Gill, B. Wen, and J. Hou, "HF radar wave and wind measurement over the Eastern China Sea," *IEEE Transactions on Geoscience and Remote Sensing*, vol. 40, no. 9, pp. 1950–1955, 2002.
- [8] W. Huang, E. Gill, S. Wu, B. Wen, Z. Yang, and J. Hou, "Measuring surface wind direction by monostatic HF ground-wave radar at the Eastern China Sea," *IEEE Journal of Oceanic Engineering*, vol. 29, no. 4, pp. 1032–1037, 2004.
- [9] K. Watanabe and K. Nomura, "Investigation of ocean wind estimating technique using wave data and SMB method," in *Proceedings of the 7th International Conference on Asian and Pacific Coasts (APAC '13)*, Bali, Indonesia, September 2013.

- [10] L. Li, X. Wu, X. Xu, and B. Liu, "An empirical model for wind speed inversion by HFSWR," *Geomatics and Information Science of Wuhan University*, vol. 37, no. 9, pp. 1096–1099, 2012.
- [11] D. Green, E. Gill, and W. Huang, "An inversion method for extraction of wind speed from high-frequency ground-wave radar oceanic Backscatter," *IEEE Transactions on Geoscience and Remote Sensing*, vol. 47, no. 10, article 8, pp. 3338–3346, 2009.
- [12] R. H. Stewart and J. R. Barnum, "Radio measurements of oceanic winds at long ranges: an evaluation," *Radio Science*, vol. 10, no. 10, pp. 853–857, 1975.
- [13] T. E. Mathew and M. C. Deo, "Inverse estimation of wind from the waves measured by high-frequency radar," *International Journal of Remote Sensing*, vol. 33, no. 10, pp. 2985–3003, 2012.
- [14] W. Shen, *An algorithm to derive wind speed and direction as well as ocean wave directional spectra from HF radar backscatter measurements based on neural network [Ph.D. thesis]*, Universität Hamburg, 2011.
- [15] S. Haykin, *Neural Networks: A Comprehensive Foundation*, MacMillan, New York, NY, USA, 1994.
- [16] D. E. Rumelhart, G. E. Hinton, and R. J. Williams, "Learning internal representations by error propagation," in *Parallel Distributed Processing: Explorations in the Microstructure of Cognition*, vol. 1, pp. 318–362, MIT Press, Boston, Mass, USA, 1986.
- [17] F. D. Foresee and M. T. Hagan, "Gauss-Newton approximation to Bayesian learning," in *Proceedings of the IEEE International Conference on Neural Networks*, vol. 3, pp. 1930–1935, IEEE, Houston, Tex, USA, June 1997.
- [18] D. J. MacKay, "A practical Bayesian framework for backpropagation networks," *Neural Computation*, vol. 4, no. 3, pp. 448–472, 1992.
- [19] H. Roarty, C. Evans, S. Glenn, and H. Zhou, "Evaluation of algorithms for wave height measurements with high frequency radar," in *Proceedings of the IEEE/OES 11th Current, Waves and Turbulence Measurement (CWTM '15)*, pp. 1–4, March 2015.
- [20] B.-Y. Wen, Z.-L. Li, H. Zhou et al., "Sea surface currents detection at the eastern china sea by HF ground wave radar OSMAR-S," *Acta Electronica Sinica*, vol. 37, no. 12, pp. 2778–2782, 2009.
- [21] H. Zhou, H. Roarty, and B. Wen, "Wave extraction with portable high-frequency surface wave radar OSMAR-S," *Journal of Ocean University of China*, vol. 13, no. 6, pp. 957–963, 2014.
- [22] H. Zhou, H. Roarty, and B. Wen, "Wave height measurement in the Taiwan Strait with a portable high frequency surface wave radar," *Acta Oceanologica Sinica*, vol. 34, no. 1, pp. 73–78, 2015.

## Research Article

# A New Method of Wave Mapping with HF Radar

Lijie Jin, Biyang Wen, and Hao Zhou

Electronic Information School, Wuhan University, Wuhan 430072, China

Correspondence should be addressed to Biyang Wen; bywen@whu.edu.cn

Received 24 March 2016; Revised 2 June 2016; Accepted 4 August 2016

Academic Editor: Björn Lund

Copyright © 2016 Lijie Jin et al. This is an open access article distributed under the Creative Commons Attribution License, which permits unrestricted use, distribution, and reproduction in any medium, provided the original work is properly cited.

Study of wave height inversion with High-Frequency Surface Wave Radars (HFSWRs) has been going on for more than 40 years. Various wave inversion methods have been proposed, and HFSWRs have achieved great success in local wave measurements. However, the method of wave mapping is still under development, especially for the broad-beam HF radars. Existing methods of wave mapping are based on narrow-beam radar with beamforming. This paper introduces a way of wave height inversion, using the ratio of the second-harmonic peak (SHP) to the Bragg peak (RSB). A new wave mapping method is proposed, which can be used in both narrow and broad-beam radars, according to the way of wave inversion based on the RSB. In addition, radar wave measurements at the buoy position are compared with the *in situ* buoy, which show a good agreement. At last, the results of wave mapping on the two-hour timescale are given.

## 1. Introduction

Extraction of wave height with HFSWRs was started since Barrick [1] deduced the second-order integral equation, relating radar sea echo to the ocean wave spectrum. Various methods of wave height inversion have been proposed, for example, Barrick [2], Wyatt [3], Howell and Walsh [4], Hisaki [5], and so forth. Except for these proposed wave height inversion methods, many research results related to the wave height are also displayed, for example, Gill and Walsh [6], Huang et al. [7], Wyatt [8, 9], and Tian et al. [10]. All of them are proved to be feasible in local wave measurements. However, the method of wave mapping, which can display the wave measurements of a large sea area at the same time, is still under development, especially for the broad-beam HF radars. Obtaining the wave maps is helpful in maritime research activities and offshore operations and so forth. Existing methods of wave mapping are based on narrow-beam radar, both the sky wave radar [11] and the ground wave radar [12]. Wave maps can be achieved every 3–6 h by beamforming and scanning in azimuth, with the Wide Aperture Research Facility (WARF) skywave radar [11]; phased array radar named Wellen Radar (WERA) is used to map the ocean wave height by digital beam forming (DBF) [12]. Both of the radars have a large aperture, which brings

some disadvantages: (1) the radar site requiring a sufficiently narrow and flat coast, which sometimes cannot be satisfied; (2) difficulties in installation and erection; and (3) high costs in operating and maintenance.

A wave height inversion method is introduced, based on the ratios of the SHPs to the Bragg peaks [13]. The Bragg peaks are caused by the waves moving toward or away from radar, with fixed wavenumber  $2k_0$  ( $k_0$  being the radar wavenumber). Surface current and wind direction information can be relatively obtained from the Bragg peaks. The second-order echo is observed from either side of the Bragg lines, and important wave information can be derived from this part of the spectrum [2]. Furthermore, some research work has been focused on the second-order echo. Studies by Wyatt [14] and Kingsley et al. [15] suggested that at high sea states this second-order part of the spectrum might change in a way that was not consistent with current theory. Ivonin et al. [16] studied the singularities (including  $f_B$ ,  $\sqrt{2}f_B$ , and  $2^{3/4}f_B$ ) in Barrick's formula and showed that SHPs were primarily due to the waves propagating parallel to the radar beam, with the wavenumber  $k_0$ . Besides, Zhang et al. [17] observed that the peak at  $\sqrt{2}f_B$  was much stronger than the surrounding spectrum and then derived another expression for the SHPs by a boundary perturbation method. Although these theories of SHPs may need further improvement, they are instructive

for potential applications on sea state extraction using these peaks other than the conventional second-order spectral continuum.

In this letter, a new wave mapping method is proposed, according to the way of wave inversion based on the RSB [13]. With the measured antenna patterns, this new method of wave mapping can be used in both narrow and broad-beam HF radars. The azimuth range of wave mapping is about 180 degrees with ground-based radar and 360 degrees with drilling platform. A broad-beam radar with compact cross-loop/monopole antennas is used here, which can receive the sea echo from different azimuths. When currents exist, the first-order spectrum will be broadened. The Bragg peaks from different Directions of Arrivals (DOAs) will be dispersed. Multiple signal classification (MUSIC) [18] is used to estimate DOAs of the Bragg peaks and SHPs. Azimuth of the wave height can be obtained by calculating the Bragg peak's DOA. With the colocated antennas, both the measured and ideal antenna patterns can be used in wave mapping, and measured antenna patterns are used here in MUSIC-based direction finding.

An experiment conducted during 2014 in Fujian Province, China, is introduced in Section 2. Section 3 describes the details of the wave mapping method with broad-beam HF radar. Section 4 shows the results of wave mapping and the comparisons between radar wave measurements and the *in situ* data. Section 5 is dedicated to the summary.

## 2. Description of Experiment

From September to October in 2014, an experiment was conducted in Fujian Province, China. The radar used is the monostatic HFSWR named Ocean State Measuring and Analyzing Radar type SD (OSMAR-SD) [19] with compact cross-loop/monopole antennas. OSMAR-SD is designed by Wuhan University of China, which is mainly used for sea state monitoring. The Frequency-Modulated Interrupted Continuous-Wave (FMICW) is used with the bandwidth of 60 KHz and the period of 0.27 s; therefore, the range resolution of the radar is 2.5 km.

The radar site, namely, PTAN ( $25^{\circ}28.3'N$ ,  $119^{\circ}47.6'E$ ), is shown in Figure 1, with two buoys. Buoy A ( $25^{\circ}28.4'N$ ,  $119^{\circ}51.8'E$ ) is about 7.3 km far from PTAN, and the azimuth is 74 degrees (the north is 0 degrees); Buoy B ( $25^{\circ}23.8'N$ ,  $119^{\circ}55.8'E$ ) is about 15.3 km, and the azimuth is 116 degrees.

## 3. Method

*3.1. The Relationship between the RSB and Significant Wave Height.* The difference of the second-harmonic peak and the Bragg peak is constant  $\Delta f = 0.414 f_B$  ( $f_B$  denotes the Bragg frequency) in Doppler domain. The ratio of the second-harmonic peak to the Bragg peak (RSB)  $r$  is given by

$$r = 10 \log_{10} \left( \frac{P_{\text{SHP}}}{P_B} \right), \quad (1)$$

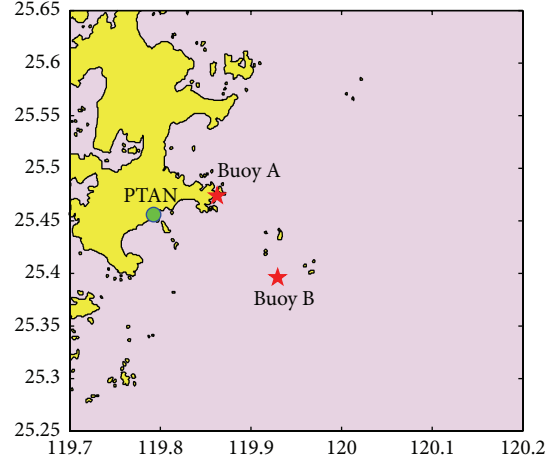


FIGURE 1: Geographic map of the observation system. PTAN is the radar operating at 13.5 MHz. Buoy A and Buoy B are the two buoys located in the sea area within radar detection range, 7.3 km and 15.3 km far from the radar, respectively.

where  $P_{\text{SHP}}$ ,  $P_B$  denote the power of the SHP and the Bragg peak, respectively. After observing the sea echo under different sea states, shown in Figure 2, the different performance of the SHP and the Bragg peak can be summarized as follows:

- (1) Under the low sea state, Figure 2(a),  $H_s = 1.0$  m (which denotes the significant wave height measured by the buoy), the second-order spectrum is not obvious, almost drowned in the noise, while the first-order spectrum is obvious. The RSB is great, about  $-21.31$  dB.
- (2) Figure 2(b) shows that with sea state increasing to the level  $H_s = 2.5$  m, the power of the second-order spectrum becomes stronger; however, the power of the first-order spectrum changes only a little, because the Bragg waves are easier to reach saturation. The RSB is about  $-17.55$  dB.
- (3) Under the high sea state, Figure 2(c),  $H_s = 3.9$  m, the power of the second-order spectrum keeps increasing to a certain degree; meanwhile, the power of the first-order spectrum changes to be smaller. The RSB is about  $-14.86$  dB.

According to the observations of the SHPs and Bragg peaks, it is easy to find that the RSB is closely related to the sea state or significant wave height. That is to say, the RSB changes with the increase of significant wave height. Besides, estimating the DOAs of the Bragg peaks and corresponding SHPs marked in Figures 2(a), 2(b), and 2(c), we can find that the Bragg peak and corresponding SHP come from almost the same direction, shown in Figure 2(d). This conclusion can be certified in [13], which analysed the data from OSMAR-S in Fujian Province during 2013. MUSIC algorithm is adopted in the data analysis of the two experiments. The difference is that measured antenna patterns are used in this paper and ideal antenna patterns in [13]. In the following section, a linear model of the RSB and significant wave height will be

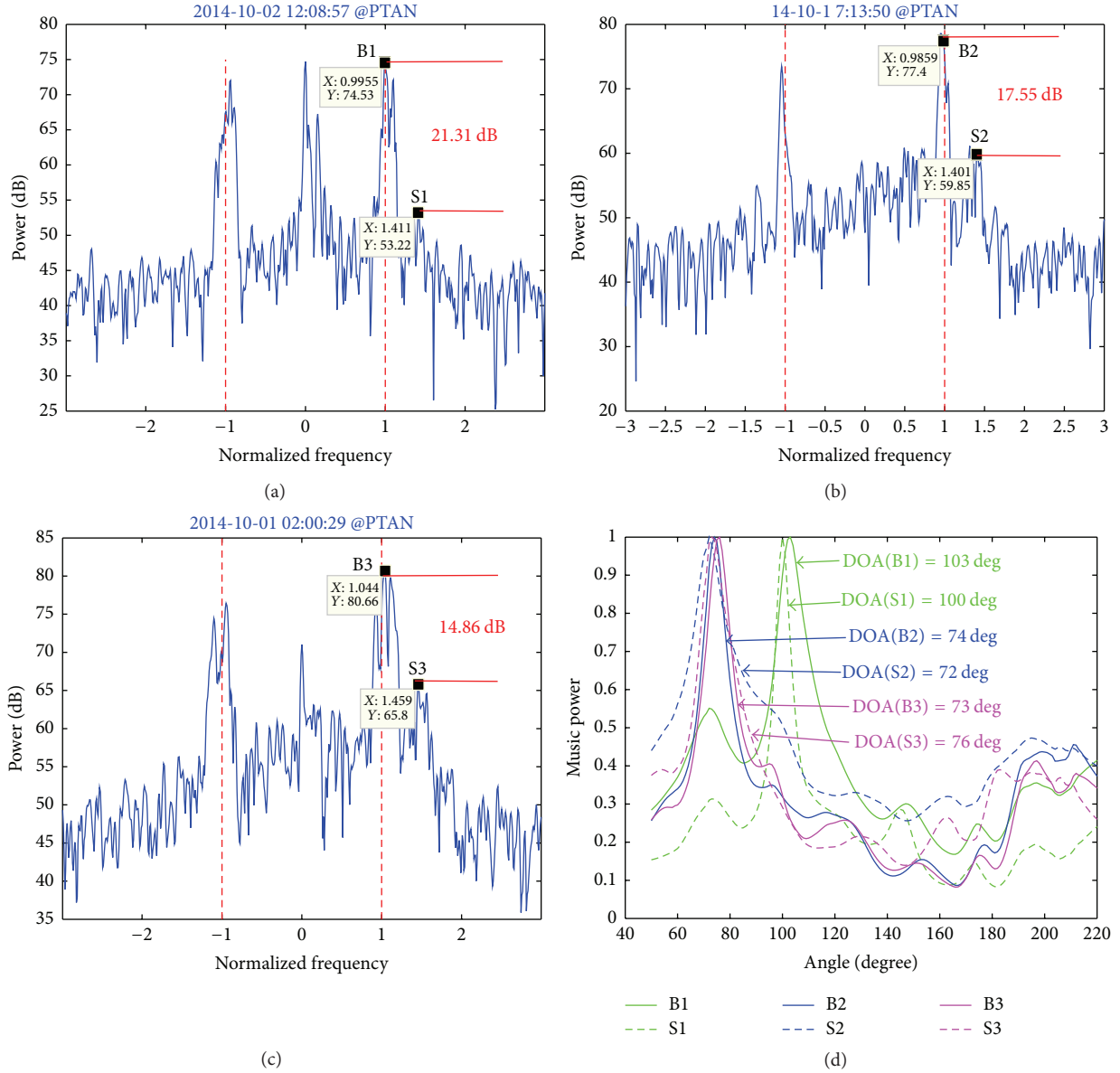


FIGURE 2: Observations of the RSB under different sea state, (a) the low sea state, (b) the normal sea state, (c) the high sea state, and (d) DOAs of the Bragg peaks and corresponding SHPs, estimated with MUSIC.

established, from which radar wave measurements can be extracted.

**3.2. The Linear Model of the RSB and Significant Wave Height by Fitting to Wave Buoy Data.** Both radar-measured data and wave buoy data are necessary, in order to get the linear model of  $r$  and  $H_s$ , where  $r$  is the RSB and  $H_s$  denotes the significant wave height. The content of this section is focused on obtaining the RSBs from radar-measured data.

With broad-beam radar, the first-order spectrum of sea echo becomes broader, including many Bragg peaks from different DOAs. The Doppler spectrum of a fixed range-bin contains many first-order peaks and corresponding SHPs. Consisted of one first-order peak and the corresponding SHP, the couple has two characteristics: the difference of their

Doppler shifts being constant  $\Delta f = 0.414f_B$  and coming from almost the same direction. According to the characteristics, the couples can be selected from the Doppler spectrum.

A wave height may correspond to a range of the RSBs, because single RSB has a certain degree of randomness; however, the median of the RSBs is highly related to the buoy wave height. Figure 3 shows the linear model of  $r$  and  $H_s$  from different directions:

$$\begin{aligned}
 r &= -23.5 + 3.10H_s, \\
 \text{DOA} &= 70 \text{ deg}, \\
 r &= -25.8 + 2.85H_s, \\
 \text{DOA} &= 120 \text{ deg}.
 \end{aligned} \tag{2}$$

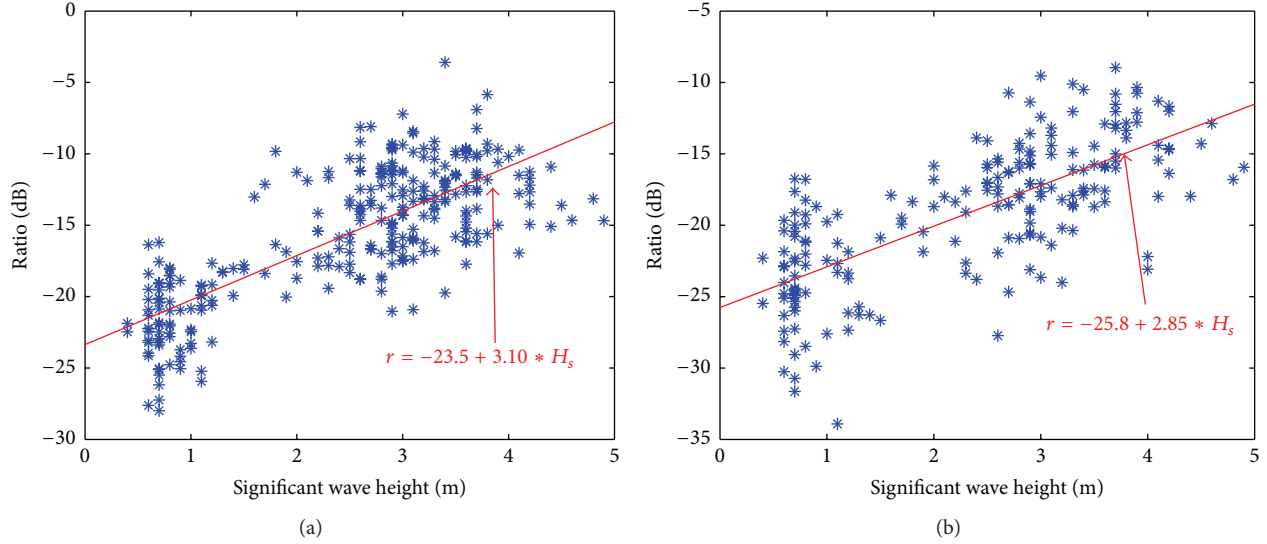


FIGURE 3: Ratios of the SHPs to the Bragg peaks fitted to the wave buoy data: (a) from 70 degrees; (b) from 120 degrees.

The difference among different directions is not great, and the final linear model can be written as

$$r = -A + B \cdot H_s, \quad (3)$$

where  $A$  and  $B$  are two parameters of the linear model, which may change in different sea areas. In this experiment, the values of  $A$  and  $B$  are 25 and 3.0, respectively. Based on this linear model, the method of extracting significant wave height is given by

$$H_{\text{radar}} = \frac{(r + A)}{B}, \quad (4)$$

where  $r$  denotes the RSB and  $H_{\text{radar}}$  is the significant wave height measured by radar. Notice that, after some more research work about the Bragg peak and the SHP, we find that the Bragg peak get saturated when sea state increases to the level  $H_s \approx 2$  m, and the SHP is  $H_s \approx 4$  m, with the radar frequency 13 MHz. When the SHP is unsaturated, the measured  $H_{\text{radar}}$  is reliable with the linear model. A higher sea state with  $H_s > 5$  m requires a lower radar frequency.

**3.3. Detail Steps of Wave Mapping.** In the above section, the method of wave extraction based on the linear model is introduced. The wave heights measured by radar contain both the range and azimuth information, related to the Bragg peaks.

To map the ocean wave height, the sea area within radar detection range is divided into a series of two-dimensional space grids. The range resolution is set to 2.5 km, according to the range resolution of radar. The azimuth resolution is 10 degrees, considering the bearing error in MUSIC-based direction finding, associated with the signal noise ratio [20]. Besides, the cumulative number of each grid also needs to be considered. The higher azimuth resolution (e.g., 6 or 3 degrees) leads to the less cumulative number, which is not conducive to the robustness of wave extraction.

Considering changes of the sea state, two hours' radar data is used in each wave map. The wave map can be obtained by the following steps.

*Step 1.* Put all the measured wave heights into the two-dimensional space grids, according to the information of range and azimuth.

*Step 2.* Calculate the median of wave heights within one certain grid and regard it as the wave height of this grid.

*Step 3.* If the cumulative number of the grid is less than 3, replace the value with the average wave height of nearby sea area. With few RSBs, the wave height measured from the linear model is not robust, because single RSB has a certain degree of randomness. Therefore, it is necessary to have enough cumulative number for the robust wave measurement.

*Step 4.* Interpolate the wave map in two-dimensional space with the linear interpolation method [21].

## 4. Results

In this section, comparisons of the local estimated wave heights versus the buoy data are given. Besides, the results of wave mapping are presented. Two parts of the radar-measured data are selected as examples for wave mapping, 21:00 to 23:00 Sep 27 and 17:30 to 19:30 Oct 9, 2014; the significant wave heights from Buoy B are about 1.8 m and 3.2 m, respectively.

As shown in Figure 4, two-hourly wave measurements from radar are compared with the *in situ* buoys. The radar data used is about 20 days from 10:00 Sep 25 to 8:00 Oct 15, 2014. Both the two local wave measurements show good agreements versus the two buoys, with correlation above 0.8. Except for the similarity, there are some differences between

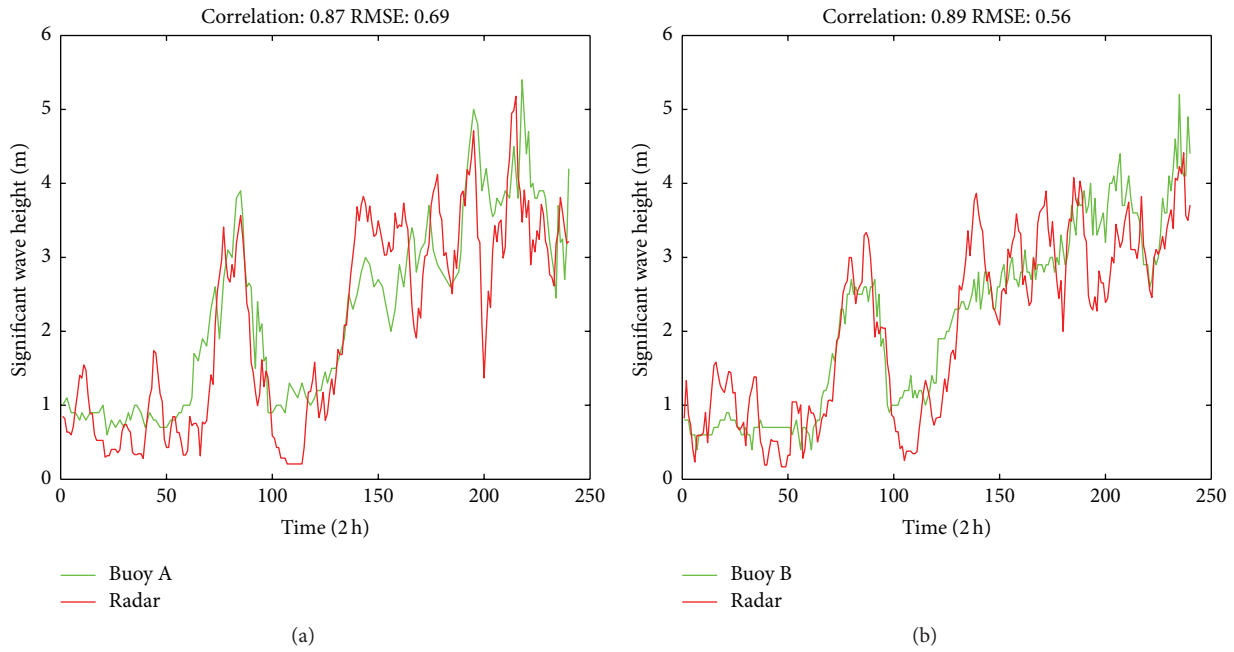


FIGURE 4: The local wave measurements between radar and buoys, time relative to 10:00 Sep 25, 2014. (a) Buoy A; (b) Buoy B.

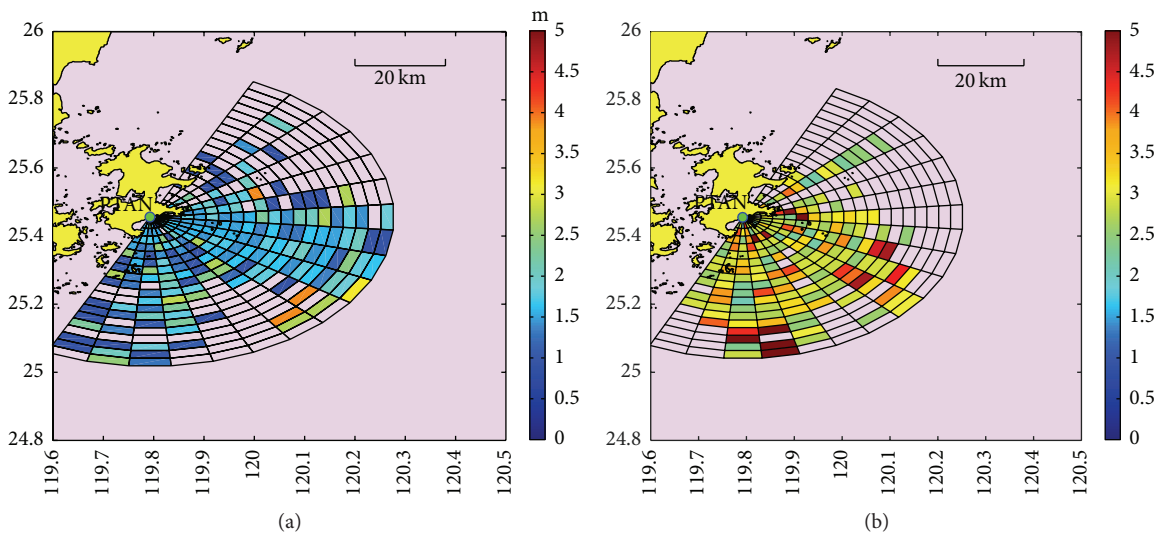


FIGURE 5: The initial wave maps, the sea area is divided into a series of two-dimensional space grids with the range resolution 2.5 km and the azimuth 10 degrees. (a) 21:00 to 23:00 Sep 27, 2014; (b) 17:30 to 19:30 Oct 9, 2014.

Figures 4(a) and 4(b). The comparison from Buoy B performs better than that from Buoy A, with a smaller Root Mean Square Error (RMSE) 0.56 m. A small part of the radar wave measurements is underestimated in Figure 4(a), because the corresponding cumulative number is only one or two. And it may be due to the location of Buoy A, which is much closer to the coast. The two comparisons with the *in situ* buoys indicate that enough cumulative number is important to obtain the robust wave measurements.

Figure 5 shows the initial wave height maps. The azimuth ranges from 20 to 200 degrees with resolution of 10 degrees. The distance ranges from the first to the eighteenth range-bin

with resolution of 2.5 km. Some of the two-dimensional space grids are empty without wave heights, mainly distributed in the range from 20 to 70 degrees. A possible reason is the shielding effect of the island, which may attenuate the signal passing through.

Figure 6 displays the wave maps after replacement, which become more gentle compared with the initial wave maps, since most of the overestimated or underestimated wave heights are replaced. Comparing the two wave maps in Figure 6, sea state of Figure 6(a) is lower than that of Figure 6(b). The coverage efficiency of offshore within 20 km is almost the same between the two wave maps. However, it is

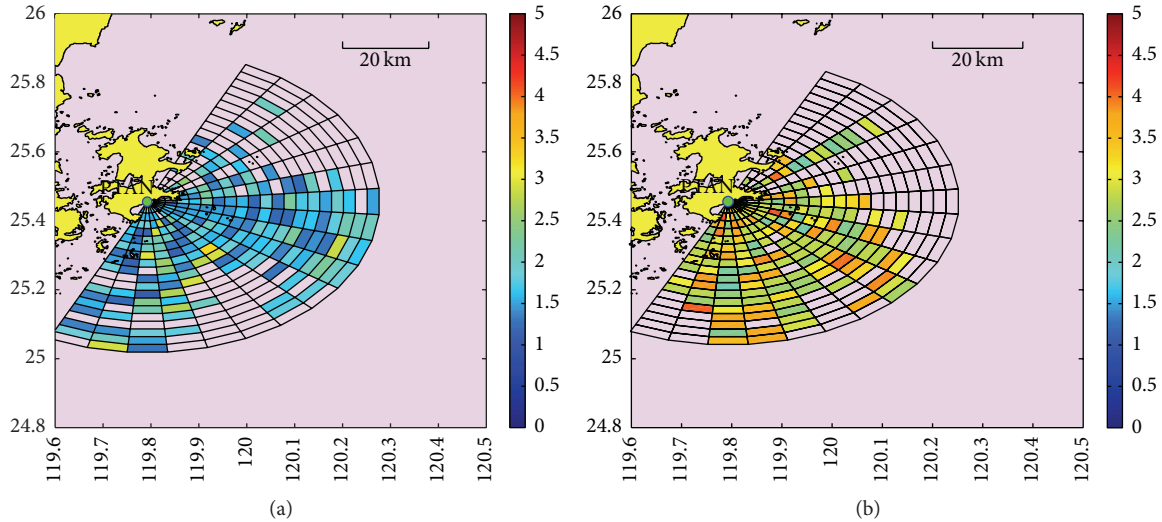


FIGURE 6: The wave maps after replacement. (a) 21:00 to 23:00 Sep 27, 2014; (b) 17:30 to 19:30 Oct 9, 2014.

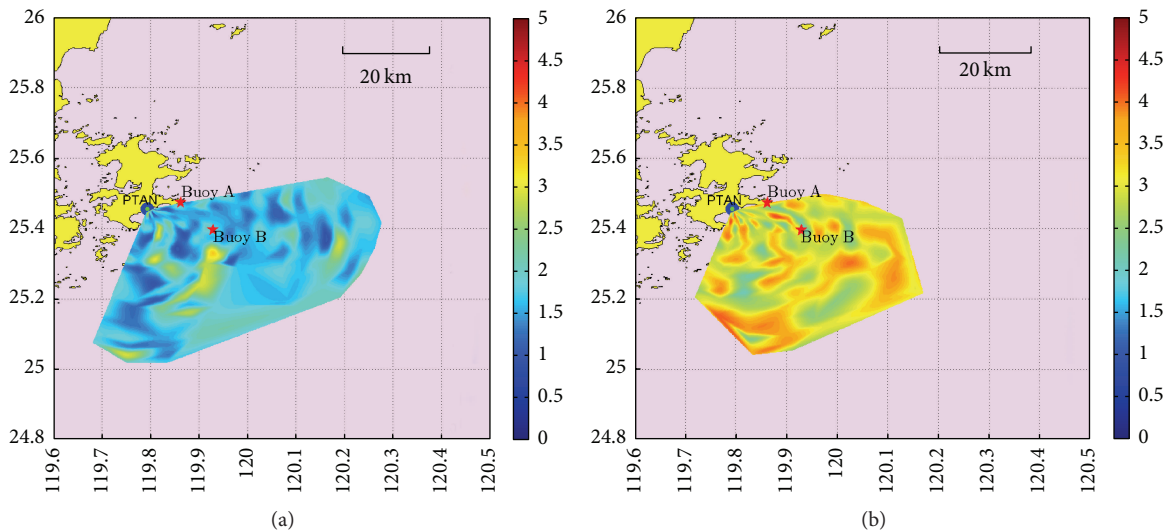


FIGURE 7: The wave maps after interpolating in two-dimensional space. (a) 21:00 to 23:00 Sep 27, 2014; (b) 17:30 to 19:30 Oct 9, 2014.

different in the further sea areas, which may be due to higher propagation losses in rough seas.

In Figure 7, the final wave maps are obtained after interpolating. The difference between most of the measured wave heights and the *in situ* buoy data is less than 0.5 m, shown in Figure 6. However, there are still a few overestimated or underestimated wave heights in the wave maps after replacement, and the final wave maps may not be so continuous. In addition, the locations of two buoys are marked. Buoy A corresponds to the azimuth of 70 degrees and the third range-bin, while Buoy B is 120 degrees and the sixth range-bin.

## 5. Summary

In this letter, a method of wave height inversion is introduced, using the linear model of RSB and significant wave height.

Based on this method, a new approach to wave mapping is proposed. In this method of wave mapping, MUSIC is used for direction finding, rather than digital beam forming. Therefore, it can be applied in both broad and narrow-beam radars. There is good agreement in comparisons of the local wave measurements from radar and buoys about 20 days, with correlation above 0.8 and RMSE about 0.6 m, which prove the effectiveness of this wave mapping method. Though the final wave maps perform well compared with buoys wave data, there are still some problems to be solved: (1) the linear model of the RSB and significant wave height ( $r = -A + B \cdot H_s$ ) is obtained by fitting to wave buoy data. A new way to obtain the wave data instead of the buoys is necessary, considering the applicability of the wave mapping method. (2) In order to get accurate wave maps, cumulative number of the space lattice should be enough, which is proportional to the timescale of radar-measured data used in each wave

map. Nevertheless, this method still keeps the potentiality to achieve wave maps with both the narrow and broad beam HF radars. Ongoing work will focus on improving the accuracy and robustness of this wave mapping method: for example, (1) conduct more experiments in different places, under different sea states; (2) find a more suitable model instead of the linear model in connecting RSB with the significant wave height; and (3) make a comparison between the measured and ideal antenna patterns in wave mapping.

## Competing Interests

The authors declare that they have no competing interests.

## Acknowledgments

The authors would like to thank the Fujian Marine Bureau for the buoys data provided.

## References

- [1] D. Barrick, "Remote sensing of sea state by radar," in *Proceedings of the IEEE International Conference on Engineering in the Ocean Environment (Ocean '72)*, pp. 186–192, Newport, RI, USA, September 1972.
- [2] D. E. Barrick, "Extraction of wave parameters from measured hf radar sea-echo doppler spectra," *Radio Science*, vol. 12, no. 3, pp. 415–424, 1977.
- [3] L. R. Wyatt, "A relaxation method for integral inversion applied to HF radar measurement of the ocean wave directional spectrum," *International Journal of Remote Sensing*, vol. 11, no. 8, pp. 1481–1494, 1990.
- [4] R. Howell and J. Walsh, "Measurement of ocean wave spectra using narrow-beam HF radar," *IEEE Journal of Oceanic Engineering*, vol. 18, no. 3, pp. 296–305, 1993.
- [5] Y. Hisaki, "Ocean wave directional spectra estimation from an HF ocean radar with a single antenna array: methodology," *Journal of Atmospheric and Oceanic Technology*, vol. 23, no. 2, pp. 268–286, 2006.
- [6] E. W. Gill and J. Walsh, "Extraction of ocean wave parameters from HF backscatter received by a four-element array: analysis and application," *IEEE Journal of Oceanic Engineering*, vol. 17, no. 4, pp. 376–386, 1992.
- [7] W. Huang, S.-C. Wu, E. Gill, B.-Y. Wen, and J.-C. Hou, "HF radar wave and wind measurement over the Eastern China Sea," *IEEE Transactions on Geoscience and Remote Sensing*, vol. 40, no. 9, pp. 1950–1955, 2002.
- [8] L. R. Wyatt and J. J. Green, "Measuring high and low waves with HF radar," in *Proceedings of the IEEE Bremen: Balancing Technology with Future Needs (OCEANS '09)*, pp. 1–5, Bremen, Germany, May 2009.
- [9] L. R. Wyatt, "Significant waveheight measurement with h.f. radar," *International Journal of Remote Sensing*, vol. 9, no. 6, pp. 1087–1095, 1988.
- [10] Y.-W. Tian, B.-Y. Wen, and H. Zhou, "Measurement of high and low waves using dual-frequency broad-beam HF radar," *IEEE Geoscience and Remote Sensing Letters*, vol. 11, no. 9, pp. 1599–1603, 2014.
- [11] J. W. Maresca Jr., T. M. Georges, C. T. Carlson, and J. P. Riley, "Two tests of real-time ocean wave-height mapping with hf skywave radar," *IEEE Journal of Oceanic Engineering*, vol. 11, no. 2, pp. 180–186, 1986.
- [12] L. R. Wyatt, "Wave mapping with HF radar," in *Proceedings of the IEEE/OES 10th Working Conference on Current, Waves and Turbulence Measurement (CWTM '11)*, pp. 25–30, Monterey, Calif, USA, March 2011.
- [13] H. Zhou and B.-Y. Wen, "Observations of the second-harmonic peaks from the sea surface with high-frequency radars," *IEEE Geoscience and Remote Sensing Letters*, vol. 11, no. 10, pp. 1682–1686, 2014.
- [14] L. Wyatt, "The measurement of the ocean wave directional spectrum from hf radar doppler spectra," *Radio Science*, vol. 21, no. 3, pp. 473–485, 1986.
- [15] S. P. Kingsley, A. Matoses, and L. R. Wyatt, "Analysis of second order HF radar sea spectra recorded in storm conditions," in *Proceedings of the IEEE OCEANS '98 Conference*, vol. 1, pp. 459–462, IEEE, Nice, France, 1998.
- [16] D. V. Ivonin, V. I. Shrira, and P. Broche, "On the singular nature of the second-order peaks in HF radar sea echo," *IEEE Journal of Oceanic Engineering*, vol. 31, no. 4, pp. 751–767, 2006.
- [17] S.-S. Zhang, B.-Y. Wen, and H. Zhou, "Analysis of the higher order Bragg scatter in HF radar," *Journal of Electromagnetic Waves and Applications*, vol. 27, no. 4, pp. 507–517, 2013.
- [18] T. De Paolo, T. Cook, and E. Terrill, "Properties of HF RADAR compact antenna arrays and their effect on the MUSIC algorithm," in *Proceedings of the Oceans*, pp. 1–10, IEEE, Vancouver, Canada, October 2007.
- [19] Y. Tian, B. Wen, J. Tan, K. Li, Z. Yan, and J. Yang, "A new fully-digital HF radar system for oceanographical remote sensing," *IEICE Electronics Express*, vol. 10, no. 14, 2013.
- [20] T. Paolo, T. Cook, and E. Terrill, "Properties of HF radar compact antenna arrays and their effect on the MUSIC algorithm," in *Proceedings of the OCEANS 2007*, pp. 1–10, IEEE, Vancouver, Canada, 2007.
- [21] D. Watson, *Contouring: A Guide to the Analysis and Display of Spatial Data*, Pergamon Press, Oxford, UK, 1992.

## Research Article

# Study of Ocean Waves Measured by Collocated HH and VV Polarized X-Band Marine Radars

Zhongbiao Chen,<sup>1</sup> Yijun He,<sup>1</sup> and Wankang Yang<sup>2</sup>

<sup>1</sup>*School of Marine Sciences, Jiangsu Engineering Technology Research Center of Marine Environment Detection, Nanjing University of Information Science and Technology, Jiangsu 210044, China*

<sup>2</sup>*The Second Institute of Oceanography, SOA, Hangzhou 310112, China*

Correspondence should be addressed to Yijun He; [yjhe@nuist.edu.cn](mailto:yjhe@nuist.edu.cn)

Received 4 April 2016; Revised 2 June 2016; Accepted 16 June 2016

Academic Editor: Björn Lund

Copyright © 2016 Zhongbiao Chen et al. This is an open access article distributed under the Creative Commons Attribution License, which permits unrestricted use, distribution, and reproduction in any medium, provided the original work is properly cited.

The significant wave height (SWH) retrieved from collocated HH and VV polarized X-band marine radars under different sea states is studied. The SWH are retrieved from different principal components of X-band marine radar image sequence. As compared with the SWH measured by a buoy, the root-mean-square errors of the SWH are 0.32–0.45 m for VV polarization, and they are 0.37–0.60 m for HH polarization. At the wind speeds of 0–5 m/s, the SWH can be derived from VV polarized radar images, while the backscatter of HH polarized radar is too weak to contain wave signals at very low wind speeds (~0–3 m/s). At the wind speeds of 5–18 m/s, the SWH retrieved from VV polarization coincide well with the SWH measured by the buoy, while the SWH retrieved from HH polarization correspond with the changes of the wind speed. At the wind speeds of 18–26 m/s, the influence of wave breaking on HH polarization is more important than that on VV polarization. This indicates that the imaging mechanisms of HH polarized X-band marine radar are different from those of VV polarized X-band marine radar.

## 1. Introduction

Ocean waves are important to marine activities and scientific studies, such as ocean engineering, coastal environment protection, and upper ocean dynamics. In situ measurements such as buoys have been operationally used to measure ocean waves since the mid-1970s, but they are expensive to deploy and maintenance [1]. In recent years, remote sensing technologies such as satellite altimetry and high-frequency (HF) radar have been used to observe ocean waves [2], but the spatial resolutions of the altimeter and HF radar are about 5–7 km [3] and 0.3–3 km [4], which are not suitable to be used in nearshore area with inhomogeneous wave field. X-band marine radar has high spatial and temporal resolutions, and it has been used in the observation of sea surface wave [5, 6], current [7, 8], wind [9, 10], and bathymetry [11].

Conventional X-band marine radar operates with HH polarization under low grazing angles. Small wind-induced ripples on the sea surface cause Bragg scattering of the incident wave energy, and this scattering is in turn modulated

by the long gravity waves, leading to the “sea clutter” in the radar image [11]. At low grazing angles, non-Bragg scattering also contributes noticeably to the backscatter from sea surface, especially for horizontal polarization [12–15]. In addition, Trizna and Carlson [16] found that there were differences between the spatial texture of HH polarized radar image and that of VV polarized radar image and attributed them to different scattering mechanisms for HH and VV polarizations. Cui et al. [17] found that there were differences in the wave and current field retrieved from dual polarized X-band marine radar images, by using a widely used algorithm based on the three-dimensional fast Fourier transform (FFT), which has been shown to be applicable in homogeneous wave field [5, 6].

In coastal zones, the wave fields are nonhomogeneous due to the influences of wind, bathymetry, and tide. To inverse nonhomogeneous wave field from X-band marine radar image sequence, new algorithms based on wavelet transform [18] and empirical orthogonal function (EOF) have been proposed [19, 20]. In the EOF method, the SWH are



FIGURE 1: Map of the experimental site. The three red dots are the positions of X-band marine radars with HH and VV polarizations (R1 and R2) and the anemometer (A). The purple dashed circle denotes the observation area of the radars. The green star denotes the location of the buoy. The yellow arrow points to north. The colors of ocean water show the changes of bathymetry.

retrieved from different principal components of X-band marine radar image sequence [19, 20]. This paper aims to study the differences between HH and VV polarized X-band marine radars in the observation of coastal waves. The organization is as follows. The experiment and method are described in Section 2. The SWH inverted from different principal components of HH and VV polarized X-band marine radars are compared in Section 3. The influences of wind and wave on the imaging of HH and VV polarizations are further discussed in Section 4. Finally, the conclusion is given in Section 5.

## 2. Experiment and Method

**2.1. Experiment.** An experiment was carried out on Haitan Island of China, from December 25, 2014, to January 17, 2015. In the experiment, two X-band marine radars with HH and VV polarizations, an anemometer, and a pitch-and-roll wave buoy were used to observe the wave field simultaneously. The distances between the HH and VV polarized X-band marine radars were 10 m in horizontal and 1 m in vertical. The two radar systems and the anemometer were set up on the shore that about 15 m above the sea level and 15–25 m from the coastline. The wave buoy was moored 1000 m from the radar stations in the azimuth of  $60^\circ$ , as shown in Figures 1 and 2.

The configurations of the two X-band marine radars are shown in Table 1, and they are the same except the polarization and the antenna rotation speed. The difference between the antenna rotation periods of the two radars is 1.07 s. There were 32 or 64 images in a single radar image sequence, so the time difference between the radars was 34.2 s or 68.5 s, during which time the changes of the SWH were small. Therefore, the influence of the antenna rotation speeds on the SWH is ignored in this study.

Dedicated 40 MHz analogue to digital converter cards were used to record the radar backscatter from the sea surface and then converted them into gray-level images with a radial resolution of 3.75 m and an azimuthal resolution of about  $0.05^\circ$ . The measurement ranges of the X-band marine radars were about 3 km, and the fields of view of them were from  $0^\circ$  to  $240^\circ$  in azimuth (Figure 1). During the experiment, the HH and VV polarized radars worked every 7–20 minutes, and

TABLE 1: Configurations of the X-band marine radar systems.

Parameters	Value	
	HH	VV
Polarization	HH	VV
Antenna rotation speed	42 rot/min	24 rot/min
Radar frequency	9410 MHz $\pm$ 30 MHz	
Pulse width	70 ns	
Pulse repetition frequency	3000 Hz	
Transmit power	25 kW	
Gain	30.2 dB	
Beam width	1.2° in horizontal, 20.5° in vertical	
Antenna	2.4 m slotted waveguide antenna	

they operated for 552 hours and 550 hours, respectively. As an example, two collocated radar images recorded by them are shown in Figure 2, where the waves came from east and are refracted toward shore (e.g., the areas in the brown boxes).

The resolutions of the anemometer are 0.1 m/s for wind speed and  $0.1^\circ$  for wind direction. The sampling frequency of the anemometer was 1 Hz, and the wind speeds and directions were averaged every 10 minutes to reduce the influence of local turbulence. There were 559 hours of wind speeds and directions in the experiment, as shown in Figure 3(a). The wind speed varied from 1.3 m/s to 25.5 m/s, and the wind mainly came from northeast.

The buoy used in the experiment was the TRIAXYS™ mini directional wave buoy (<http://axystechnologies.com/products/triaxys-mini-directional-wave-buoy/>). It sampled the sea surface for 20 minutes every hour and then output the wave parameters, including the SWH, the peak wave direction, and the peak wave period. The measurement ranges and accuracies of the SWH are 20 m and 1%, and those of the peak wave direction are  $0\text{--}360^\circ$  and  $3^\circ$ , respectively. The diameter of the buoy is 0.72 m. Because of the malfunctions of the buoy, there were abnormal values (i.e.,  $\text{SWH} > 10$  m) and missing values in the observation. After excluding the abnormal values, there were 506 hours of wave parameters. Figure 3(b) shows the SWH and the peak wave direction measured by the buoy. The SWH varied from 0.2 m to 3.5 m, and the wave directions were mainly from northeast to east.

In addition, the correlation coefficient between the wind speed measured by the anemometer and the SWH measured by the buoy is 0.81, and Figures 3(a) and 3(b) indicate that the variation of the SWH was similar to that of the wind speed, except the hours when the SWH were less than about 1 m (i.e., the hours of 83–157 and 230–280); although there were deviations between the directions of wind and wave, the influence of wind on wave was important in the observation area.

**2.2. Method.** In this study, the SWH is retrieved from X-band marine radar image sequence by using the method based on EOF analysis [19]. X-band marine radar image sequence is firstly decomposed into different principal components, and then the SWH is estimated by a linear relationship:

$$\text{SWH} = A \cdot \text{std}(z_i) + B, \quad (1)$$

where  $z_i$  ( $i = 1, 2, \dots, n$ ) is one principal component,  $\text{std}(\cdot)$  is the standard deviation,  $n$  is the number of principal

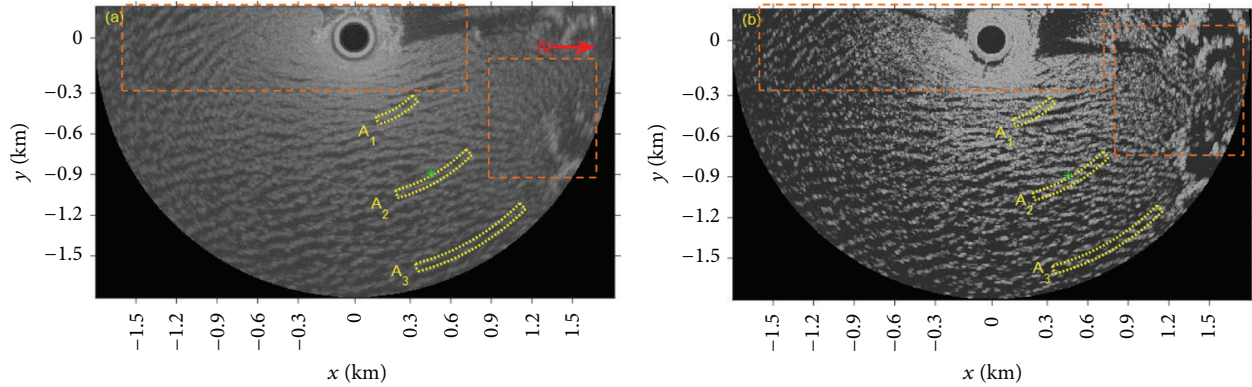


FIGURE 2: Two X-band marine radar images captured at 12:15 on December 27, 2014, by (a) VV polarized radar and (b) HH polarized radar. The red arrow points to the north direction. The yellow bins A1, A2, and A3 are the study regions. The green stars denote the location of the buoy. The brown boxes show the refraction of waves.

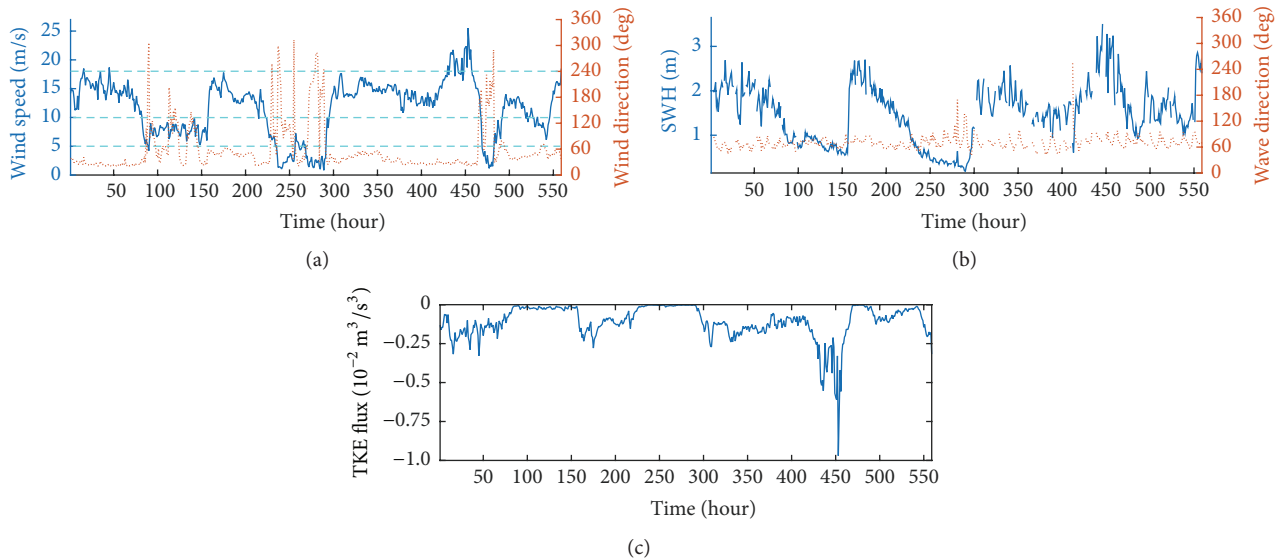


FIGURE 3: (a) The wind speed and wind direction measured by the anemometer, (b) the SWH and peak wave direction measured by the buoy, and (c) the TKE flux through the sea surface due to whitecapping. The cyan dashed lines in (a) denote the wind speeds of 5 m/s, 10 m/s, and 18 m/s.

components, and  $A$  and  $B$  are two coefficients that need to be calibrated by in situ measurements of the buoy. To compare with the SWH measured by the buoy, the SWH retrieved from X-band marine radar image sequences during the working time of the buoy are averaged every hour.

The coefficients  $A$  and  $B$  (Equation (1)) are calibrated as follows. First, the SWH measured by the buoy are divided into several groups with an interval of 0.5 m. Second, half of the SWH are randomly selected from each group to get the training dataset, while the other half of the SWH are used as the test dataset. Third, the training dataset and the SWH retrieved from simultaneous X-band marine radar image sequences are fitted to determine the coefficients, and the test dataset is used to evaluate the fitting.

To study the difference between the SWH retrieved from HH and VV polarized X-band marine radars, three study regions are selected, as shown in Figure 2. The azimuths

of Regions A1, A2, and A3 are  $135\text{--}165^\circ$ , and the ranges of them are  $450.0\text{--}510.0\text{ m}$ ,  $1012.5\text{--}1072.5\text{ m}$ , and  $1575.0\text{--}1635.0\text{ m}$ , respectively. Because there was only one buoy near Region A2, the SWH of Regions A1–A3 are all calibrated by using the buoy, although the SWH in different regions may be different. This may be reasonable for Region A3, but there may be large error for Region A1, because the water depths of Regions A2 and A3 were close (i.e., 25–30 m) while that of Region A1 was about 10–15 m.

Moreover, whitecapping often occurred on the sea surface, especially under high sea states. To study the influence of wave breaking on HH and VV polarizations, the turbulent kinematic energy (TKE) flux through the sea surface due to whitecap is estimated from the wind speeds by the model [21], as shown in Figure 3(c). The absolute values of the TKE fluxes at low wind speeds were smaller than those at moderate and high wind speeds, which indicate that whitecapping was

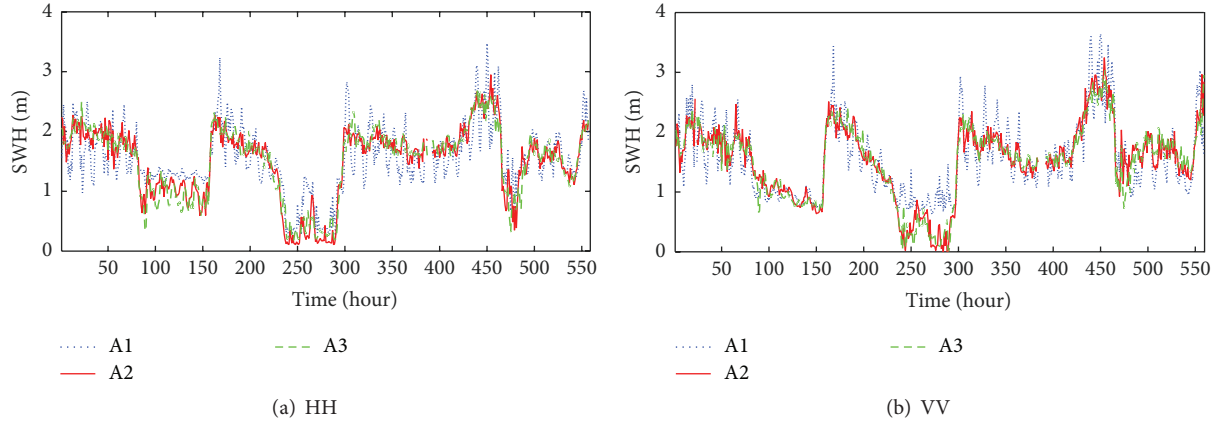


FIGURE 4: The SWH retrieved from the first principal component of X-band marine radars in Regions A1–A3. (a) HH polarization and (b) VV polarization.

TABLE 2: The calibration coefficients for the first principal component of HH and VV polarized X-band marine radars in Regions A1–A3.

	A (HH)	B (HH)	A (VV)	B (VV)
Region A1	0.0024	0.0470	0.0061	0.0697
Region A2	0.0020	-0.0604	0.0062	-0.2835
Region A3	0.0027	-0.0247	0.0078	-0.3000

active in this region under moderate and high sea states. It is noted that the model [21] is a parameterization of whitecapping, and the TKE flux is used here as a reference for the activeness of wave breaking, while the exact locations or areas of whitecapping cannot be obtained.

### 3. Result and Discussion

In this section, the SWH are retrieved from HH and VV polarized X-band marine radars and then compared with the SWH measured by the buoy and the wind speed measured by the anemometer. The spectra of different principal components are also analyzed.

**3.1. Validation of the SWH.** To retrieve the SWH from X-band marine radar image sequences by (1), the coefficients  $A$  and  $B$  are firstly calibrated. Take the first principal component as an example, the calibration coefficients for HH and VV polarizations are shown in Table 2, and the inversed SWH are shown in Figure 4. Although the SWH retrieved from X-band marine radar image sequences of different polarizations are close, there are some differences between them. For example, in the hours of 83–157, the SWH retrieved from HH polarization decreased suddenly and then fluctuated periodically (Figure 4(a)), while the SWH retrieved from VV polarization decreased gradually (Figure 4(b)). For both HH and VV polarizations, the SWH in Region A2 is close to that in Region A3, while the SWH in Region A1 shows an apparent period of about 12 hours. Because the semidiurnal tide is the major tidal constituent in the observation area [22], the

influence of tide on the SWH in Region A1 was important [23].

To evaluate the SWH retrieved from X-band marine radar image sequences, they are compared with the measurements of the buoy and the anemometer, as shown in Figure 5.

The root-mean-square error (RMSE) between the SWH measured by the buoy and those retrieved from different polarized radars is shown in Figure 5(a). The RMSE of the SWH retrieved from VV polarization are 0.32–0.45 m in Regions A1–A3, which are smaller than those retrieved from HH polarization (i.e., 0.37–0.60 m), except the 1–3 principal components in Region A1. For VV polarization, the RMSE in Regions A2 and A3 are close, which are larger than the RMSE in Region A1; for HH polarization, the RMSE increase from Region A3 to Region A1.

The correlation coefficients between the wind speed and the SWH retrieved from X-band marine radars are shown in Figure 5(b). For both HH and VV polarizations, the correlation coefficients decrease from offshore (Region A3) to nearshore (Region A1), because the influence of tide on waves increases as the waves propagate toward shore. There are differences between HH and VV polarizations. First, the changes of the correlation coefficients of VV polarization (i.e., 0.75–0.90) are smaller than those of HH polarization (i.e., 0.52–0.95) in Regions A1–A3. Second, the correlation coefficients maximize at the 1-2nd principal component for HH polarization, while they maximize at the 3-4th principal component for VV polarization. Therefore, the influences of wind on HH polarization are different from that on VV polarization, which coincides with previous studies [16].

**3.2. Comparison with the SWH Measured by the Buoy.** To study the differences between HH and VV polarizations under different sea states, the observations are divided into four sea states according to the wind speeds. Because the sea states change a little in a short time period, continuous observations are divided into the same dataset as far as possible (Figure 3(a)), as shown in Table 3.

The RMSE between the SWH measured by the buoy and those retrieved from different principal components of HH

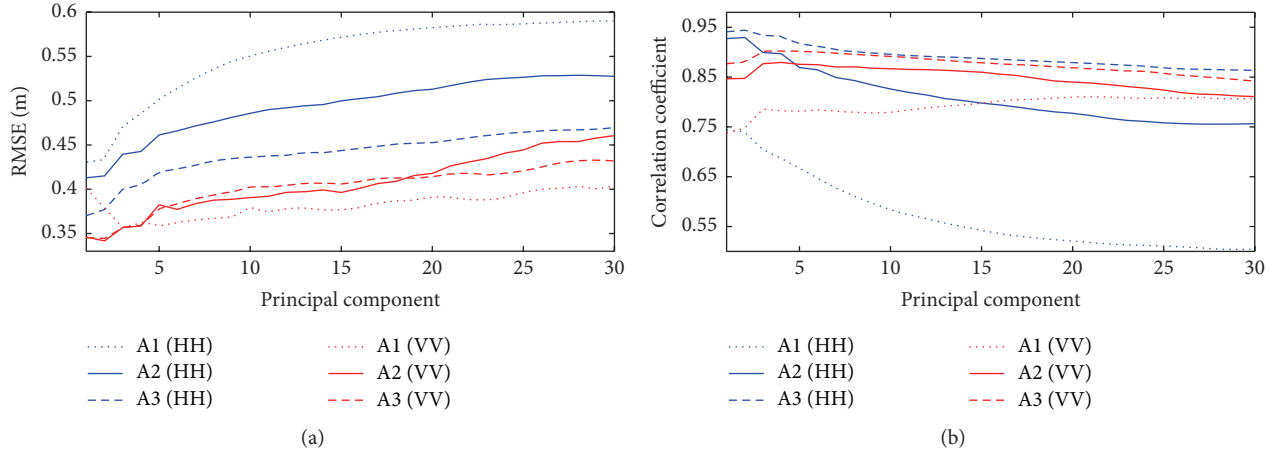


FIGURE 5: (a) The RMSE between the SWH measured by the buoy and those retrieved from different principal components of X-band marine radars, and (b) the correlation coefficients between the wind speed and the SWH retrieved from different principal components of X-band marine radars in Regions A1–A3.

TABLE 3: Division of the sea states.

Number	Sea states	Wind speed (m/s)	Time period (hour)
1	Low	$0 \leq u < 5$	235–291, 469–482
2	Low to moderate	$5 \leq u < 10$	83–157 1–82, 158–222,
3	Moderate to high	$10 \leq u < 18$	296–429, 458–467, 492–520
4	High	$18 \leq u < 26$	429–458

and VV polarized X-band marine radar image sequences are shown in Figure 6.

At the wind speeds of 0–5 m/s (Figure 6(a)), the RMSE of the 1–5th principal component of VV polarization are smaller than those of HH polarization in Regions A1–A3. The RMSE of the 6–30th principal component change irregularly, because the backscatter from sea surface is weak, and there is little information on ocean wave in these principal components.

At the wind speeds of 5–26 m/s (Figures 6(b)–6(d)), the variations of RMSE with the principal components are the same as that in Figure 5(a), but the RMSE are different for different sea states. The RMSE at the wind speeds of 10–18 m/s (Figure 6(c)) are smallest, that is, 0.27–0.37 m for VV polarization and 0.32–0.48 m for HH polarization. The RMSE at the wind speeds of 18–26 m/s (Figure 6(d)) are largest, that is, 0.42–0.82 m for VV polarization and 0.50–1.28 m for HH polarization. Because the whitecap was energetic at high wind speeds (Figure 3(c)), which have more important influence on HH polarization than on VV polarization [24], the large errors at high wind speeds are possibly caused by breaking waves.

TABLE 4: The correlation coefficients between the SWH measured by the buoy and those retrieved from first principal components of HH and VV polarized radars, and the correlation coefficients between the wind speeds and the retrieved SWH in Region A2 under different sea states.

	SWH measured by the buoy	Wind speed
SWH of HH (sea state 2)	0.27	0.63
SWH of VV (sea state 2)	0.73	0.27
SWH of HH (sea state 3)	0.51	0.67
SWH of VV (sea state 3)	0.66	0.52

Moreover, Table 4 lists the correlation coefficients between the SWH retrieved from the first principal component and the SWH measured by the buoy in Region A2 and the correlation coefficients between the retrieved SWH and the wind speeds. It shows that the SWH retrieved from HH polarized radar coincide better with the wind speed, while the SWH retrieved from VV polarized radar coincide better with the SWH measured by the buoy under sea states 2 and 3 (i.e., at the wind speeds of 5–18 m/s). Take the SWH in sea state 2 as an example. As shown in Figure 4, the SWH retrieved from HH polarization decreased suddenly in the hours of 83–157, which coincides well with the variation of the wind speed (Figure 3(a)); the SWH retrieved from VV polarization decreased gradually in the hours of 83–157, which is the same as the variation of the SWH measured by the buoy. Because the wave buoy measures only the waves with wavelengths greater than the diameter of the buoy (i.e., >0.72 m here) [25], while ripples or capillary waves are mainly caused by winds [26], long gravity waves are important to the imaging of VV polarization while ripples or capillary waves are more important to the imaging of HH polarized X-band marine radar.

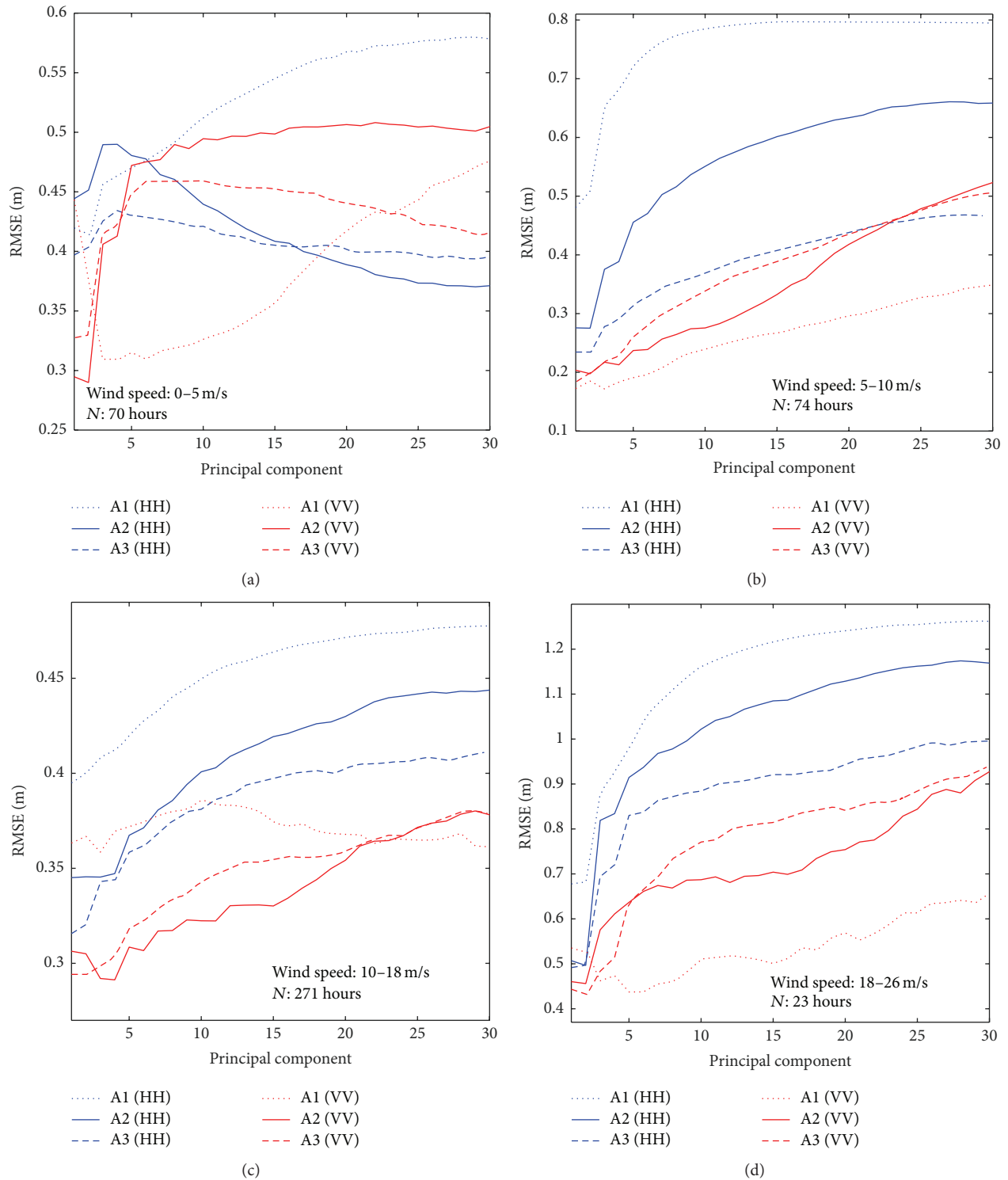
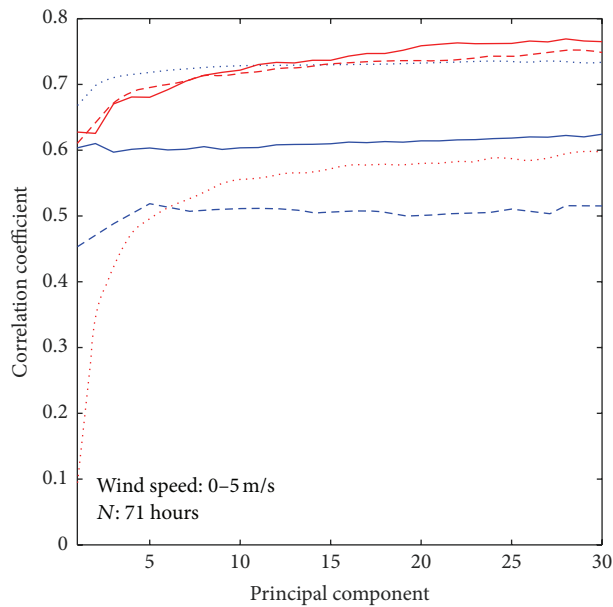


FIGURE 6: The RMSE between the SWH measured by the buoy and those retrieved from different principal components of X-band marine radars, at the wind speeds of (a) 0–5 m/s, (b) 5–10 m/s, (c) 10–18 m/s, and (d) 18–26 m/s. The number “ $N$ ” at the bottom of each panel denotes the number of hours used in the statistics.

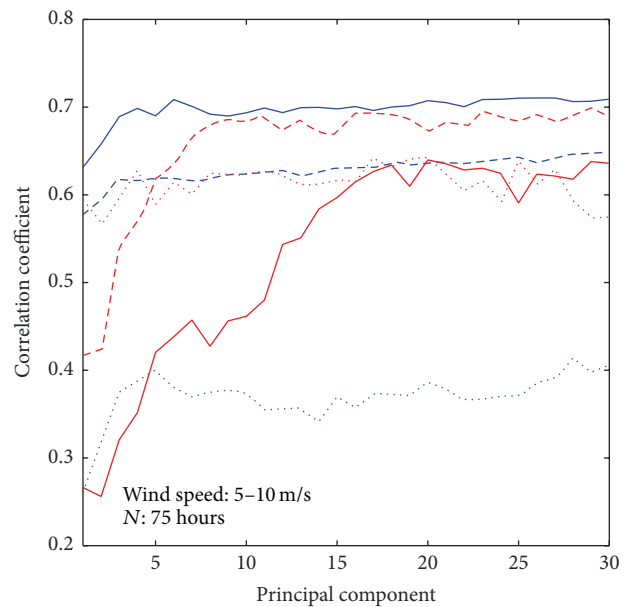
**3.3. Comparison with the Wind Speed.** To study the influence of wind on HH and VV polarizations, the correlation coefficients between the wind speed and the SWH retrieved

from X-band marine radars are shown in Figure 7. It indicates that the relationship between the SWH and the wind speed is very different for HH and VV polarizations.



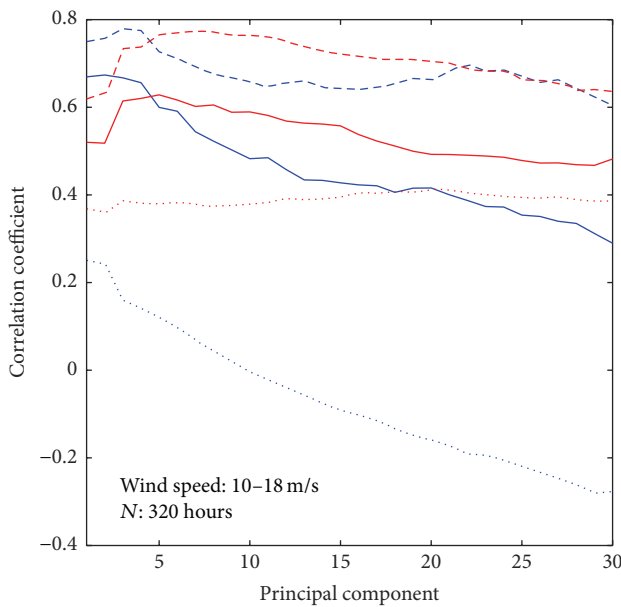
..... A1 (HH)      ..... A1 (VV)  
 — A2 (HH)      — A2 (VV)  
 - - - A3 (HH)      - - - A3 (VV)

(a)



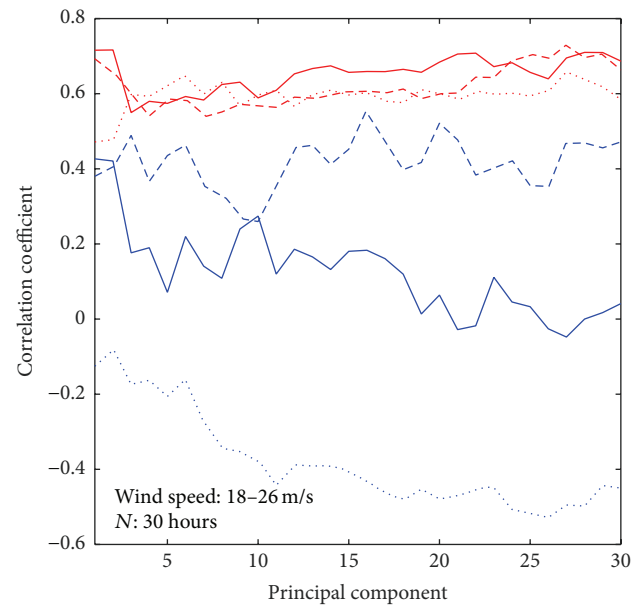
..... A1 (HH)      ..... A1 (VV)  
 — A2 (HH)      — A2 (VV)  
 - - - A3 (HH)      - - - A3 (VV)

(b)



..... A1 (HH)      ..... A1 (VV)  
 — A2 (HH)      — A2 (VV)  
 - - - A3 (HH)      - - - A3 (VV)

(c)



..... A1 (HH)      ..... A1 (VV)  
 — A2 (HH)      — A2 (VV)  
 - - - A3 (HH)      - - - A3 (VV)

(d)

FIGURE 7: The correlation coefficients between the wind speed and the SWH retrieved from different principal components of HH and VV polarized X-band marine radars, at the wind speeds of (a) 0–5 m/s, (b) 5–10 m/s, (c) 10–18 m/s, and (d) 18–26 m/s. The number “N” at the bottom of each panel denotes the number of hours used in the statistics.

For HH polarization, one has the following:

- (i) At low wind speed (Figure 7(a)), the correlation coefficients between the SWH in Region A1 and the wind speed are largest, and they decrease from nearshore (Region A1) to offshore (Region A3). This is because the backscatter from sea surface is too weak to contain wave signal at low wind speeds [27], and it also attenuates with the ranges from the radar station.
- (ii) At the wind speeds of 5–10 m/s (Figure 7(b)), the correlation coefficients in Regions A2 are larger than those in Regions A3 and A1; at the wind speeds of 10–26 m/s (Figures 7(c) and 7(d)), the correlation coefficients are largest in Region A3 and decrease from offshore (Region A3) to nearshore (Region A1). This is because the backscatter from sea surface increases as the wind speed increases.
- (iii) Comparing Figures 7(c) with 7(d), the correlation coefficients under moderate sea states are larger than those under high sea states. Because wave breaking becomes important at high wind speeds (Figure 3(c)), this may also indicate that HH polarization is greatly affected by wave breaking.

For VV polarization, one has the following:

- (i) At low wind speed (Figure 7(a)), the correlation coefficients in Regions A2 and A3 are larger than those in Region A1. This indicates that the backscatter from sea surface in offshore regions (Regions A2 and A3) contains wave signals at low wind speed, and the small correlation coefficients in Region A1 are caused by the tide (Figure 4(b)) or the saturation of backscatter in this region.
- (ii) At the wind speeds of 5–10 m/s (Figure 7(b)), the correlation coefficients of the first several principal components (i.e., 1–15 in Region A2 and 1–8 in Region A3) are small. This further indicates that VV polarization is insensitive to rapid changes of the wind speed, and thus the influence of long gravity waves may be more important than that of capillary waves on VV polarization.
- (iii) Comparing Figures 7(c) with 7(d), the correlation coefficients of Regions A2 and A3 change a little from moderate sea state to high sea state, so the influence of wave breaking on VV polarization is small. The correlation coefficients in Region A1 increase with increasing wind speeds, which indicate the influence of wind is more important than that of tide on waves.

**3.4. Wave Spectra of Different Principal Components.** The SWH are retrieved from different principal components of HH and VV polarized X-band marine radar image sequences, so the normalized wavenumber spectra of different principal components are studied. The spectrum is calculated as follows. First, decompose one X-band marine radar image sequence into different principal components [19]; second, choose one of the principal components and reconstruct

a new image; third, the two-dimensional wavenumber spectrum of the selected principal component is obtained by two-dimensional Fourier transform of the reconstructed image, and the directional ambiguity of the spectrum is eliminated according to the wave direction; finally, the one-dimensional wavenumber spectrum is derived by integrating the two-dimensional spectrum and then normalized by dividing the maximum of the spectrum.

The wavenumber spectra of different principal components at four typical wind speeds are shown in Figure 8. The four wind speeds are chosen from four sea states, which occurred in the hours of 237, 93, 52, and 453, respectively (Figure 3(a)). The study region is selected to be 135–165° in azimuthal direction and 520–1480 m in radial direction, which is centered on the location of the buoy. The 2nd, 7th, 12th, and 20th principal components are selected as examples. The black dashed lines show the peak wavenumbers measured by the buoy, which are close to the peak wavenumbers of the 2nd principal components (the red dotted lines) except those under low sea states [19]. The peak wavenumber measured by the buoy does not coincide exactly with the spectral peaks of the original radar images (the blue lines), because a modulation transfer function is needed to convert the spectra of radar images into the spectra of ocean waves [28], which is not taken into consideration here.

Figures 8(a) and 8(b) show the wavenumber spectra at the wind speed of 1.3 m/s. The spectra of the original VV and HH polarized radar images (the blue lines) are very different, and there are three peaks in Figure 8(a) at the wavenumbers of 0.014 rad/m, 0.056 rad/m and 0.097 rad/m, while there are many small peaks in Figure 8(b). The peak ocean wavenumber can be estimated from the peak wavenumbers of VV polarization, while the peak ocean wavenumber is contaminated in the spectrum of HH polarization. This indicates that VV polarization is less affected than HH polarization by low sea state.

At the wind speeds of 8.0 m/s, 14.3 m/s, and 25.5 m/s (Figures 8(c)–8(h)), the spectral peaks of the original images are the same for HH and VV polarizations (i.e., 0.076 rad/m, 0.069 rad/m, and 0.055 rad/m, resp.), so the peak wave signals were acquired by both polarizations.

There is one peak in the spectrum of the 2nd or 7th principal component, which is close to the peak frequency of ocean wave, because the first several principal components (usually named main principal components in EOF analysis) account for most of the information of ocean waves [19]. The red and green lines in Figure 8 show that the peak wavenumbers of the main principal components of VV polarization are usually smaller than those of HH polarization; for example, at the wind speed of 14.3 m/s, the peak wavenumbers of the 2nd principal component are 0.069 rad/m and 0.076 rad/m for VV and HH polarizations (Figures 8(e) and 8(f)); at the wind speeds of 14.3 m/s and 25.5 m/s (Figures 8(e)–8(h)), the peak wavenumbers of the 7th principal component are 0.900 rad/m and 0.055 rad/m for VV polarization, while they are 0.110 rad/m and 0.083 rad/m for HH polarization, respectively. Because the spectral peaks of the main principal components are possibly caused by the ocean waves with different wavelengths [19], this also

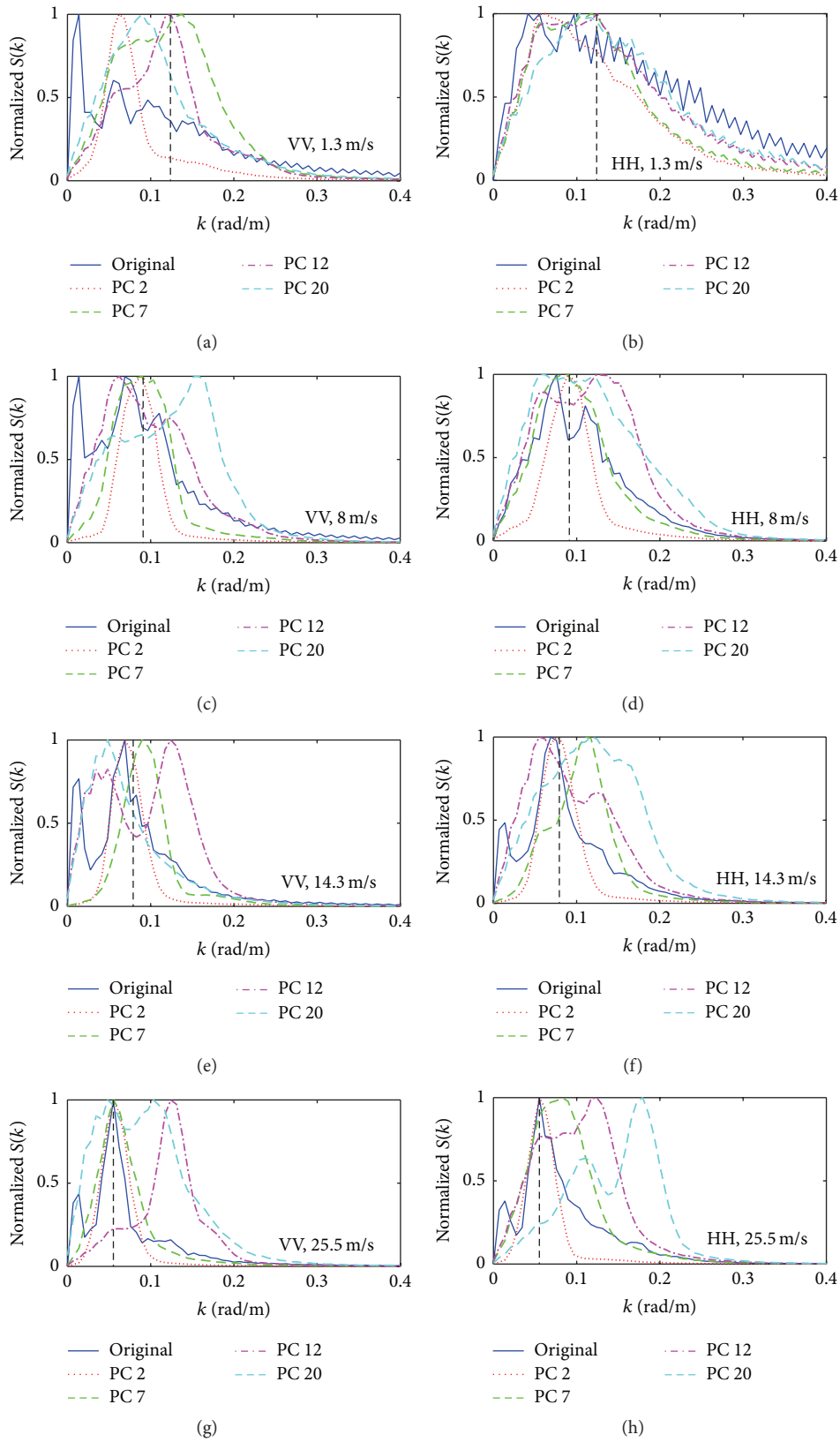


FIGURE 8: The normalized wavenumber spectra of different principal components of HH and VV polarized X-band marine radars, at the wind speeds of ((a) and (b)) 1.3 m/s, ((c) and (d)) 8.0 m/s, ((e) and (f)) 14.3 m/s, and ((g) and (h)) 25.5 m/s. The vertical black dashed lines denote the peak wavenumbers measured by the buoy.

indicates that VV polarization is mainly affected by long waves while HH polarization is affected by short waves.

There are two or more peaks in the spectrum of the 12th or 20th principal component. Because the spectral densities of these principal components are much smaller than the spectral densities of the original radar images (the blue lines in Figure 8), they are easily contaminated by random noises from the wave field and the radar systems. Therefore, there are large differences in these principal components between HH and VV polarizations.

In addition, the peak at 0.014 rad/m occurs in the spectra of VV polarization under different sea states (Figures 8(a), 8(c), 8(e), and 8(g)), which is most significant at low wind speed, and weakens as the wind speed increases (the changes of the peaks are in a relative sense because normalized spectra are used). It also occurs in the spectra of HH polarization under moderate and high sea states (Figures 8(f) and 8(h)). Therefore, the peak may be caused by the background noise of radar system, long gravity waves, or non-Bragg scattering mechanisms, but more observations are needed to determine the reasons.

#### 4. Discussion

There are differences between the SWH inversed from HH and VV polarized X-band marine radars, which indicate that the imaging mechanisms of HH and VV polarizations are different. The influences of wind and wave on different polarizations are further analyzed.

During low wind speeds, there is usually some residual energy (e.g., swell) on lower frequencies that might even be of the same order as the high-frequency part, which follows a  $f^{-4}$  wind dependent power law [29, 30]. Moreover, the low-frequency part is well resolved by the wave buoy, while the high-frequency part is not (the measurement range of frequency was 0.03–0.67 Hz for the buoy in the experiment). For HH polarization, the inversed SWH have a low correlation with the SWH measured by the buoy but a high correlation with the wind speeds (Figures 6 and 7 and Table 4), so the HH polarized radar mainly measures the higher frequencies of ocean wave. For VV polarization, the inversed SWH correlates with these lower frequency SWH measured by the wave buoy, while they get little information about the wind speed since there is no longer wave under the influence of the wind, so the VV polarized radar mainly measures the lower frequencies of ocean wave.

During high wind speeds, the waves that are under the direct influence of the wind will grow to even the lower frequencies. This means that any “residual” lower frequency energy is dominated by the wind driven waves. Since these waves follow the wind dependent  $f^{-4}$  power law [29, 30], even the lower frequency waves will now contain information about the wind. For HH polarization, correlation with the wind speed will still be high, since the high-frequency part still follows the wind speed dependent  $f^{-4}$  power law; the correlation with the buoy SWH will go up even if the HH polarization can only measure the high-frequency part, since both the high- and low-frequency waves now follow the same power law. For VV polarization, the correlation with

the wind speed will go up because the power law at the lower frequencies gives information about the wind speed; the correlation with the buoy SWH will stay high, since most of the energy is contained in the lower frequencies, which are readily measured by the wave buoy.

The explanation presented here does not depend directly on wave breaking (although wave dissipation plays a part in forming the  $f^{-4}$  power law), and multiple contributing factors are also a possibility.

#### 5. Conclusion

In coastal area, the wave fields are inhomogeneous due to the influences of wind, bathymetry and tide, and so forth. X-band marine radar has high spatial and temporal resolutions, so they are suitable to be used in the observation of coastal wave field. To study the differences between HH and VV polarizations in the observation of coastal waves, the SWH retrieved from different principal components of radar image sequences are compared with in situ measurements, and the following are found:

- (i) The RMSE between the SWH measured by the buoy and those retrieved from different principal components of X-band marine radar image sequences are 0.32–0.45 m for VV polarization, and they are 0.37–0.60 m for HH polarization. The RMSE are also different under different sea states.
- (ii) At the wind speeds of 0–5 m/s, the RMSE of the 1–5th principal component of VV polarization are smaller than those of HH polarization, and there are distinct peaks in the wavenumber spectrum of VV polarization. At very low wind speed (1–3 m/s in the experiment), the backscatter from HH polarization was too weak to extract information on ocean waves, while the backscatters from VV polarization can be used to estimate the SWH.
- (iii) At the wind speeds of 5–18 m/s, the SWH retrieved from VV polarized radar images coincide well with the SWH measured by the buoy, while the SWH retrieved from HH polarization correspond to the variation of the wind speeds. Moreover, the peak spectral wavenumbers of the main principal components of VV polarization are smaller than those of HH polarization. So long gravity waves are important to the imaging of VV polarization, while the wind-induced ripples or capillary waves have more important influence on the imaging of HH polarization. This is different from the composite-surface scattering model for moderate incidence angles [31], so it may be helpful for improving the scattering models under low grazing angles.
- (iv) At high wind speeds of 18–26 m/s, both the SWH measured by the buoy and the wind speeds correspond better with the SWH retrieved from VV polarization than with the SWH retrieved from HH polarization. The influence of wave breaking on HH polarization is more important than that on VV polarization.

Therefore, the imaging mechanisms of HH and VV polarized X-band marine radars are different. In the future, more experiments will be carried out to study the differences between them, especially the non-Bragg scattering mechanisms such as wave breaking. Based on this, the accuracy of the SWH retrieved from X-band marine radar image sequence may be improved.

## Competing Interests

The authors declare that there is no conflict of interests regarding the publication of this paper.

## Acknowledgments

This work was supported by Natural Science Youth Foundation of Jiangsu Province, Grant BK20150905, National Natural Science Youth Foundation of China, Grant 41506199, the Startup Foundation for Introducing Talent of NUIST, 2241061301078, the Fund of Oceanic Telemetry Engineering and Technology Research Center, State Oceanic Administration, under Project no. 2015003, a project funded by the Priority Academic Program Development of Jiangsu Higher Education Institutions (PAPD), and special fund project of the Central Research Institute, numerical prediction of storm surge in typical bays and research on the risk of overflow dam JG1408.

## References

- [1] Stennis Space Center, *Nondirectional and Directional Wave Data Analysis Procedures*, US Department of Commerce, 1996.
- [2] B. Lipa, D. Barrick, A. Alonso-Martirena, M. Fernandes, M. I. Ferrer, and B. Nyden, "Braham project high frequency radar ocean measurements: currents, winds, waves and their interactions," *Remote Sensing*, vol. 6, no. 12, pp. 12094–12117, 2014.
- [3] V. Barale, J. F. R. Gower, and L. Alberotanza, *Oceanography from Space*, Springer, Berlin, Germany, 2010.
- [4] J. D. Paduan and H. C. Graber, "Introduction to high-frequency radar: reality and myth," *Oceanography*, vol. 10, no. 2, pp. 36–39, 1997.
- [5] J. C. Nieto-Borge, K. Hessner, P. Jarabo-Amores, and D. de la Mata-Moya, "Signal-to-noise ratio analysis to estimate ocean wave heights from X-band marine radar image time series," *IET Radar, Sonar and Navigation*, vol. 2, no. 1, pp. 35–41, 2008.
- [6] I. R. Young, W. Rosenthal, and F. Ziemer, "A three-dimensional analysis of marine radar images for the determination of ocean wave directionality and surface currents," *Journal of Geophysical Research*, vol. 90, no. 1, pp. 1049–1059, 1985.
- [7] R. Gangekar, "Ocean current estimated from X-band radar sea surface images," *IEEE Transactions on Geoscience and Remote Sensing*, vol. 40, no. 4, pp. 783–792, 2002.
- [8] C. M. Senet, J. Seemann, S. Flampouris, and F. Ziemer, "Determination of bathymetric and current maps by the method DiSC based on the analysis of nautical X-band radar image sequences of the sea surface (November 2007)," *IEEE Transactions on Geoscience and Remote Sensing*, vol. 46, no. 8, pp. 2267–2279, 2008.
- [9] H. Dankert and J. Horstmann, "A marine radar wind sensor," *Journal of Atmospheric and Oceanic Technology*, vol. 24, no. 9, pp. 1629–1642, 2007.
- [10] B. Lund, H. C. Graber, and R. Romeiser, "Wind retrieval from shipborne nautical X-band radar data," *IEEE Transactions on Geoscience and Remote Sensing*, vol. 50, no. 10, pp. 3800–3811, 2012.
- [11] P. S. Bell, "Shallow water bathymetry derived from an analysis of X-band marine radar images of waves," *Coastal Engineering*, vol. 37, no. 3-4, pp. 513–527, 1999.
- [12] G. S. Brown, "Guest editorial: special issue on low-grazing-angle backscatter from rough surfaces," *IEEE Transactions on Geoscience and Remote Sensing*, vol. 46, no. 1, pp. 1–2, 1998.
- [13] P. Forget, M. Saillard, and P. Broche, "Observations of the sea surface by coherent L band radar at low grazing angles in a nearshore environment," *Journal of Geophysical Research: Oceans*, vol. 111, no. 9, Article ID C09015, 2006.
- [14] P. A. Hwang, M. A. Sletten, and J. V. Toporkov, "Analysis of radar sea return for breaking wave investigation," *Journal of Geophysical Research: Oceans*, vol. 113, no. 2, Article ID C02003, pp. 1–16, 2008.
- [15] P. H. Y. Lee, J. D. Barter, K. L. Beach et al., "X band microwave backscattering from ocean waves," *Journal of Geophysical Research*, vol. 100, no. 2, pp. 2591–2611, 1995.
- [16] D. B. Trizna and D. J. Carlson, "Studies of dual polarized low grazing angle radar sea scatter in nearshore regions," *IEEE Transactions on Geoscience and Remote Sensing*, vol. 34, no. 3, pp. 747–757, 1996.
- [17] L. Cui, Y. He, H. Shen, and H. Lü, "Measurements of ocean wave and current field using dual polarized X-band radar," *Chinese Journal of Oceanology and Limnology*, vol. 28, no. 5, pp. 1021–1028, 2010.
- [18] J. An, W. Huang, and E. W. Gill, "A self-adaptive wavelet-based algorithm for wave measurement using nautical radar," *IEEE Transactions on Geoscience and Remote Sensing*, vol. 53, no. 1, pp. 567–577, 2015.
- [19] Z. Chen, Y. He, B. Zhang, Z. Qiu, and B. Yin, "A new algorithm to retrieve wave parameters from marine X-band radar image sequences," *IEEE Transactions on Geoscience and Remote Sensing*, vol. 52, no. 7, pp. 4083–4091, 2014.
- [20] Z. Chen, Y. He, B. Zhang, Z. Qiu, and B. Yin, "A new method to retrieve significant wave height from X-band marine radar image sequences," *International Journal of Remote Sensing*, vol. 35, no. 11-12, pp. 4559–4571, 2014.
- [21] G. P. Gerbi, S. E. Kastner, and G. Brett, "The role of whitecapping in thickening the ocean surface boundary layer," *Journal of Physical Oceanography*, vol. 45, no. 8, pp. 2006–2024, 2015.
- [22] Z. Wang, "Tides in the Taiwan strait," *Taiwan Strait*, vol. 4, no. 2, pp. 120–128, 1985.
- [23] Z. Chen, Y. He, J. Pan et al., "Observation of tide from X-band marine radar image sequences," in *Proceedings of the IEEE International Geoscience and Remote Sensing Symposium*, Beijing, China, July 2016.
- [24] O. M. Phillips, "Radar returns from the sea surface—bragg scattering and breaking waves," *Journal of Physical Oceanography*, vol. 18, no. 8, pp. 1065–1074, 1988.
- [25] R. H. Stewart, *Introduction to Physical Oceanography*, Department of Oceanography, Texas A&M University, College Station, Tex, USA, 2008.
- [26] O. M. Phillips, "Spectral and statistical properties of the equilibrium range in wind-generated gravity waves," *Journal of Fluid Mechanics*, vol. 156, pp. 505–531, 1985.
- [27] H. Hatten, J. Seemann, J. Horstmann, and F. Ziemer, "Azimuthal dependence of the radar cross section and the spectral background noise of a nautical radar at grazing incidence," in

*Proceedings of the IEEE International Geoscience and Remote Sensing Symposium (IGARSS '98)*, pp. 2490–2492, July 1998.

- [28] J. C. Nieto-Borge, G. N. R. Rodriguez, K. Hessner, and P. I. González, “Inversion of marine radar images for surface wave analysis,” *Journal of Atmospheric and Oceanic Technology*, vol. 21, no. 8, pp. 1291–1300, 2004.
- [29] W. J. Pierson and L. Moskowitz, “A proposed spectral form for fully developed wind seas based on the similarity theory of S. A. Kitaigorodskii,” *Journal of Geophysical Research*, vol. 69, no. 24, pp. 5181–5190, 1964.
- [30] J. Henrique, G. M. Alves, M. L. Banner, and I. R. Young, “Revisiting the Pierson-Moskowitz asymptotic limits for fully developed wind waves,” *Journal of Physical Oceanography*, vol. 33, pp. 1301–1323, 2003.
- [31] G. R. Valenzuela, “Theories for the interaction of electromagnetic and oceanic waves—a review,” *Boundary-Layer Meteorology*, vol. 13, no. 1–4, pp. 61–85, 1978.

## Research Article

# Bistatic High Frequency Radar Ocean Surface Cross Section for an FMCW Source with an Antenna on a Floating Platform

**Yue Ma, Weimin Huang, and Eric W. Gill**

*Faculty of Engineering and Applied Science, Memorial University of Newfoundland, St. John's, NL, Canada A1B 3X5*

Correspondence should be addressed to Yue Ma; [ym4428@mun.ca](mailto:ym4428@mun.ca)

Received 5 February 2016; Revised 13 May 2016; Accepted 29 May 2016

Academic Editor: Atsushi Mase

Copyright © 2016 Yue Ma et al. This is an open access article distributed under the Creative Commons Attribution License, which permits unrestricted use, distribution, and reproduction in any medium, provided the original work is properly cited.

The first- and second-order bistatic high frequency radar cross sections of the ocean surface with an antenna on a floating platform are derived for a frequency-modulated continuous wave (FMCW) source. Based on previous work, the derivation begins with the general bistatic electric field in the frequency domain for the case of a floating antenna. Demodulation and range transformation are used to obtain the range information, distinguishing the process from that used for a pulsed radar. After Fourier-transforming the autocorrelation and comparing the result with the radar range equation, the radar cross sections are derived. The new first- and second-order antenna-motion-incorporated bistatic radar cross section models for an FMCW source are simulated and compared with those for a pulsed source. Results show that, for the same radar operating parameters, the first-order radar cross section for the FMCW waveform is a little lower than that for a pulsed source. The second-order radar cross section for the FMCW waveform reduces to that for the pulsed waveform when the scattering patch limit approaches infinity. The effect of platform motion on the radar cross sections for an FMCW waveform is investigated for a variety of sea states and operating frequencies and, in general, is found to be similar to that for a pulsed waveform.

## 1. Introduction

The derivation of high frequency radar ocean surface cross sections has been studied for over four decades. The first-order high frequency radar scatter cross section was developed and analysed in [1]. Later, Walsh and Gill [2] analysed the scattering of high frequency electromagnetic radiation of the ocean surface for a pulse radar. Then, Gill and Walsh [3] developed the bistatic radar cross section of the ocean surface. Following these analyses, the work was extended to the high frequency monostatic radar cross sections for an antenna on a floating platform [4, 5].

All of the models mentioned above were developed specifically for pulsed radar. However, there are inherent disadvantages to using pulsed radar systems. For example, the detectable range capability is determined by the average transmitted power. In a pulsed radar system, both the range resolution and the average transmitted power are dependent on the pulse width. Narrower pulses, bringing better range resolution, require large peak powers to be useful at long

range. Compared to this, FMCW radar systems are able to achieve satisfactory range resolution and long range with moderate peak power due to a 100% duty cycle. Thus, in recent years, FMCW radars have been widely used in ocean remote sensing applications.

A good summary of the digital processing of an FMCW signal for radar systems has been reported by Barrick [6]. Two processing techniques were analysed and compared. Based on that work, the design of a frequency-modulated interrupted continuous wave radar was described and implemented in [7]. Then, techniques for range and unambiguous velocity measurement for an FMCW radar were outlined in [8]. More recently, Walsh et al. [9] developed the first- and second-order monostatic radar ocean surface cross sections for an FMCW waveform. Also, the first-order FMCW radar cross section model for mixed-path ionosphere-ocean propagation has been established and simulated in [10].

In this paper, the first- and second-order bistatic radar ocean surface cross sections for an antenna on a floating platform and incorporating an FMCW source are presented.

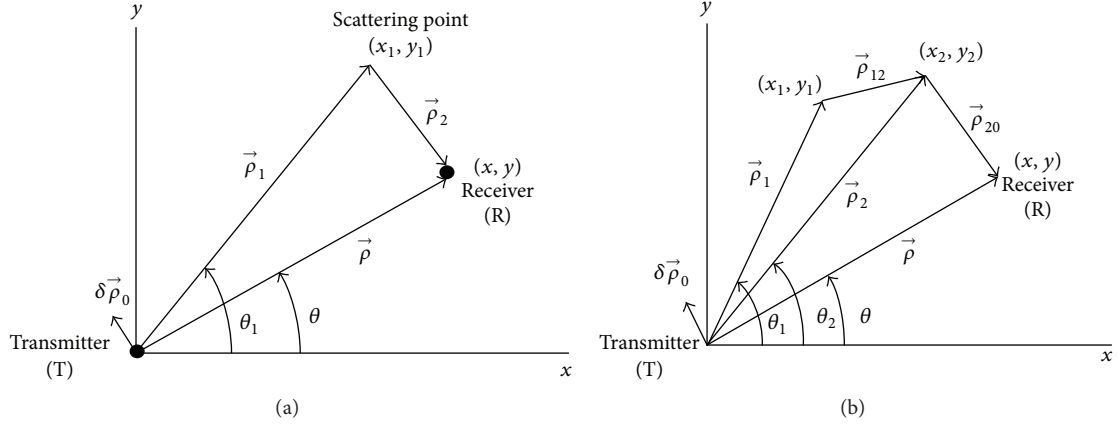


FIGURE 1: General (a) first-order and (b) second-order bistatic scatter geometry with antenna motion.

In Section 2, the derivation process of the first- and second-order received electric field is reviewed. Then, a method similar to that in [3] is used to obtain the first- and second-order radar cross section in Section 3. Section 4 contains model simulations and comparisons with the pulsed waveform. Section 5 provides conclusions.

## 2. Radar Received Field Equations

*2.1. General First- and Second-Order Electric Field Equation.* By using a small displacement vector,  $\delta\vec{\rho}_0 = (\delta\rho_0, \theta_0)$ , to represent the sway motion of the platform (see Figure 1) and adding this small displacement in the source term, the first-order bistatic scattered field for the case of a floating transmitter and a fixed receiver appearing in [11] may be written for a vertical dipole source as

$$(E_n)_1 = \frac{kC_0}{(2\pi)^{3/2}} \sum_{\vec{K}} P_{\vec{K}} \sqrt{K} e^{j(\rho K/2) \cos(\theta_K - \theta)} \cdot \int_{\rho/2}^{\infty} \frac{F(\rho_1) F(\rho_2)}{\sqrt{\rho_s [\rho_s^2 - (\rho/2)^2]}} e^{-j(\pi/4)} \sqrt{\cos \phi} \cdot e^{jk\delta\rho_0 [\cos \phi \cos(\theta_K - \theta_0) + \sin \phi \sin(\theta_K - \theta_0)]} \cdot e^{j\rho_s [K \cos \phi - 2k]} d\rho_s. \quad (1)$$

Here,  $C_0 = I\Delta l k^2 / j\omega\epsilon_0$  is the dipole constant, with  $I$  being the current on the dipole of length  $\Delta l$ .  $\omega$  and  $k$  are the radian frequency and wavenumber of the dipole current, respectively, in a space with permittivity of  $\epsilon_0$ .  $P_{\vec{K}}$  represents the Fourier coefficient of a surface component whose wave vector has magnitude  $K$  and direction  $\theta_K$  (i.e.,  $\vec{K} = (K, \theta_K)$ ). With reference to Figure 1(a),  $\vec{\rho} = (\rho, \theta)$  is a distance vector, pointing from the transmitter to the receiver without incorporating the platform motion.  $\rho_s = (\rho_1 + \rho_2)/2$  and  $\phi$  is the bistatic angle.  $F$  represents the Sommerfeld attenuation function.

The second-order bistatic received electric field corresponding to the first-order found in (1) appears in [12] as

$$(E_n)_2 = \frac{-kC_0}{(2\pi)^{3/2}} \sum_{\vec{K}_1, \vec{K}_2} \frac{P_{\vec{K}_1} P_{\vec{K}_2}}{\sqrt{K}} e^{j(\rho K/2) \cos(\theta_K - \theta)} \cdot \int_{\rho/2}^{\infty} \frac{(-k\chi) F(\rho_2) F(\rho_{20}) e^{-j(\pi/4)}}{\sqrt{\rho_s [\rho_s^2 - (\rho/2)^2]} \sqrt{\cos \phi}} \cdot e^{jk\delta\rho_0 [\cos \phi \cos(\theta_K - \theta_0) + \sin \phi \sin(\theta_K - \theta_0)]} \cdot e^{j\rho_s [K \cos \phi - 2k]} d\rho_s. \quad (2)$$

This expression accounts for the electric field arising due to the transmitted signal being scattered twice by the rough surface.  $\vec{K}_1$  and  $\vec{K}_2$  are the first and the second scattering wave vectors of the rough surface. The rough surface may be represented by a Fourier series with  $P_{\vec{K}_1}$  and  $P_{\vec{K}_2}$  being the Fourier coefficients associated with  $\vec{K}_1$  and  $\vec{K}_2$ , respectively. Here,  $\vec{K} = \vec{K}_1 + \vec{K}_2$ . Again, with reference to Figure 1, defining  $\vec{K}_s(\hat{\rho}_2, \vec{K}_1) = k\hat{\rho}_2 - \vec{K}_1$  allows  $\chi$  to be expressed as [12]

$$\chi = j(\vec{K}_1 \cdot \hat{\rho}_2)(\vec{K}_s \cdot \vec{K}_2) \cdot G[K_s(\hat{\rho}_2, \vec{K}_1)], \quad (3)$$

where

$$G[K_s(\hat{\rho}_2, \vec{K}_1)] = \frac{1}{K_s} \left\{ 1 - j \frac{k(1 + \Delta)}{\sqrt{K_s^2 - k^2 + jk\Delta}} \right\}, \quad (4)$$

with  $\Delta$  being the intrinsic impedance of the surface. At this stage, the current waveform on the dipole source has not been specified.

2.2. *Applications to an FMCW Radar.* Following a similar analysis as in [3, 11], (1) may be inversely Fourier-transformed to give the received electric field in the time domain as

$$\begin{aligned} \mathcal{F}^{-1} [(E_n)_1] (t) &= \frac{1}{(2\pi)^{3/2}} \\ &\cdot \mathcal{F}^{-1} \left[ -j \frac{\eta_0 \Delta l}{c^2} \omega^2 I(\omega) \right] \overset{t}{*} \mathcal{F}^{-1} \left\{ \sum_{\tilde{K}} P_{\tilde{K}} \right. \\ &\cdot \sqrt{K} e^{j(\rho K/2) \cos(\theta_K - \theta)} \\ &\cdot \int_{\rho/2}^{\infty} \frac{F(\rho_1) F(\rho_2)}{\sqrt{\rho_s [\rho_s^2 - (\rho/2)^2]}} e^{-j(\pi/4)} \sqrt{\cos \phi} \\ &\cdot e^{jk\delta\rho_0 [\cos \phi \cos(\theta_K - \theta_0) + \sin \phi \sin(\theta_K - \theta_0)]} \\ &\left. \cdot e^{j\rho_s [K \cos \phi - 2k]} d\rho_s \right\}. \end{aligned} \quad (5)$$

The current waveform of an FMCW radar may be written as [6, 9]

$$i(t) = I_0 e^{j(\omega_0 t + \alpha \pi t^2)} \left\{ h \left[ t + \frac{T_r}{2} \right] - h \left[ t - \frac{T_r}{2} \right] \right\}, \quad (6)$$

where  $I_0$  is the peak current and  $\omega_0 = 2\pi f_0$  is the center radian frequency of the sweep waveform.  $T_r$  represents the sweep interval and the sweep rate may be expressed as  $\alpha = B/T_r$  where  $B$  is the sweep bandwidth.  $h$  is the Heaviside function.

It is known from [9] that, for an FMCW waveform,

$$\begin{aligned} \mathcal{F}^{-1} \left[ -j \frac{\eta_0 \Delta l}{c^2} \omega^2 I(\omega) \right] \\ = -j I_0 \frac{\eta_0 \Delta l \omega_0^2}{c^2} e^{j(\omega_0 t + \alpha \pi t^2)} \\ \cdot \left\{ h \left[ t + \frac{T_r}{2} \right] - h \left[ t - \frac{T_r}{2} \right] \right\}. \end{aligned} \quad (7)$$

By direct comparison with the corresponding first-order case for a pulsed dipole [11], the first-order time domain electric field for an FMCW source may be written as

$$\begin{aligned} (E_n)_1 (t_r) &= \frac{-j I_0 \eta_0 \Delta l k_0^2}{(2\pi)^{3/2}} \sum_{\tilde{K}} P_{\tilde{K}} \sqrt{K} e^{j(\rho K/2) \cos(\theta_K - \theta)} \\ &\cdot \int_{\rho/2}^{\infty} \frac{F(\rho_1, \omega_0) F(\rho_2, \omega_0)}{\sqrt{\rho_s [\rho_s^2 - (\rho/2)^2]}} e^{-j(\pi/4)} \sqrt{\cos \phi} e^{j\rho_s K \cos \phi} \\ &\cdot e^{j(\omega_0 t_r + \alpha \pi t_r^2)} e^{-jk_0(2\rho_s - \delta\rho_{s0})} e^{-j(2\pi\alpha(2\rho_s - \delta\rho_{s0})/c)t_r} \\ &\cdot e^{j(\pi\alpha(2\rho_s - \delta\rho_{s0})^2/c^2)} \left\{ h \left[ t_r + \frac{T_r}{2} - \frac{2\rho_s - \delta\rho_{s0}}{c} \right] \right. \\ &\left. - h \left[ t_r - \frac{T_r}{2} - \frac{2\rho_s - \delta\rho_{s0}}{c} \right] \right\} d\rho_s, \end{aligned} \quad (8)$$

where  $\delta\rho_{s0} = \delta\rho_0 [\cos \phi \cos(\theta_K - \theta_0) + \sin \phi \sin(\theta_K - \theta_0)]$ .  $t$  is renamed as  $t_r$  to indicate that the time is within a sweep repetition interval  $((2\rho_s - \delta\rho_{s0})/c - T_r/2, (2\rho_s - \delta\rho_{s0})/c + T_r/2)$ . As stated in [6, 9], the frequency difference between the transmitted waveform and the received waveform may be Fourier-transformed within this interval to obtain the range information. This is the so-called ‘‘range transform.’’ Because the received signals in the given time interval reflect the information for an extremely large range of ocean surface, here range transformation is taken to accurately acquire a patch of ocean surface to analyse. The frequency difference may be obtained by the demodulation process, in which the transmitted signals and the received signals are mixed and then low-pass-filtered.

After the demodulation preprocess, the exponential factor  $e^{j(\omega_0 t_r + \alpha \pi t_r^2)}$  in (8) will be eliminated. Then, Fourier-transforming with respect to  $t_r$  gives

$$\begin{aligned} (E_n)_1 (\omega_r) \\ = \frac{-j I_0 \eta_0 \Delta l k_0^2 T_r}{(2\pi)^{3/2}} \sum_{\tilde{K}} P_{\tilde{K}} \sqrt{K} e^{j(\rho K/2) \cos(\theta_K - \theta)} \\ \cdot \int_{\rho/2}^{\infty} \frac{F(\rho_1, \omega_0) F(\rho_2, \omega_0)}{\sqrt{\rho_s [\rho_s^2 - (\rho/2)^2]}} e^{-j(\pi/4)} \sqrt{\cos \phi} e^{j\rho_s K \cos \phi} \\ \cdot e^{-jk_0(2\rho_s - \delta\rho_{s0})} e^{j\omega_r(2\rho_s - \delta\rho_{s0})/c} e^{-j(\pi\alpha(2\rho_s - \delta\rho_{s0})^2/c^2)} \\ \cdot \text{Sa} \left[ \frac{T_r}{2} \left( \omega_r - \frac{2\pi\alpha(2\rho_s - \delta\rho_{s0})}{c} \right) \right] d\rho_s, \end{aligned} \quad (9)$$

where  $\omega_r$  is the transform variable in the frequency domain. Here, it is helpful to define

$$\rho'_s = \rho_s - \frac{\delta\rho_{s0}}{2}. \quad (10)$$

Changing the integration variable from  $\rho_s$  to  $\rho'_s$  and ignoring the  $\delta\rho_{s0}/2$  factor in the magnitude terms give

$$\begin{aligned} (E_n)_1 (\omega_r) \\ = \frac{-j I_0 \eta_0 \Delta l k_0^2 T_r}{(2\pi)^{3/2}} \sum_{\tilde{K}} P_{\tilde{K}} \sqrt{K} e^{j(\rho K/2) \cos(\theta_K - \theta)} \\ \cdot \int_{\rho/2}^{\infty} \frac{F(\rho_1, \omega_0) F(\rho_2, \omega_0)}{\sqrt{\rho_s [\rho_s^2 - (\rho/2)^2]}} e^{-j(\pi/4)} \sqrt{\cos \phi} \\ \cdot e^{j(K \cos \phi - 2k_0 + 2\omega_r/c)\rho'_s} e^{-j(4\pi\alpha(\rho'_s)^2/c^2)} e^{j\delta\rho_{s0} K \cos \phi/2} \\ \cdot \text{Sa} \left[ \frac{T_r}{2} \left( \omega_r - \frac{4\pi\alpha}{c} \rho'_s \right) \right] d\rho'_s. \end{aligned} \quad (11)$$

Since the maximum of the sampling function  $\text{Sa}(x)$  occurs at  $x = 0$ , a representative range  $\rho_r$  may be defined as

$$\rho_r = \frac{c\omega_r}{4\pi\alpha}. \quad (12)$$

Based on the representative range, defining the corresponding range variable

$$\rho_s'' = \rho_s' - \rho_r \quad (13)$$

and changing the integration variable from  $\rho_s'$  to  $\rho_s''$ , (11) becomes

$$\begin{aligned} (E_n)_1(\omega_r) &= \frac{-jI_0\eta_0\Delta lk_0^2 T_r}{(2\pi)^{3/2}} \sum_{\vec{K}} P_{\vec{K}} \sqrt{K} e^{j(\rho K/2) \cos(\theta_K - \theta)} \\ &\cdot \int_{\rho_s''_{\min}}^{\rho_s''_{\max}} \frac{F(\rho_1, \omega_0) F(\rho_2, \omega_0)}{\sqrt{\rho_s [\rho_s^2 - (\rho/2)^2]}} e^{-j(\pi/4)} \sqrt{\cos \phi} \\ &\cdot e^{j(-2k_0 + k_r)\rho_r} e^{j(-2k_0)\rho_s''} e^{j\rho_s K \cos \phi} \\ &\cdot e^{-j(k_r/\rho_r)(\rho_s'')^2} \text{Sa} [k_B \rho_s''] d\rho_s'', \end{aligned} \quad (14)$$

where  $k_B = 2\pi B/c$  and  $k_r = \omega_r/c$ . A process similar to that in [11] is used to simplify the terms in the integral. Then, (14) reduces to

$$\begin{aligned} (E_n)_1(\omega_r) &= \frac{-jI_0\eta_0\Delta lk_0^2 T_r}{(2\pi)^{3/2}} \sum_{\vec{K}} P_{\vec{K}} \sqrt{K} e^{j(\rho K/2) \cos(\theta_K - \theta)} \\ &\cdot e^{-j(\pi/4)} \sqrt{\cos \phi_0} e^{j(K \cos \phi_0 - 2k_0 + k_r)\rho_r} \\ &\cdot \frac{F(\rho_{01}, \omega_0) F(\rho_{02}, \omega_0)}{\sqrt{\rho_r [\rho_r^2 - (\rho/2)^2]}} e^{j(\delta\rho_{s0}/2)(K/\cos \phi_0)} \\ &\cdot \int_{\rho_s''_{\min}}^{\rho_s''_{\max}} e^{j(K/\cos \phi_0 - 2k_0)\rho_s''} \\ &\cdot e^{-j(k_r/\rho_r)(\rho_s'')^2} \text{Sa} [k_B \rho_s''] d\rho_s'', \end{aligned} \quad (15)$$

where  $\rho_{01}$  and  $\rho_{02}$  are representative values of  $\rho_1$  and  $\rho_2$  (see Figure 1), respectively. By directly comparing (15) with (24) in [9], the first-order bistatic received electric field for an FMCW waveform with an antenna on a floating platform may be expressed as

$$\begin{aligned} (E_n)_1(\omega_r) &= \frac{-jI_0\eta_0\Delta lk_0^2}{(2\pi)^{3/2}} \sum_{\vec{K}} P_{\vec{K}} \sqrt{K} e^{j(\rho K/2) \cos(\theta_K - \theta)} \\ &\cdot e^{-j(\pi/4)} \sqrt{\cos \phi_0} e^{j(K \cos \phi_0 - 2k_0 + k_r)\rho_r} \\ &\cdot \frac{F(\rho_{01}, \omega_0) F(\rho_{02}, \omega_0)}{\sqrt{\rho_r [\rho_r^2 - (\rho/2)^2]}} e^{j(\delta\rho_{s0}/2)(K/\cos \phi_0)} \\ &\cdot (T_r \Delta \rho) \text{Sm}(K, \cos \phi_0, k_B, \Delta r). \end{aligned} \quad (16)$$

$\pm \Delta r$  are the symmetrical limits of the integral in (15), where a sampling function dominates this integral. If only the values of  $\rho_s''$  within the main lobe of the sampling function are considered in the integral, that is,  $-\pi/2 < k_B \rho_s'' < \pi/2$ , it can be deduced as in [9] that  $\Delta r = \Delta \rho/2 = c/4B$ . Consider

$$\begin{aligned} \text{Sm}(K, \cos \phi_0, k_B, \Delta r) &= \frac{1}{\pi} \left\{ \text{Si} \left[ \left( \frac{K}{\cos \phi_0} - 2k_0 + k_B \right) \Delta r \right] \right. \\ &\left. - \text{Si} \left[ \left( \frac{K}{\cos \phi_0} - 2k_0 - k_B \right) \Delta r \right] \right\}, \end{aligned} \quad (17)$$

where  $\text{Si}(x) = \int_0^x (\sin(t)/t) dt$ .

Following a similar procedure to the first-order case, the second-order bistatic received electric field with a transmitter on a floating platform for an FMCW waveform may be written as

$$\begin{aligned} (E_n)_{2E}(\omega_r) &= \frac{-jI_0\eta_0\Delta lk_0^2}{(2\pi)^{3/2}} \sum_{\vec{K}_1, \vec{K}_2} P_{\vec{K}_1} P_{\vec{K}_2} \sqrt{K} e^{-j(\pi/4)} \\ &\cdot e^{j(\rho K/2) \cos(\theta_K - \theta)} \sqrt{\cos \phi_0} e^{j(K \cos \phi_0 - 2k_0 + k_r)\rho_r} \\ &\cdot \frac{{}_{\text{SE}}\Gamma_P F(\rho_{02}, \omega_0) F(\rho_{020}, \omega_0)}{\sqrt{\rho_r [\rho_r^2 - (\rho/2)^2]}} e^{j(\delta\rho_{s0}/2)(K/\cos \phi_0)} \\ &\cdot (T_r \Delta \rho) \text{Sm}(K, \cos \phi_0, k_B, \Delta r), \end{aligned} \quad (18)$$

where  $\rho_{02}$  and  $\rho_{020}$  are the representative values of  $\rho_2$  and  $\rho_{20}$ , respectively. The symmetrical electromagnetic coupling coefficient,  ${}_{\text{SE}}\Gamma_P$ , may be expressed as [12]

$$\begin{aligned} {}_{\text{SE}}\Gamma_P(\vec{K}_1, \vec{K}_2) &= \frac{jk_0}{2K \cos \phi_0} \left\{ (\vec{K}_1 \cdot \hat{\rho}_2) \right. \\ &\cdot [\vec{K}_s(\hat{\rho}_2, \vec{K}_1) \cdot \vec{K}_2] G[K_s(\hat{\rho}_2, \vec{K}_1)] \\ &\left. + (\vec{K}_2 \cdot \hat{\rho}_2) [\vec{K}_s(\hat{\rho}_2, \vec{K}_2) \cdot \vec{K}_1] G[K_s(\hat{\rho}_2, \vec{K}_2)] \right\} \end{aligned} \quad (19)$$

with  $\vec{K}_s(\hat{\rho}_2, \vec{K}_2) = k\hat{\rho}_2 - \vec{K}_2$  and

$$G[K_s(\hat{\rho}_2, \vec{K}_1)] = \frac{1}{K_s} \left\{ 1 - j \frac{k(1 + \Delta)}{\sqrt{K_s^2 - k^2 + jk\Delta}} \right\}. \quad (20)$$

### 3. Radar Cross Sections

**3.1. First-Order Radar Cross Section.** In developing the ocean radar cross section, a time-varying ocean surface, represented as  $\xi(\vec{\rho}, t) = \sum_{\vec{\rho}, t} P_{\vec{K}, \omega} e^{j\vec{K} \cdot \vec{\rho}} e^{j\omega t}$ , is used to replace the time-invariant case  $\xi(\vec{\rho}) = \sum_{\vec{\rho}} P_{\vec{K}} e^{j\vec{K} \cdot \vec{\rho}}$ . This gives the time-varying received electric field corresponding to (16) as

$$\begin{aligned} (E_n)_1(\omega_r, t) &= \frac{-jI_0\eta_0\Delta k_0^2}{(2\pi)^{3/2}} \sum_{\vec{K}, \omega} P_{\vec{K}, \omega} \sqrt{K} e^{j(\rho K/2) \cos(\theta_K - \theta)} \\ &\cdot e^{j(K \cos \phi_0 - 2k_0 + k_r)\rho_r} e^{-j(\pi/4)} \sqrt{\cos \phi_0} e^{j\omega t} \\ &\cdot \frac{F(\rho_{01}, \omega_0) F(\rho_{02}, \omega_0)}{\sqrt{\rho_r [\rho_r^2 - (\rho/2)^2]}} e^{j(\delta\rho_{s0}/2)(K/\cos \phi_0)} \\ &\cdot (T_r \Delta \rho) \text{Sm}(K, \cos \phi_0, k_B, \Delta r). \end{aligned} \quad (21)$$

A technique similar to that in [9, 11] is used to obtain the radar cross section from the received electric field equation. The initial step of the approach is to write the autocorrelation,  $R(\tau)$ , as

$$R(\tau) = \frac{A_r}{2\eta_0} \frac{1}{T_r^2} \langle (E_n)_1(\omega_r, t + \tau) (E_n)_1^*(\omega_r, t) \rangle, \quad (22)$$

where  $A_r = (\lambda_0^2/4\pi)G_r$ , with  $G_r$  being the gain of the receiving array. Here,  $\omega_r$  represents the fixed patch over two sweep intervals, whose time interval is  $\tau$ .

After Fourier-transforming the autocorrelation and comparing directly with the radar range equation, the radar cross section,  $\sigma_1(\omega_d)$ , may be written as

$$\begin{aligned} \sigma_1(\omega_d) &= 2^3 \pi k_0^2 \Delta \rho \sum_{m=\pm 1} \int_K S_1(m\vec{K}) K^2 \cos \phi_0 \\ &\cdot \text{Sm}^2(K, \cos \phi_0, k_B, \Delta r) \\ &\cdot \left\{ J_0^2 \left[ \frac{aK}{2} \left| \cos(\theta_K - \theta_{K_p}) \right. \right] \right. \\ &+ \tan \phi_0 \sin(\theta_K - \theta_{K_p}) \left. \right\} \cdot \delta(\omega_d + m\sqrt{gK}) \\ &+ \sum_{n=1}^{\infty} J_n^2 \left[ \frac{aK}{2} \left| \cos(\theta_K - \theta_{K_p}) \right. \right] \\ &+ \tan \phi_0 \sin(\theta_K - \theta_{K_p}) \left. \right\} \cdot \left[ \delta(\omega_d + m\sqrt{gK} \right. \\ &\left. - n\omega_p) + \delta(\omega_d + m\sqrt{gK} + n\omega_p) \right] dK, \end{aligned} \quad (23)$$

where  $J_n$  represents the  $n$ th-order Bessel functions. For simulation purposes (see Section 4) and in keeping with [4, 11], it will be assumed that the antenna motion is caused by the dominant ocean waves.  $a$ ,  $\omega_p$ , and  $\theta_{K_p}$  represent the antenna platform sway amplitude, frequency, and direction, respectively.

**3.2. Second-Order Radar Cross Section.** It is known that the second-order radar cross section contains two portions: an hydrodynamic contribution and an electromagnetic contribution. Using the Fourier coefficient for the second-order ocean waves  $\sum_{\vec{K}_1} \sum_{\vec{K}_2} {}_H\Gamma P_{\vec{K}_1} P_{\vec{K}_2}$  to replace the first-order case  $\sum_{\vec{K}} P_{\vec{K}}$  in (16), the hydrodynamic second-order electric field may be written as

$$\begin{aligned} (E_n)_{2H}(\omega_r) &= \frac{-jI_0\eta_0\Delta k_0^2}{(2\pi)^{3/2}} \sum_{\vec{K}_1} \sum_{\vec{K}_2} P_{\vec{K}_1} P_{\vec{K}_2} \sqrt{K} e^{-j(\pi/4)} \\ &\cdot e^{j(\rho K/2) \cos(\theta_K - \theta)} \sqrt{\cos \phi_0} e^{j(K \cos \phi_0 - 2k_0 + k_r)\rho_r} \\ &\cdot \frac{{}_H\Gamma F(\rho_{01}, \omega_0) F(\rho_{02}, \omega_0)}{\sqrt{\rho_r [\rho_r^2 - (\rho/2)^2]}} e^{j(\delta\rho_{s0}/2)(K/\cos \phi_0)} \\ &\cdot (T_r \Delta \rho) \text{Sm}(K, \cos \phi_0, k_B, \Delta r), \end{aligned} \quad (24)$$

where  ${}_H\Gamma$  is the hydrodynamic coupling coefficient [13], accounting for the coupling of two first-order ocean waves, whose wavenumbers are  $K_1$  and  $K_2$ , respectively. Adding the electromagnetic contribution (18) and the hydrodynamic contribution (24) together and using the time-varying ocean wave surface to replace the time-invariant case, the total second-order bistatic electric field for an FMCW source with an antenna on a floating platform may be expressed as

$$\begin{aligned} (E_n)_2(\omega_r, t) &= \frac{-jI_0\eta_0\Delta k_0^2}{(2\pi)^{3/2}} \sum_{\vec{K}_1, \omega_1} \sum_{\vec{K}_2, \omega_2} P_{\vec{K}_1, \omega_1} P_{\vec{K}_2, \omega_2} \\ &\cdot {}_S\Gamma_P \sqrt{K} e^{j(\rho K/2) \cos(\theta_K - \theta)} e^{-j(\pi/4)} \\ &\cdot \sqrt{\cos \phi_0} e^{j(K \cos \phi_0 - 2k_0 + k_r)\rho_r} e^{j\omega t} \\ &\cdot \frac{F(\rho_{01}, \omega_0) F(\rho_{02}, \omega_0)}{\sqrt{\rho_r [\rho_r^2 - (\rho/2)^2]}} e^{j(\delta\rho_{s0}/2)(K/\cos \phi_0)} \\ &\cdot (T_r \Delta \rho) \text{Sm}(K, \cos \phi_0, k_B, \Delta r), \end{aligned} \quad (25)$$

where  ${}_S\Gamma_P = {}_S\Gamma_P + {}_H\Gamma$ .

Following the same procedure as for the first-order case, based on the total second-order time-varying received electric field (25), the corresponding second-order radar cross section,  $\sigma_2(\omega_d)$ , may be obtained as

$$\begin{aligned}
\sigma_2(\omega_d) = & 2^3 \pi k_0^2 \Delta \rho \sum_{m_1=\pm 1} \sum_{m_2=\pm 1} \int_0^\infty \int_{-\pi}^\pi \int_0^\infty S_1(m_1 \vec{k}_1) S_1(m_2 \vec{k}_2) |_{S\Gamma_P}|^2 K^2 \cos \phi_0 K_1 \text{Sm}^2(K, \cos \phi_0, k_B, \Delta r) \\
& \cdot \left\{ J_0^2 \left\{ \frac{aK}{2} \left| \cos(\theta_K - \theta_{K_p}) + \tan \phi_0 \sin(\theta_K - \theta_{K_p}) \right| \right\} \cdot \delta \left( \omega_d + m_1 \sqrt{gK_1} + m_2 \sqrt{gK_2} \right) \right. \\
& + \sum_{n=1}^\infty J_n^2 \left\{ \frac{aK}{2} \left| \cos(\theta_K - \theta_{K_p}) + \tan \phi_0 \sin(\theta_K - \theta_{K_p}) \right| \right\} \\
& \cdot \left[ \delta \left( \omega_d + m_1 \sqrt{gK_1} + m_2 \sqrt{gK_2} - n\omega_p \right) + \delta \left( \omega_d + m_1 \sqrt{gK_1} + m_2 \sqrt{gK_2} + n\omega_p \right) \right] \Big\} dK_1 d\theta_{\vec{k}_1} dK.
\end{aligned} \tag{26}$$

#### 4. Simulation and Discussion

Based on a Pierson-Moskowitz (PM) ocean spectral model [14], the newly derived radar cross sections, accounting for antenna sway, can be simulated to illustrate the differences in the FMCW and pulsed waveform cases. The sweep bandwidth of the FMCW waveform is chosen as 50 kHz. The operating frequency, defined as the central frequency of the FMCW waveform, is taken to be 25 MHz. The bistatic angle is  $30^\circ$  and the wind speed is 20 knots. The scattering ellipse normal and the wind direction are  $90^\circ$  and  $180^\circ$ , respectively, as measured from the positive  $x$ -axis (the line connecting the transmitter with the receiver). The sway amplitude and frequency depend on the wind velocity, and in keeping with an example used earlier [4], for the purpose of illustration, here these values are taken as 1.228 m and 0.127 Hz, respectively. The sway direction is chosen to be the same as the wind direction.

**4.1. First-Order Radar Cross Section.** Figure 2 shows a comparison of the first-order radar cross section for a pulsed source and that for an FMCW source. For the FMCW waveform,  $\Delta r = 1500$  m, which equals half the width of the scattering patch ( $\Delta \rho = 3000$  m) for the pulsed waveform, in order to keep the same bandwidth for both waveforms. A hamming window is used to smooth the curve and reduce the oscillations. From this figure, it can be observed that additional peaks caused by the antenna motion appear symmetrically in the Doppler spectrum with respect to the Bragg peaks. A detailed description and properties of these motion-induced peaks were discussed in [11]. It can also be seen that the magnitude of the radar cross sections for the FMCW waveform is a little lower than that for the corresponding pulsed waveform, which may be caused by the value of  $\Delta r$ .  $\Delta r$  is the limit value of the integral, where a sampling function dominates this integral.  $\Delta r$  is usually taken to be  $\Delta r = \Delta \rho / 2$ , which means only the contributions in the main lobe of the sampling function are considered and no interaction between the range bins is assumed in the ideal case.

It is clear that the first-order radar cross section has a certain relationship with the integral limit  $\Delta r$ . In Section 2, it may be observed that there is no mathematical limit for the parameter  $\Delta r$ . By varying  $\Delta r$ , the effect on the radar cross section can be examined. Keeping the value of  $\Delta \rho = 3000$  m,

$\Delta r = 0.5\Delta \rho$  and  $\Delta r = 10\Delta \rho$  are simulated in Figures 3(a) and 3(b), respectively. It should be mentioned that the hamming window smoothing process is not used in Figure 3 in order to clearly show the side lobe levels of the first-order radar cross sections. The side lobe structure appears in the radar Doppler spectra due to the side lobes of the Sm function for the FMCW waveform. By comparing Figures 3(a) and 3(b), the magnitude of the side lobes for FMCW source is found to decrease with increasing  $\Delta r$  and the main lobe level is a little raised with increasing  $\Delta r$  due to the properties of the Sm function. This seems to indicate an advantage of an FMCW system. When the value of  $\Delta r$  is taken to be larger than  $\Delta \rho / 2$ , the interactions between the range bins (the contributions in the side lobe of the sampling function) are considered and appear in the received electric field at a fixed distance. Increasing  $\Delta r$  means the received signal is scattered from a larger ocean surface region. When  $\Delta r$  approaches infinity, the radar cross section for the FMCW waveform becomes a rectangular function, whose width is determined by  $B/(2f_0\omega_B)$ . However, when the patch width  $\Delta \rho$  approaches infinity, the sampling functions in the first-order pulse radar ocean cross section reduce to delta functions.

By varying the radar bandwidth and keeping the relationships  $\Delta \rho = c/2B$  and  $\Delta r = \Delta \rho / 2$ , the effect of the bandwidth on the radar cross sections is illustrated in Figure 4. From this figure, it can be seen that, with increased bandwidth, the magnitudes of the Bragg peaks and the motion-induced peaks are found to be reduced, while the rest of the radar cross section increases. In addition, the width of the Bragg peaks and the motion-induced peaks is also broadened. Therefore, if a large radar bandwidth is used for ocean remote sensing, the Bragg peaks may be significantly contaminated by the motion-induced peaks.

**4.2. Second-Order Radar Cross Section.** A similar technique is used to simplify and simulate the second-order radar ocean cross section for the FMCW waveform as that for the pulsed waveform in [12, 15]. For the case of large  $\Delta r$ , it can be shown that

$$\begin{aligned}
\lim_{\Delta r \rightarrow \infty} \left[ \Delta \rho \text{Sm}^2(K, \cos \phi_0, k_B, \Delta r) \right] & \approx \Delta \rho \cos \phi_0 \\
& \cdot \{ h [K - \cos \phi_0 (2k_0 - k_B)] \\
& - h [K - \cos \phi_0 (2k_0 + k_B)] \}.
\end{aligned} \tag{27}$$

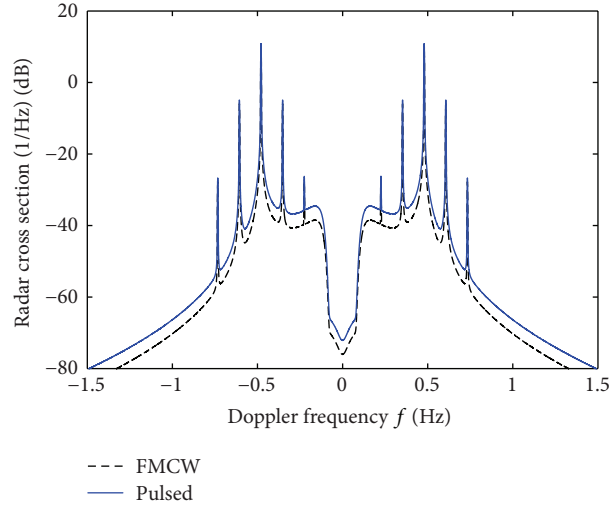


FIGURE 2: Comparison of the first-order radar cross sections for the FMCW waveform with that for the pulsed waveform.

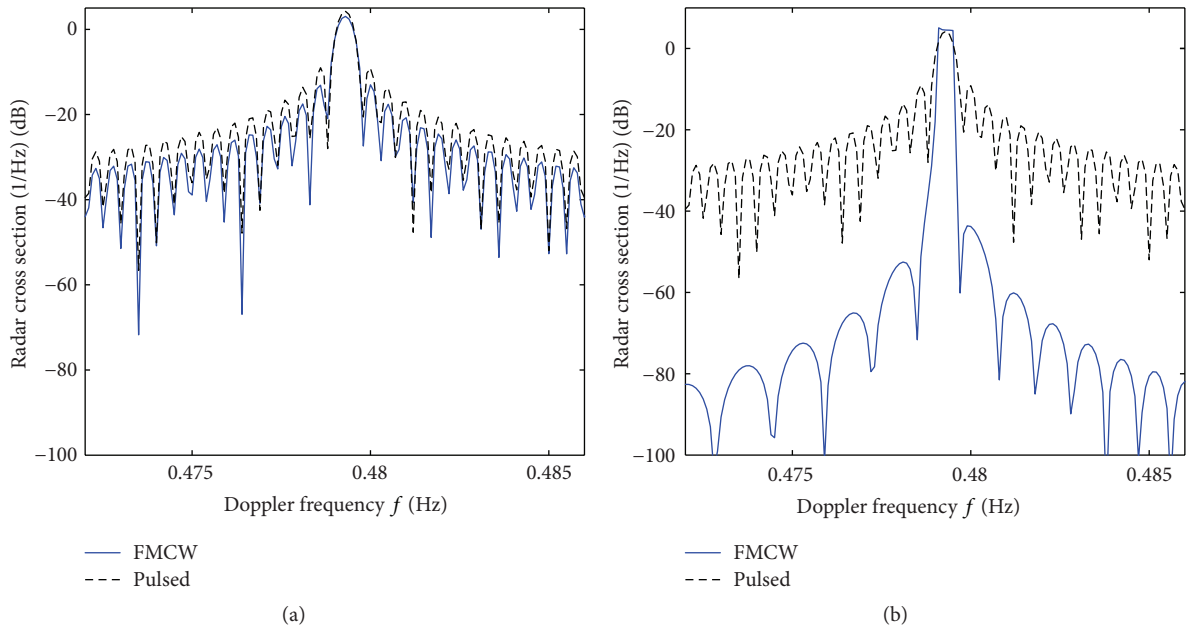


FIGURE 3: Comparison of the side lobe levels of the first-order radar cross sections for the pulsed and FMCW waveform. (a)  $\Delta r = 0.5\Delta\rho$  and (b)  $\Delta r = 10\Delta\rho$ .

Assuming that the other terms in (26) are slowly varying within the interval

$$\cos\phi_0(2k_0 - k_B) < K < \cos\phi_0(2k_0 + k_B) \quad (28)$$

and carrying out the  $K$  integration, (26) reduces to

$$\begin{aligned} \sigma_2(\omega_d) = & 64\pi^2 k_0^4 \cos^4\phi_0 \sum_{m_1=\pm 1} \sum_{m_2=\pm 1} \int_0^\infty \int_{-\pi}^\pi S_1(m_1 \vec{K}_1) \\ & \cdot S_1(m_2 \vec{K}_2) |_{S\Gamma_P}{}^2 K_1 \\ & \cdot \left\{ J_0^2 \left\{ \frac{aK}{2} \left| \cos(\theta_K - \theta_{K_p}) + \tan\phi_0 \right. \right. \right. \\ & \cdot \left. \left. \sin(\theta_K - \theta_{K_p}) \right\} \right\} \end{aligned}$$

$$\begin{aligned} & \cdot \delta\left(\omega_d + m_1 \sqrt{gK_1} + m_2 \sqrt{gK_2}\right) \\ & + \sum_{n=1}^\infty J_n^2 \left\{ \frac{aK}{2} \left| \cos(\theta_K - \theta_{K_p}) + \tan\phi_0 \right. \right. \\ & \cdot \left. \left. \sin(\theta_K - \theta_{K_p}) \right\} \right\} \\ & \cdot \left[ \delta\left(\omega_d + m_1 \sqrt{gK_1} + m_2 \sqrt{gK_2} - n\omega_p\right) \right. \\ & \left. + \delta\left(\omega_d + m_1 \sqrt{gK_1} + m_2 \sqrt{gK_2} + n\omega_p\right) \right] \\ & \cdot dK_1 d\theta_{\vec{K}_1}. \end{aligned}$$

(29)

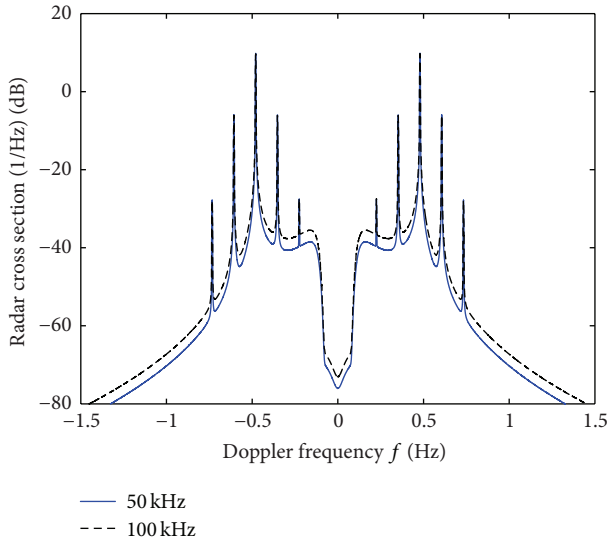


FIGURE 4: The effect of the bandwidth on the first-order radar cross sections.

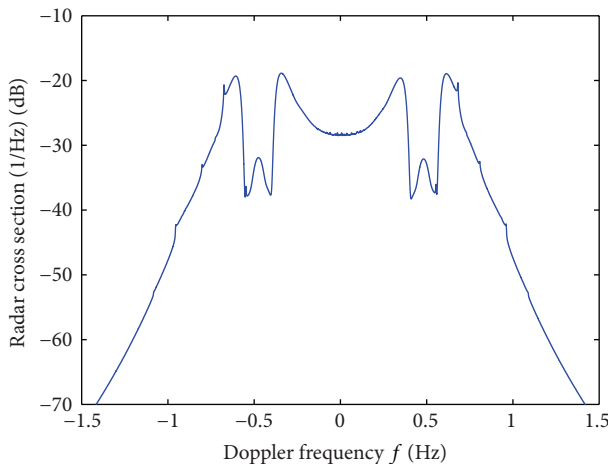


FIGURE 5: Second-order bistatic radar cross section with a transmitter on a floating platform.

Equation (29) is exactly the same as the corresponding model for the pulsed waveform when the scattering patch  $\Delta\rho$  approaches infinity. Therefore, the second-order cross section model for the FMCW waveform shows the same features in the Doppler spectra as the model for the pulsed waveform in [12], for a given sea state, radar operating parameters, and platform motion. An example of the second-order bistatic radar cross section with a transmitter on a floating platform and a fixed receiver is shown in Figure 5, for the case of the scattering patch being assumed to be infinite in extent.

## 5. Conclusion

The first- and second-order bistatic radar ocean cross sections for an antenna on a floating platform have been presented for the case of an FMCW waveform. In the derivation process, the first- and second-order models begin with

the bistatically received electric field equations derived in [11, 12]. Subsequently, the derivation is carried out for an FMCW radar, which is different from [11, 12] where a pulsed radar is considered. In particular, the distinguishing feature between the current work and that presented earlier is that demodulation and range transformation must be used to obtain the range information. Based on the new models, simulations are made to compare the radar cross sections for the FMCW waveform with that for the pulsed waveform. It is found that the first-order radar cross section for the FMCW waveform is a little lower than that for a pulsed source with the same simulation parameters. With increased radar operating bandwidth, the magnitude and width of Bragg peaks and motion-induced peaks are found to be reduced and broadened, respectively. For an FMCW waveform, there is no definite mathematical limit for a patch width, which is different from that for a pulsed waveform. Therefore, the magnitude of the range bin is varied to examine the effect on the radar cross section. The side lobe level is found to be reduced with increasing magnitude of the range bin. When the range bin approaches infinity, the first-order radar cross section for an FMCW waveform approaches a rectangular function and the second-order radar cross section model for the FMCW waveform is reduced to that of the pulsed waveform.

## Competing Interests

The authors declare that there are no competing interests regarding the publication of this paper.

## Acknowledgments

The work was supported in part by Natural Sciences and Engineering Research Council of Canada (NSERC) under Discovery Grants to Weimin Huang (NSERC 402313-2012) and Eric W. Gill (NSERC 238263-2010 and RGPIN-2015-05289) and by an Atlantic Innovation Fund Award (Eric W. Gill, principal investigator).

## References

- [1] D. E. Barrick, "First-order theory and analysis of MF/HF/VHF scatter from the sea," *IEEE Transactions on Antennas and Propagation*, vol. 20, no. 1, pp. 2–10, 1972.
- [2] J. Walsh and E. W. Gill, "An analysis of the scattering of high-frequency electromagnetic radiation from rough surfaces with application to pulse radar operating in backscatter mode," *Radio Science*, vol. 35, no. 6, pp. 1337–1359, 2000.
- [3] E. W. Gill and J. Walsh, "High-frequency bistatic cross sections of the ocean surface," *Radio Science*, vol. 36, no. 6, pp. 1459–1475, 2001.
- [4] J. Walsh, W. Huang, and E. Gill, "The first-order high frequency radar ocean surface cross section for an antenna on a floating platform," *IEEE Transactions on Antennas and Propagation*, vol. 58, no. 9, pp. 2994–3003, 2010.
- [5] J. Walsh, W. Huang, and E. Gill, "The second-order high frequency radar ocean surface cross section for an antenna

- on a floating platform,” *IEEE Transactions on Antennas and Propagation*, vol. 60, no. 10, pp. 4804–4813, 2012.
- [6] D. E. Barrick, “FM/CW radar signals and digital processing,” Tech. Rep. ERL 283-WPL 26, NOAA, 1973.
- [7] R. Khan, B. Gamberg, D. Power et al., “Target detection and tracking with a high frequency ground wave radar,” *IEEE Journal of Oceanic Engineering*, vol. 19, no. 4, pp. 540–548, 1994.
- [8] A. Wojthiewicz, J. Misiurewicz, M. Nalecz, K. Jedrzejewski, and K. Kulpa, “Two dimensional signal processing in FMCW radars,” in *Proceedings of the Conference on Circuit Theory and Electronics Circuits*, pp. 474–480, Kolobrzeg, Poland, October 1997.
- [9] J. Walsh, J. Zhang, and E. W. Gill, “High-frequency radar cross section of the ocean surface for an FMCW waveform,” *IEEE Journal of Oceanic Engineering*, vol. 36, no. 4, pp. 615–626, 2011.
- [10] S. Chen, E. W. Gill, and W. Huang, “A first-order HF radar cross-section model for mixed-path ionosphere-ocean propagation with an FMCW source,” *IEEE Journal of Oceanic Engineering*, 2016.
- [11] Y. Ma, E. Gill, and W. Huang, “The first-order bistatic high frequency radar ocean surface cross section for an antenna on a floating platform,” *IET Radar, Sonar & Navigation*, vol. 10, no. 6, pp. 1136–1144, 2016.
- [12] Y. Ma, W. Huang, and E. Gill, “The second-order bistatic high frequency radar ocean surface cross section for an antenna on a floating platform,” *Canadian Journal of Remote Sensing*, vol. 42, no. 4, pp. 332–343, 2016.
- [13] K. Hasselmann, “On the non-linear energy transfer in a gravity-wave spectrum part 1. General theory,” *Journal of Fluid Mechanics*, vol. 12, pp. 481–500, 1962.
- [14] W. J. Pierson and L. Moskowitz, “A proposed spectral form for fully developed wind seas based on the similarity theory of S. A. Kitaigorodskii,” *Journal of Geophysical Research*, vol. 69, no. 24, pp. 5181–5190, 1964.
- [15] B. J. Lipa and D. E. Barrick, “Extraction of sea state from HF radar sea echo: mathematical theory and modeling,” *Radio Science*, vol. 21, no. 1, pp. 81–100, 1986.